



**HAL**  
open science

# Optical absorption by design in a ferroelectric: co-doping in BaTiO<sub>3</sub>

Shenglan Hao

► **To cite this version:**

Shenglan Hao. Optical absorption by design in a ferroelectric: co-doping in BaTiO<sub>3</sub>. Theoretical and/or physical chemistry. Université Paris-Saclay, 2022. English. NNT: 2022UPAST006. tel-04404495

**HAL Id: tel-04404495**

**<https://theses.hal.science/tel-04404495v1>**

Submitted on 19 Jan 2024

**HAL** is a multi-disciplinary open access archive for the deposit and dissemination of scientific research documents, whether they are published or not. The documents may come from teaching and research institutions in France or abroad, or from public or private research centers.

L'archive ouverte pluridisciplinaire **HAL**, est destinée au dépôt et à la diffusion de documents scientifiques de niveau recherche, publiés ou non, émanant des établissements d'enseignement et de recherche français ou étrangers, des laboratoires publics ou privés.

# Absorption optique par conception dans un ferroélectrique: co-dopage dans BaTiO<sub>3</sub>

*Optical absorption by design in a ferroelectric: co-doping in BaTiO<sub>3</sub>*

## Thèse de doctorat de l'université Paris-Saclay

École doctorale n° 573 d'Interfaces : approches interdisciplinaires, fondements, applications et innovation (Interfaces)

Spécialité de doctorat : Physique

Graduate School : Sciences de l'ingénierie et des systèmes. Référent : CentraleSupélec

Thèse préparée dans le **Laboratoire SPMS** (Université Paris-Saclay, CentraleSupélec, CNRS), sous la direction de **Igor KORNEV**, professeur, et le co-encadrement de **Charles PAILLARD** et **Brahim DKHIL**, Maîtres de conférences

Thèse soutenue à Paris-Saclay, le 18 janvier 2022, par

**Shenglan HAO**

## Composition du Jury

<b>Raphaël Haumont</b> Professeur, Université Paris-Saclay	Président
<b>Doru Lupascu</b> Professeur, University of Duisburg-Essen	Rapporteur & Examineur
<b>Maël Guennou</b> Professeur, University of Luxembourg	Rapporteur & Examineur
<b>Mojca Otoničar</b> Professeur associé, Jožef Stefan Institute	Examinatrice
<b>Igor Kornev</b> Professeur, Université Paris-Saclay	Directeur de thèse
<b>Brahim Dkhil</b> Maître de conférences, Université Paris-Saclay	Co-Directeur de thèse
<b>Charles Paillard</b> Maître de conférences, Université Paris-Saclay	Co-Directeur de thèse



**Titre :** Absorption optique par conception dans un ferroélectrique : co-dopage dans BaTiO<sub>3</sub>

**Mots clés :** Ferroélectrique, Photovoltaïque, Titanate de baryum, Ingénierie Bandgap, Co-dopage

**Résumé :** Les dispositifs photovoltaïques basés sur des ferroélectriques ont suscité un grand intérêt en raison de leurs perspectives prometteuses dans la récupération d'énergie solaire, les photocatalyseurs ou les dispositifs électro-optiques. Les ferroélectriques ont une polarisation spontanée, ce qui est utile pour séparer les porteurs photogénérés. Le défi est que la plupart des ferroélectriques ont une bande interdite supérieure à 3 eV, limitant l'absorption du spectre solaire. Généralement, la bande interdite des oxydes de structure pérovskite ABO<sub>3</sub> peuvent être manipulée par substitution chimique. Dans ce travail, tout d'abord, l'effet du codopage (Mn<sup>3+</sup>, Nb<sup>5+</sup>) de BaTiO<sub>3</sub> sur le site B de la pérovskite (BaTi<sub>1-x</sub>(Mn<sub>1/2</sub>Nb<sub>1/2</sub>)<sub>x</sub>O<sub>3</sub>) a été étudié. La bande interdite passe de 3,4 eV pour le BaTiO<sub>3</sub> pur à 2,5 eV pour les échantillons dopés. Par ailleurs, le début d'absorption se fait dès 1.5 eV, ce qui est prometteur pour la récupération d'énergie solaire. En revanche, les propriétés ferroélectriques se détériorent avec l'augmentation du taux de dopage en particulier au-delà de 0,075 de dopage. L'influence du taux de dopage sur la structure a également été étudiée. Puis, nous avons étudié les effets des paramètres de synthèse sur la microstructure, les propriétés électriques et optiques des matériaux BaTi<sub>1-x</sub>(Mn<sub>1/2</sub>Nb<sub>1/2</sub>)<sub>x</sub>O<sub>3</sub> (x = 0,075). La température de Curie T<sub>c</sub> varie fortement avec les conditions de synthèse, notamment en fonction de la vitesse de broyage. Cependant bien que les propriétés ferroélectriques sont impactées, il n'y a qu'une faible variation de l'absorption optique. Nous avons aussi étudié l'absorption optique du codopage BaTi<sub>1-x</sub>(X<sub>1/2</sub>Y<sub>1/2</sub>)<sub>x</sub>O<sub>3</sub>, X = Sc, Mn, Fe, Co; Y = Nb, Ta). On constate que le co-dopage (Co<sup>3+</sup>, Nb<sup>5+</sup>) montre une polarisation spontanée plus élevée que pour les autres dopants, et que l'absorption démarre dès 1,5 eV. Nous avons confirmé ce résultat par des calculs de la Théorie de la Fonctionnelle Densité (DFT), qui montrent que le codopage avec des ions 3d<sup>≠0</sup> insère des niveaux intra-gap qui vont être responsables de la réduction « artificielle » de la bande interdite. Ceci est tout à fait en accord avec nos observations expérimentales. La tétragonalité et la longueur de cohérence polaire diminuent après le co-dopage, impactant les caractéristiques ferroélectriques. La photoconductivité mesurée confirme que le dopage (Co<sup>3+</sup>, Nb<sup>5+</sup>) a une absorption supérieure aux autres dopants. Nous avons aussi considéré un codopage du BaTiO<sub>3</sub> par des ions (X<sup>2+</sup>, Y<sup>6+</sup>) sur le site B ou les sites A-B. Contrairement à nos calculs par DFT, l'absorption optique montre un léger changement en fonction des différents couples de dopage, et la bande interdite n'a que peu de changement. Le comportement ferroélectrique est en revanche modifié avec des courbes d'hystérésis qui s'affinent de sorte qu'avec le codopage (Zn<sup>2+</sup>, Mo<sup>6+</sup>) et (Zn<sup>2+</sup>, W<sup>6+</sup>) on obtient des réponses de stockage d'énergie plus élevée que le BaTiO<sub>3</sub> pur. En conclusion, ce travail de recherche montre l'efficacité de cette stratégie de codopage dans le matériau ferroélectrique modèle BaTiO<sub>3</sub> et comment en parallèle les propriétés ferroélectriques peuvent être impactées. Ces matériaux peuvent ainsi avoir des retombées dans de futurs dispositifs optoélectroniques.

**Title :** Optical absorption by design in a ferroelectric: co-doping in BaTiO<sub>3</sub>

**Keywords :** Ferroelectric, Photovoltaic, BaTiO<sub>3</sub>, Bandgap engineering, Co-doping

**Abstract :** Photovoltaic devices based on ferroelectrics have aroused vast interest due to their promising prospective in solar energy harvesting, photocatalysts, or optic-electro devices. Ferroelectrics have spontaneous polarization, which is helpful to separate the photogenerated carriers. The challenge is that most ferroelectrics have a typical bandgap larger than 3 eV, limiting the absorption of the solar spectrum. Generally, the bandgap ABO<sub>3</sub> perovskite oxides can be tuned by chemical substitution. In the present work, firstly, the effect of (Mn<sup>3+</sup>, Nb<sup>5+</sup>) co-doping BaTiO<sub>3</sub> on the B sites (BaTi<sub>1-x</sub>(Mn<sub>1/2</sub>Nb<sub>1/2</sub>)<sub>x</sub>O<sub>3</sub>) was investigated. The bandgap decreases from 3.4 eV for pure BaTiO<sub>3</sub> to 2.5 eV for doped samples. Besides, the onset absorption drops down to 1.5 eV, which is promising for solar energy harvesting. The ferroelectricity decreases with the increase of doping levels. There is no ferroelectric properties with doping higher than 0.075. The influence of doping concentration on the structure was also investigated. Secondly, we have investigated the effects of the synthesis parameters on the microstructure, electrical and optical properties of BaTi<sub>1-x</sub>(Mn<sub>1/2</sub>Nb<sub>1/2</sub>)<sub>x</sub>O<sub>3</sub> (x = 0.075) materials. The Curie temperature  $T_c$  shows strong variations on the synthesis conditions, specifically it depends on the ball-milling rate. Nevertheless, while the ferroelectric properties are affected, the absorption properties are weakly, if any, changes. We also studied the optical absorption of co-doped BaTi<sub>1-x</sub>(X<sub>1/2</sub>Y<sub>1/2</sub>)<sub>x</sub>O<sub>3</sub>, (X = Sc, Mn, Fe, Co; Y= Nb, Ta) systems. It is found that (Co<sup>3+</sup>, Nb<sup>5+</sup>) co-doping shows higher remnant polarization than the others, and the onset of absorption of this doping can decrease down to 1.5 eV. We have confirmed this by Density Functional Theory (DFT) calculations, demonstrating that the co-doping with 3d<sup>≠0</sup> ions inserts intra-gap levels responsible for "artificially" reducing the optical bandgap, fully in line with our experimental observations. The tetragonality and the polar coherence length decrease after co-doping, impacting the ferroelectric features. The measured photoconductivity confirms that (Co<sup>3+</sup>, Nb<sup>5+</sup>) doping has superior absorption than others. Finally, we also considered (X<sup>2+</sup>, Y<sup>6+</sup>) co-doping of BaTiO<sub>3</sub> by substitution on B sites or A-B sites. In contrast to our DFT calculations, the optical absorption shows a slight change whatever the dopants investigated, and the bandgap has only a tiny change. However, the ferroelectric behavior degenerates after doping, making the hysteresis loops slimmer, which permits (Zn<sup>2+</sup>, Mo<sup>6+</sup>) and (Zn<sup>2+</sup>, W<sup>6+</sup>) co-doping to show high energy storage responses, bigger than pure BaTiO<sub>3</sub>. Finally, this research work shows that co-doping in BaTiO<sub>3</sub> is a good strategy for narrowing the bandgap and how the ferroelectric properties are impacted, providing key ingredients for the application of such materials in optoelectronic devices.

# Acknowledgments

Time is flying. The three years study life in France is short but memorable. I have known so many interesting people here and learned a lot of new things. I am grateful to everyone I know here. Before starting, I would like to thank all the jury members, Prof. Doru Lupascu, Prof. Maël Guennou, Prof. Raphaël Haumont, and Asst. Prof. Mojca Otoničar. I am honored that they would like to come to my defense and take the time to read this manuscript. I would like to thank Prof. Igor Kornev, my official supervisor, who always makes the admission work go well.

I would like to express my gratitude to my thesis supervisor Dr. Brahim Dkhil for giving me the opportunity to work with him. He is one of the most knowledgeable and wise supervisors I know. He seems to know everything. During the three years, he always gives me helpful advice, encouragement, and invaluable help in academics and real life. I have learned a lot from him to do research and enjoy life. Physics is complicated for me, but he can always explain everything and make it easy to understand, which has been impressive and important to me. Thanks to him, my Ph.D. life is not so hard or stressed. I am grateful to work with him. I will miss him and, of course, the funny jokes.

I would also like to thank everyone in SPMS for their help in my work. More specially, I would like to thank Charles Paillard for the simulation part of my work and all the suggestions he gave me that made the work go well. I also acknowledge Pascale Gemeiner for all her help in the Raman and optical measurements. Thank Christine Bogicevic and Fabienne Karolak for their help in experiments, who support us to work in a very convenient atmosphere in the chemistry lab. Thank Nicolas Guiblin and Omar Ibder for their help and support in the measurements. I appreciate it. I am grateful to Pierre-Eymeric Janolin and Guilhem Dezanneau for their helpful suggestions, and they are always ready to help me. I also would like to thank Pascale Salvini, Céline Freydier, Agnès Benard, and Thierry Martin for their help during the three years. I thank all the Ph.D. students in SPMS who are always ready to help me and give me an excellent study

and working atmosphere, and lovely memories.

I would also like to thank Prof. Mojca Otonicar, who helped me a lot do the microscopy of the ceramics; thanks for her patience and hard work. Thank Prof. Houssny Bouyanfif, who taught me how to grow thin film; thanks for his indispensable help to give the future of this work. I would also like to thank Prof. Pascal Ruello. Thanks for his help or suggestions on my work. Thanks for their corrections and hard work on the paper or abstract I submitted.

Finally, I would also like to thank a lot the China government and the China Scholarship Council for the support of funding. Thanks for all the help and support from my family and friends during the three years. Thanks to everyone who knows my name.

# General preamble

The manuscript was written using article-based formatting and composed of one published, submitted article (Chapter 4). The title is:

Optical absorption by design in a ferroelectric: co-doping in BaTiO<sub>3</sub>. *Journal of Materials Chemistry C*, 10(1), 227 – 234, 2022. Hao, S., Yao, M., Vitali-Derrien, G., Gemeiner, P., Otoničar, M., Ruello, P., Bouyanfif, H., Janolin, P.-E., Dkhil, B., & Paillard, C. <https://doi.org/10.1039/d1tc04250e>

In this work, the calculation part was done with the help of Charles Paillard.



# Contents

Acknowledgments.....	I
General preamble.....	I
1 Introduction.....	1
1.1 Conventional Solar Cells.....	1
1.2 Ferroelectric materials.....	2
1.3 Photovoltaic effect in ferroelectrics.....	4
1.3.1 Bulk photovoltaic effect.....	5
1.3.2 Domain wall contribution.....	7
1.3.3 Depolarization field model.....	8
1.3.4 Schottky-junction effect.....	9
1.4 Recent progress of ferroelectric photovoltaics.....	10
1.4.1 Power conversion efficiency.....	10
1.4.2 Applications.....	13
1.5 Bandgap engineering.....	14
1.5.1 Chemical substitution.....	15
1.5.2 Alloying solutions.....	20
1.6 Plan of this work.....	21
2 Enhanced optical absorption in ferroelectric BaTiO <sub>3</sub> by Mn and Nb co-doping.....	25
Abstract.....	25
2.1 Introduction.....	25
2.2 Experimental procedure.....	27
2.2.1 Material preparation.....	27
2.2.2 Characterization.....	27
2.3 Results and discussion.....	28
2.3.1 Microstructure of pure and co-doped BTO samples.....	28
2.3.2 Optical absorption of pure and co-doped BTO samples.....	33
2.3.3 Dielectric spectroscopy of pure and co-doped BTO samples.....	35
2.3.4 Ferroelectric properties of pure and co-doped BTO samples.....	36
2.3.5 Temperature-dependent evolution of different physical properties.....	38
2.4 Conclusions.....	52
3 The impact of synthesis conditions on the properties of Mn and Nb co-doped BaTiO <sub>3</sub> .....	55
Abstract.....	55
3.1 Introduction.....	55
3.2 Experimental procedure.....	57
3.2.1 Material preparation.....	57

3.2.2	Characterization.....	57
3.3	Results and Discussion.....	58
3.3.1	The dependence of the microstructure on synthesis conditions .....	58
3.3.2	The dependence of the optical absorption on synthesis conditions .....	65
3.3.3	The dependence of the electrical properties on synthesis conditions .....	67
3.4	Conclusions .....	71
3.5	Supporting Information .....	72
4	Optical absorption of ferroelectric ( $X^{3+}$ , $Y^{5+}$ ) co-doped $BaTiO_3$ .....	77
	Abstract.....	77
4.1	Introduction .....	77
4.2	Experimental procedure .....	81
4.2.1	Material preparation .....	81
4.2.2	Characterization.....	81
4.2.3	Computational Methods .....	82
4.3	Results and Discussion.....	83
4.3.1	The microstructure of undoped BTO and co-doped BTO .....	83
4.3.2	The ferroelectric properties of undoped BTO and co-doped BTO.....	86
4.3.3	The optical absorption of undoped BTO and co-doped BTO .....	88
4.3.4	The photoresponse with light illumination.....	91
4.4	Conclusions .....	93
5	Optical absorption of ferroelectric ( $X^{2+}$ , $Y^{6+}$ ) co-doped $BaTiO_3$ .....	95
	Abstract.....	95
5.1	Introduction .....	95
5.2	Experimental procedure .....	99
5.3	Results and Discussion .....	99
5.3.1	$BaTi_{1-x}(Mg_{1/2}W_{1/2})_xO_3$ ( $x = 0.025 \sim 0.5$ ) solid solutions.....	99
5.3.2	$BaTi_{1-x}(X_{1/2}Y_{1/2})_xO_3$ ( $X = Ni$ or $Zn$ , $Y = W$ or $Mo$ , $x = 0.075$ ) solid solutions...	101
5.3.3	$Ba_{1-x}X_xTi_{1-3/2x}Y_xO_3$ ( $X = Ni$ , $Y = W$ or $Mo$ , $x = 0.075$ ) solid solutions.....	105
5.4	Conclusions .....	108
5.5	Supporting information .....	108
6	Conclusions and perspectives.....	111
6.1	Conclusions .....	111
6.2	Perspectives .....	112
6.2.1	( $Co^{3+}$ , $Nb^{5+}$ ) doped BTO thin film.....	113
6.2.2	Optical absorption of ( $Co^{3+}$ , $Nb^{5+}$ ) co-doped BFO.....	114
	References .....	115
	Résumé français de la thèse.....	131

# 1 Introduction

Photovoltaics (PV) directly converts solar energy into electricity. It offers sustainable and clean energy sources to meet the increasing demands of reliable energy and clean fuel sources. Silicon-based solar cells are one of the most commercially available photovoltaic devices, with high efficiency reaching a record value of about 25.6 %. However, this value is getting closer to the theoretical limit, known as Shockley-Queisser's (S-Q) limit.<sup>[1]</sup> So there is still a need to develop the technology to further improve energy conversion efficiencies and design new simple and alternative materials for PV applications. Ferroelectric materials are among these alternative materials, as they exhibit anomalous PV effects, which are not limited by the S-Q theory. Ferroelectrics have been worldwide challenged as PV solar cell components and the efficiency of ferroelectric perovskite solar cells has significantly improved in recent years.

## 1.1 Conventional Solar Cells

In a traditional single *p-n* junction-based photovoltaic device, as shown in Fig. 1-1, the photogenerated charge carriers (electron-hole pairs) are separated by the built-in electric field in the depletion layer at the *p-n* junction interface. In photovoltaic devices, when the incident energy is lower than the bandgap of the semiconductors, the energy cannot be absorbed and used for generating electron-hole pairs, and only above bandgap absorption can photogenerate electrons and holes. However, only a part of the light absorbed will be suitable for generating electricity. Indeed, when photons with energy above the bandgap photoinduce electrons and holes in the semiconductor, there is a process of thermalization by energy disexcitation through phonons. As a consequence, the excess energy will raise the temperature of the device through photon-phonon interaction. Besides, there are also other losses, which may come from the reflection, electrodes, or the interface of the solar cell devices. So finally, all these losses lead to the limit of energy conversion efficiency to 33.7 % for a single-junction

solar cell using an optimal semiconductor with a bandgap of 1.34 eV, which is the so-called Shockley-Queisser (S-Q) limit.<sup>[2]</sup>

The current-voltage characteristics that include the short-circuit current and the open-circuit voltage are the main factors for determining the efficiency of PV devices. The magnitude of the open-circuit voltage ( $V_{oc}$ ) of p-n junction cells is determined by the quasi-Fermi energy difference of photogenerated electrons and holes, which is limited by the bandgap of the absorption materials. There are several approaches to improve the efficiency, such as using optimum transparent conductors, increasing the scattering of the visible light, combining with luminescent solar concentrators, thin films, and heterojunctions. By optimizing all these parameters, a solar cell efficiency of 47.1 % was achieved using a multijunction concentrator.<sup>[3]</sup> However, because of the S-Q limit, fabrication cost, and limited  $V_{oc}$ , among others, there is an active research for finding new alternative materials.

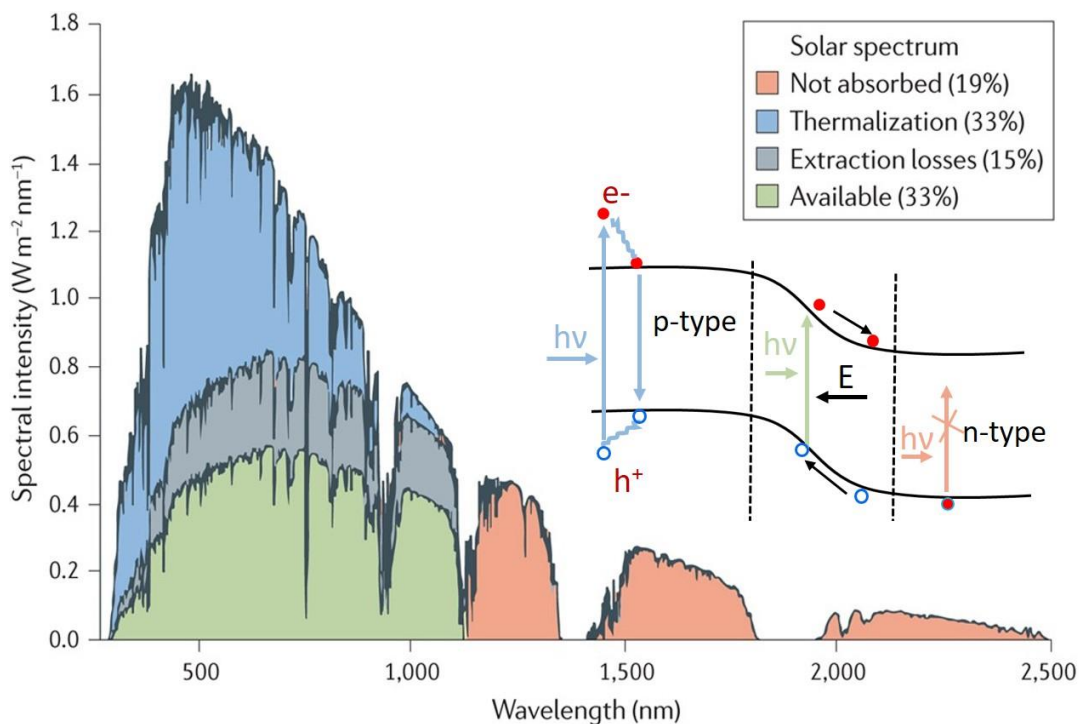


Fig. 1-1 The solar spectrum and mechanism of the p-n junction. Reproduced from Ref.<sup>[4]</sup>

## 1.2 Ferroelectric materials

Ferroelectric materials exhibit a spontaneous polarization that can be reversed by

applying an electric field. The interaction between the polarization ( $P$ ) and electric field ( $E$ ) yields a hysteresis loop (see Fig. 1-2a).<sup>[5]</sup> This curve is analogous to the ferromagnetic materials, which possess a reversible spontaneous magnetization under a magnetic field. As shown in Fig. 1-2a, the remnant polarization ( $P_r$  or  $-P_r$ ) is the polarization amplitude with zero electric field. The saturation polarization  $P_s$  is observed when the polarization becomes roughly unchanged at a high electric field. The electric field corresponding to the polarization switchability, i.e. when  $P = 0$  is named coercive field ( $E_c$ ). These are the essential parameters associated to ferroelectricity, which only exist below the Curie temperature ( $T_c$ ), at which a phase transition between the ferroelectric and paraelectric phases occurs. Here, the phase transition can be described with the Landau theory taking  $P$  as the order parameter.<sup>[6]</sup> The free energy can be expressed as a Taylor expansion:

$$F = \frac{1}{2}a(T - T_c)P^2 + \frac{1}{4}bP^4 + \dots \quad (1-1)$$

As shown in Fig. 1-2b, for ferroelectrics with a second-order phase transition, the constant  $a$  is positive, so when  $T > T_c$ , it shows a parabolic shape, the polarization is zero at the minimum energy because the structure is centrosymmetric in the paraelectric phase. When the temperature  $T < T_c$ , the energy versus polarization shows a double-well shape. In one dimension, there are two polarization directions as the dipoles are formed due to the displacement of ions from their ideal center. It has to be noted that here we take a perovskite oxide ( $ABO_3$ ) ferroelectric as an example, but not all the ferroelectrics crystalize in the perovskite structure. The change of polarization can be smooth at the Curie temperature, and then the transition is coined as second-order transition, while for a first-order phase transition, the polarization is discontinuous at  $T_c$ . In addition to the order-disorder mechanism to explain ferroelectricity, the soft mode theory, based on the phonon frequency ( $\omega$ ) renormalization due to the thermal anharmonicity, is also used to describe the displacive nature of the phase transition.<sup>[5,7]</sup> The squared phonon vibration frequency linearly decreases/softens with cooling temperature, as described in the equation below. When the temperature is below  $T_c$ , the mode becomes unstable, the vibration frequency falls to 0 at  $T_c$ , and the ferroelectric state takes place instead of the centrosymmetric paraelectric phase.

$$\bar{\omega}^2 = -\frac{\omega_0^2}{T_c}(T - T_c) \quad (1-2)$$

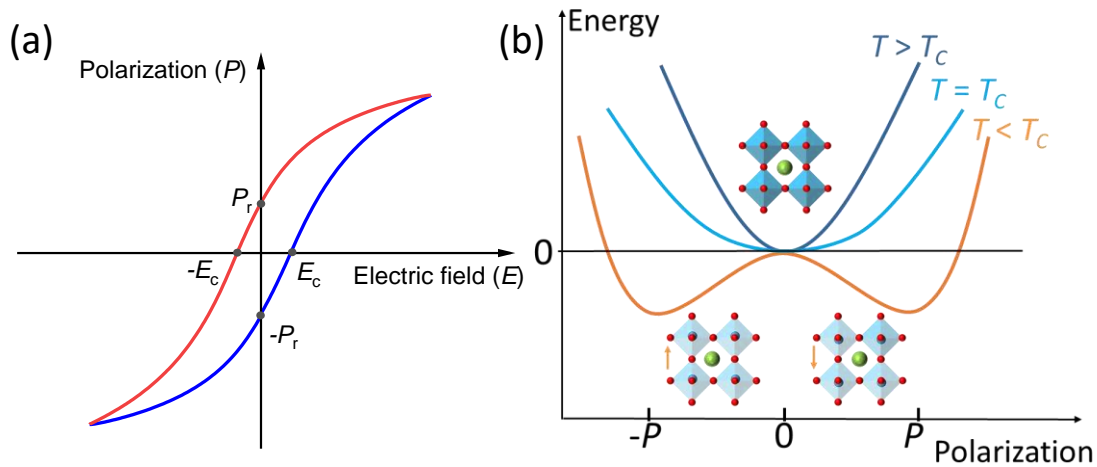


Fig. 1-2 (a) P-E hysteresis loop of a ferroelectric; (b) Landau type energy landscape with a perovskite oxide as an example

## 1.3 Photovoltaic effect in ferroelectrics

Ferroelectrics have aroused broad interest due to their potential use in optical applications, including photovoltaic solar cells, photocatalysts, or innovative elasto-optic devices.<sup>[8-11]</sup> Ferroelectrics exhibit an intrinsic spontaneous electric polarization that is the core of their photovoltaic properties, different from those based on the  $p$ - $n$  junction in classical semiconductors. Under the illumination, the photogenerated electrons and holes are separated by the polarization-induced internal electric field in opposite directions, as depicted in Fig. 1-3. The efficiency of the ferroelectric-based devices is suggested to surpass the S-Q limit. The ferroelectric photovoltaic effect shows many unique and essential features. The remnant polarization and the associated polarization-induced internal electric field exist over the whole bulk region of the ferroelectric rather than within a thin interfacial depletion layer. The output voltage is proportional to the polarization magnitude and electrode spacing, which can generate above bandgap photo-voltage, and opens new perspectives for designing novel photovoltaic devices.<sup>[12]</sup> In addition, the direction of the photocurrent can also be switched by reversing the direction of the polarization.<sup>[13-15]</sup> It is worth noting that composites using multiferroic or ferromagnetic materials can also lead to the control of

the photovoltaic effect by a magnetic field.

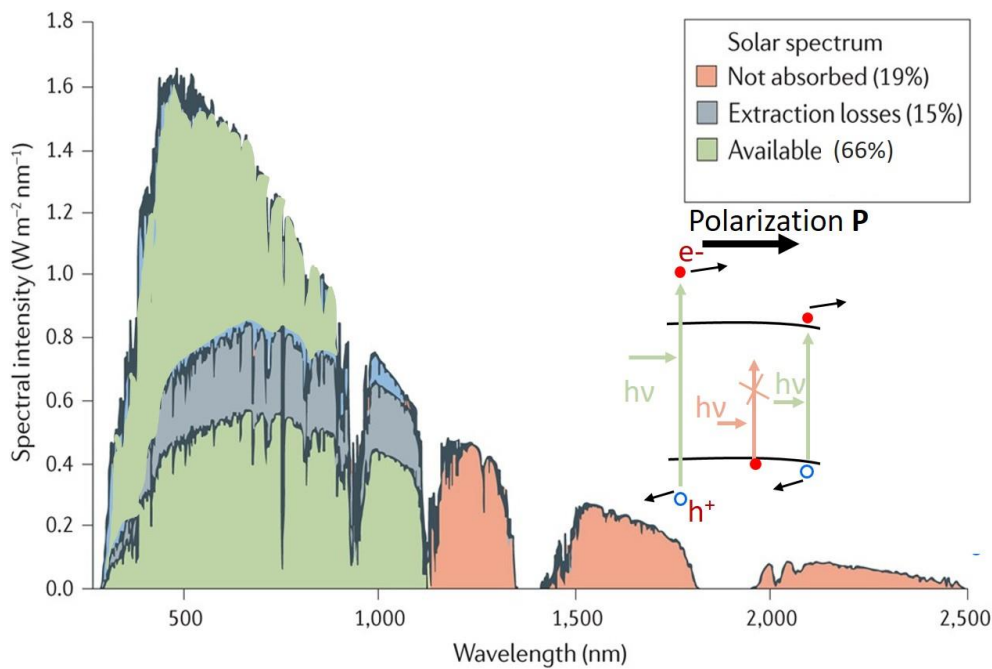


Fig. 1-3 Schematic illustrations of the mechanism of ferroelectric photovoltaic effect

Since the discovery of the so-called anomalous photovoltaic effect, in order to investigate the ultrahigh photovoltage output, several models have been proposed. In the following, the mechanisms widely considered for the charge separation in ferroelectrics are described, despite the need for further understanding advancements.<sup>[10,16,17]</sup>

### 1.3.1 Bulk photovoltaic effect

The bulk photovoltaic effect (BPE) was firstly discovered in bulk ferroelectric crystals characterized by the absence of the symmetry center.<sup>[18]</sup> Different from the classical semiconductor-based photovoltaic, in the BPE, the polarization and the depolarization field exist over the whole bulk region of the ferroelectric materials instead of only within the depletion layer. Thus, the photogenerated voltage can be much higher than the bandgap of the materials and is proportional to the electrode distance in the polarization direction. According to the Glass model, a steady short-circuit photocurrent  $J_{pv}$  is generated in the BPE, described as<sup>[19,20]</sup>:

$$J_{pv} = \alpha GI \quad (1-3)$$

### 1.3 Photovoltaic effect in ferroelectrics

where  $G$  and  $\alpha$  are the Glass coefficient and absorption coefficient, respectively, and  $I$  is the light intensity. In the open-circuit conditions, the total current  $J = 0$ , so the photovoltage can be described as:

$$V_{oc} = Ed = \frac{J_{pv}d}{\sigma_d + \sigma_{pv}} \quad (1-4)$$

where  $\sigma_d$  and  $\sigma_{pv}$  are dark conductivity and photoconductivity, respectively,  $d$  is the distance between two electrodes.<sup>[21]</sup> As reported in the  $\text{LiNbO}_3:\text{Fe}$  crystal,<sup>[22]</sup> the iron impurities provide the asymmetric centers, allowing the photogenerated electrons to transfer in one direction and then generate the current. The photoexcited electrons descend to the bottom of the conduction band, leading to the shift in space  $l_0$ , as shown in Fig. 1-4a. The imbalance shift forms an asymmetric momentum distribution, which results in a photovoltaic current. The diffusion length  $l_0$  is estimated at 10-100 nm, and then, the optimal current can be obtained when the thickness of the crystal is similar to the length. So for photovoltaic devices, it is essential to have thin films.<sup>[21,23]</sup> According to the equation, the voltage is expected to increase linearly with the light intensity when it is in a small range, and the  $\sigma_{pv}$  can be considered to be a constant, significantly lower than  $\sigma_d$ .<sup>[19]</sup> In addition, when  $\sigma_{pv}$  is much larger than  $\sigma_d$ , the  $V_{oc}$  has no dependence on the light intensity  $I$ , and it will become saturated. Fig. 1-4b exhibits the photocurrent measurement of BTO thin films, suggesting the same photovoltage for different light intensities.<sup>[21]</sup>

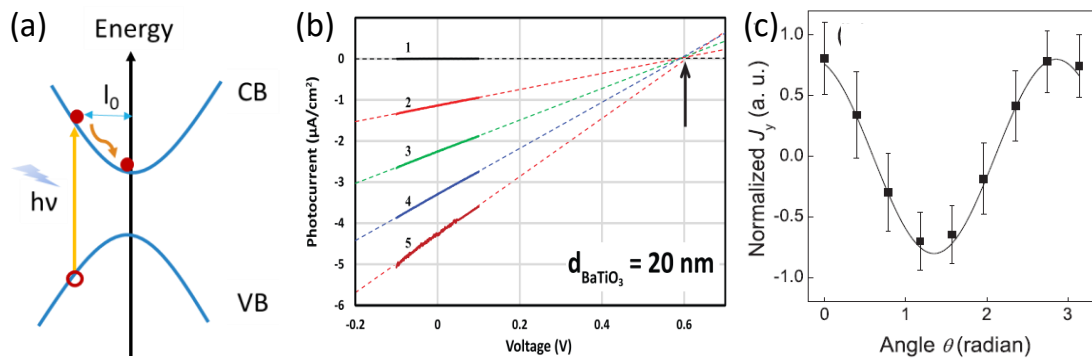


Fig. 1-4 (a) Photoexcited carries momentum distribution non-centrosymmetric crystals corresponding to the BPE; (b) Photovoltaic current of BTO thin films with the dependence of different light intensity, ranging from dark to  $0.75 \text{ W}/\text{cm}^2$ ; (c) Normalized current density in y-axis direction at different polarization angles. Reproduced from Ref<sup>[21,24]</sup>

V. Fridkin developed a model where the photocurrent is proportional to a third-rank

tensor, which is described as<sup>[20,25]</sup>:

$$J_i = \alpha I G_{ijk} e_j e_k \quad (1-5)$$

where  $G_{ijk}$  is a third-rank tensor of Glass coefficient and  $e_j, e_k$  are the unit of the light polarization vector. For example, Ji *et al.* reported that the current density was affected by the variation in light when the polarizer was rotated.<sup>[24]</sup> As shown in Fig. 1-4(c), the current along the  $y$  axis direction (the direction perpendicular to the electrode in-plane) follows a cosine function of  $2\theta$ , where  $\theta$  is the angle between the  $y$  axis and the light polarization direction. In addition, it has also been observed that the current in BiFeO<sub>3</sub> (BFO) (001) film was much larger than in (111) oriented film with the same light intensity. This is because the polarization in BFO is along (111) directions and the BPE photocurrent flowed in the opposite direction of the depolarization field, which canceled the overall photocurrent.

### 1.3.2 Domain wall contribution

Yang *et al.* reported that the large photovoltage (up to 16 V) in a BFO single crystal originated from the domain walls rather than the bulk effect.<sup>[12]</sup> They investigated two different device geometries. A large photovoltage was obtained with in-plane electrodes parallel to the domain walls shown in Fig. 1-5a-b. The photovoltaic effect disappeared with electrodes oriented perpendicular to the domain walls (see Fig. 1-5c-d). In addition, the voltage is proportional to the number of domain walls, and it can increase in multiple domain walls arranged in series.<sup>[12]</sup> However, there is no photovoltaic effect in a single domain BFO sample.<sup>[26]</sup> It is argued that in domain walls, similar to the depletion layer of a p-n junction, there is an electrostatic potential drop across the domain wall, which causes a much stronger electric field.<sup>[27,28]</sup> So the charge carriers can separate effectively. In contrast, there is a quick recombination of charge carriers in the bulk domain before diffusing to each side.<sup>[29]</sup>

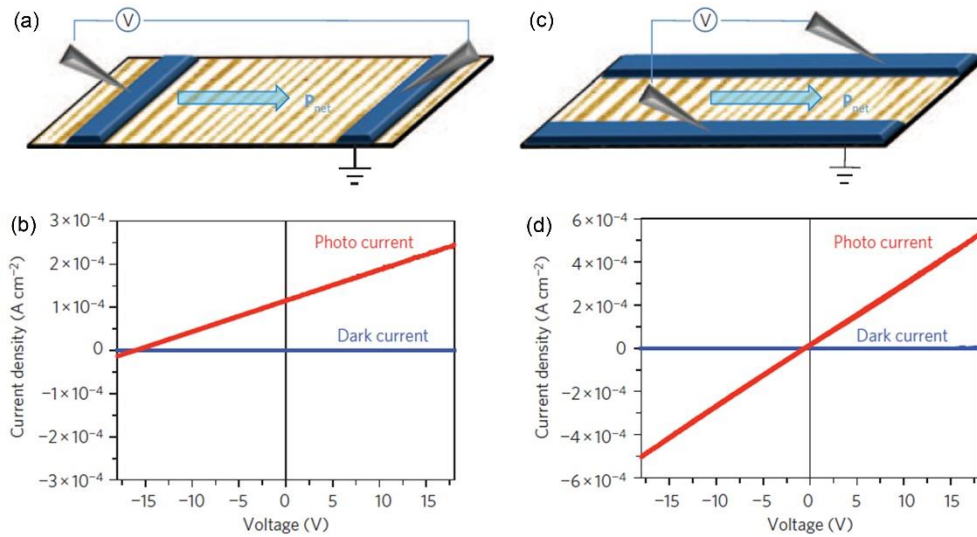


Fig. 1-5 Schematics of photovoltaic devices with the orientation of electrodes (a) parallel and (c) perpendicular to domain walls. Corresponding  $I$ - $V$  measurement of two electrodes geometry (b) parallel and (d) perpendicular. Reprinted with permission from Ref.<sup>[12]</sup>

However, there are still some phenomena that the present domain wall effect cannot explain. Alexe *et al.* have observed similar large photocurrent in both the domain walls and domains by atomic force microscopy (AFM) conductive tips. Similar lifetimes of photogenerated carriers are observed in the bulk and domain walls, suggesting that the recombination in bulk crystals is not as fast as expected.<sup>[30,31]</sup> In addition, a high photovoltage could be observed in BFO thin films under both electrode configurations, changing as a function of temperature instead of the geometry of the device setup.<sup>[32]</sup> When the temperature decreases, the conductivity of the domain walls drops at the same time. According to Equation (1-4), a higher voltage can also be obtained in perpendicular orientations. The other important thing is that the photocurrent in BFO films follows the rotating direction of the light polarization, consistent with the tensor model of BPE mentioned before.<sup>[24,32,33]</sup> Thus, it is pointed out that the anomalous photovoltaic effect is more attributed to BPE than the domain wall effect, but its contribution cannot be discarded.

### 1.3.3 Depolarization field model

The polarization charges due to the spontaneous polarization are distributed on the two surfaces in polarized ferroelectric materials, which in turn form a depolarization field with an opposite direction to the polarization. The depolarization field is the driving

force to separate the photogenerated electron-holes. But in bulk ferroelectrics, the distance between the two electrodes is much longer than the diffusion length, which is typically less than 100  $\mu\text{m}$ . The photocarriers are easily recombined before reaching the electrodes. However, in ferroelectric films, because of the thickness lower than a hundred nanometers, the separation becomes possible with limited recombination. The depolarization field is affected by the screening of the surfaces charges by adsorbed molecules and the contacted metal or semiconductor electrodes. Therefore, the screening charge distribution and the film thickness can influence the photovoltaic effect. Qin *et al.* have investigated the effect of electrodes, interfaces, and thickness on the PV mechanisms in ferroelectric thin films.<sup>[34,35]</sup> In their model, the higher dielectric constant of the electrodes (La, Sr)MnO<sub>3</sub> (LSMO) makes the screening charges distribute away from the interface, weakening the screening effect and further enhancing the photocurrent of PLZT film. There is also a threshold for ferroelectric film thickness to give rise to a larger photocurrent, which changes depending on the materials.<sup>[35]</sup> Eventually, the higher photovoltaic efficiency can be obtained by reducing the size of the devices and considering the electrodes as well.

Moreover, the depolarization field approach can also explain the change of the current direction by tailoring the ferroelectric polarization. As Choi *et al.* reported, the polarization can switch the directions of the photovoltaic current in a single domain of BFO crystal, which behaves like a diode.<sup>[33]</sup> Note that except for the BFO system, there are many reports about the switchable photovoltaic effect on other perovskite ferroelectrics, such as doped BTO or PLZT.<sup>[14,35,36]</sup> The switching ability of the photovoltaic current is also in line with the mechanism of BPE mentioned before.

### 1.3.4 Schottky-junction effect

When ferroelectrics are in contact with electrodes, a Schottky barrier forms at the interface, which can improve the photovoltage. The electrodes, the polarization charge, or defects can control the Schottky effect. Firstly, the electrodes can affect the photovoltaic efficiency.<sup>[34,37]</sup> As we have summarized in the previous section, it has been reported that the electrodes with a high dielectric constant could improve the photovoltaic efficiency due to the decrease of screening effect and space charges region

limit.<sup>[34]</sup> The modification of polarization charges can also impact the interface by tuning its Schottky to Ohmic character, enhancing the photovoltaic effect.<sup>[13,15,38]</sup> It is also found that the Schottky barrier height can be adjusted by controlling the polarization direction and amplified, e.g., in BFO thin films or Sc doped BFO (BFSO) with a structure ITO/BFSO/LNO.<sup>[15,38]</sup> In addition, the Schottky barrier effect is also related to charged defects, like oxygen vacancies usually present in the ferroelectric oxides.<sup>[15,39–42]</sup> The migration of oxygen vacancies can change the switchability of the polarization and can happen in a lower poling electric field (lower than the coercive field). It has been reported that the electromigration of oxygen vacancies is helpful to the Schottky-to-Ohmic transition effect.

## 1.4 Recent progress of ferroelectric photovoltaics

The ferroelectric photovoltaics effect has been investigated in several perovskite ferroelectric oxides, such as in BaTiO<sub>3</sub>, PbTiO<sub>3</sub>, BiFeO<sub>3</sub>, LiNbO<sub>3</sub>, and their derivatives. Indeed, the first work of a photovoltaic effect in ferroelectric was observed in BaTiO<sub>3</sub> in 1956.<sup>[18]</sup> They found a steady photovoltaic current following the pyroelectric current when light is on. Consequently, the photovoltaic effect was also observed on LiNbO<sub>3</sub> doped with Fe<sup>2+</sup> in 1970's.<sup>[22]</sup> In the beginning, researchers mainly focused on the bulk photovoltaic effect and the mechanism behind it. Choi *et al.* are the first to find the photovoltaic effect in BFO single crystal, which renewed the interest in ferroelectric materials for photovoltaic effect.<sup>[33]</sup> Yang *et al.* made a step forward for the ferroelectric photovoltaic research, reporting that domain walls of such materials can be engineered to exhibit a photovoltaic effect with an impressively high voltage output.<sup>[12]</sup> Then the field developed quickly, allowing it to reach a record 8.1% power conversion efficiency, which is predicted to attain 19.5% by designing BFO thin film and its domain types.

### 1.4.1 Power conversion efficiency

We know that the photovoltaic effect includes two fundamental processes: the absorption of light to generate the photoexcited electrons and holes and then the

separation of the photogenerated carries. Thus, the two most important things for energy conversion efficiency are an efficient optical absorption and a strong internal electric field for the charge separation/transport. However, most of the ferroelectrics have a high bandgap ( $> 3$  eV), which limits the absorption. We will talk about the bandgap engineering of ferroelectric materials in the next section. Here, we consider the recent research on how to enhance the photovoltaic effect. The low conversion efficiency for a ferroelectric solar cell is also attributed to their intrinsic low bulk conductivity (affecting the output voltage). Many parameters can affect the charge carries transport, like the migration or diffusion length and the internal electric field. Considering that, many works have been done for enhancing the ferroelectric photovoltaic effect by electric field or polar order engineering and by combining ferroelectrics with other materials.

Alex *et al.* have reported the lifetime of the carries generation and recombination, which is in picosecond scale and tens of microseconds, respectively.<sup>[31]</sup> They have observed the open voltage as high as 50 V in BFO films by controlling the conductivity of domain walls.<sup>[32]</sup> The photoconductivity is much higher than in bulk BFO. Reducing the thickness is also a good strategy to increase the power conversion efficiency by decreasing the recombination of photogenerated carries. This has been confirmed on  $(\text{Pb, La})(\text{Zr, Ti})\text{O}_3$  using calculations and experimental approaches<sup>[43,44]</sup> as well as in  $\text{Bi}_2\text{Fe}(\text{Mo, Ni})\text{O}_6$ <sup>[45]</sup>. In contrast, if it is in ultra-thin film, it will restrain the optical absorption.

Besides, the combination of ferroelectrics with other materials (metal/ferroelectric/semiconductor/metal) in heterostructures has been investigated. It is an excellent strategy to enhance the photovoltaic effect by taking both advantages of semiconductors or some oxides with a high light response and ferroelectrics with high residual polarization. The photovoltaic studies on BFO/ZnO, BLFO/ZnO, PZT/ZnO, PZT/ZnO/Cu<sub>2</sub>O demonstrated that those heterojunctions could present better photocurrent and higher power conversion efficiency.<sup>[46–51]</sup> For instance, the multilayers ITO/ZnO/BFO/Pt shows a current density  $J_{sc}$  of  $340 \mu\text{A}/\text{cm}^2$  and a power conversion efficiency 0.33%, which significantly increases compared to the ITO/BFO/Pt. This is due to the abundant photogenerated carries and the built-in fields formed at the interfaces.<sup>[46]</sup> Moreover, the research has suggested that the engineering of the

#### 1.4 Recent progress of ferroelectric photovoltaics

Schottky barrier by selecting different electrodes with different work functions or by tuning the surface could improve the photovoltaic effect. This is attributed to the increase of the depolarizing field (the same direction as the built-in electric field) and the reduction of the screening effect.<sup>[48]</sup> The research on BFO/ZnO with a graphene/ITO electrode could further improve the energy efficiency from 4.1% to 7.4%.<sup>[52]</sup> Moreover, using BFO/Au/ZnO<sup>[53]</sup> allows a high current density than BFO/ZnO. Furthermore, plasmonic gold nanorods allow improving the charge transfer at Bi(Fe, Cr)O<sub>3</sub>/graphene interface, achieving a current density of 2.56 mA/cm<sup>2</sup> and 0.63 V open voltage.<sup>[54]</sup> Fig. 1-6 shows the different devices and the current before and after forming a composite with Au nanorods.

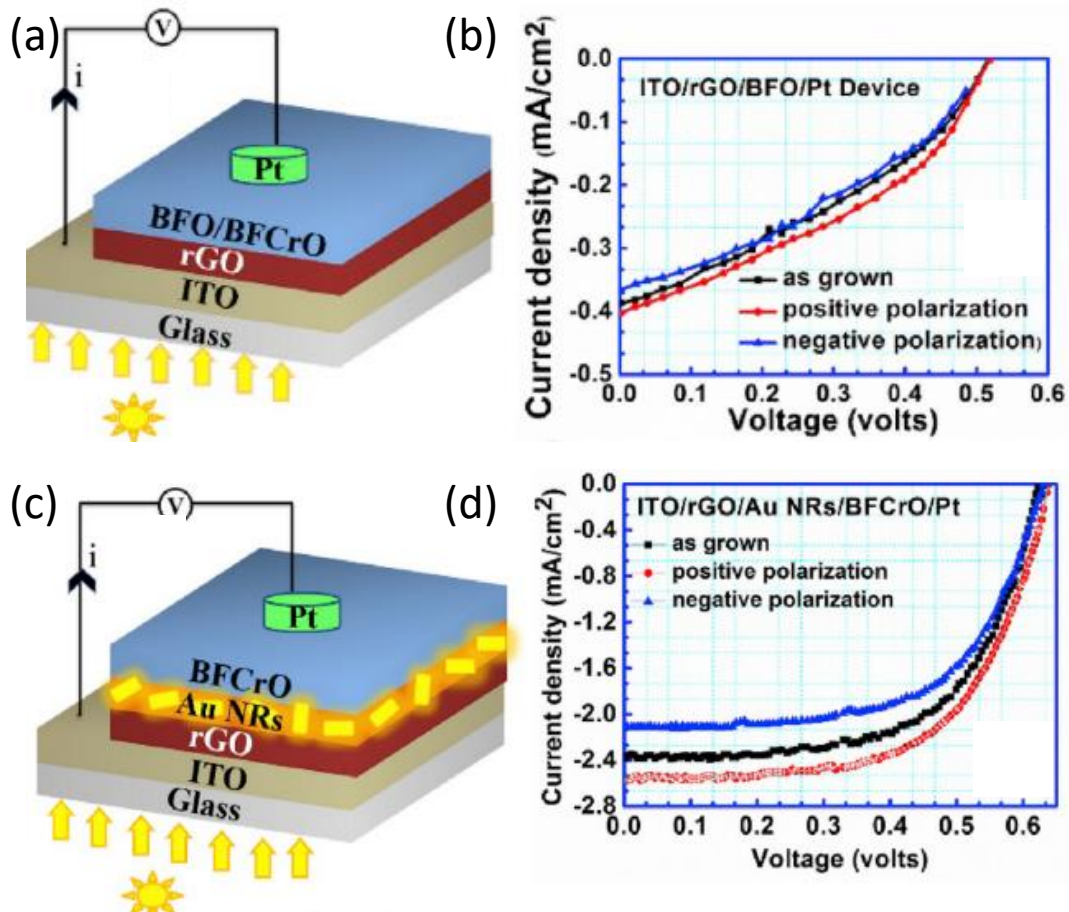


Fig. 1-6 Schematic of the ITO/rGO/BFO or BFCrO/Pt PV (a) and (c) ITO/rGO/ Au NRs/BFO/Pt PV devices; (b) and (d) J-V characteristics of the sample as grown, positive poled and negative poled. Reprinted with permission from Ref.<sup>[54]</sup>

It is known that changing the chemical composition can change the structure, affecting the photovoltaic performance. Sc substitution improves the bulk conductivity of BFO at

the ITO/Bi(Fe, Sc)O<sub>3</sub>/LaNiO<sub>3</sub> ferroelectric thin film.<sup>[38]</sup> It modifies the Schottky-Ohmic contact heterostructure compared to the pure BFO. La substituted BFO improved the photovoltaic efficiency by the polar order, affecting the charge transfer instead of narrowing the bandgap.<sup>[55]</sup> Apart from the studies of perovskite oxide ferroelectrics, many works focus on the halide perovskite or even some 1D or two-dimensional ferroelectrics for photovoltaic applications.<sup>[56–58]</sup> All these works provide a practical approach to designing photovoltaic ferroelectric devices with high performances.

## 1.4.2 Applications

As we have mentioned before, the most promising application for the ferroelectric photovoltaic effect is the solar cell. Apart from the solar cell, in this section, we present applications of ferroelectric photovoltaics in other areas, like ferroelectric memories and synapses (see Fig. 1-7 ).<sup>[59–62]</sup> Furthermore, beyond photovoltaic, there are also other polarization-induced processes like photostriction<sup>[63,64]</sup> and photocatalysis<sup>[65,66]</sup>.

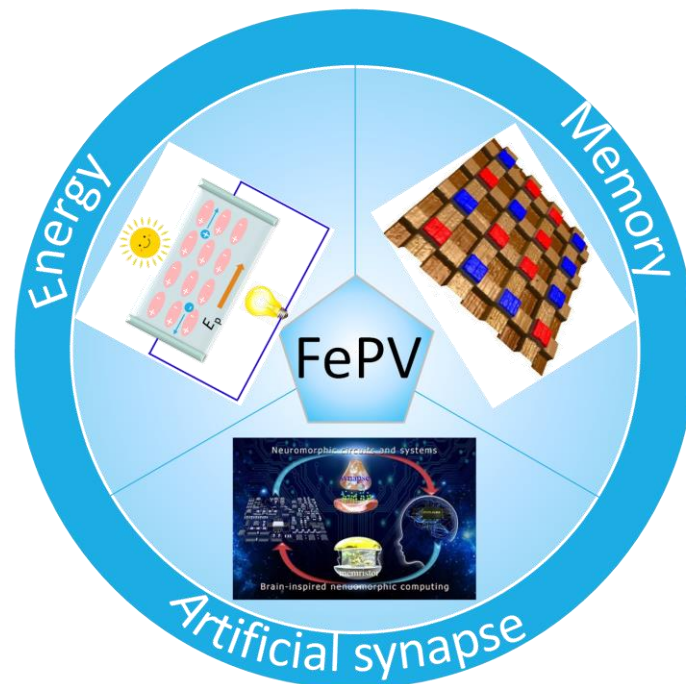


Fig. 1-7 The application of ferroelectric photovoltaic (FePV) range in different areas.  
Reproduced from Ref.<sup>[60,67]</sup>

It is reported that the ferroelectric photovoltaic effect can be used for non-volatile memory, which has a much higher operation and a lower energy loss than the flash memory.<sup>[60]</sup> Guo *et al.* reported a novel method for ferroelectric memory in BFO film by

## 1.5 Bandgap engineering

controlling the polarization direction. As shown in Fig. 1-8, the values change slightly for each direction, suggesting the feasibility of a ferroelectric memory.

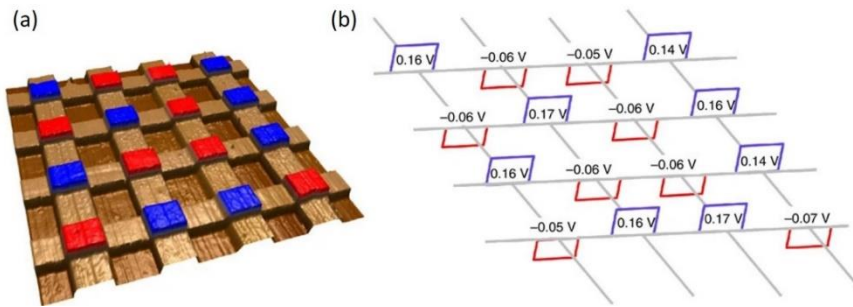


Fig. 1-8 Schematic of a prototype 16-cell memory based on the cross-bar architecture; blue and red present opposite polarization direction. Reprinted with permission from Ref.<sup>[60]</sup>

In addition, recently, ferroelectric photovoltaic studies have considered a new area as synapses. Fan et al. have reported new highly controlled synapses for neuromorphic computing. It is based on Pt/Pb(Zr, Ti)O<sub>3</sub>/LaNiO<sub>3</sub> ferroelectric thin film grown on the silicon substrate. It uses photocurrent as the weight of the synapse by gradually controlling the polarization. Such a device provides a new way toward neuromorphic computing (see Fig. 1-9).<sup>[62]</sup>

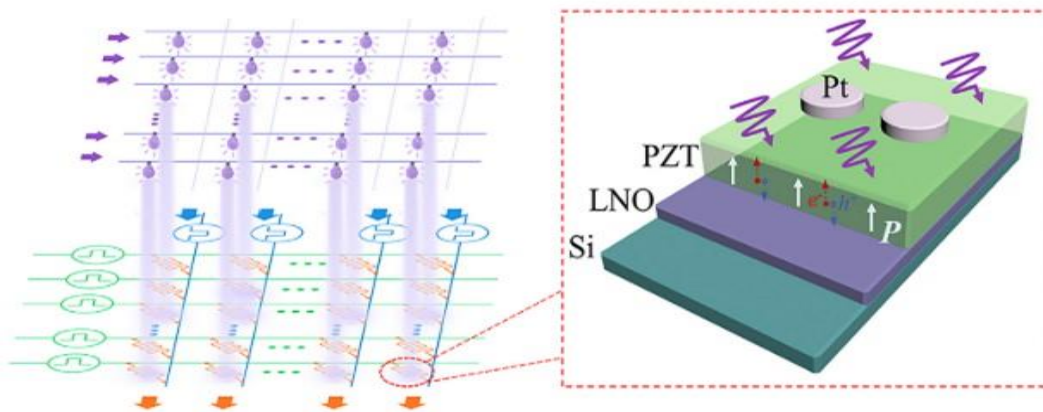


Fig. 1-9 Schematic illustrations of the structures of the single ferroelectric synapse device and the systems for the neural network. Reprinted with permission from Ref.<sup>[62]</sup>

## 1.5 Bandgap engineering

Many ferroelectrics crystallize in the perovskite ABO<sub>3</sub> structure and mostly have a high bandgap, such as 3.3 eV for BaTiO<sub>3</sub>, 3.2 eV for PbTiO<sub>3</sub>, 2.7 eV for BiFeO<sub>3</sub>, 3.8 eV for

LiNbO<sub>3</sub>, and 3.3 eV for KNbO<sub>3</sub>. In ferroelectric perovskite oxides, the wide bandgap is electronically characterized by a valence band (VB) derived from O 2p states and a conduction band (CB) originating from the B-site transition metal 3d states.<sup>[10]</sup> Bandgap engineering strategies have already been devised in an attempt to increase optical absorption. The most common way to overcome these problems is to introduce dopants in the host materials by doping with either transition metals or non-metal elements. Most studies have focused on chemical substitutions and alloying solutions. However, the strong hybridization between the transition metal orbitals (especially 3d<sup>0</sup> states) causes symmetry breaking and leads to polar displacements at the origin of ferroelectric polarization. Therefore, altering the bandgap may also significantly impact the polarization and the related ferroelectric properties. Fig. 1-10 shows the bandgap value of the most common ferroelectric materials with their polarization. A compromise between having a narrower bandgap while keeping a significant polarization amplitude is thus challenging. Most of the following works presented in this section have been published during the Ph.D. period, i.e., since 2018.

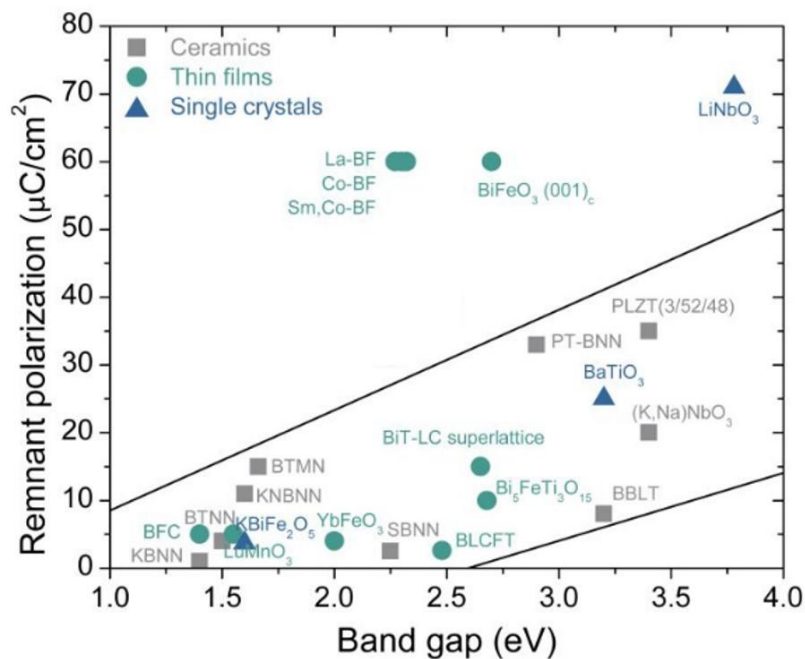


Fig. 1-10 The measured bandgap and remnant polarization of most studied ferroelectric materials. Reprinted with permission from Ref.<sup>[68]</sup>

### 1.5.1 Chemical substitution

Chemical substitution is one of the most important strategies that manipulate bandgap

energy. The doping can cause the structure disorder or introduce vacancies then change the band structure, leading to creating extra energy levels or reducing the bandgap energy. This section separates the substitution into two parts: on the A site or B site, respectively, according to the structure.

### 1.5.1.1 Substitution on A site

Most works of bandgap narrowing through substitution on the A site of BaTiO<sub>3</sub> focus on co-substitution with bismuth or lanthanum and some alkali metals, i.e., lithium, sodium, and potassium. It was found that Bi/Li co-doped BTO (Ba<sub>1-x</sub>(Bi<sub>0.5</sub>Li<sub>0.5</sub>)<sub>x</sub>TiO<sub>3</sub>, BBLT) shows a tiny effect on the optical absorption of BTO, presenting nearly the same bandgap as pure BTO (3.2 eV) (see Fig. 1-11).<sup>[14,69]</sup> The failure to narrow the bandgap can be attributed to the nature of forming the valence and conductive band states. The same group has also investigated the absorption and photovoltaic response on Ba<sub>1-x</sub>(Bi<sub>0.5</sub>K<sub>0.5</sub>)<sub>x</sub>TiO<sub>3</sub> (BBKT) in search of a large photovoltaic response. Interestingly, there is an absorption band at a lower energy in doped samples, in addition to that at 3.2 eV, which is the same as pure BTO.<sup>[70]</sup> As shown in Fig. 1-11b, the bandgap reduces from 3.2 to 2.6 eV upon doping and keeps invariant with a further increase of the doping amount. The decrease of the bandgap is attributed to the contribution of the Bi-2p state to the conduction band. The difference from the system BBLT is that the radius of K<sup>+</sup> (r = 1.51 Å) is larger than Li<sup>+</sup> (r = 0.92 Å); the former is more appropriate for substitution of Ba<sup>2+</sup> (r = 1.42 Å), which could reduce the lattice distortion compared to Li<sup>+</sup>. However, the narrowing of the bandgap is not enough (1.12 eV for silicon solar cells) for applications such as photovoltaic or energy harvesters. In addition, Alkathy *et al.* have studied a series of La/Na and Ni/Na co-doped BaTiO<sub>3</sub> on the A-site, which could decrease the bandgap to 2.68 eV with an increase of the doping levels.<sup>[71,72]</sup> This can be explained by the formation of additional energy levels between the valence and conduction bands. La<sup>3+</sup> or Na<sup>+</sup> can act as a donor or an acceptor, respectively, creating oxygen vacancies and localized states. On the other hand, the co-substitution can induce the distortion of octahedra, which can decrease the angle of M-O-M, resulting in a significant reduction of the optical bandgap.

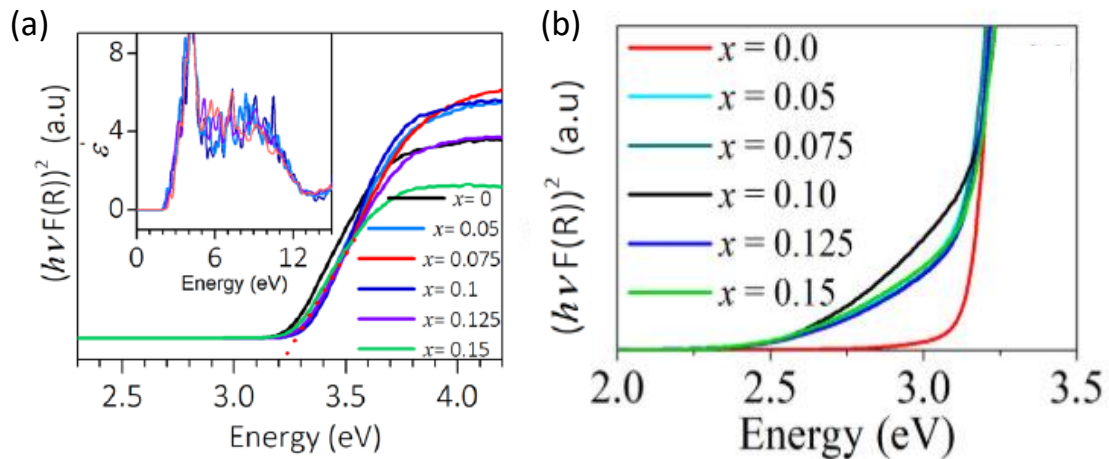


Fig. 1-11 The optical absorption of (a) BBLT and (b) BBKT, respectively. Reprinted with permission from Ref.<sup>[14,70]</sup>

### 1.5.1.2 Substitution on B site

The bandgap can decrease when the substitution is made on the B-site with transition metals, like  $\text{Fe}^{3+}$ ,  $\text{Mn}^{3+}$ ,  $\text{Co}^{3+}$ ,  $\text{Cr}^{3+}$  or  $\text{Ni}^{2+}$ . Yang *et al.* have systematically investigated the effect of single doping of metal elements on B site of BTO and observed defect levels which can lead to narrowing the bandgap energy.<sup>[73]</sup> Note that there are also a lot of works showing that the doping causes the decrease of bandgap by first-principles calculations.<sup>[73-76]</sup> As shown in Fig. 1-12a, it was reported that the control of the  $\text{Fe}^{2+}$  and  $\text{Fe}^{3+}$  oxide state in  $\text{BaTiO}_3$ , acting as donor and acceptor, respectively, contributed to the improvement of the PV effect.<sup>[74]</sup> From experiments,  $\text{Cr}^{3+}$  doped BTO has been explored, and the absorption edge presents a redshift because of the  $d-d$  band transitions between the  $\text{Cr}^{3+}$  center and  $\text{Ti}^{4+}$  sites.<sup>[77]</sup> And the reduction of bandgap shows independence with the concentration of the dopants (see Fig. 1-13 a). It is also observed that the  $\text{Sn}^{2+}$  doped BTO ( $\text{BaTi}_{1-x}\text{Sn}_x\text{O}_3$ ) shows a narrower bandgap than pure BTO samples.<sup>[78]</sup> In those compounds, the proximity of phase transitions is also believed to increase the open-circuit photovoltage. Except for the oxides BTO, the doping in  $\text{BiFeO}_3$  oxides has also been explored, like doping with  $\text{Mn}^{3+}$ .<sup>[76,79,80]</sup> It was found that the extra formed defect states between the VB and CB could be a support for optical absorption (see Fig. 1-12b). However, it is known that the ferroelectric properties usually deteriorate due to the unfilled occupied state of the 3d-orbitals of these ions.<sup>[81]</sup> In addition, it is worth noting that Yi *et al.* have reported that nitrogen-doped BTO shows narrower bandgap, the ferroelectric properties are maintained after N-doping, and

electric field-induced strain is also enhanced.<sup>[82,83]</sup>

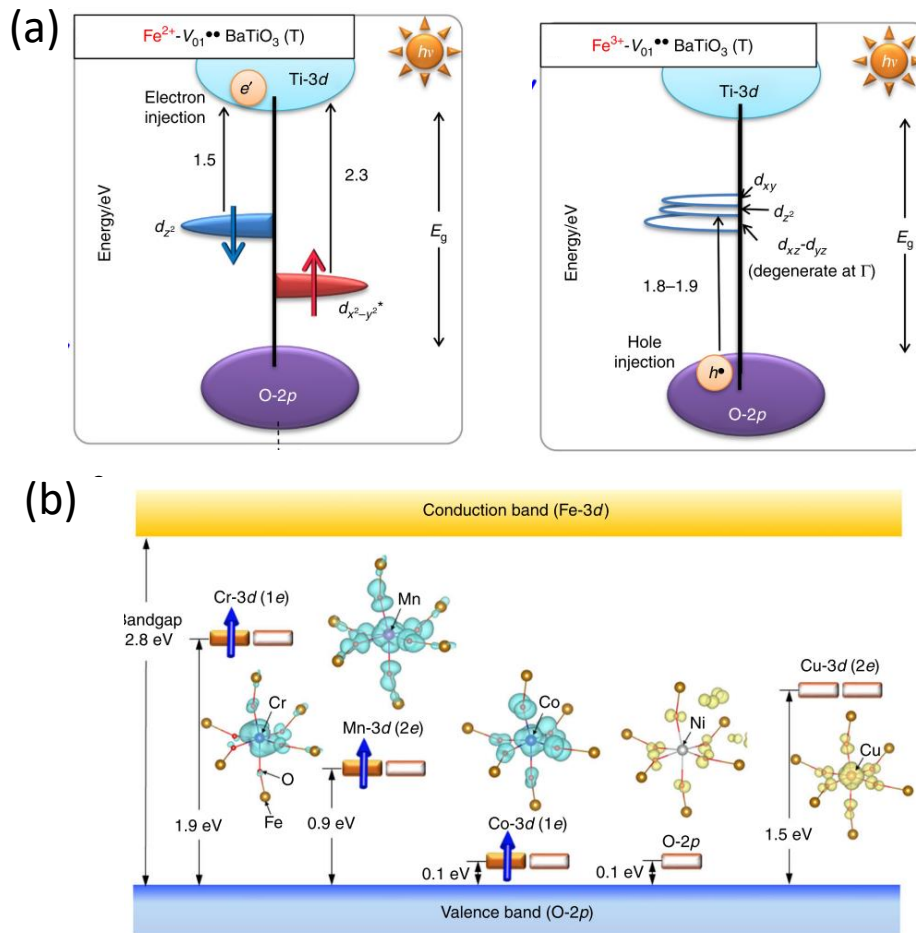


Fig. 1-12 Energy band Schematics of (a)  $\text{Fe}^{2+}/\text{Fe}^{3+}$  doped BTO and (b) 3d metal cations doped BFO. Reprinted with permission from Ref.<sup>[74,76]</sup>

Das *et al.* explored a different strategy to narrow the bandgap by co-doping with  $\text{Mn}^{3+}$  and  $\text{Nb}^{5+}$  pairs on B sites.<sup>[84]</sup> Meanwhile, the doped BTO can keep relatively stable polarization. In this co-doping strategy,  $\text{Mn}^{3+}$  as an acceptor reduces the bandgap due to the Jahn–Teller (JT) effect and induces a partial loss of polarization. On the other hand,  $\text{Nb}^{5+}$  supports the ferroelectric properties like in the system of the ferroelectric niobates.<sup>[16]</sup> Then, the optical absorption of Ni/Nb and Co/Nb co-doping BTO are also investigated, which all show a reduced bandgap estimated to be about 1.3 eV compared to BTO (see Fig. 1-13b).<sup>[85–87]</sup> Interestingly, in the work of  $\text{BaTi}_{1-x}(\text{Ni}_{1/2}\text{Nb}_{1/2})_x\text{O}_{3-\sigma}$ , the bulk ceramics can show strong absorption of visible light. However, for the powders, the bandgap has invariant change compared to the pure BTO, which can be attributed to the oxygen vacancies enriched at the grain boundaries, contributing to the optical

absorption.<sup>[85]</sup> It has also been reported that  $(1-x)\text{BaTiO}_3-x\text{BaMg}_{1/2}\text{Mo}_{1/2}\text{O}_3$  shows good photovoltaic behavior by using the first-principles theory. The reduction of the bandgap is attributed to the increase of conduction bandwidth due to the change of the angle of Ti–O–Mo bonds and the larger electronegativity of  $\text{Mo}^{6+}$  than  $\text{Ti}^{4+}$ .<sup>[88]</sup>

Control of the oxygen vacancy concentration has also been investigated to reduce the bandgap. As shown in Fig. 1-13c, the optical bandgap of doped  $\text{BaTiO}_3$  significantly reduces to 1.5 eV by changing the concentration of oxygen vacancies.<sup>[87]</sup> In addition, compared to doping with a single ion, the absorption edge of the co-doped BTO presents a more pronounced redshift.<sup>[77]</sup> Furthermore, the ferroelectric properties Co/Nb co-doping BTO ceramics could also improve by optimizing doping concentration.<sup>[86]</sup>

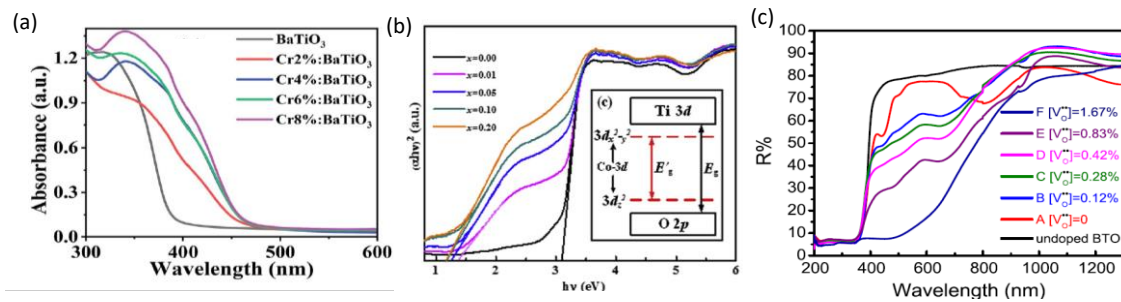


Fig. 1-13 The absorption of (a)  $\text{Cr}^{3+}$  doped BTO; (b)  $\text{Co}^{3+}$ ,  $\text{Nb}^{5+}$  co-doped BTO; (c) the reflectance of different oxygen vacancies concentration in  $\text{Ni}^{2+}$ ,  $\text{Nb}^{5+}$  doped BTO. Reprinted with permission from Ref.<sup>[77,86,87]</sup>

Of course, apart from work focusing on  $\text{BaTiO}_3$ , there are also many reports about the bandgap modification on  $\text{BiFeO}_3$ ,  $\text{KNbO}_3$ , and other ferroelectric oxides. For instance, Nechache *et al.* reported a new approach to effectively tune the bandgap of double perovskite multiferroic oxides  $\text{Bi}_2\text{FeCrO}_6$  by tailoring the Fe/Cr cation ordering.<sup>[89]</sup> In such a method, the bandgap can be adjusted to 1.4 eV without altering the ferroelectric properties, and a good power conversion efficiency of 8.1% is obtained for the thin-film cells. It has also been reported that  $\text{Bi}_2\text{FeMo}_{0.7}\text{Ni}_{0.3}\text{O}_6$  ferroelectric thin film exhibits a bandgap of 1.92 eV by controlling the thickness, which can also improve the photocurrent because of the self-polarization and the interface barrier.<sup>[45,90]</sup> There is another double perovskite oxide  $\text{Ba}_2\text{Bi}_{1+x}\text{Nb}_{1-x}\text{O}_6$ , showing a narrowing direct bandgap of 1.64 eV and an effective water splitting for hydrogen production.<sup>[91]</sup>

Note that there are also some works on bandgap engineering by substituting on both A

and B sites. Ce and Mn co-doped BFO thin films show invariant bandgap varying from 2.65 to 2.62 eV with increasing thickness, but the photocurrent is much higher in 110 nm thin film than the other thickness.<sup>[92]</sup> In contrast, Bi-Fe co-doped BaTiO<sub>3</sub> (Ba<sub>1-x</sub>Bi<sub>x</sub>Ti<sub>0.9</sub>Fe<sub>0.1</sub>O<sub>3-δ</sub>) exhibits a low bandgap (1.55 eV), high ferroelectric polarization, and reasonable conductivity.<sup>[93]</sup> Besides, as we have mentioned before, Alkathy *et al.* have studied a series of La/Na and Ni/Na co-doped BaTiO<sub>3</sub>.<sup>[71,72]</sup> Meanwhile, the same group has also investigated the bandgap narrowing by doping Bi/Na on the A-site and different transition metals (Co, Fe, and N) on B-site.<sup>[94]</sup> All the results dedicated to the absorption properties have a redshift and a minor reduction of the bandgap. The decrease of the bandgap can be understood by the defect levels inside the bandgap formed by the oxygen vacancies and the disorder of the structure or Jahn-Teller distortion.

### 1.5.2 Alloying solutions

An alloying solution was also explored as a possible approach to decrease the bandgap in ferroelectrics, for example, mainly reported on the KNbO<sub>3</sub> (KNO) system.<sup>[95-97]</sup> In principle, the narrowing bandgap of KNO is based on the substitution of Nb<sup>5+</sup> by lower valence transition metals and the replacement of K<sup>+</sup> by Ba<sup>2+</sup>. For instance, KNO mixed with BaNi<sub>1/2</sub>Nb<sub>1/2</sub>O<sub>3-σ</sub> was investigated and exhibits both ferroelectricity and a wide variation of direct band gaps in the range 1.1-2 eV by introducing Ni<sup>2+</sup> on the B-site and oxygen vacancies creating an extra electronic state within the band.<sup>[98-100]</sup> Similar work of solid solutions of KNO mixed with BaFe<sub>1/2</sub>Nb<sub>1/2</sub>O<sub>3</sub> and BaCo<sub>1/2</sub>Nb<sub>1/2</sub>O<sub>3-σ</sub> showed that the bandgap could be shifted down to 1.7 and 2.4 eV.<sup>[101,102]</sup> What's more, such materials can present some ferromagnetic properties that can be tuned by the doping concentration. Liang *et al.* employed the study of the first principles for bandgap engineering of KNO mixed with BaNb<sub>2/3</sub>B'<sub>1/3</sub>O<sub>3</sub>, where B' is a 3d transition metal. The results suggested that the bandgap changes with different doping by shifting the bands or forming intermediate ones within the forbidden gap.<sup>[103]</sup> Pascual *et al.* investigated the bandgap of KNbO<sub>3</sub>-doped with Bi(Yb, Me)O<sub>3</sub> (where Me = Fe or Mn), and they found that the narrowing bandgap could be observed in KNbO<sub>3</sub>-BiYbO<sub>3</sub> system, which also maintains long-range polar order over a wide temperature range.<sup>[104]</sup> The solar cell, using this material and combined with TiO<sub>2</sub> nanoparticles, shows a power conversion efficiency of 0.85%.<sup>[105]</sup> KNbO<sub>3</sub>-mixed with BiFeO<sub>3</sub> or LaFeO<sub>3</sub>, and KTi<sub>1/2</sub>Mo<sub>1/2</sub>O<sub>3</sub> also

present a narrowing of the bandgap with increasing the doping, which makes them promising for photovoltaic devices.<sup>[106–108]</sup> Moreover, the bandgap tuning of BiFeO<sub>3</sub> and PbTiO<sub>3</sub> are also studied, like BiFeO<sub>3</sub>-LaFeO<sub>3</sub>-LaMnO<sub>3</sub>, PbTiO<sub>3</sub>-Bi(Co<sub>2/3</sub>Nb<sub>1/3</sub>)O<sub>3</sub>, PbTiO<sub>3</sub>-BiFeO<sub>3</sub>-Bi(Ni<sub>1/2</sub>Ti<sub>1/2</sub>)O<sub>3</sub>.<sup>[68,109,110]</sup> Most bandgap engineering by introducing intra-gap levels or controlling the oxygen vacancies to narrow the bandgap provide a route to viable ferroelectric-based cells for exploring solar energy conversion and photovoltaic applications.

## 1.6 Plan of this work

One of the widely studied ferroelectric materials is the perovskite oxide BaTiO<sub>3</sub>, which has good ferroelectric properties at room temperature. In BaTiO<sub>3</sub>, as depicted in Fig. 1-14, Ba<sup>2+</sup> are located on the A site, at the corners of the unit cell; Ti<sup>4+</sup> is on B site, the center of unit cell, while O<sup>2-</sup> are located on the face centers of the unit cell. Non-coincidence of the positive and negative charges results in the dipole moment and spontaneous polarization in BaTiO<sub>3</sub>. By applying the electric field, the direction of the polarization can be reoriented, resulting in various properties. Most ferroelectric materials undergo a phase transition from a high temperature centrosymmetric stable into a ferroelectric phase at low temperature. When cooling, BaTiO<sub>3</sub> undergoes several transitions from cubic to tetragonal (120 °C), then to orthorhombic (0 °C), and finally to the rhombohedral phase (-90 °C), which correspond to various directions of the spontaneous polarization (see Fig. 1-14). At the transitions, the dielectric properties also change as shown in Fig. 1-14.<sup>[111]</sup> Other properties are also observed in ferroelectrics such as pyroelectricity (variation of temperature results in electrical changes) or piezoelectricity (variation of strain results in electrical changes and vice-versa).

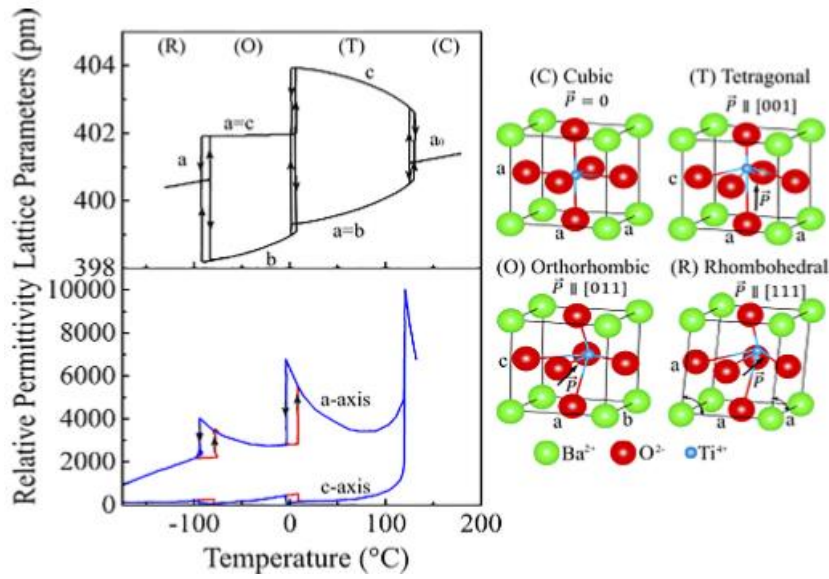


Fig. 1-14 The change of dielectric permittivity and parameters of the unit cell of the  $BaTiO_3$  with temperature. The right schematics show the Ti-displacement in the oxygen octahedron in different phases. Reprinted with permission from Ref.<sup>[111]</sup>

The bandgap of  $BaTiO_3$  is 3.3 eV. In  $BaTiO_3$ , the bandgap can decrease when substituting the ions on the B site, as reported previously. By lowering the bandgap, it would offer promising perspectives in using them for photovoltaic-based applications. Meanwhile, the substitution can cause the degradation of the ferroelectric properties to some extent. It is needed that  $BaTiO_3$  has a lower bandgap for better absorption of the light while keeping strong polarization for the separation of photogenerated carriers. Although lots of works have been reported during this Ph.D. work on the narrowing of the bandgap by co-doping (mentioned in section 1.5), it is still needed to understand the influence of the different dopants on the optical and electrical properties.

Thus, in this manuscript, the work is organized as follows:

First, in chapter 2, we study the properties of  $(Mn^{3+}, Nb^{5+})$  co-doped  $BaTiO_3$  with changing the doping concentration by substitution of  $Ti^{4+}$  ( $BaTi_{1-x}(Mn_{1/2}Nb_{1/2})_xO_3$ , abbreviated as  $xMnNb$ ,  $x$  changes from 0 to 0.15). Dielectric measurements show that the ferroelectric phase transition temperature abruptly shifts towards lower temperatures with the increase of the concentration of Mn and Nb. The sample 0.075MnNb shows a transition from a cubic to a tetragonal phase at 296 K. The hysteresis loop turns slim and shows lower ferroelectric properties with increased doping. The electrical bandgap decreases from 3.4 eV for pure BTO to 2.5 eV for

0.15MnNb. Besides, the onset of absorption can drop down to 1.5 eV. The temperature-dependent properties are also investigated.

Then in chapter 3, the effect of the synthesis process on the optical and ferroelectric properties of 0.075MnNb is investigated. During the process, the ball milling parameters, i.e., milling rate and time, are changed, and also the sintering conditions. Both the Curie temperature and the remnant polarization show a strong variation with respect to mechanical milling and sintering time. The process could affect the structure, the chemical distribution, and the grain size. In contrast, the optical absorption is invariant whatever the chemical route of synthesis.

Then in chapter 4, the optical absorption of BaTiO<sub>3</sub> co-doping (BaTi<sub>1-x</sub>(X<sub>1/2</sub>Y<sub>1/2</sub>)<sub>x</sub>O<sub>3</sub>) with different trivalent and pentavalent transition metal ions (X = Sc, Mn, Fe, Co; Y= Nb, Ta; with x = 0.075) is investigated. It is found that the onset of absorption can decrease down to 1.5 eV, especially with the (Co<sup>3+</sup>, Nb<sup>5+</sup>) co-doped samples, which simultaneously exhibit higher polarization than the other co-doping ions. The measured photoconductivity confirms that (Co<sup>3+</sup>, Nb<sup>5+</sup>) doping has superior absorption than the others. Our Density Functional Theory calculations demonstrate that the co-doping inserts intra-gap levels responsible for the lowering in the energy of the optical absorption fully in line with our experimental observations. This work opens new perspectives for the use of ferroelectrics in optoelectronic devices.

In chapter 5, we also study the optical and ferroelectric properties of co-doping with different divalent and hexavalent transition metal ions (X<sup>2+</sup>, Y<sup>6+</sup>) in BaTiO<sub>3</sub>, i.e., X = Mg, Zn, Ni; Y= W, Mo. In contrast to (X<sup>3+</sup>, Y<sup>5+</sup>), the bandgap cannot decrease for the (X<sup>2+</sup>, Y<sup>6+</sup>) doping, but it rather increases if compared to pure BaTiO<sub>3</sub>. Although the ferroelectric properties deteriorate, the samples exhibit relaxor-like ferroelectric behavior. The capacitive energy storage efficiency is found to be improved.

Finally, in chapter 6, we provide a conclusion of our work as well as perspectives by suggesting some works for improving the absorption and photovoltaic responses.



# 2 Enhanced optical absorption in ferroelectric BaTiO<sub>3</sub> by Mn and Nb co-doping

## Abstract

Ferroelectric perovskite BaTiO<sub>3</sub> oxides with Mn and Nb co-doping (BaTi<sub>1-x</sub>(Mn<sub>1/2</sub>Nb<sub>1/2</sub>)<sub>x</sub>O<sub>3</sub>) were fabricated through the traditional solid-state reaction. We have investigated the influence of doping concentration on the structure and electrical properties at room temperature. The X-ray diffraction and Raman spectroscopy show a decrease of the Ti–O polar correlation length and ferroelectricity as more Ti sites are substituted by Mn and Nb. The bandgap of the co-doping BaTiO<sub>3</sub> could be tuned between 3.2 eV to 1.5 eV due to the Jahn-Teller effect by changing the different doping concentrations. We have also studied diffraction data, Raman spectroscopy, and the ferroelectric polarization and bandgap behaviors as a function of temperature. By substituting Ti ions, the ferroelectric phase transition temperature decreases with a higher doping concentration, and the other low temperature phase transitions also shift down to a lower temperature. Meanwhile, the bandgap value reduces with increasing temperature.

## 2.1 Introduction

In conventional solar cells, the photo-excited electron-hole pairs are separated by the built-in electric field at the p-n junction, and the power conversion efficiency is limited by the Schokley-Queisser limit. Ferroelectrics have recently attracted attention as a promising candidate in photovoltaic technologies and coupling with other functional properties.<sup>[9,10]</sup> Ferroelectrics with asymmetric structures have a spontaneous polarization, which can promote the separation of photo-generated carriers and photovoltaic effect with voltage beyond the bandgap.<sup>[32,96]</sup> However, most of the

perovskite ferroelectric oxides ( $ABO_3$ ) have a bandgap much larger than 3 eV, between oxygen 2p states at valence band and the d states at the conduction band of the transitional metals. The higher bandgap makes only a small part of the solar spectrum to be absorbed, which also limits the enhancement of photovoltaic performance. Thus, it is desirable to reduce the bandgap and enlarge the absorption properties. Many works have been performed on bandgap engineering by chemical substitution in  $BaTiO_3$ ,  $BiFeO_3$ , and  $KNbO_3$ . [70,71,74,99,104]

$BaTiO_3$  (BTO), as one of the most studied ferroelectric oxides, has good ferroelectric and piezoelectric properties. The  $Ti^{4+}$  in the B site dominates the ferroelectric properties, its off-centering inducing the large polarization. The bandgap engineering through the substitution of  $Ti^{4+}$  by transition metals ( $Cr^{3+}$ ,  $Fe^{3+}$ ,  $Mn^{3+}$ ,  $Co^{3+}$ ) could tune the band structure. But meanwhile, the substitution could also suppress the ferroelectric properties by forming a stable non-ferroelectric hexagonal phase.<sup>[112–115]</sup> For the photovoltaic devices, it is aimed to design materials with significant optical absorption and ferroelectric properties to enhance the energy conversion efficiency. It has been reported that doping with two different transition metals in BTO is a good strategy, one as acceptors to reduce the bandgap ( $Mn$ ,  $d^4$ ) and another as the donor to keep the ferroelectric properties ( $Nb$ ,  $d^0$ ).<sup>[84]</sup> In this work, the bandgap can decrease to 1.5 eV, and the polarization retained to about 70 % of pure BTO. The calculation results also demonstrate that the doping could introduce midgap states between the conduction and valence bands due to the Jahn-Teller effect. Then, plenty of work confirmed that co-doping with two dopants could improve the optical absorption, as shown in experimental or theoretical works.<sup>[85,86,88]</sup>

In the current work, Mn and Nb co-doped  $BaTiO_3$  samples were fabricated. It is still necessary to investigate the effect of different doping concentrations on the structure and see how it affects the physical properties. In the present work, we also investigated the structure and properties changing with temperature. The X-ray diffraction and the Raman spectroscopy versus temperature show that the doping makes the transition temperature from cubic to tetragonal phase shift down to below room temperature and also reduces the temperature value for the other low temperature transitions. We also studied the influence on optical absorption with temperature. The change of the

bandgap can be associated with the evolution of the phases and the other physical properties.

## 2.2 Experimental procedure

### 2.2.1 Material preparation

All the BaTi<sub>1-x</sub>(Mn<sub>1/2</sub>Nb<sub>1/2</sub>)<sub>x</sub>O<sub>3</sub> ( $x = 0.025 \sim 0.15$ ) ceramic samples were synthesized by the traditional solid-state reaction method. The raw materials used were BaCO<sub>3</sub> (Strem 99.9%), TiO<sub>2</sub> (Prolabo 99%), Mn<sub>2</sub>O<sub>3</sub> (Strem 99%), and Nb<sub>2</sub>O<sub>5</sub> (Alfa Aesa 99.9%). Firstly, BaCO<sub>3</sub> was preheated at 500 °C for 5 hours to remove any absorbed moisture. Then, the raw powders were weighed stoichiometrically and mixed by dry ball-milling in a tungsten carbon jar. Then the milled powder was heated at 1000 °C for 12 hours. After calcination, the powder was pressed into pellets of 8 mm diameter and 1 mm thickness with polyvinyl alcohol (PVA) (35 wt %) as a binding agent. The pellets were then sintered at 1280 °C for 10 hours.

The pure BaTiO<sub>3</sub>, as a reference, was also prepared by the conventional solid-state method. The stoichiometric powder was mixed in a ZrO<sub>2</sub> jar with different ball milling rates and duration times. After calcination at 900°C for 12 hours, the pellets were ground and then were again pressed into pellets with PVA for sintering at 1280 °C for 10 hours.

### 2.2.2 Characterization

The powder X-ray diffraction (XRD) patterns were recorded in a Bruker D2 phase diffractometer using Cu-K<sub>α</sub> radiation ( $\lambda=1.5406 \text{ \AA}$ ) at room temperature with a step of 0.02° for 2 seconds. The temperature-dependent diffraction patterns were collected using Cu-K<sub>β</sub> radiation in the range of 90 K – 470 K within steps of 10 K. Raman spectroscopy (Labram-Horiba) were performed at room temperature and over the range of 100 - 500 K with a He-Ne, 633 nm laser as an excitation source. The scanning electron microscopy (SEM) images of all the ceramics were collected in a backscattered electron mode (FE-SEM; JSM7600, Jeol Ltd., Tokyo, Japan). Diffuse reflectance spectra

were recorded using Perkin Elmer UV-visible NIR spectroscopy (Perkin Elmer Lambda 850), and the optical absorption was also registered as a function of temperature. Before measurements, the powders were obtained from the pellets crushed into fine powders and annealed at 400°C for 1 hour to remove the mechanical strain.

Before all the electrical measurements, silver electrodes were painted onto both sides of the polished pellets. Dielectric measurements were collected using an impedance analyzer (HP4294A) within the temperature range of 80 to 450 K, a frequency ranging from 40 Hz to 1.1MHz. The polarization dependence on electric field ( $P$ - $E$ ) hysteresis loops at a frequency of 5 Hz were recorded in silicone oil using a ferroelectric tester (AixACCT). The thermal measurements of the polarization were also performed using the AixACCT tester.

## 2.3 Results and discussion

### 2.3.1 Microstructure of pure and co-doped BTO samples

Fig. 2-1 shows the powder X-ray diffraction patterns of all the samples collected at room temperature. Compared with the tetragonal phase of BTO (JCPDS card #05-0626), no secondary phases could be evidenced on these diffractions patterns. From Fig. 2-1b, we can see that with the increase of doping concentration, the peak (200) and (002) merge to one peak gradually, especially after  $x = 0.05$ . The splitting of this (200) cubic peak represents the tetragonal distortion. Note that because of  $K_{\alpha 1}$  and  $K_{\alpha 2}$  X-ray radiation, all the Bragg peaks show doubling even when the cubic phase is reached. When the doping amount is 0.05, it only shows one (200) peak, meaning the tetragonality is suppressed. The results thus suggest that with an increase of doping concentration, the reduction of the ferroelectric properties should be observed.

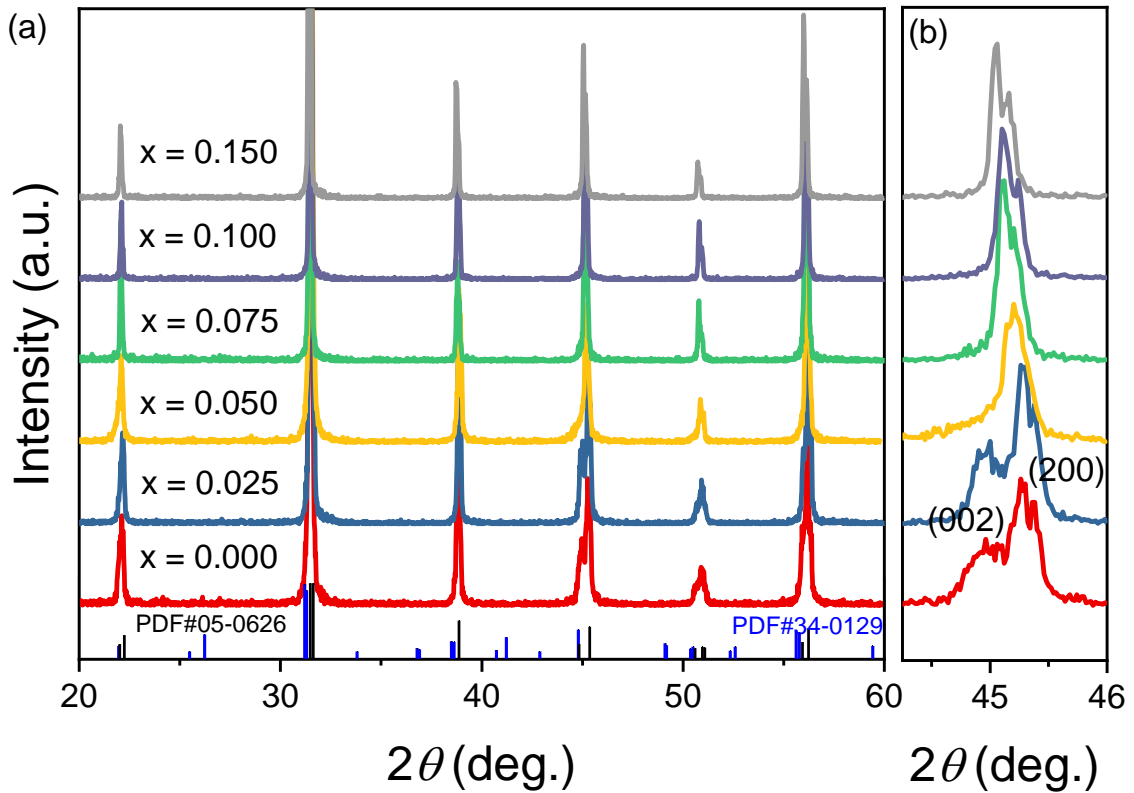


Fig. 2-1 (a) Powder X-ray diffraction patterns of pure BTO and (Mn<sup>3+</sup>, Nb<sup>5+</sup>) co-doped BTO. (b) The magnified peak of (200) around 45°

The microstructures of all the ceramics are shown in Fig. 2-2, presenting the bimodal distribution of the grain size. The porosity of all the ceramics decreases with the increase of dopant amount, except for the doping with  $x = 0.05$ , which shows high porosity. The high porosity may be attributed to carbon, tungsten, and silicon pollution during ball milling. The energy-dispersive X-ray spectroscopy (EDS) results show the inhomogeneous distribution of the elements with some impurities (see Fig. 2-3). We can also observe that the grain size increases with higher doping, especially with  $x = 0.10$  and  $x = 0.15$ , much larger than ten  $\mu\text{m}$ , while for pure BTO, the size is 0.6  $\mu\text{m}$  on average.

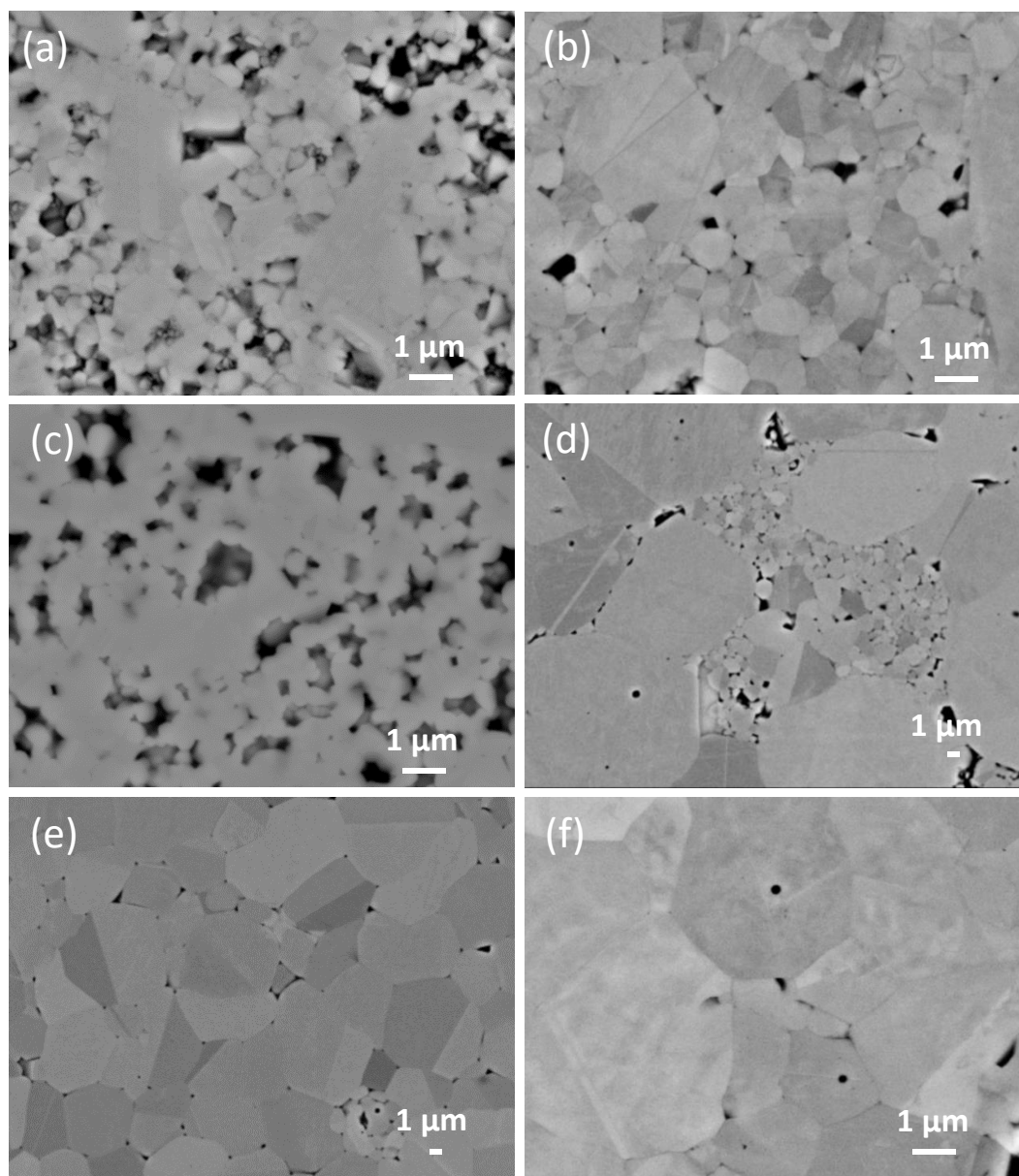


Fig. 2-2 The microstructure of all the ceramics (a) pure BTO and (b-f) ( $\text{Mn}^{3+}$ ,  $\text{Nb}^{5+}$ ) co-doped BTO: b)  $x = 0.025$ , c)  $x = 0.05$ , d)  $x = 0.075$ , e)  $x = 0.10$ , f)  $x = 0.15$

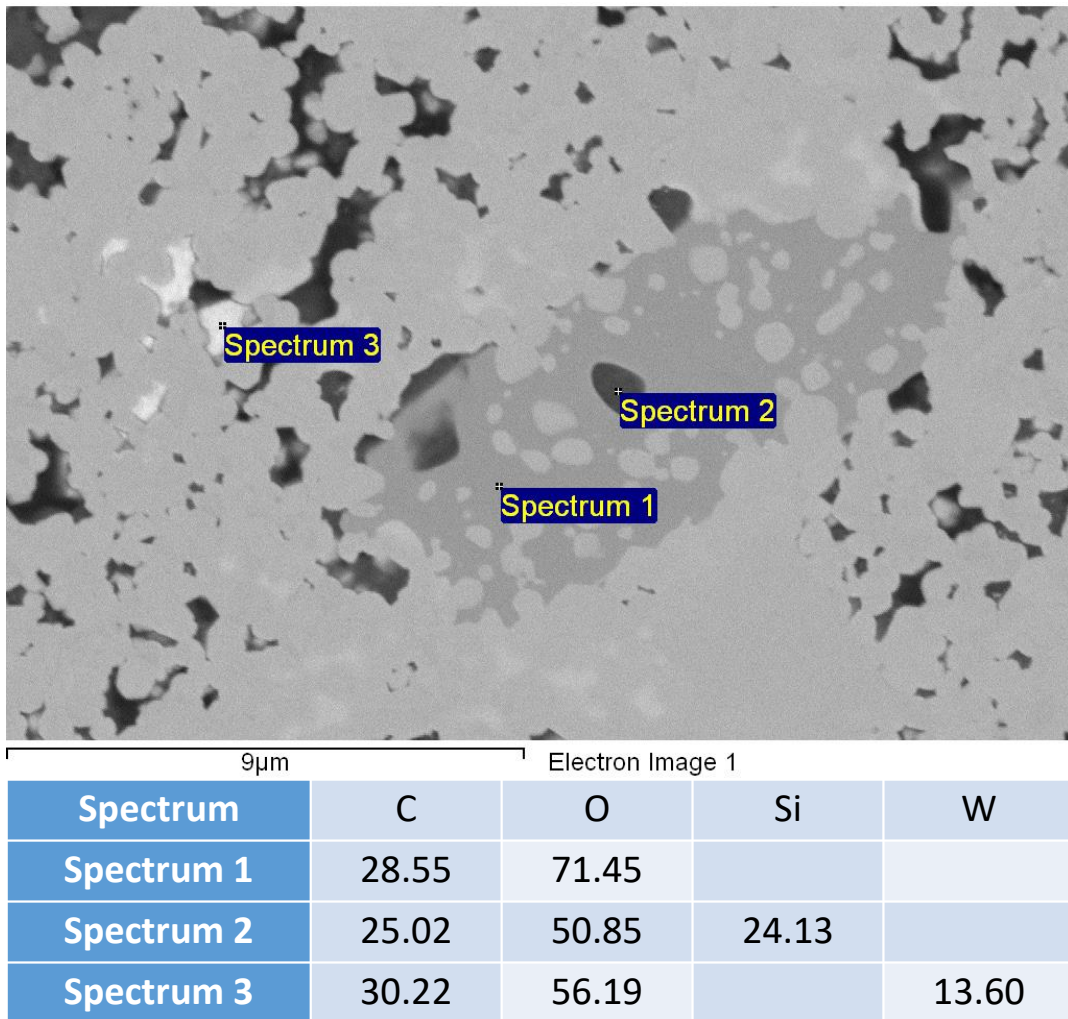


Fig. 2-3 The EDS results of sample  $x = 0.05$ , the table shows all results in atomic (%)

Fig. 2-4 shows Raman spectroscopy for all the samples at room temperature. Firstly, pure BTO and the sample doped with  $x = 0.025$  show a sharp peak at  $305\text{ cm}^{-1}$ , which is related to the displacement of  $\text{Ti}^{4+}$  in Ti-O chains, representing the ferroelectric polar phase. It corresponds to the mode of  $\text{B1}(\text{TO})/\text{E}(\text{TO}+\text{LO})$ , TO and LO refer to transverse and longitudinal optic modes, respectively. The peaks between  $200\text{-}400\text{ cm}^{-1}$  are usually attributed to vibrations of polar  $\text{TiO}_6$  octahedra in ferroelectric perovskite oxides.<sup>[116,117]</sup> When the doping concentration increases continuously beyond  $x = 0.05$ , the sharp peak of the  $305\text{ cm}^{-1}$   $\text{E}(\text{TO}_1)$  mode becomes wide and disappears. The intensity reduction and the width increase of this peak are associated to a decrease of the polarization and the tetragonality. It is reported that doping can impact the local chemical order, the chemical defects, and the  $\text{TiO}_6$  octahedra distortion.<sup>[16,118]</sup> It is also important to note that with the increase of doping, the mode at  $260\text{ cm}^{-1}$   $\text{A1}(\text{TO}_2)$  becomes weaker in

intensity with doping at  $x = 0.05$ , while in contrast, in the spectral range of  $80\text{-}200\text{ cm}^{-1}$ , new modes at  $190\text{ cm}^{-1}$ ,  $115\text{ cm}^{-1}$  and  $90\text{ cm}^{-1}$  are formed. The intensity of these modes and especially that at  $190\text{ cm}^{-1}$  assigned as polar  $A_1(\text{TO}_1)$  mode increases with doping, and thus may be attributed to the existence of local polar-regions and the increase of the structure distortion by doping.<sup>[119]</sup> Indeed, as shown in Fig. 2-12, the Raman spectra of BTO at high temperature also show these new modes which therefore do also exist even in the cubic phase, and are due to the presence of some local polar disorder structure. We can also see the decrease of the tetragonal phase from the modes at  $520\text{ cm}^{-1}$  and  $720\text{ cm}^{-1}$ , the  $A_1(\text{TO})/\text{E}(\text{TO})$  and  $A_1(\text{LO})/\text{E}(\text{LO})$  modes, respectively.  $A_1(\text{TO})$  mode corresponds to Ti-O displacement along  $c$ -axis, also seen at  $260\text{ cm}^{-1}$  due to the polar vibrations; and E modes due to the distortion in the  $\text{TiO}_4$  plane at  $520\text{ cm}^{-1}$ . The  $A_1(\text{LO})/\text{E}(\text{LO})$  mode at  $720\text{ cm}^{-1}$  is also associated with the bending and stretching of  $\text{BO}_6$  octahedra. The two bands also become much broader, suggesting that the substitution of  $\text{Ti}^{4+}$  is destroying the long-range order of ferroelectricity. In addition, there is another peak at  $635\text{ cm}^{-1}$  observed only when  $x$  is higher than 0.05, whose intensity is increasing with the higher doping, corresponding to the  $A_{1g}$  mode of the hexagonal phase of BTO.<sup>[114,115,120]</sup> Similarly, there is also an extra peak at  $780\text{ cm}^{-1}$ . It is known that this mode is related to the asymmetric breathing of  $\text{BO}_6$  affected by the ionic size of the doping transition metals,<sup>[118]</sup> possibly demonstrating that there are different  $\text{MnO}_6$  or  $\text{NbO}_6$  octahedra with breathing mode different from that of  $\text{TiO}_6$ . As we will show later with Raman spectroscopy versus temperature, these modes do not change with the temperature (see Fig. 2-15), which these of the perovskite vary, attesting these extra modes are related to parasitic hexagonal phase. This parasitic phase is probably in weak amount and/or of small size because of no peak diffraction (see Fig. 2-1) associated with this phase. Indeed, there is no trace, for instance, of the “hexagonal phase” Bragg peak (103) located at  $2\theta = 26.24^\circ$  shown in blue color in between the (100) and (110) perovskite Bragg peaks.

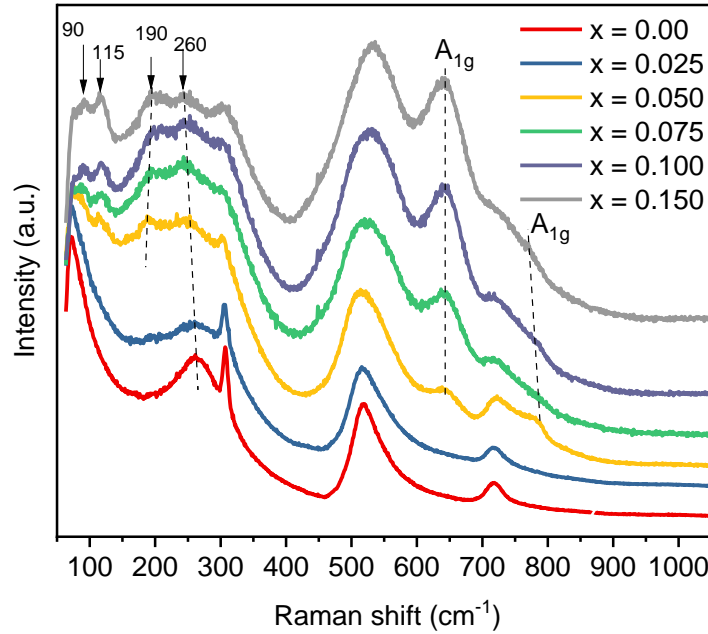


Fig. 2-4 Raman spectra of pure BTO and (Mn<sup>3+</sup>, Nb<sup>5+</sup>) co-doped BTO at 300 K

### 2.3.2 Optical absorption of pure and co-doped BTO samples

The diffuse reflectance of all the doped samples and pure BTO are recorded at room temperature. The optical band gap was estimated by the Tauc plot of the Kubelka-Munk function<sup>[121]</sup>,  $F_{KM}$ , which is proportional to the absorption:

$$F_{KM} = \frac{K}{S} = \frac{(1-R)^2}{2R} \quad (2-1)$$

where  $R$  is the reflectance,  $K$  and  $S$  are regarded as the absorption and back-scattering coefficients. Note that calculations<sup>[122]</sup> have shown that the bandgap value of BTO between the direct bandgap ( $\Gamma$ - $\Gamma$ ) Brillouin zone points and indirect bandgap ( $\Gamma$ - $R$ ) is very close in energy (less than 0.05 eV whatever the hybrid functional). As a result, in the following, we assume a direct bandgap. Then we can get the direct bandgap  $E_g$  from the fitting of the linear region close to the absorption edge by<sup>[123]</sup>:

$$(h\nu F_{KM})^2 = A (h\nu - E_g) \quad (2-2)$$

where  $h$  is the Planck coefficient,  $\nu$  is frequency,  $A$  is a proportional constant, the slope of the linear region is close to the absorption edge, and  $E_g$  is the direct bandgap energy. Fig. 2-5 exhibits the absorption differences between pure BTO (the red line) and the

doped BTO samples. Table 2-1 shows the value of the direct bandgap obtained from the Tauc plot of all the compositions. We can see the bandgap show a slight decrease from 3.4 eV for pure BTO to 3.13-3.18 eV for  $x = 0.025-0.05$ , then down to 2.59 eV for  $x = 0.075$  doping, 2.56 eV for  $x = 0.15$ . However, as shown from the inset figure in Fig. 2-5b, the onset of absorption corresponding to optical bandgap has a significant reduction. The pure BTO shows an onset of absorption of 3.2 eV. The doped samples with  $x = 0.025$  and  $x = 0.05$  show a close value, 2.3-2.2 eV. But the onset of absorption is about 1.5 eV with higher doping amounts. The increase of absorption in lower energy is attributed to the doping with  $Mn^{3+}(3d^4)$ , which acts as an acceptor and causes the crystal field splitting with the Jahn-Teller effect, which in turn forms extra gap states between the conduction band and valence band. The phenomenon is similar to the recently reported work on bandgap engineering of BTO by two transition metals co-doping.<sup>[84–87]</sup>

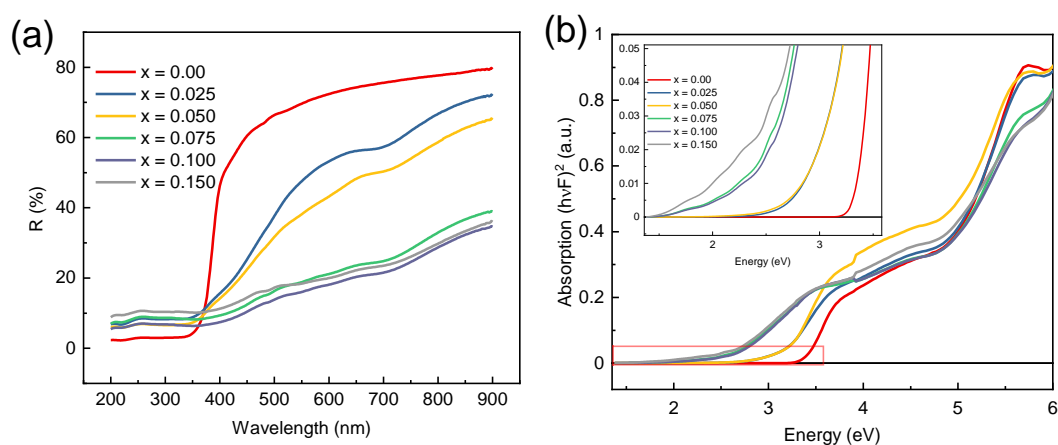


Fig. 2-5 (a) The diffuse reflectance spectra of pure BTO and ( $Mn^{3+}$ ,  $Nb^{5+}$ ) co-doped BTO; (b) Absorption as a function of photon energy for all the compositions, the inset shows the magnified part of the absorption curves in lower intensity

Table 2-1 The bandgap energy of all the pure and co-doped BTO samples

Composition (x)	0.00	0.025	0.05	0.075	0.10	0.15
Bandgap $E_g$ (eV)	3.40	3.13	3.18	2.67	2.65	2.66
Onset absorption (eV)	3.20	2.3	2.2	1.5	1.5	1.5

### 2.3.3 Dielectric spectroscopy of pure and co-doped BTO samples

The dielectric properties are investigated (shown in Fig. 2-6). As we have mentioned before, it is known that with the decrease of temperature, pure BTO undergoes three phase transitions from cubic (C) to tetragonal (T) phase, then orthorhombic (O) phase, and finally rhombohedral (R) phase. With the doping increase, the phase transition temperature from cubic paraelectric phase to tetragonal ferroelectric phase, i.e., the Curie temperature ( $T_c$ ), shifts to a lower value, especially for the doping above  $x = 0.05$ , it decreases down close to room temperature. As shown in Fig. 2-6, the phase transition temperature reduces to 364 K for  $x = 0.025$ , 300 K for  $x = 0.05$ , 297 K for  $x = 0.075$ . The transition temperature ( $T_c$ ) of the doped samples with  $x = 0.10$  and  $0.15$  shifts down towards temperatures much lower than room temperature. It can also be linked with the result of XRD and Raman spectra, which have suggested the reduction of the tetragonal phase or ferroelectricity at room temperature when doping. Besides, the dielectric response becomes broader (less sharp than the one of pure BTO). This is due to the other phase transitions, which are close to that corresponding to the main dielectric peak, and also, most likely to the decrease of the coherence length of the polar order by doping resulting in polar clusters with small sizes, resembling relaxor-like behavior.

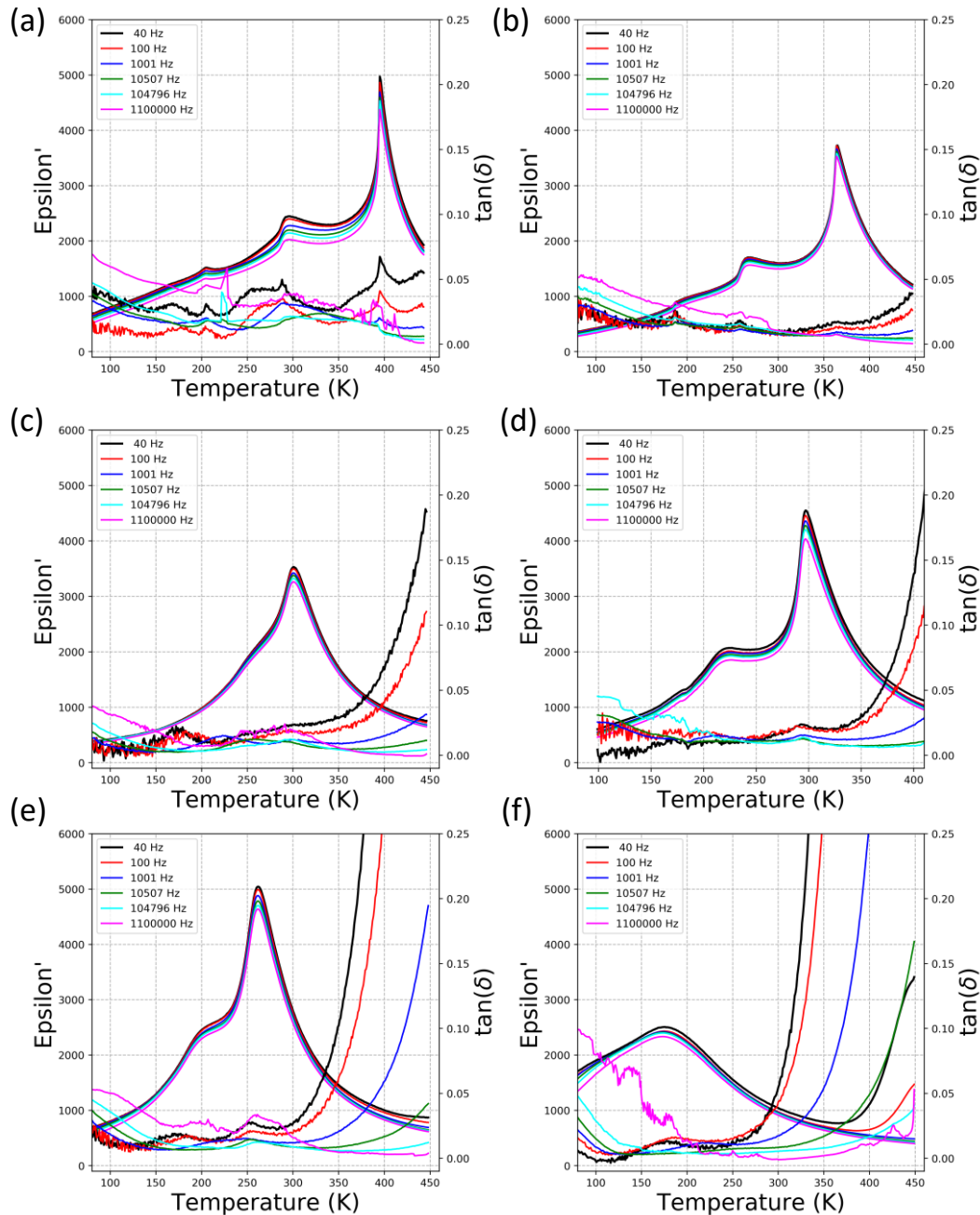


Fig. 2-6 The dielectric constant and loss as a function of temperature measured with a frequency range in 40 Hz to 1.1 MHz for (a) pure BTO and (b-f) ( $\text{Mn}^{3+}$ ,  $\text{Nb}^{5+}$ ) co-doped: b)  $x = 0.025$ , c)  $x = 0.05$ , d)  $x = 0.075$ , e)  $x = 0.10$ , f)  $x = 0.15$

### 2.3.4 Ferroelectric properties of pure and co-doped BTO samples

The hysteresis loops of polarization versus the applied electric field ( $P$ - $E$ ) and current versus the electric field ( $I$ - $E$ ) measured at room temperature for all the compounds are shown in Fig. 2-7. The pure BTO (see Fig. 2-7a) presents the typical hysteresis loop with ferroelectric properties. We notice that the loops are getting slimmer compared to the

pure BTO and look more like a ferroelectric relaxor after doping with the remnant polarization going close to zero. The saturation polarization and remnant polarization for all the doped samples are lower than those of pure BTO. This is in agreement with other works reporting that the substitution of Ti<sup>4+</sup> would decrease the ferroelectric properties, like (Fe, Nb) co-doped BTO.<sup>[124]</sup> For the sample  $x = 0.025$ , the  $P$ - $E$  curve shows a pinched loop, and there are two current peaks different from the others, which can be attributed to defect dipoles.<sup>[125]</sup> After many cycles (i.e., fatigue measurements), the loops open, suggesting the defect dipoles moved after applying the field many times. In addition, when doping  $x = 0.15$ , the loop shows a linear-like dielectric shape, which further demonstrates the suppression of the ferroelectric phase.

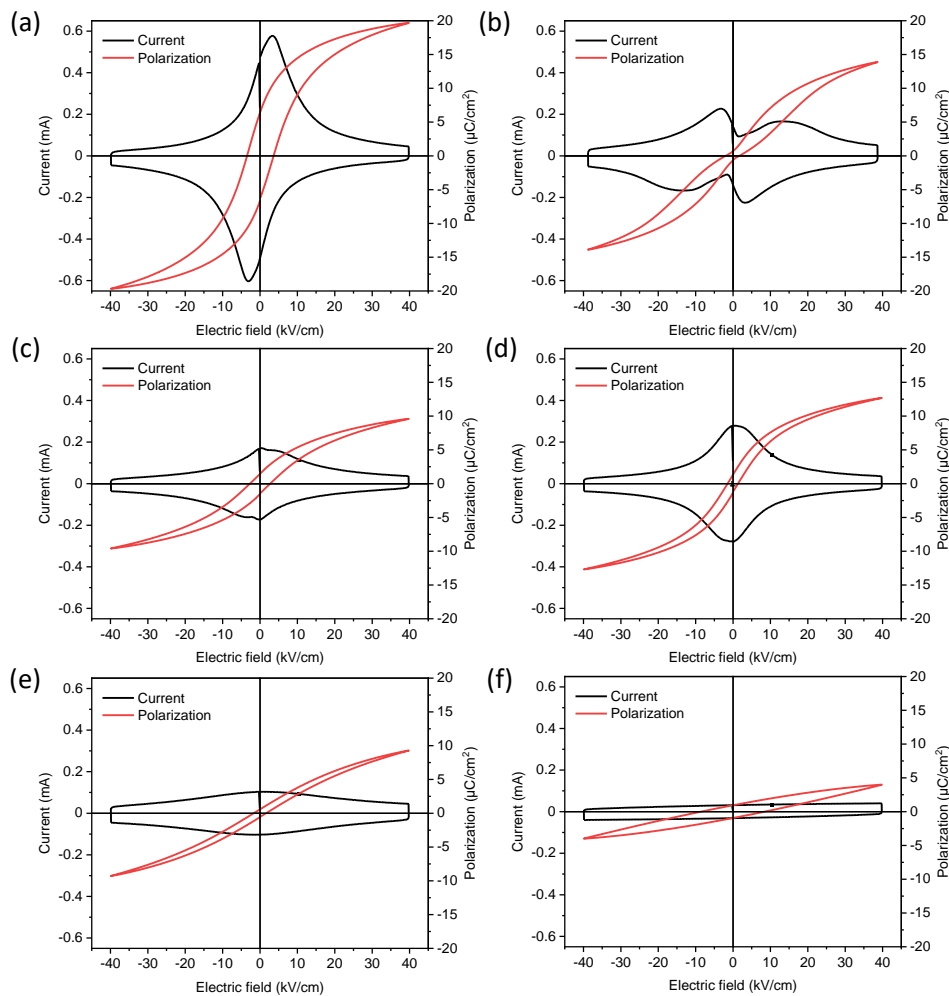


Fig. 2-7 The hysteresis loops ( $P$ - $E$  and  $I$ - $E$  loops) for (a) pure BTO and (b-f) ( $Mn^{3+}$ ,  $Nb^{5+}$ ) co-doped: b)  $x = 0.025$ , c)  $x = 0.05$ , d)  $x = 0.075$ , e)  $x = 0.10$ , f)  $x = 0.15$

## 2.3.5 Temperature-dependent evolution of different physical properties

### 2.3.5.1 X-ray diffraction versus temperature

We investigated the structure as a function of temperature by following the characteristic Bragg peaks (110), (111), (200). It is known that these three peaks allow following the three phase transitions i.e., to tetragonal (T), orthorhombic (O), and rhombohedral (R) phases. Fig. 2-8 shows the three peaks of pure BTO, and the lattice parameters change with temperature are shown in Fig. 2-11a. We can clearly see the phase transitions from the peak (200), which are in agreement with the reference.<sup>[111]</sup> Firstly, the cubic to tetragonal phase transitions at 390-400 K, where the (200) peak starts to split into two peaks (002) and (200). The next phase transition, tetragonal to orthorhombic phase, starts at 280-290 K, where the intensity ratio of peak (002) over (200) reverses. Finally, the transition from orthorhombic to rhombohedral phase is seen at 180-190 K, where these two peaks merge into one peak. Fig. 2-9 and Fig. 2-10 show the XRD patterns versus temperature of sample  $x = 0.025$  and  $x = 0.10$ , respectively. We can still see the three-phase transitions, which are in good agreement with the results obtained from the dielectric measurements. Compared to the pure BTO, the phase transition temperatures shift down to lower values. Except for the change of peak (200), it is also observed that the peak (111) has a right shift with decreasing temperature.

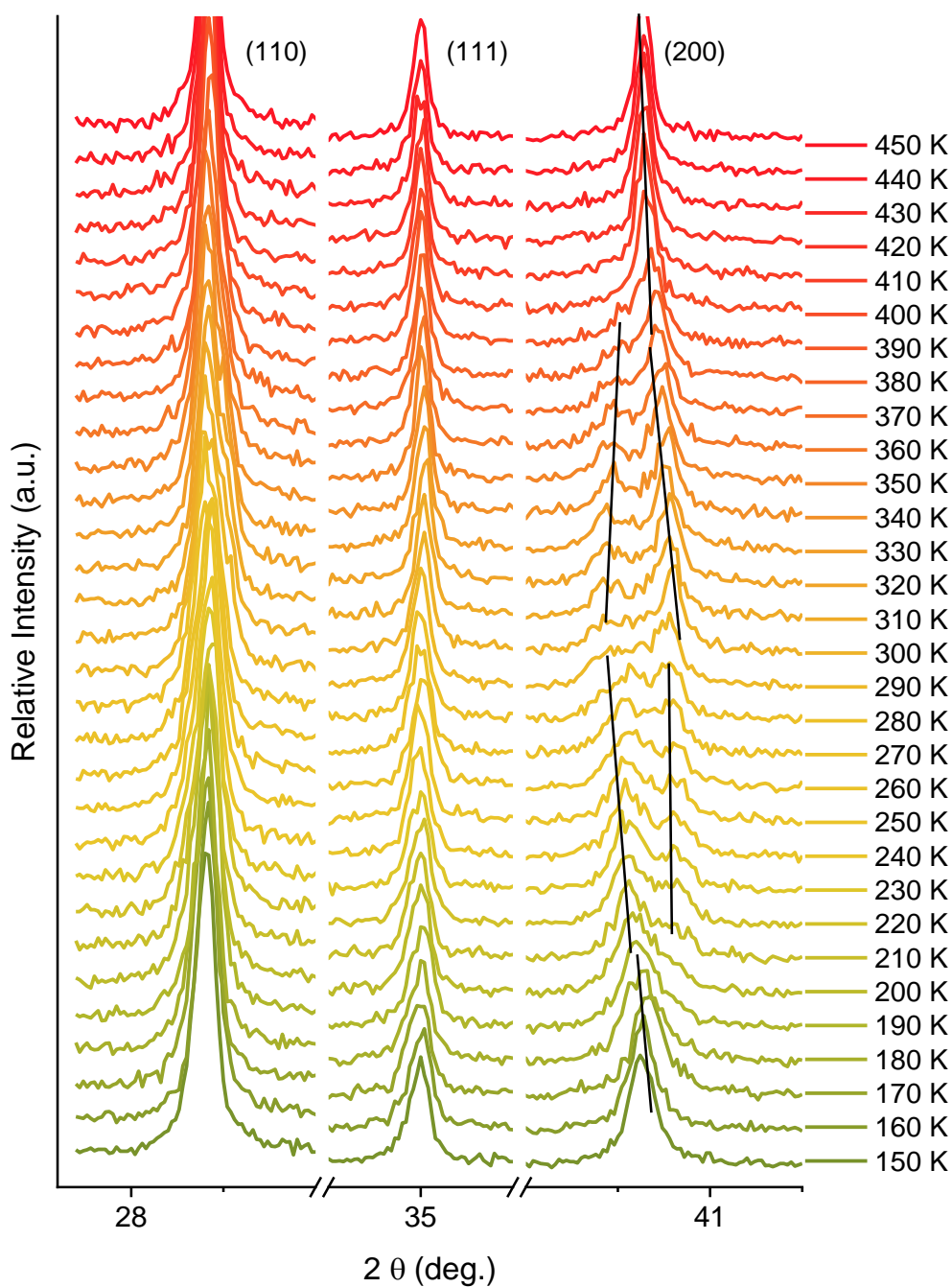


Fig. 2-8 The XRD patterns in (110), (111), and (200) peak of pure BTO as a function of temperature

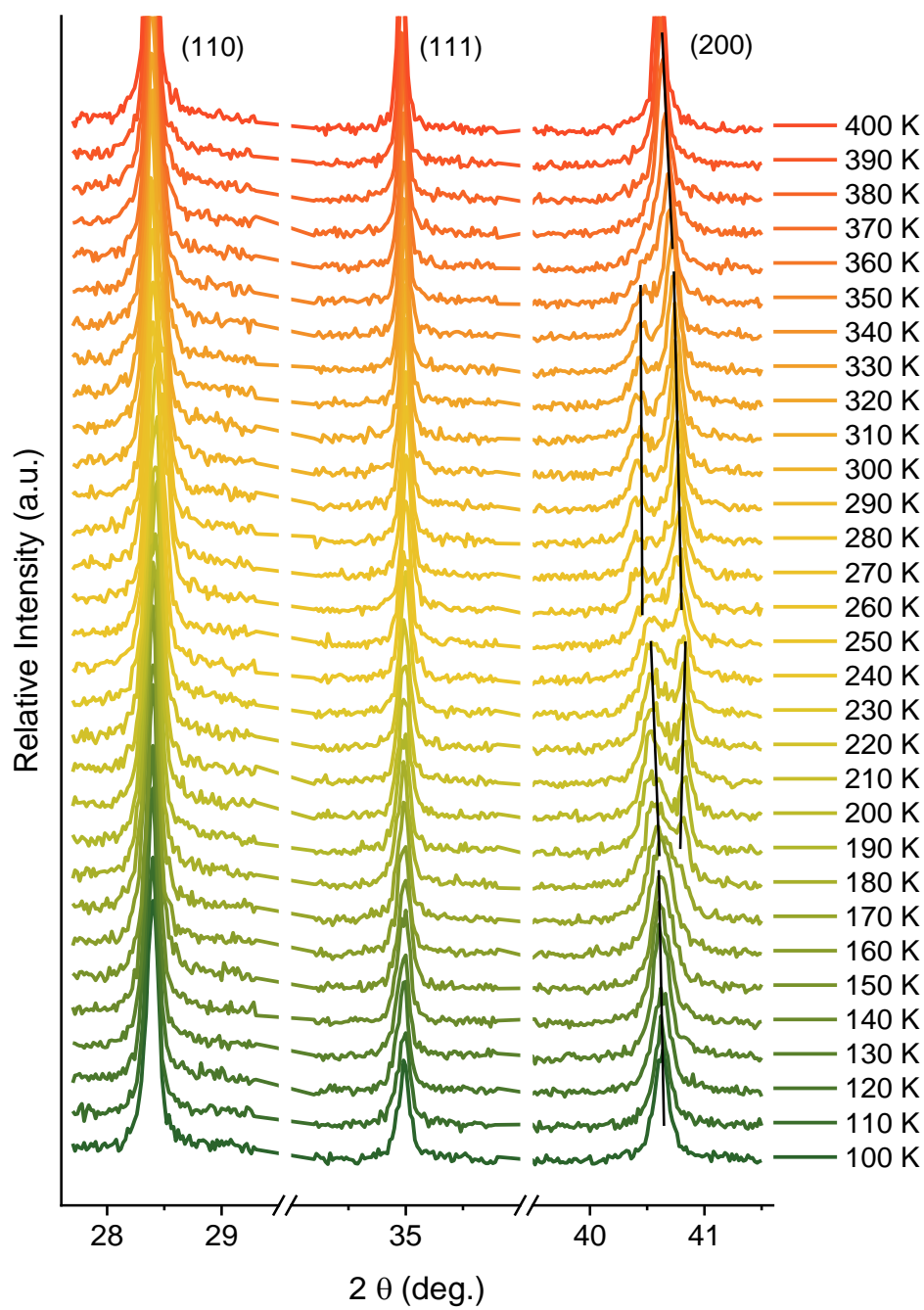


Fig. 2-9 The XRD patterns in (110), (111), and (200) peak of  $x = 0.025$  as a function of temperature

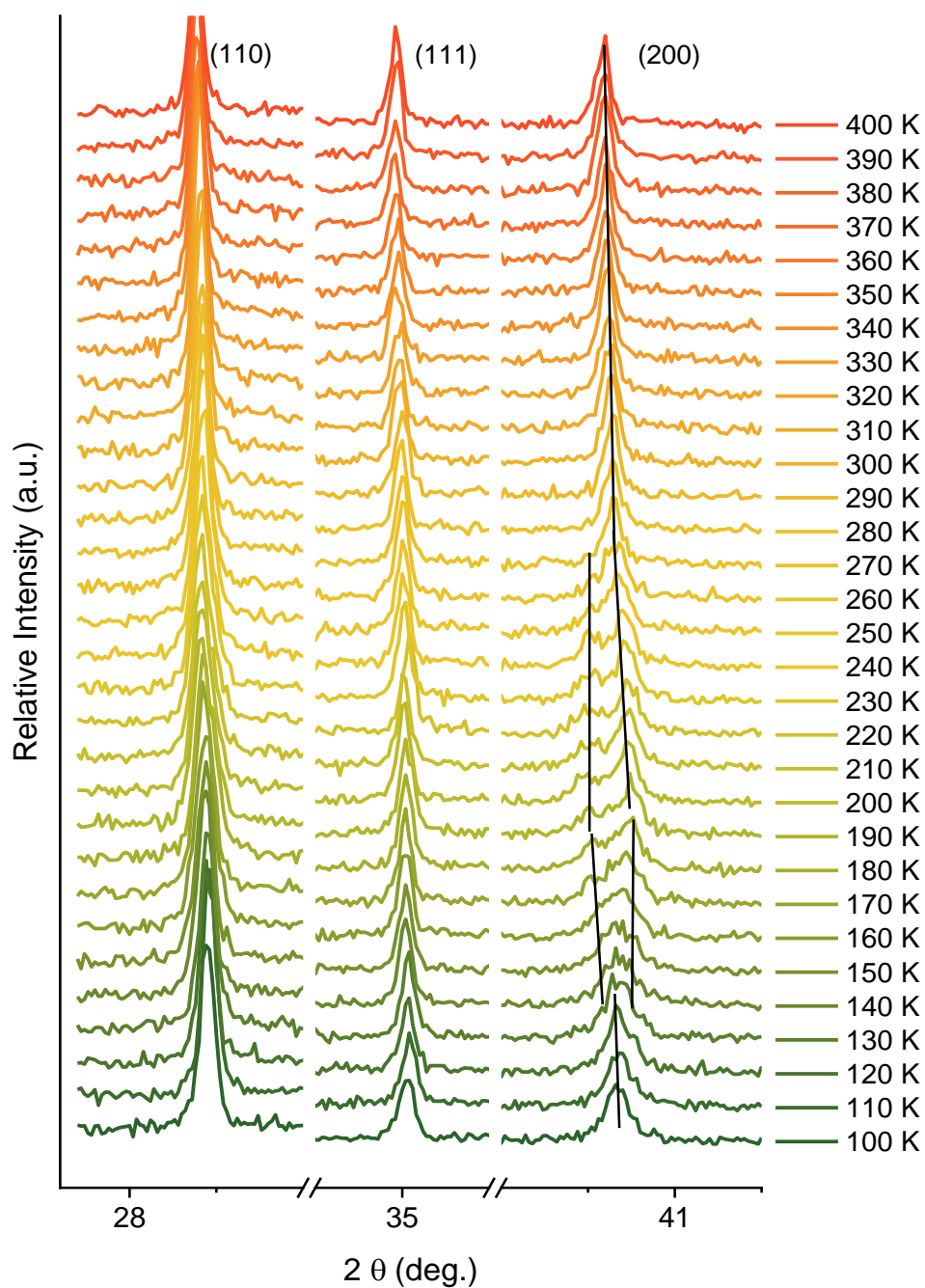


Fig. 2-10 The XRD patterns in (110), (111), and (200) peak of  $x = 0.10$  as a function of temperature

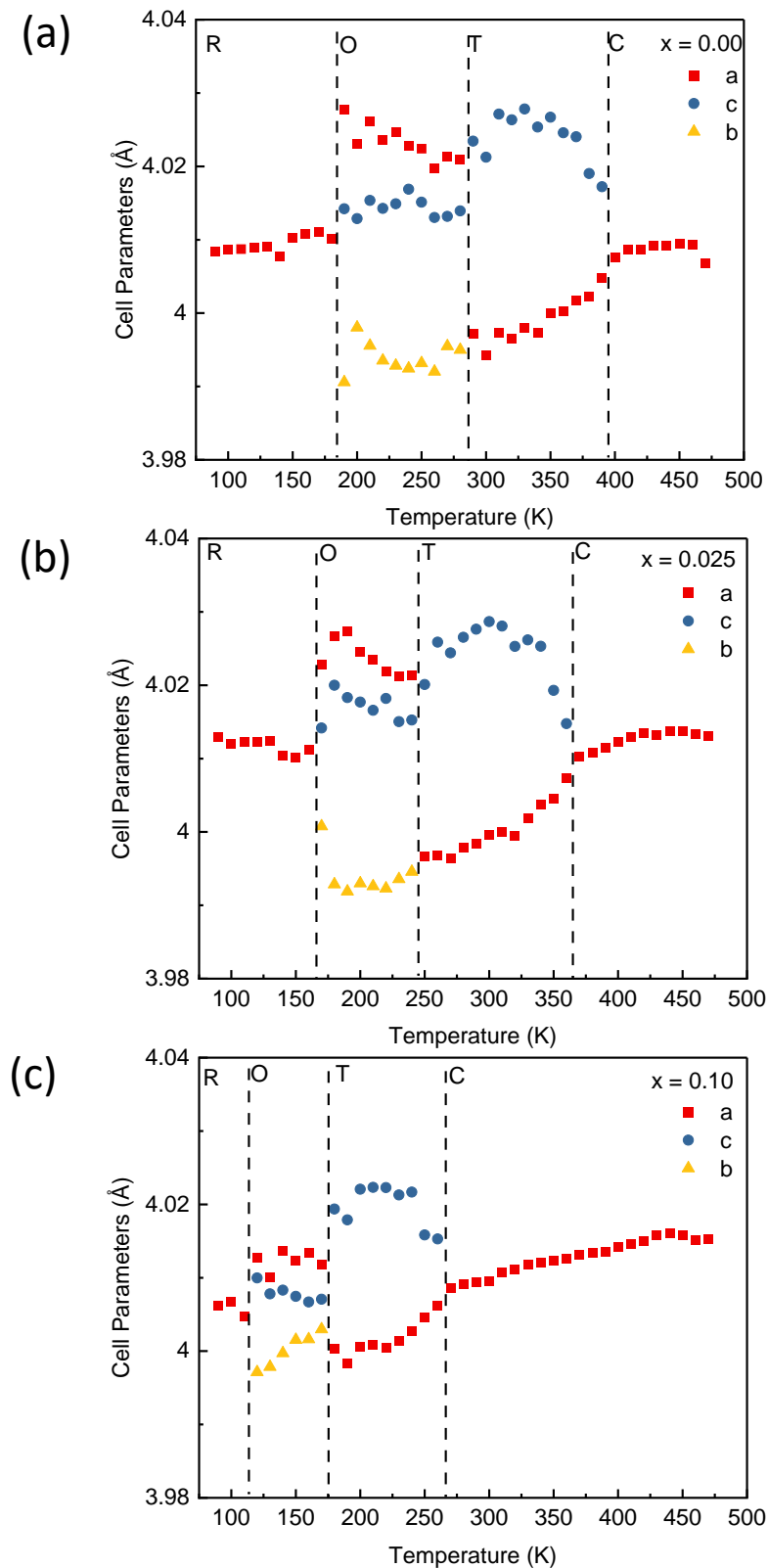


Fig. 2-11 Evolution of lattice parameters with dependence of temperature for samples: (a) pure BTO, (b)  $x = 0.025$ , (c)  $x = 0.10$

### 2.3.5.2 Raman spectra versus temperature

The Raman spectra of BTO are plotted in Fig. 2-12. The mode  $305\text{ cm}^{-1}$  becomes weaker

and disappears above 400 K, as well as the modes at 260 cm<sup>-1</sup> and 720 cm<sup>-1</sup>, indicating the decrease of the ferroelectric phase. Here the phase transition temperature is close to 400 K, in agreement with classical BTO. The other characteristic mode (520 cm<sup>-1</sup>) is also getting broader and weaker with increasing temperature, but it still exists above 400 K due to the Ti atom displacements from their special site in a cubic phase or remaining polar nano regions. The temperature dependence of Raman spectra for doped BTO series are presented in Fig. 2-14 to Fig. 2-18. Similar to pure BTO, it is evident that the intrinsic characteristic modes of the tetragonal phase are getting broader and disappear with an increase in temperature. The three-phase transitions are also evidenced. As we can see, there exist two broad modes at 190 cm<sup>-1</sup> and 490 cm<sup>-1</sup> at lower temperatures, which belong to the rhombohedral phase and disappear gradually when the temperature is increasing, but we can still see these modes in the orthorhombic phase. At higher doping, the mode at 490 cm<sup>-1</sup> still exists in the tetragonal phase (see Fig. 2-17 and Fig. 2-18), which can be explained in terms of local disorder or some nanoclusters of rhombohedral and/or orthorhombic phases. As the temperature further increases, the sharp peak at 305 cm<sup>-1</sup> vanishes, and the modes at 520 cm<sup>-1</sup> and 720 cm<sup>-1</sup> become broader, suggesting that the phase transition from tetragonal to cubic phase occurs. We can also see that the new mode (at 635 cm<sup>-1</sup>) we attributed to the hexagonal phase also turns to be wider as expected from the temperature effect. Its relative intensity increases when the doping increases, demonstrating that the substitution of Ti ions induces the hexagonal phase. For the sample  $x = 0.15$ , we cannot see the sharp modes at 305 cm<sup>-1</sup>, and the intensity of the mode at 635 cm<sup>-1</sup> is much stronger than the mode at 520 cm<sup>-1</sup>, which further suggests that the hexagonal phase exists at higher doping. In addition, there is another new mode (570 cm<sup>-1</sup>) that starts appearing from doping  $x = 0.05$ , but it only persists at lower temperatures and can be attributed to the oxygen vacancies due to the substitution by Mn<sup>3+</sup>.

The shift of mode A<sub>1</sub> (TO<sub>3</sub>) at 520 cm<sup>-1</sup> can be used to depict the phase transitions. As we can see, this mode shifts to lower wavenumbers with increasing temperature, and it becomes broader when it comes to the cubic phase, then the position of this mode increases (shift to the right) for sample  $x = 0.025, 0.05, 0.075$ . Fig. 2-13 exhibits the position shift of the mode at 520 cm<sup>-1</sup> as a function of temperature. For pure BTO, the

transition from the tetragonal to the cubic phase occurs at 400 K. For the doped samples  $x = 0.025 - 0.10$ , the three-phase transitions from rhombohedral to orthorhombic to tetragonal and then to cubic are evidenced, which is in agreement with the results from XRD and dielectric measurements. The phase transition is not clear in sample  $x = 0.15$  (see Fig. 2-18). Even the intensity of the mode ( $305\text{ cm}^{-1}$ ) stays weak at low temperatures, probably suggesting the presence of the tetragonal phase. As shown in Fig. 2-13, by comparing the position change of the mode at  $520\text{ cm}^{-1}$  for different doping levels in the tetragonal phase (except for the doping  $x = 0.10$ ), one can see that the slope decreases with an increase of doping going from 0.10 for  $x = 0$  to 0.011 for  $x = 0.075$ . With doping, the strength of the tetragonal phase and its coherence length decrease. This change related to the structure can also be linked to the bandgap. Indeed, similar trends are observed once fitting the bandgap variation with the temperature (see Fig. 2-19), which shows that the temperature-dependence of the bandgap is weaker (the slope decreases) when doping below  $x = 0.10$ .

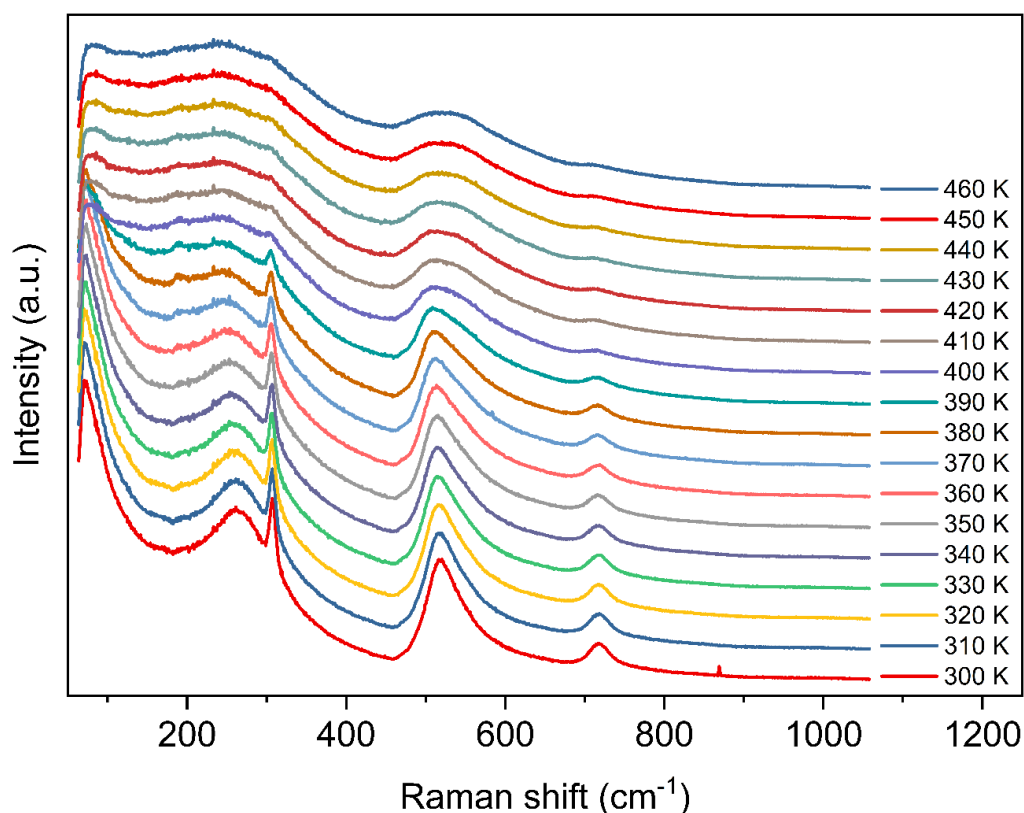


Fig. 2-12 Raman spectra versus temperature for pure BTO ( $x = 0.00$ )

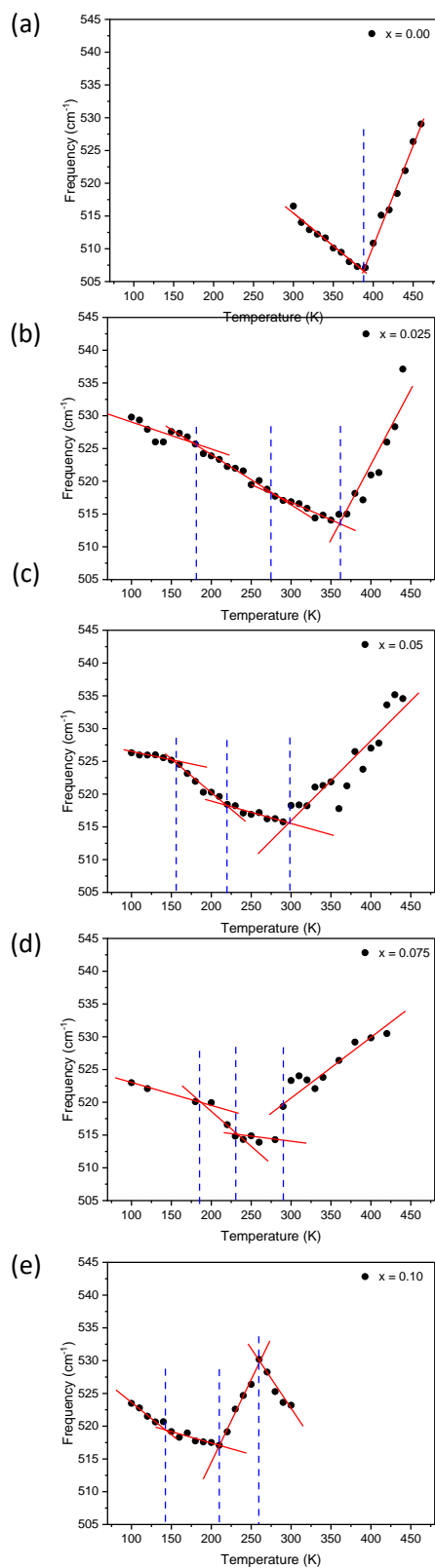


Fig. 2-13 Thermal variations of 520 cm<sup>-1</sup> positions for pure BTO (a) and doped BTO (b-e)

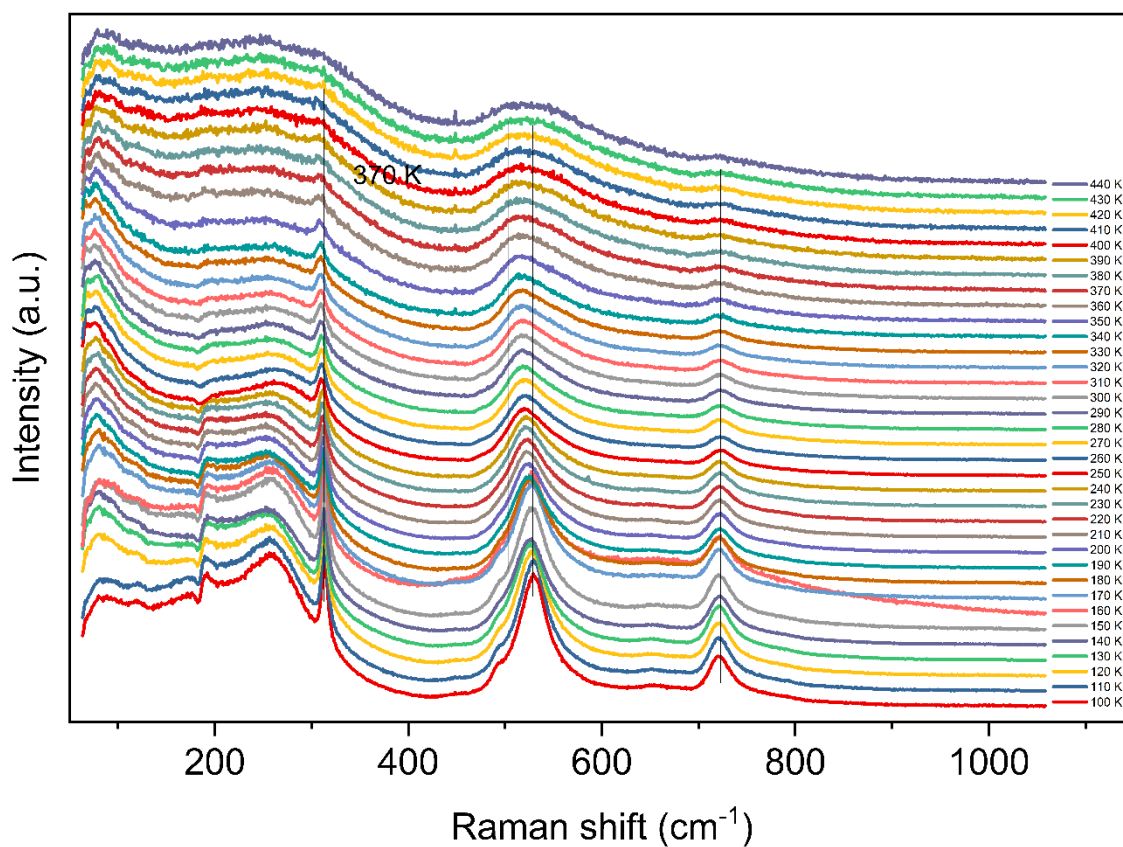


Fig. 2-14 Raman spectra versus temperature for sample  $x = 0.025$

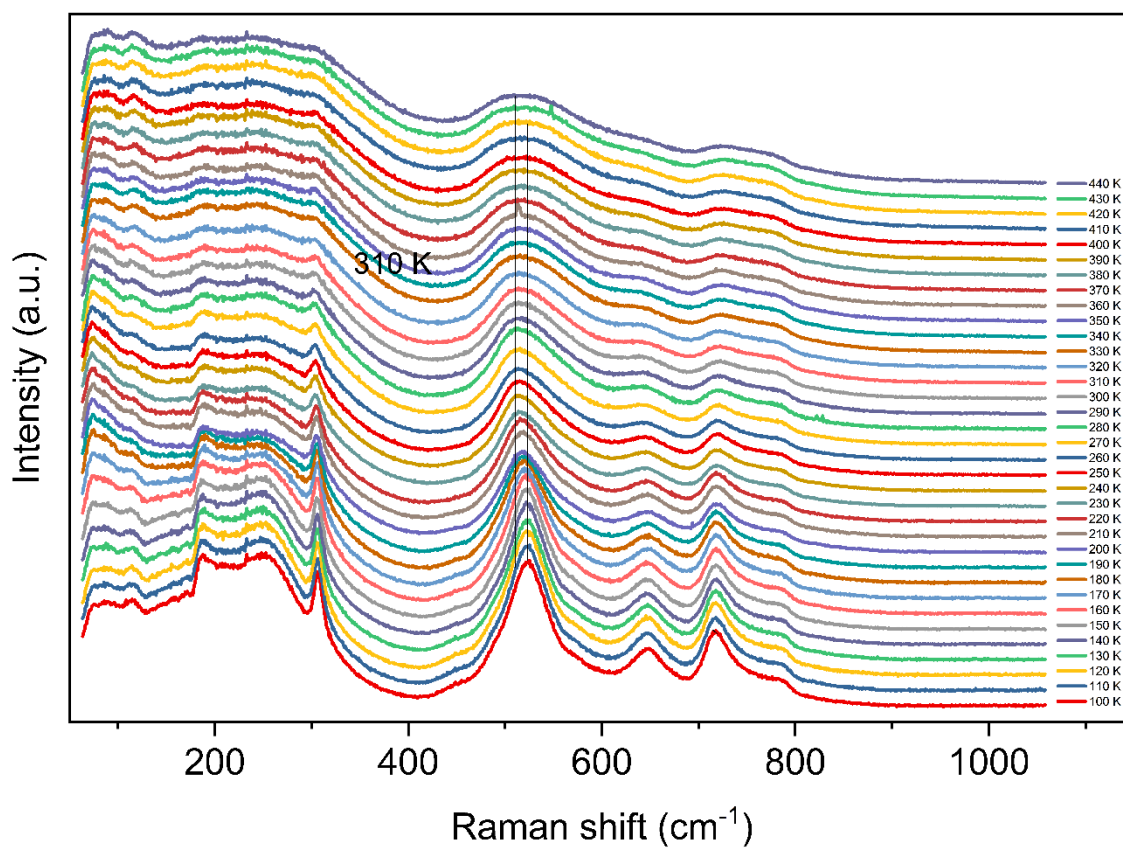


Fig. 2-15 Raman spectra versus temperature for sample  $x = 0.05$

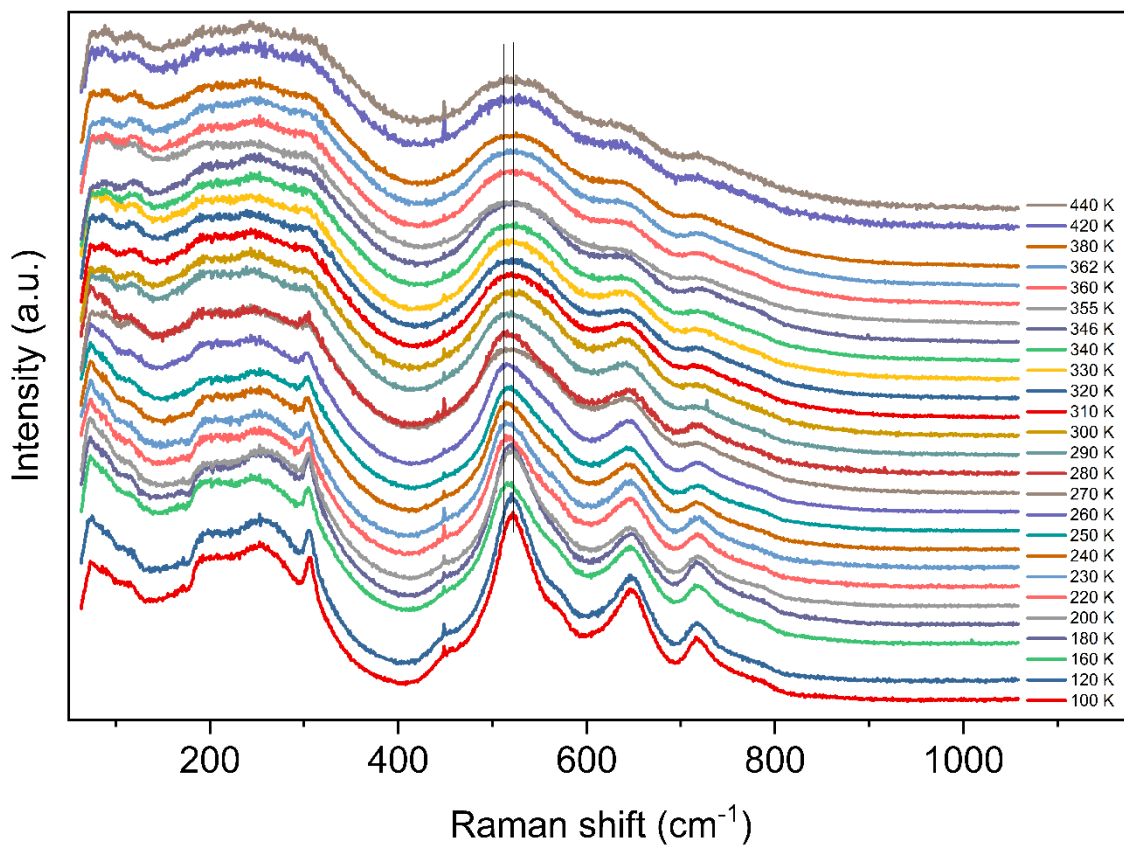


Fig. 2-16 Raman spectra versus temperature for sample x = 0.075

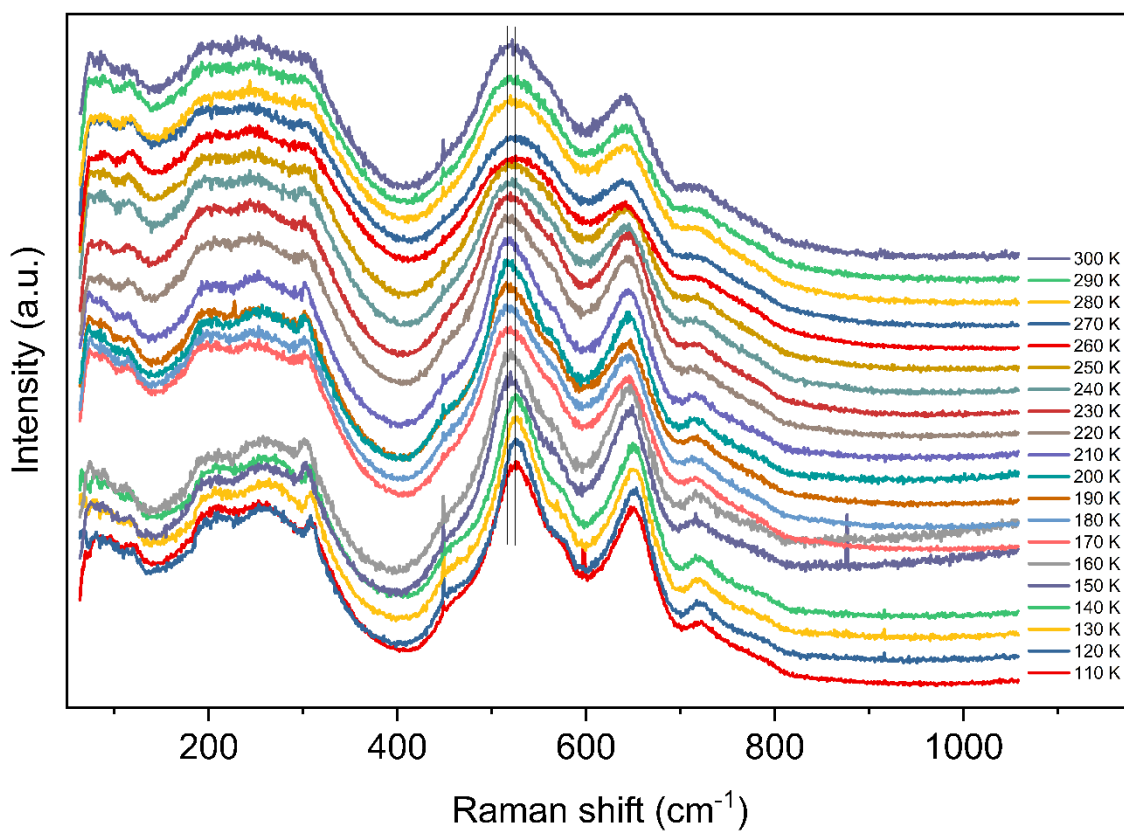


Fig. 2-17 Raman spectra versus temperature for sample x = 0.10

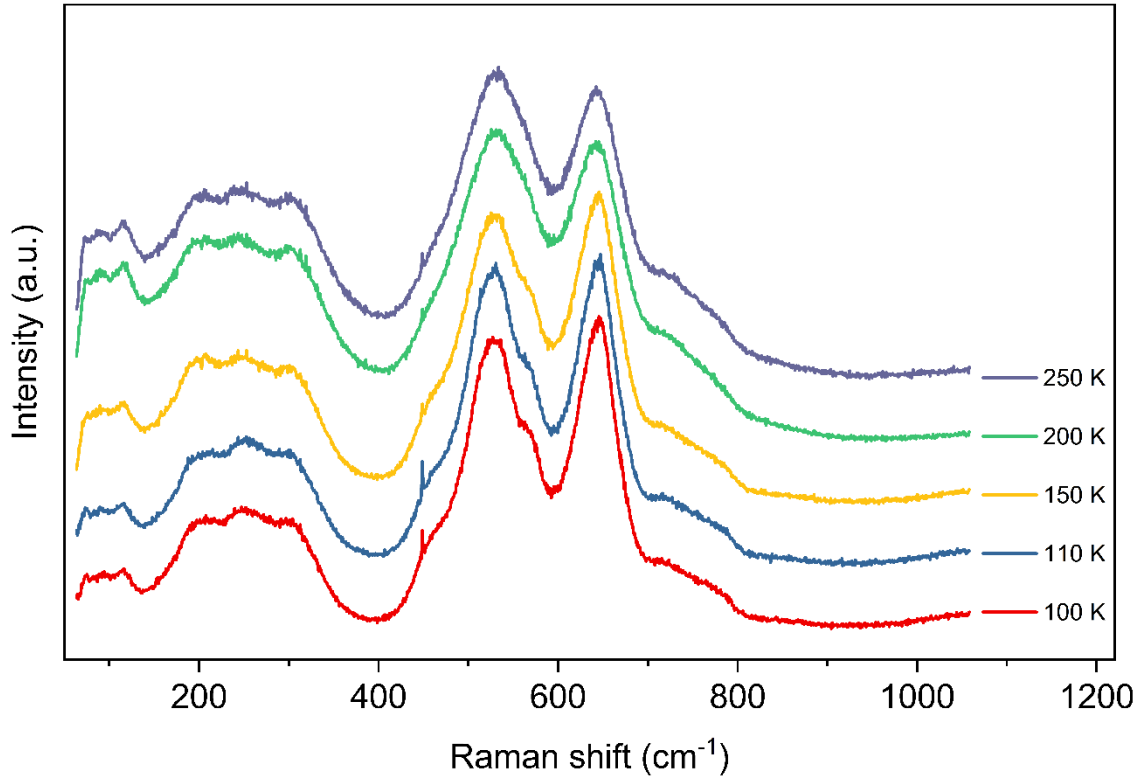


Fig. 2-18 Raman spectra versus temperature for sample  $x = 0.15$

### 2.3.5.3 Temperature dependence of the optical absorption

We collected the diffuse reflectance of the different samples in the temperature range 300 K to 500 K. The absorption and the direct bandgap values versus temperature are presented in Fig. 2-19. When the temperature increases, the energy bandgap tends to decrease due to the interaction of electrons and phonons, exhibiting an almost linear decrease. It is important to note that Varshni's expression can be used to verify the relationship between bandgap and temperature above or below the phase transition temperature.<sup>[126]</sup> Varshni's expression is shown as follows:

$$E_g(T) = E_g(0) - \frac{\alpha T^2}{\beta + T} \quad (2-3)$$

where  $E_g(T)$  is the bandgap at temperature  $T$ ,  $E_g(0)$  is the value at 0 K,  $\alpha$  and  $\beta$  are the constant parameters specific to the material. This expression can be considered as linear with temperature when considering our BTO-based samples. In the tetragonal phase, the bandgap decreases faster (the slope is bigger) than in the cubic phase (the slope is smaller). When varying the amount of co-doping, similarly to the Raman results, the slope, i.e., the temperature variation of the bandgap, becomes weaker, passing from

$8.6 \times 10^{-4}$  (eV·K<sup>-1</sup>) for pure BTO to  $4.4 \times 10^{-4}$  (eV·K<sup>-1</sup>) for  $x = 0.05$  doping. For sample  $x = 0.10$ , we cannot see the transition above room temperature, in agreement with the other measurement results.

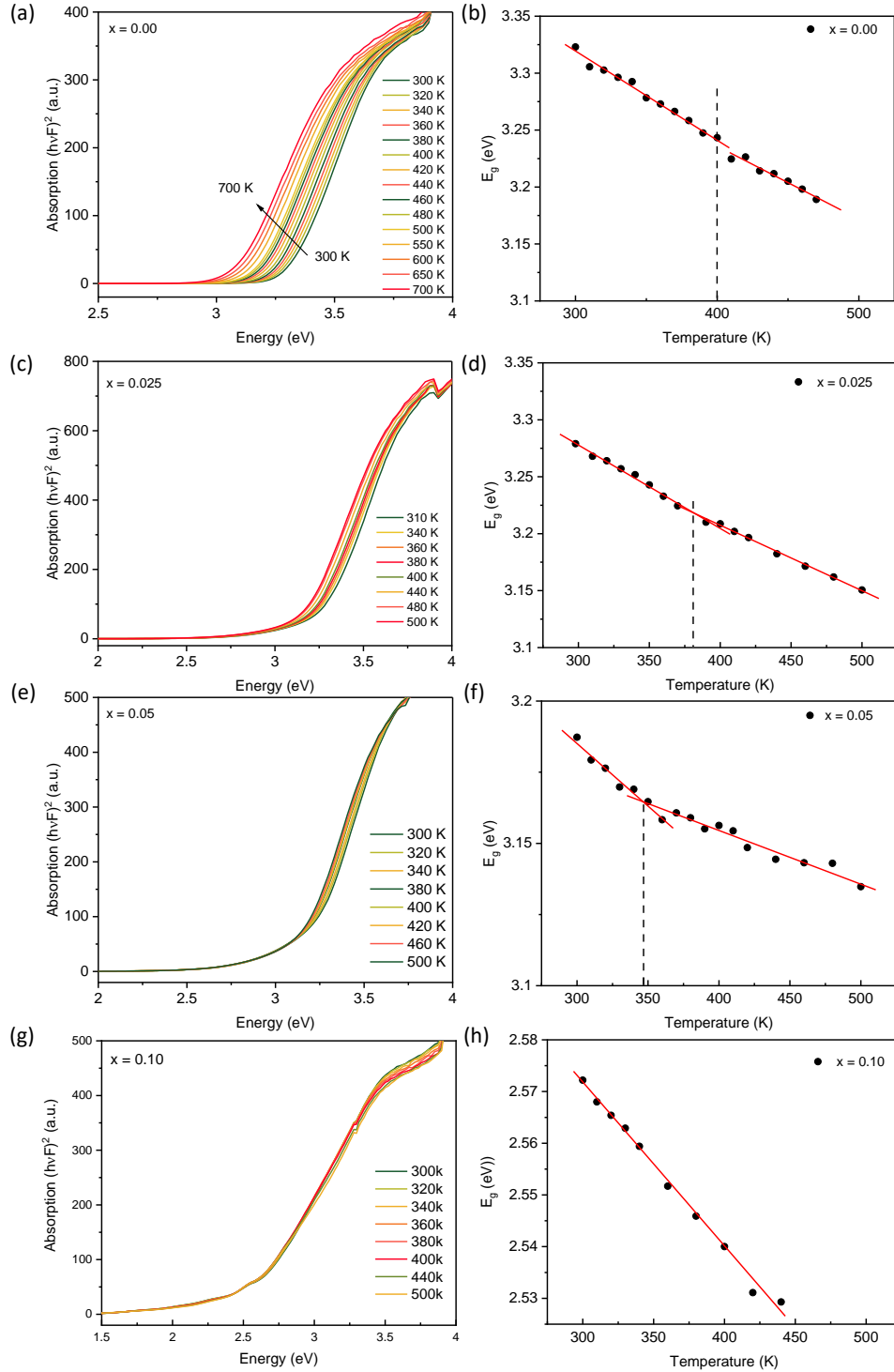


Fig. 2-19 Optical absorption and Bandgap  $E_g$  versus temperature of (a, b)  $x = 0.00$ , (c, d)  $x = 0.025$ , (e, f)  $x = 0.05$ , (g, h)  $x = 0.10$

#### 2.3.5.4 Ferroelectric polarization versus temperature

To better understand the ferroelectric and phase transition behaviors of all these samples, we studied the  $P$ - $E$  loops at different temperatures with a frequency of 5 Hz. Some selected loops are shown in Fig. 2-20 for different compositions. For pure BTO, the  $P$ - $E$  loops get slimmer with increasing the temperature, and the polarization reduces. Then, the loops become linear-like above  $T_c$  and then an ellipse shape takes place at a much higher temperature due to the high conductivity. The sample  $x = 0.025$  presents a pinched loop at room temperature, which becomes open gradually at a higher temperature, and totally open at about 100°C. On the contrary, the loops become again pinched when the temperature decreases down to room temperature. This could be attributed to the defect dipoles, which can easily move at higher temperatures. However, the loops do not fully return to the original state after cooling; there is a slight upward shift. The loops of  $x = 0.05$  (Fig. 2-20c) and  $x = 0.075$  (Fig. 2-20d) show similar behaviors at different temperatures, and they also present the pinched loops at lower temperatures. With much higher substitution, the samples show weak ferroelectric properties. And at lower temperatures, the hysteresis loops perform slimmer behaviors, similar to the most B-site doped BTO with ferroelectric degeneration properties. In addition, Fig. 2-21 presents the evolution of the remnant polarization of  $P_{r+}/P_{r-}$  as a function of temperature. It is found that the ferroelectric phase transition temperatures are in agreement with other measurements (XRD, Raman, or dielectric measurements).

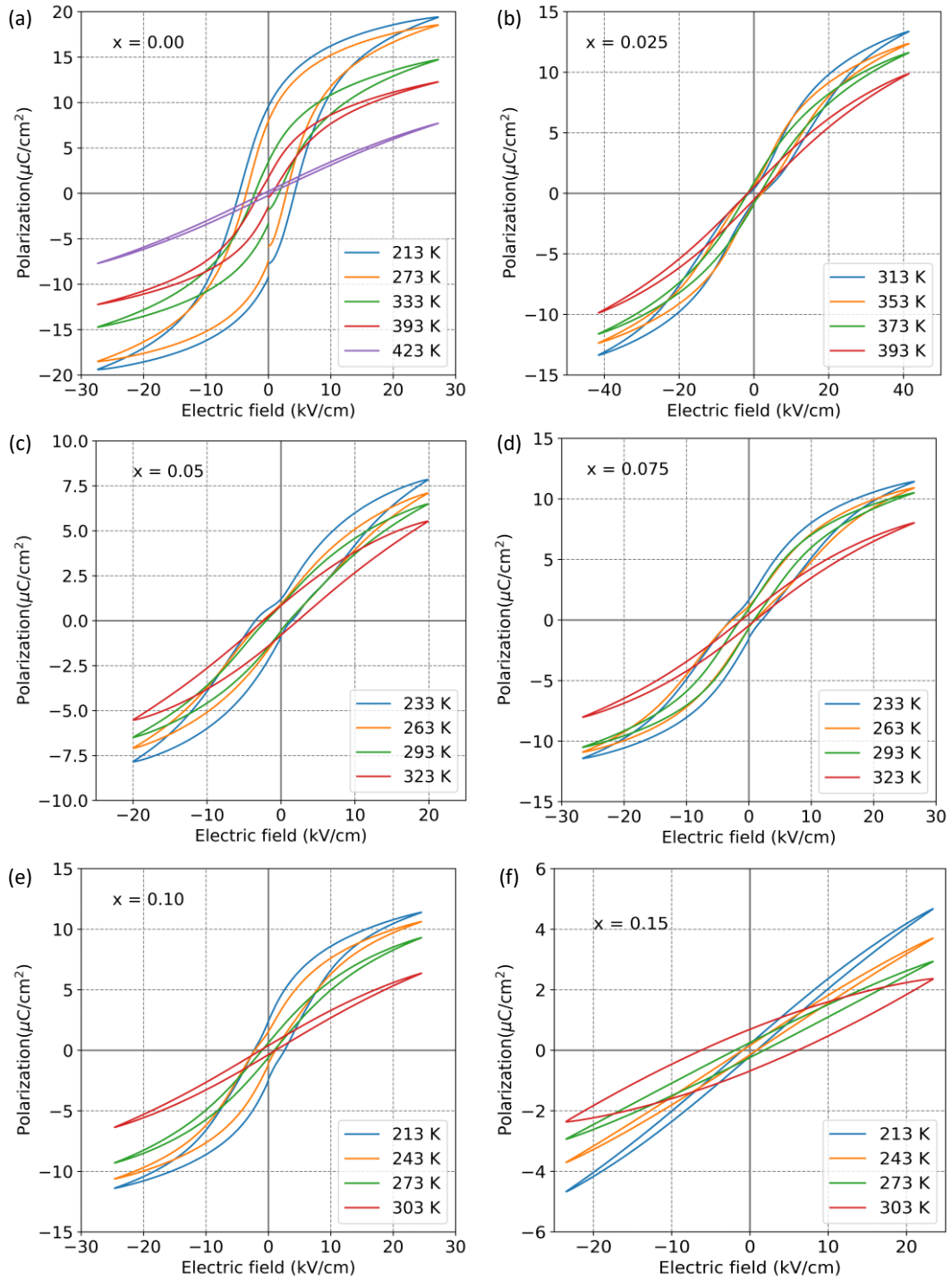


Fig. 2-20 Temperature dependence of ferroelectric loops of (a) pure BaTiO<sub>3</sub> and (b-f) (Mn<sup>3+</sup>, Nb<sup>5+</sup>) co-doped: b)  $x = 0.025$ , c)  $x = 0.05$ , d)  $x = 0.075$ , e)  $x = 0.10$ , f)  $x = 0.15$

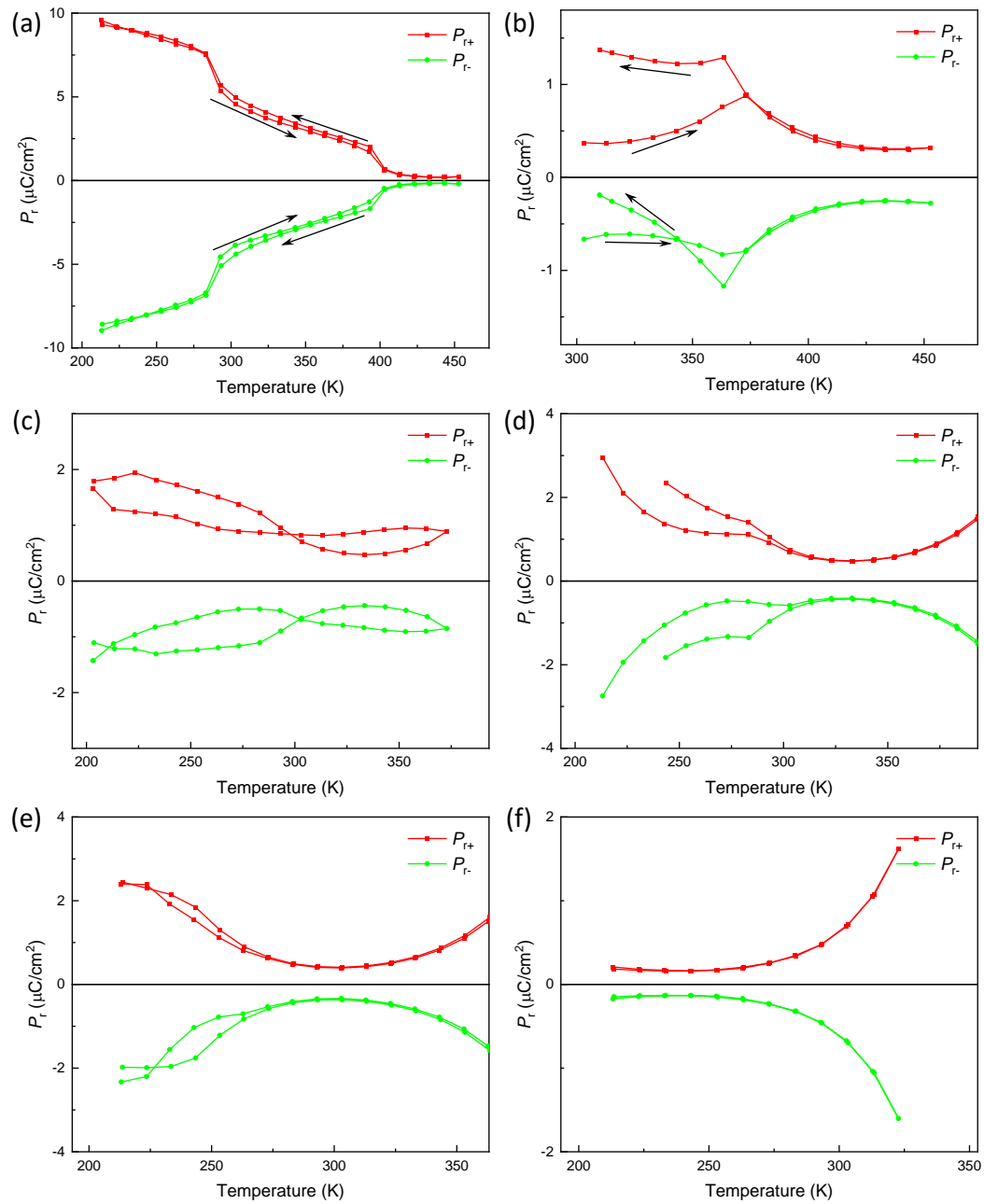


Fig. 2-21 Variation of remnant polarization versus temperature for (a) pure BTO and (b-f) ( $\text{Mn}^{3+}$ ,  $\text{Nb}^{5+}$ ) co-doped: b)  $x = 0.025$ , c)  $x = 0.05$ , d)  $x = 0.075$ , e)  $x = 0.10$ , f)  $x = 0.15$

## 2.4 Conclusions

In this chapter, the samples of  $\text{BaTi}_{1-x}(\text{Mn}_{1/2}\text{Nb}_{1/2})_x\text{O}_3$  are synthesized with  $x$  up to 0.15. At room temperature, with the Mn and Nb amount increasing, the structure changes from tetragonal phase to cubic phase. At higher doping, there is some hexagonal phase that can be seen from the Raman spectra and not from XRD, meaning that this parasitic

phase is in weak quantity and/or of tiny size. According to our dielectric measurements, the ferroelectric phase transition ( $T_c$ ) shifts from 390-400 K for pure BTO to below room temperature ( $x = 0.10, 0.15$ ). The higher Ti substitution destroys the ferroelectricity. The characteristic temperature changes observed from X-ray diffraction and Raman spectra are linked with the dielectric spectroscopy results. We also investigated the optical absorption and ferroelectric polarization versus temperature properties. We integrate all the characteristics in the temperature composition diagram in Fig. 2-22.

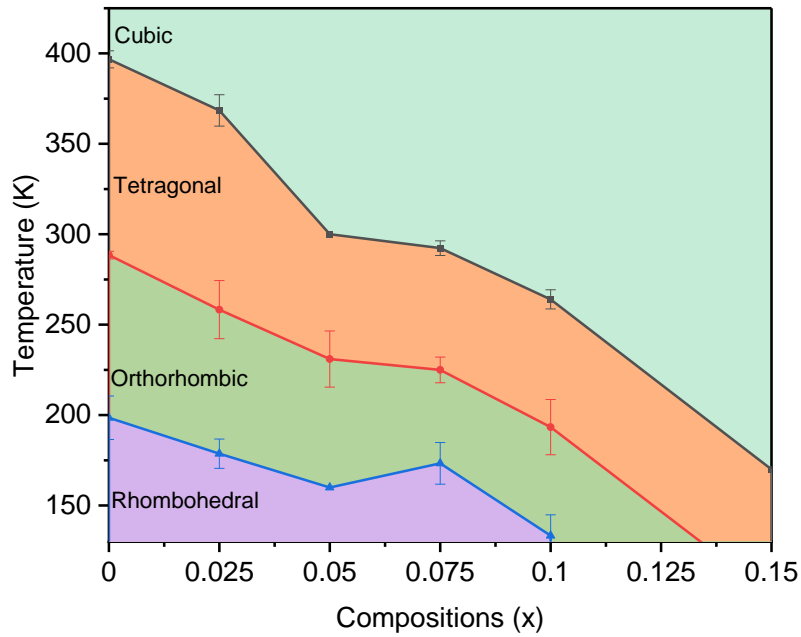


Fig. 2-22 The combined phase diagram with characteristic temperatures and different doping compositions



# 3 The impact of synthesis conditions on the properties of Mn and Nb co-doped BaTiO<sub>3</sub>

## Abstract

BaTi<sub>0.925</sub>(Mn<sub>1/2</sub>Nb<sub>1/2</sub>)<sub>0.075</sub>O<sub>3</sub> ceramics were fabricated by the conventional solid-state reaction method, changing the ball milling parameters and the sintering time during the process. We investigated the effects of the synthesis procedure on the lattice symmetry, microstructure, electrical and optical properties of the co-doped BaTiO<sub>3</sub>. X-ray diffraction at room temperature shows the ratio  $c/a$  values become smaller with increasing milling time and speed, indicating that the tetragonality decreases gradually. The dielectric measurements versus temperature exhibit a shift to lower temperature, meaning the decrease of ferroelectric phase transition temperature. Meanwhile, the hysteresis loops demonstrate the deterioration of the ferroelectric properties. The overall performance can be linked to the microstructure and chemical distribution. The reduced time and lower speed of ball milling allow obtaining an inhomogeneous and bimodal grain size distribution. At a longer time and higher rate, a homogeneous distribution is achieved, and the ferroelectric properties weaken at room temperature. The optical absorption improves effectively after doping. The onset of energy decreased to as low as 1.5 eV, which slightly changes depending on the conditions, suggesting that the MnNb co-doped BaTiO<sub>3</sub> materials are promising candidates for ferroelectric photovoltaic applications.

## 3.1 Introduction

BaTiO<sub>3</sub> (BTO) is widely investigated in various electronic devices due to its high dielectric permittivity and excellent electrical properties.<sup>[127,128]</sup> It has been reported that chemical

modification is an effective strategy to tune the functional properties. Replacing the A- or B- site cations with isovalent or alivalent dopants and modifiers can raise or lower the temperature and alter the properties.<sup>[129–131]</sup> For example, the BT-based ceramics would change from a normal ferroelectric to a relaxor by Mn and Nb co-doped on B sites.<sup>[132]</sup> Meanwhile, microstructural engineering, such as grain size, texturing, or composite, profoundly affects the dielectric and piezoelectric properties of the ferroelectric.<sup>[133–135]</sup> The synthesis procedure, solid-state reaction, or hydrothermal methods, significantly impact the structure or properties. However, still, there is few, if any, works dealing with the consequences of the microstructure on the optical properties in ferroelectrics.

Recently, ferroelectrics have received significant interest due to their potential in optical applications, including photovoltaic solar cells, photocatalysts, or innovative elasto-optic devices.<sup>[8,10,11]</sup> However, most perovskite ferroelectrics like BaTiO<sub>3</sub>, BiFeO<sub>3</sub>, and KNbO<sub>3</sub> have a large bandgap, which is almost larger than 3 eV.<sup>[10,122,136]</sup> If the ferroelectric materials could have a small band gap and a higher optical absorption efficiency, it would be helpful for the application of photovoltaic devices. BaTiO<sub>3</sub> has a relatively high bandgap (3.2 eV) due to the significant difference in electronegativity between the 3d electron state of transition metal on B-site and the 2p state of the oxygen atoms. As already mentioned, in recent years, especially since 2018 when this Ph.D. work started, BaTiO<sub>3</sub> based materials have been widely studied to tune the bandgap and the optical absorption for the photovoltaic application by chemical substitutions.<sup>[14,84–86]</sup> Unfortunately, the polarization at room temperature or the Curie temperature usually deteriorates when the materials show a lower bandgap. These improved bandgaps fail to lead to the bulk photovoltaic effect triggered by the polarization. Nevertheless, Das et al. showed that both Mn and Nb co-doped ceramics have a lower bandgap and sizable polarization at room temperature.<sup>[84]</sup> A lot of work has been done on the co-doped BaTiO<sub>3</sub> materials. For example, in 2019, Ni and Ni-Nb substituted in BaTiO<sub>3</sub> present interesting infrared-ultraviolet light-absorbing properties, as the optical band gap lowered to ~ 1.5 eV.<sup>[87]</sup> Chu et al. reported in 2020 that the bandgap of Co/Nb co-doped BaTiO<sub>3</sub> is about 1.3 eV apart from the ferroelectric and ferromagnetic properties at room temperature.<sup>[86]</sup> In most cases, the ferroelectric properties deteriorate with the increase of doping concentration. It is known that the

synthesis and the chemical process significantly influence the chemical functional properties of ferroelectric ceramic materials. Thin-film heterostructures or multilayers are also good ways to keep significant spontaneous polarization.<sup>[32,42,137]</sup>

In this chapter, we study both the absorption and ferroelectric properties of Mn and Nb co-doped BaTiO<sub>3</sub> by changing the synthesis process. We have found that the Curie temperature and the remnant polarization could be tuned by varying the mechanical milling and sintering time conditions. The process affects the structure, the chemical distribution, and the grain size. In contrast, the optical absorption has only weak changes depending on the chemical route synthesis conditions.

## 3.2 Experimental procedure

### 3.2.1 Material preparation

BaTi<sub>0.925</sub>(Mn<sub>1/2</sub>Nb<sub>1/2</sub>)<sub>0.075</sub>O<sub>3</sub> ceramic samples were prepared by the traditional solid-state synthesis methods. BaCO<sub>3</sub> (Strem 99.9%), TiO<sub>2</sub> (Prolabo 99%), Mn<sub>2</sub>O<sub>3</sub> (Strem 99%) and Nb<sub>2</sub>O<sub>5</sub> (Alfa Aesa 99.9%) were used as starting raw materials. Before mixing, BaCO<sub>3</sub> was heated at 500 °C for 5 hours to remove any absorbed moisture. Then, the powders were weighed in stoichiometric amounts and mixed by ball-milling. Here, we chose different ball-milling parameters, changing the time and speed of ball-milling, 1h-150rpm, 1h-450rpm, 4h-450rpm, and 8h-450rpm. Besides, all the doped systems are dry milled, except for the 1h-150rpm sample where alcohol was used. After drying, the milled powders were calcined at 900-1000 °C for 12 hours. The powder obtained after this step was pressed into pellets of about 8 mm diameter and 1 mm thickness with polyvinyl alcohol (PVA) as a binding agent. The pellets were then sintered at 1280 °C for 10 hours and 20 hours.

### 3.2.2 Characterization

The X-ray diffraction (XRD) patterns were collected on a Bruker D2 phase diffractometer using Cu radiation. Raman spectroscopy was recorded at a temperature over the range of 100-500 K. The scanning electron microscopy (SEM) was performed on the pellets

after polishing. Diffuse reflectance spectra for powder were obtained using Perkin Elmer UV-visible NIR spectroscopy (Lambda 850). The optical band gap was estimated by the Tauc plot of the Kubelka-Munk function  $F_{KM} = (1-R)^2/2R$ , where R is the reflectance.<sup>[121]</sup> For the measurement of electrical properties, silver electrodes were painted onto both sides of the polished pellets. Dielectric constants as a function of temperature and frequency were conducted by an impedance analyzer (HP4294A). The polarization loops in different temperatures were collected using a ferroelectric tester (AixACCT) in the silicone oil.

## 3.3 Results and Discussion

### 3.3.1 The dependence of the microstructure on synthesis conditions

The XRD patterns of these samples at room temperature are presented in Fig. 3-1. The patterns show diffraction peaks that correspond to the BaTiO<sub>3</sub> tetragonal *P4mm* space group (JCPDS # 05-0626). As shown in Fig. 3-1a, all samples show pure phase without evidence of any secondary phase, indicating that Mn and Nb have been introduced into the BaTiO<sub>3</sub> lattice. A selected plot around the (002)/(200) peak in Fig. 3-1b shows that the tetragonal distortion decreases with increasing the milling process's parameters. The longer milling time and higher milling rate mean that the raw powder is better and completely mixed, which significantly influences the structure and properties. From the values of lattice parameters, the ratio *c/a* decreases, as illustrated in Fig. 3-1c. It is found that the tetragonality decreases, and the structure becomes close to a cubic phase at room temperature.

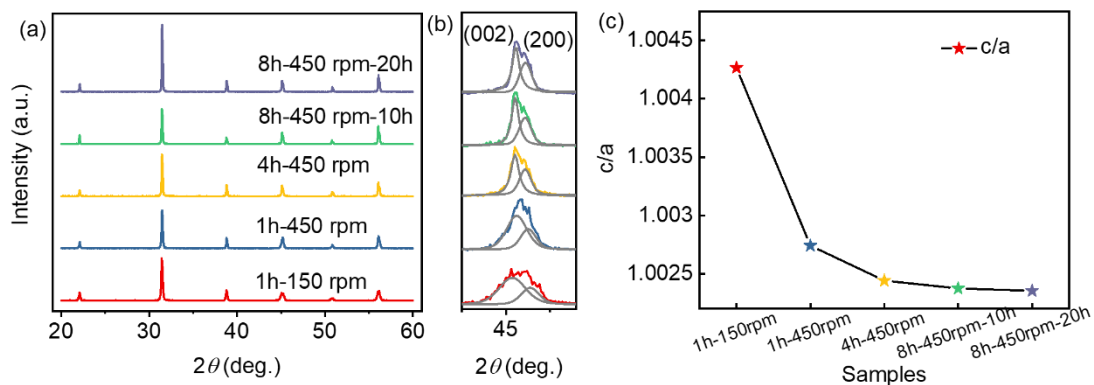


Fig. 3-1 (a) XRD patterns of the samples BaTi<sub>0.925</sub>(Mn<sub>1/2</sub>Nb<sub>1/2</sub>)<sub>0.075</sub>O<sub>3</sub> in different processes measured at room temperature. (b) Magnified (200) peak. (c) Lattice parameters  $c/a$  as a function of the synthesis procedure

We have also investigated the diffraction patterns of the sample 1h-150rpm as a function of temperature (see Fig. 3-2). When fitting the XRD patterns, we can see that the first phase transition from cubic to tetragonal takes place at about 350 K, and then the orthorhombic phase occurs at about 250 K, and finally, it turns to rhombohedral phase at about 160 K. The sample exhibits higher tetragonality at room temperature when compared to the sample made with high rate milling. As shown in Fig. S 3-1 and Fig. S 3-2, the ferroelectric phase transition temperature is about 360 K for 0.05MnNb and 300 K for 0.10MnNb, respectively.

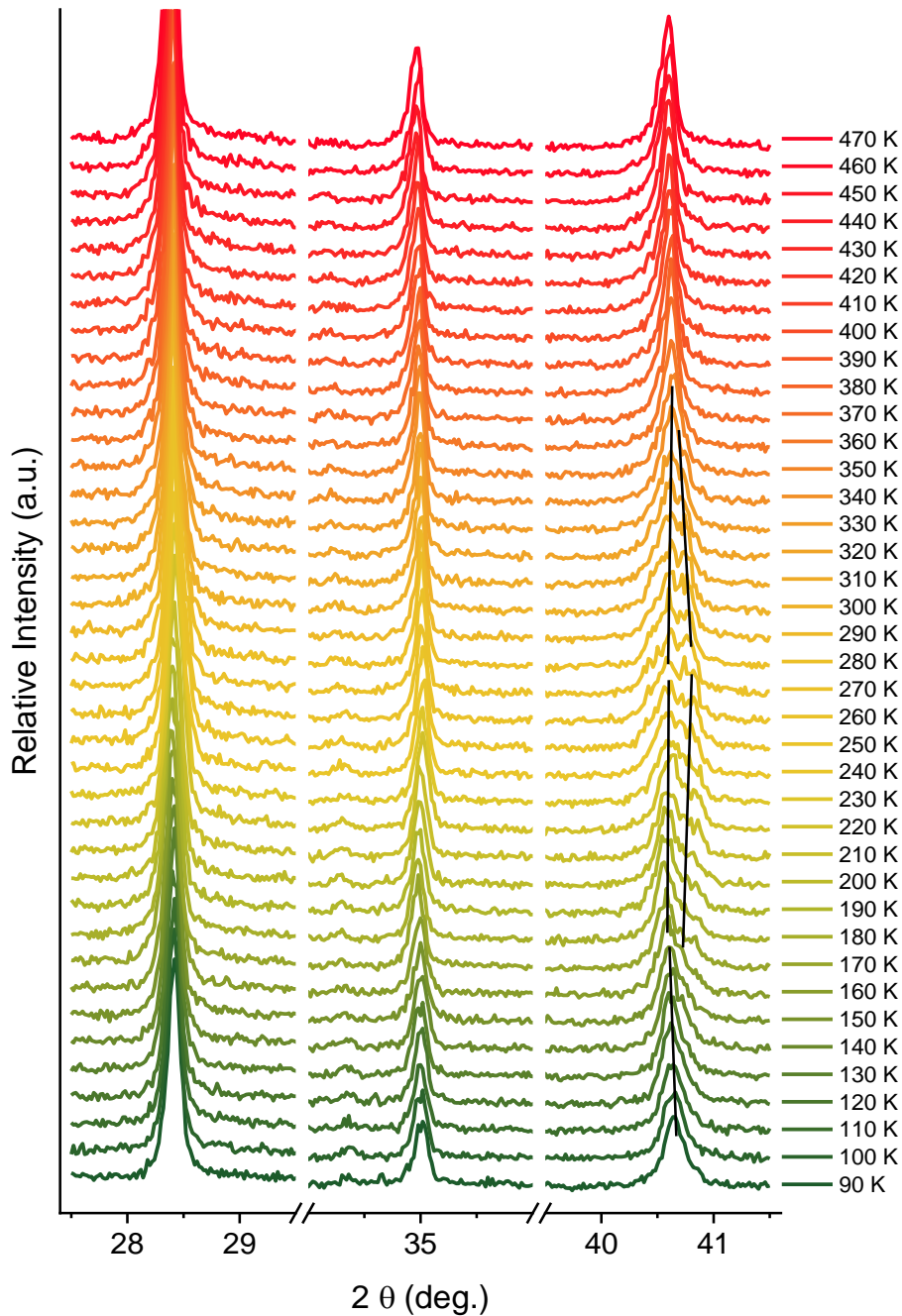


Fig. 3-2 The XRD patterns in (110), (111), and (200) peak of sample 1h-150rpm as a function of temperature

To further investigate the phase transitions and microstructures of the different samples, Raman scattering spectra are also collected. All the Raman spectra at room temperature are depicted in Fig. 3-3. As known, the primitive unit cell of pure  $\text{BaTiO}_3$  has five atoms, and therefore 12 different optical modes are active. The main features of the  $\text{BaTiO}_3$  spectrum are the three major groups of modes, which are at low-frequency  $A_1(\text{TO}_1)$  at  $260 \text{ cm}^{-1}$  and  $B_1(\text{TO}_2)$ ,  $E(\text{TO}_2+\text{LO}_2)$  at  $305 \text{ cm}^{-1}$ , in mid-frequency  $A_1(\text{TO}_3)$  at  $512 \text{ cm}^{-1}$ ,

and the high-frequency A1(LO<sub>2</sub>) (with a possible mixture of E(LO<sub>3</sub>) character) at 716 cm<sup>-1</sup>.<sup>[118]</sup> Note that LO and TO stand for Longitudinal optic and Transverse optic modes, respectively. The acquired spectrum of the specimen (1h-150rpm) is deconvoluted for illustration using Voigt functions. Fig. 3-3b shows the FWHM of the 305 cm<sup>-1</sup> mode, which is commonly considered for characterizing the tetragonality. The broad mode at 260 cm<sup>-1</sup> is the BO<sub>6</sub> octahedral bending vibration, and the sharp mode at 305 cm<sup>-1</sup> is connected with the long-range ferroelectric phase. This sharp mode gradually becomes broader and roughly disappears at the sample 8h-450rpm, indicating lesser tetragonality, in agreement with the XRD results. In addition to the perovskite BTO phase, there is also some parasitic phase because of the mode at about 636 cm<sup>-1</sup> (A<sub>1g</sub>), which belongs to the hexagonal BTO phase.<sup>[114,115]</sup> The other two modes at a higher frequency are associated with the oxygen octahedrons and are becoming progressively broader, suggesting an increase of the disorder and/ or the insertion of Mn and Nb at the place of Ti, leading to three different oxygen octahedra.

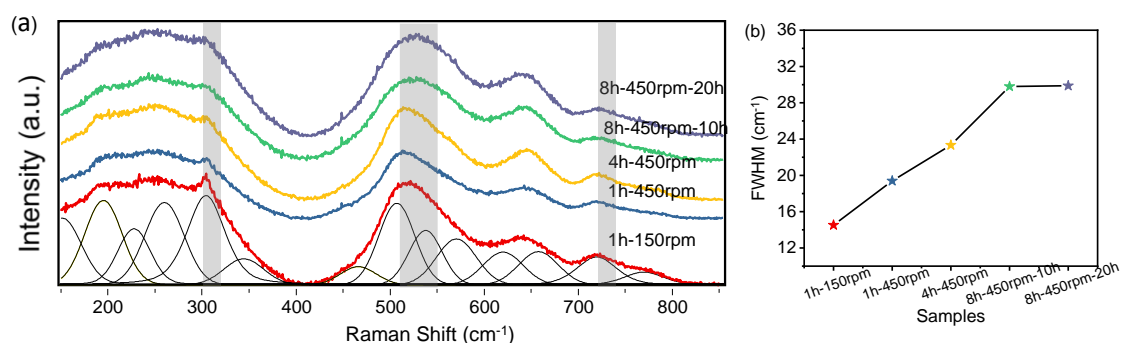


Fig. 3-3 (a) Raman spectra and (b) FWHM of 305 cm<sup>-1</sup> phonon mode of the MnNb co-doped samples

The Raman spectra versus temperature are also collected and shown in Fig. 3-4 to Fig. 3-6. It is observed that the intrinsic characteristic modes of the tetragonal phase (305 cm<sup>-1</sup>, 520 cm<sup>-1</sup>, and 720 cm<sup>-1</sup>) become broader and weaker or disappear with an increase of temperature. As shown in Fig. 3-4, for the sample 1h-150rpm, the mode of 305 cm<sup>-1</sup>, which represents the ferroelectric polar phase, disappears at about 350 K, where the phase transition happens. The position of mode 520 cm<sup>-1</sup> turns wide and first shifts to lower wavenumbers with increasing temperature and then to higher wavenumbers above about 350 K. The situation is similar to the other samples, and the ferroelectric phase transition are also evidenced, comparable to that obtained from the dielectric

### 3.3 Results and Discussion

measurements. At lower temperature, the  $A_{1g}$  mode ( $\sim 780\text{ cm}^{-1}$ ) is much better seen, and as we have mentioned in chapter 2, it belongs to the octahedral breathing mode, related to the B site doping. Compared to the Raman spectra of sample 8h-450rpm (shown in Fig. 2-16), it is found that the relative intensity of the mode at  $635\text{ cm}^{-1}$  due to the presence of a parasitic phase increases by longer milling time and higher speed milling.

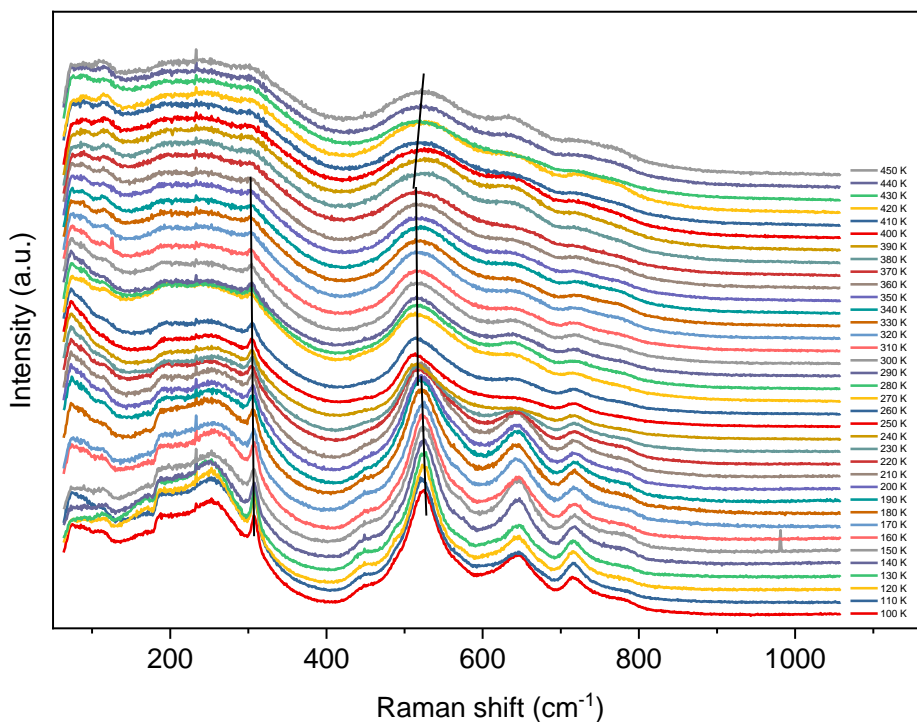


Fig. 3-4 Raman spectra versus temperature for sample 1h-150rpm

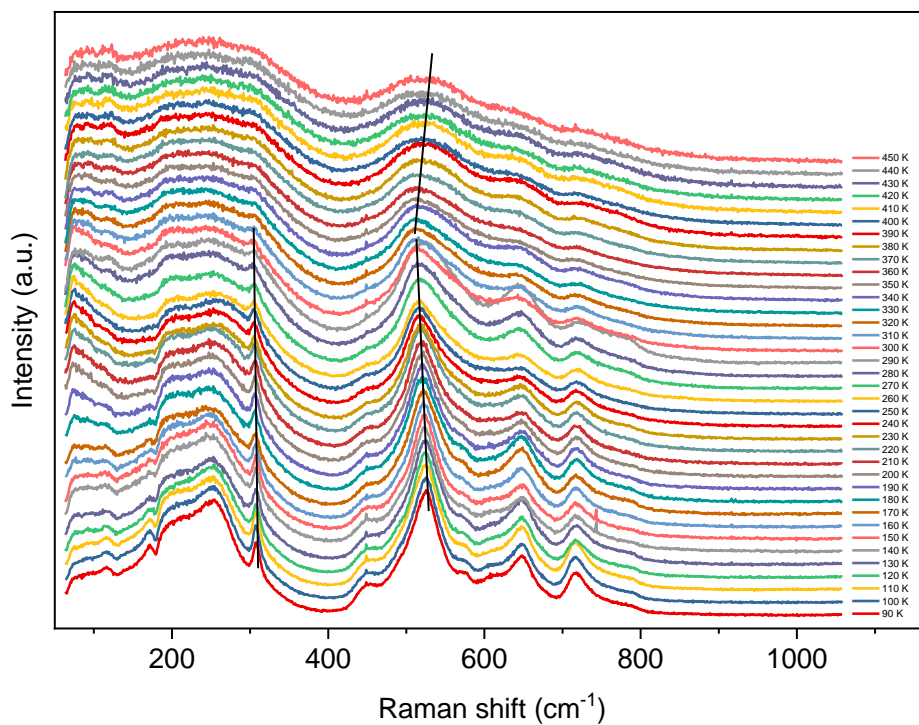


Fig. 3-5 Raman spectra versus temperature for sample 1h-450rpm

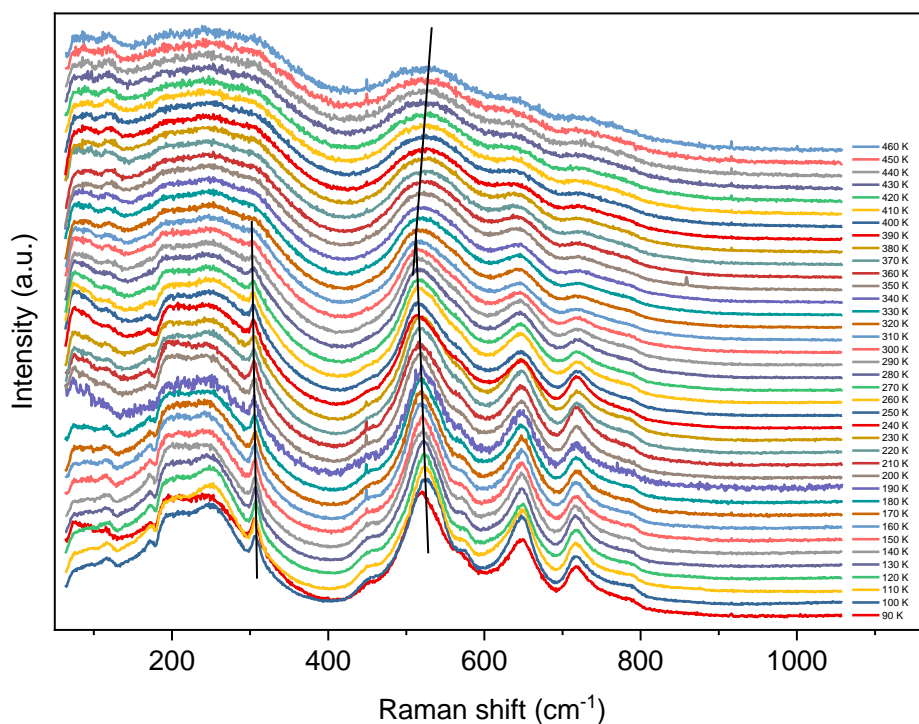


Fig. 3-6 Raman spectra versus temperature for sample 4h-450rpm

Fig. 3-7 illustrates the surface morphology of all the sintered ceramics via different synthesis procedures. It is found that the grain sizes are strongly dependent on the synthesis/sintering process. It is evident that the specimen, prepared by ball milling 1h-

### 3.3 Results and Discussion

150rpm, shows more porosity than the other samples, showing that this milling step can have a significant impact on the microstructure. It displays bimodal grain size distribution, with the smaller grains being surrounded by the larger grains. Although there are still bimodal grain size distribution when increasing the ball milling time and speed, the average grain size increases from about 1  $\mu\text{m}$  (1h-150rpm) to  $\sim 2.3 \mu\text{m}$  (8h-450rpm). From Fig. 3-8, it is clear that the sample 8h-450rpm still exhibits a bimodal distribution. In contrast, the sample sintered for 20 hours shows unimodal grain size distribution, and the mean size is much larger than the others, being about 21  $\mu\text{m}$ .

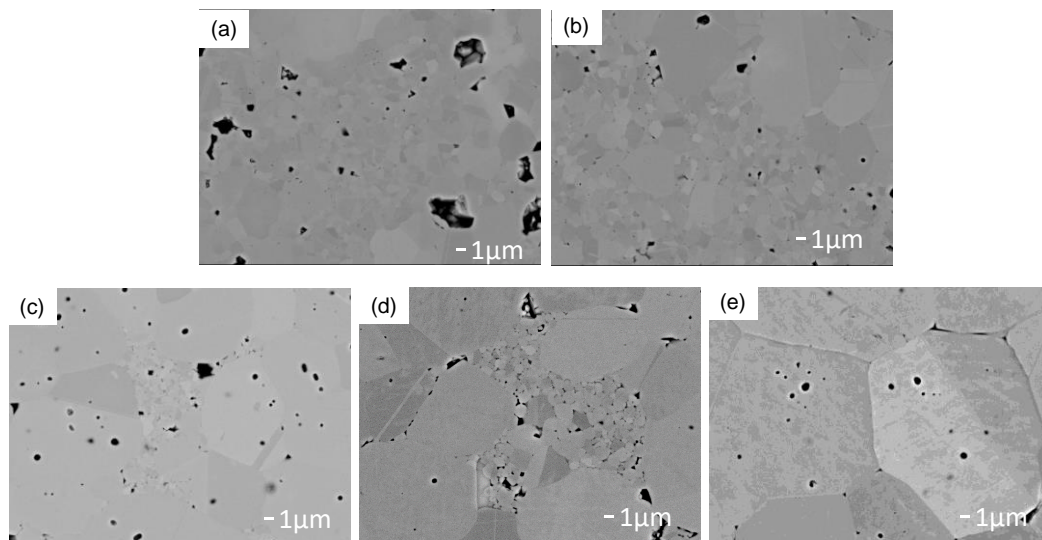


Fig. 3-7 SEM images of the ceramics corresponding to the different procedure (inset): (a) 1h-150rpm; (b) 1h-450rpm; (c) 4h-450rpm; (d) 8h-450rpm-10h; (e) 8h-450rpm-20h

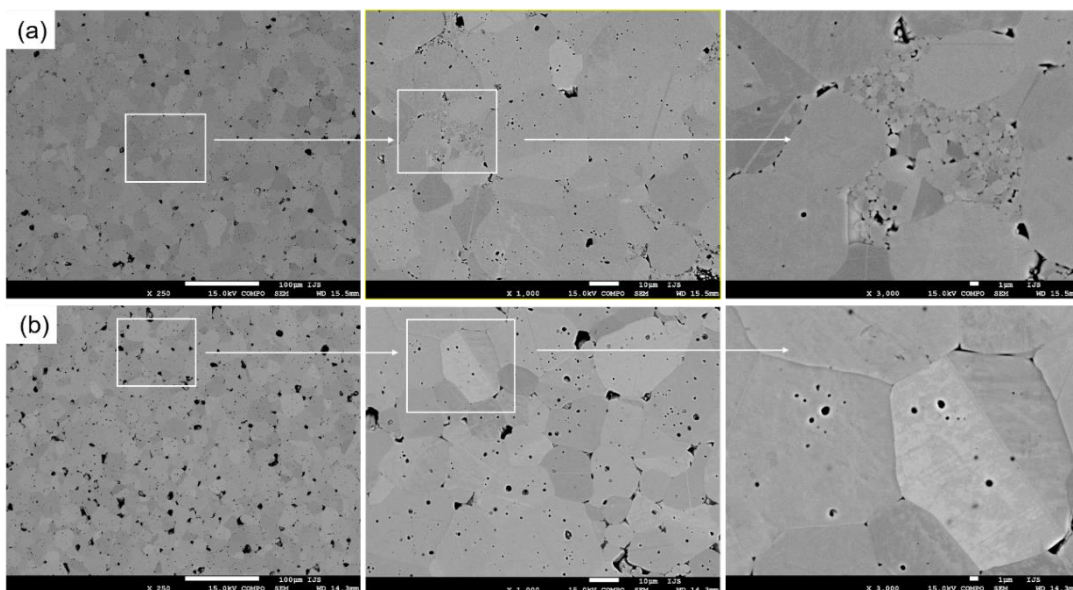


Fig. 3-8 The SEM images of (a) 8h-450rpm-10h and (b) 8h-450rpm-20h in different magnification

To further investigate the effect of the synthesis process, the chemical distribution in the different ceramics is also studied. The sample 1h-150rpm shows a pretty low homogeneous distribution of Mn and Nb. Fig. 3-9 shows the chemical distribution of the sample 1h-450rpm and 8h-450rpm, respectively. For the sample 1h-450rpm, we can find that the doping elements Mn and Nb show inhomogeneous distribution, which might be responsible for the inhibited grain growth and the highest porosity. Meanwhile, it seems that there are more Mn and Nb in smaller grains than the larger grains, as shown in Fig. 3-9a. In contrast, for the sample 8h-450rpm, in Fig. 3-9b, there is no apparent chemical difference between smaller and larger grains. It presents a more homogeneous chemical distribution that has been achieved thanks to longer milling and despite a bimodal distribution of grain sizes.

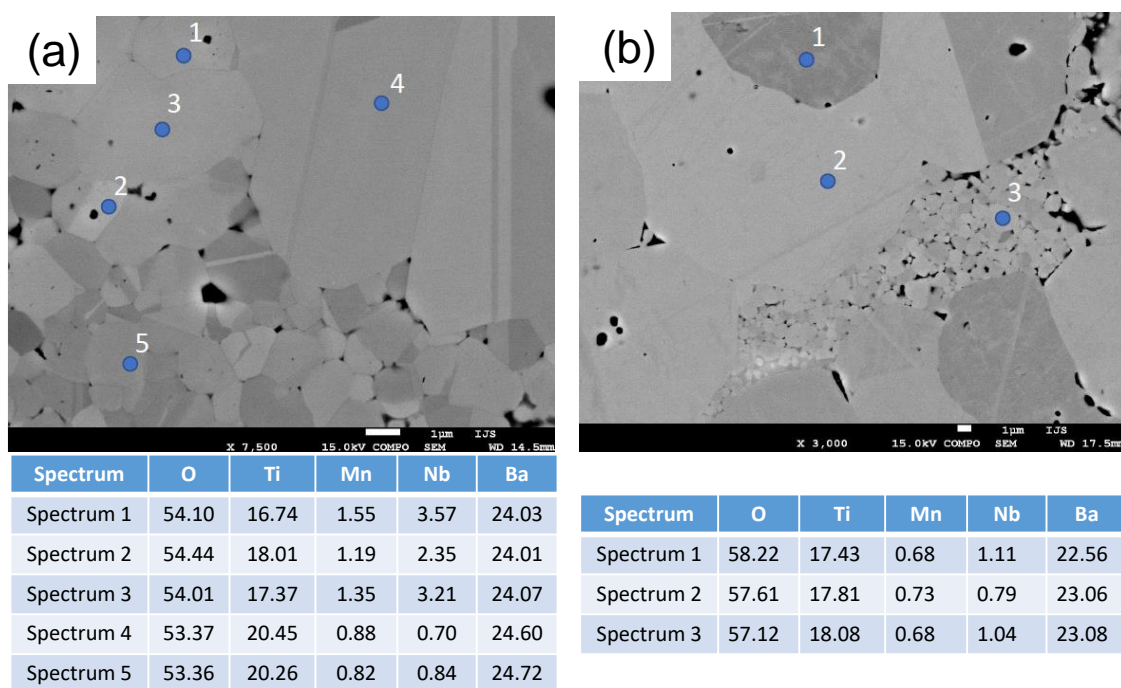


Fig. 3-9 EDX spectra for (a) 1h-450rpm and (b) 8h-450rpm, the table shows the proportion of each element in atomic (%)

### 3.3.2 The dependence of the optical absorption on synthesis conditions

The optical absorption spectra of these samples are collected by measuring the diffuse reflectance and compared to that of the pure BaTiO<sub>3</sub> sample, as shown in Fig. 3-10a. Thanks to the Kubelka-Munk function, the absorption spectra against energy are depicted in Fig. 3-10b. The bandgap  $E_g$  values can be obtained from the intersection

### 3.3 Results and Discussion

point between the tangent line from the inflection point of the curve and the abscissa line at zero absorption. It can be seen that Mn, Nb co-doped samples show visible light absorption as the bandgap decreases from 3.4 eV (pure BTO) to ~2.7 eV. From a zoom plot inset of Fig. 3-10b, we can find that the doped samples can absorb visible light with an absorption edge of ~1.5 eV. All the bandgap and the onset of absorption of the different samples are listed in Table 3-1. It is concluded that the synthesis processes have no substantial influence on the optical absorption. The optical absorption of sample 1h-150rpm as a function of temperature is also collected and shown in Fig. 3-11. The bandgap decreases with increasing temperature with a change of slope attesting to the phase transition that occurs at about 360 K, in agreement with the other measurements.

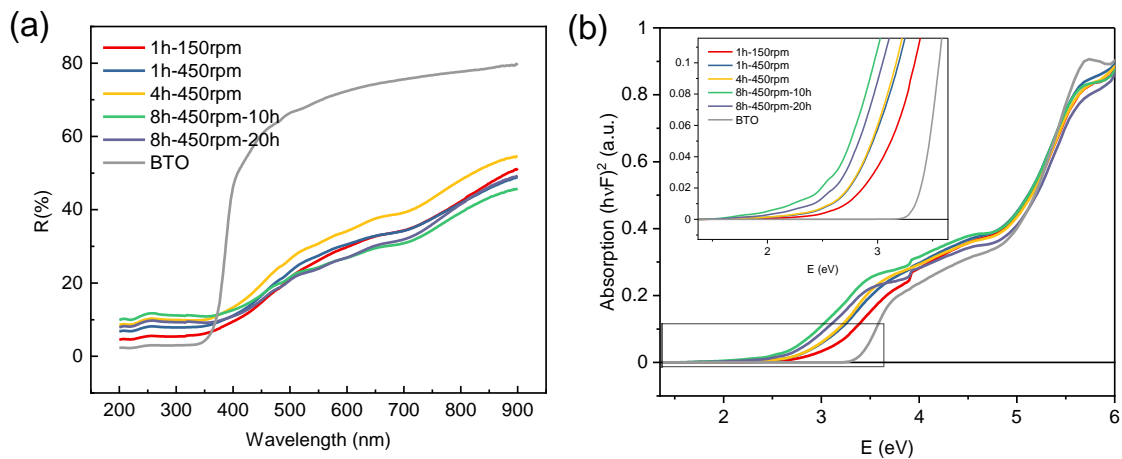


Fig. 3-10 (a) Diffuse reflectance spectra of the MnNb co-doped samples with BTO as a reference. (b) Absorption as a function of incident energy for all the samples; Inset: a zoom-in of the absorption curve

Table 3-1 The optical bandgap of the samples with different synthesis processes

Sample	BTO	1h-150rpm	1h-450rpm	4h-450rpm	8h-450rpm-10h	8h-450rpm-20h
$E_g$ (eV)	3.40	3.03	2.93	2.95	2.67	2.76
Onset (eV)	3.20	1.50	1.50	1.51	1.50	1.50

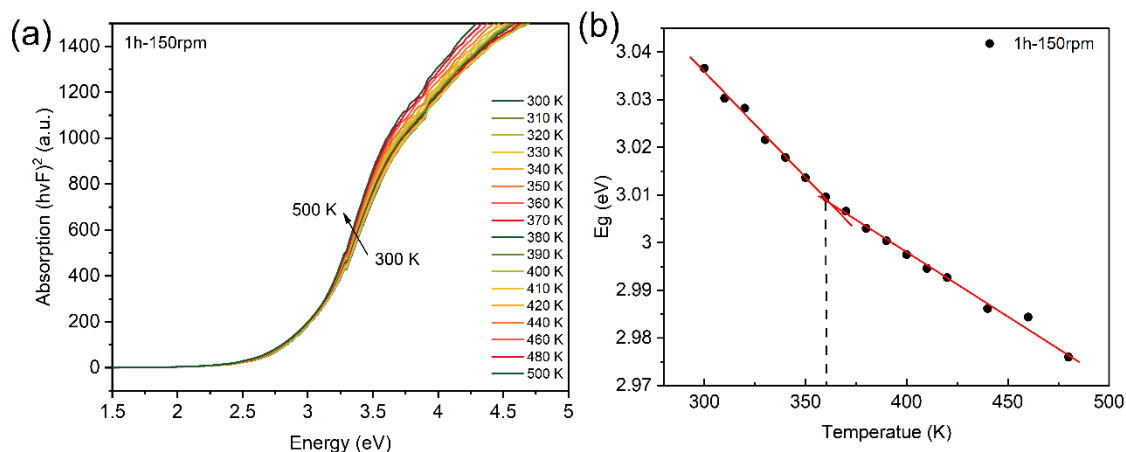


Fig. 3-11 Optical absorptions and bandgap versus temperature of sample 1h-150rpm

### 3.3.3 The dependence of the electrical properties on synthesis conditions

Fig. 3-12 exhibits the temperature dependence of dielectric constant and dielectric losses of these ceramics from 75 K to 450 K. It is clear that the Curie temperature ( $T_c$ ) shifts to lower temperature depending on the milling time. For pure BTO, the phase changes from cubic phase to tetragonal phase ( $T_c$ , 400 K), then to an orthorhombic ferroelectric phase, and finally to a rhombohedral phase. As shown in Fig. 3-13, in the sample 1h-150rpm, the maximum temperature  $T_m$  is around 353 K. The peak is broad with some dispersion due to the inhomogeneous distribution of Mn-Nb and a possible existence of polar nano/micro region.<sup>[124,132,138]</sup> By increasing the time and speed of milling,  $T_c$  decreases close to 290 K (4h-450rpm), 296 K (8h-450rpm); and by increasing sintering time, the phase transition temperature does not change (296 K for 8h-450rpm sintering 20 hours). This is consistent with the results from Raman spectroscopy and XRD at room temperature.

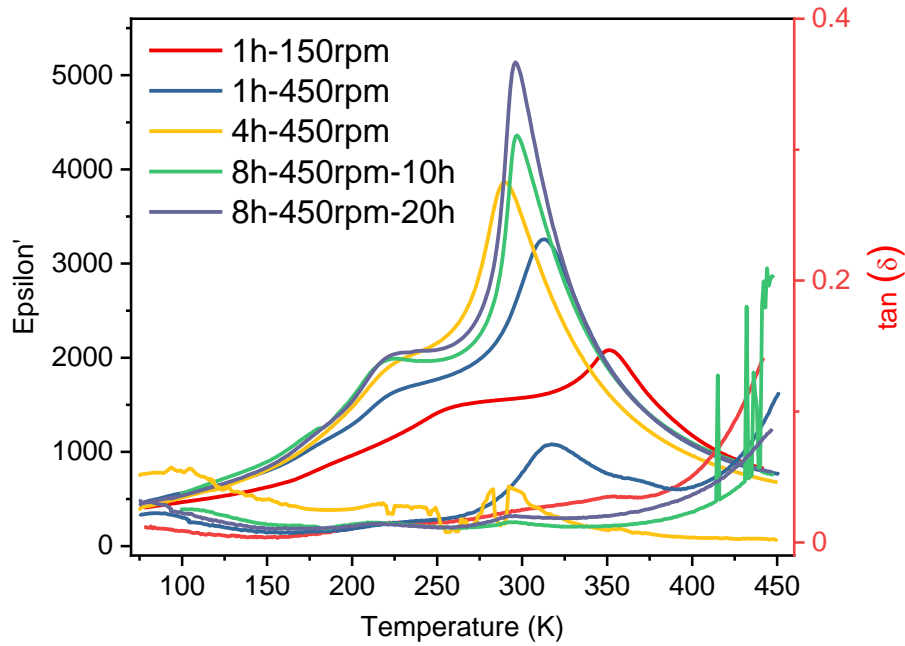


Fig. 3-12 Temperature dependence of dielectric constants and losses of MnNb co-doped samples at 1001 Hz

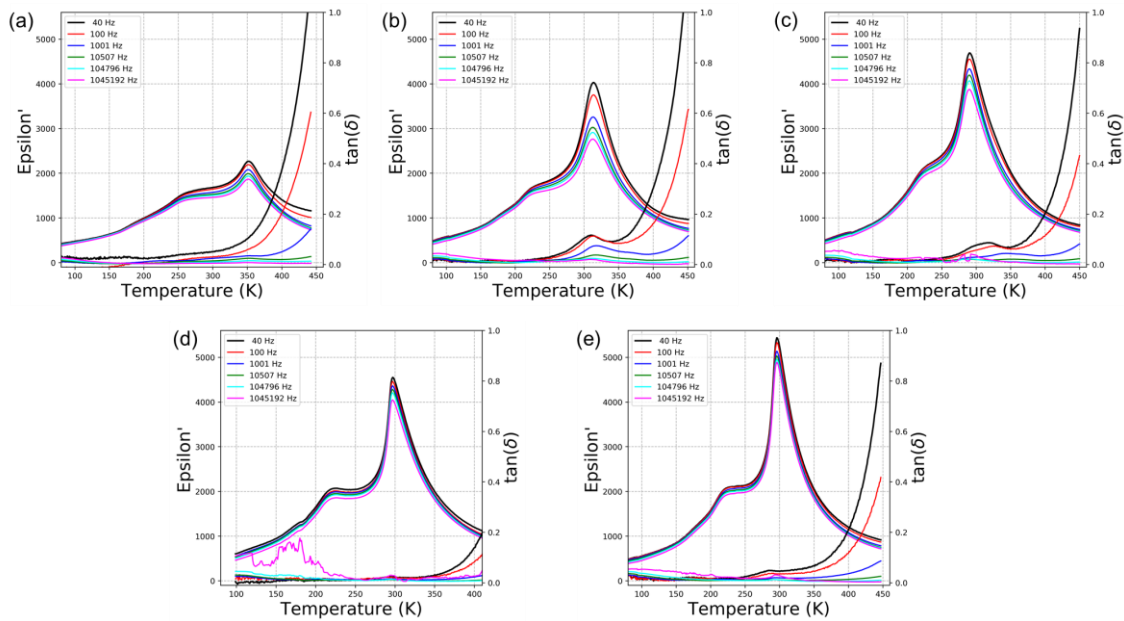


Fig. 3-13 Temperature dependence of dielectric constants and losses of the MnNb co-doped samples: (a) 1h-150rpm; (b) 1h-450rpm; (c) 4h-450rpm; (d) 8h-450rpm-10h; (e) 8h-450rpm-20h

The  $P$ - $E$  hysteresis loops at  $f = 5$  Hz have been measured at room temperature, as depicted in Fig. 3-14. We can see that after doping the hysteresis loops become slimmer, resembling to that of a relaxor ferroelectric and some are also pinched, suggesting the presence of defect dipoles. From  $I$ - $V$  curves, one positive and negative current density peak means a typical domain switching process. However, it is observed that there are

two current density peaks in Fig. 3-15a-b. The two peaks correspond to the pinched *P-E* loops in Fig. 3-14(a-b), respectively, which may be attributed to the existence of defect dipoles that occur with lower milling time and speed rate. After one-hour milling, phase separation and the defect dipoles are formed. The Mn and Nb can keep the balance of charge deficiency. However, the oxygen vacancies are able to couple with other defects to create bi-defects, like  $[Mn''_{Ti} - V_O^{\bullet\bullet}]$  or  $[2Mn'_{Ti} - V_O^{\bullet\bullet}]$ . As a result, the pinched behavior is then observed and is associated with these defect dipoles, which cannot be easily switched but provide a restoring force to the domain switching.<sup>[139]</sup> Thus, the remnant polarization decreases almost to zero after removing the electric field. However, the pinched loops are not seen in the samples with milling for a longer time and thus presenting homogeneous distribution. We have also investigated the behaviors of hysteresis loops versus temperature. As shown in Fig. S 3-3 for sample 1h-150rpm (1h-450rpm and 4h-450rpm in Fig. S 3-4 and Fig. S 3-5, respectively), the pinched loops are more evidenced during cooling. The loops open gradually during heating, and they can return to a pinched state again after it comes back to room temperature. This can be explained by the defect dipoles that are trapped at low temperature, so that the remnant polarization and the coercive field both decrease. When the temperature increases, the charges can more easily displace (Note that it is also potential that the domain wall mobility is higher at higher temperature), and then typical hysteresis loops are observed. The changes of remnant polarization as a function of temperature are shown in Fig. S 3-6. Fig. 3-16 shows the *P-E* loops and *S-E* loops of these ceramics, and the small inset is a zoom of *P-E* loops near-zero electric field. Table 3-2 displays the remnant polarization ( $P_r$ ) and the values of the coercive field ( $E_c$ ). The degradation of the ferroelectricity can also be linked to the Curie temperature downshifting to room temperature. Nevertheless, the values of polarization and coercive field show an increasing trend by extending the sintering time and can be attributed to the larger grain sizes than other samples.

### 3.3 Results and Discussion

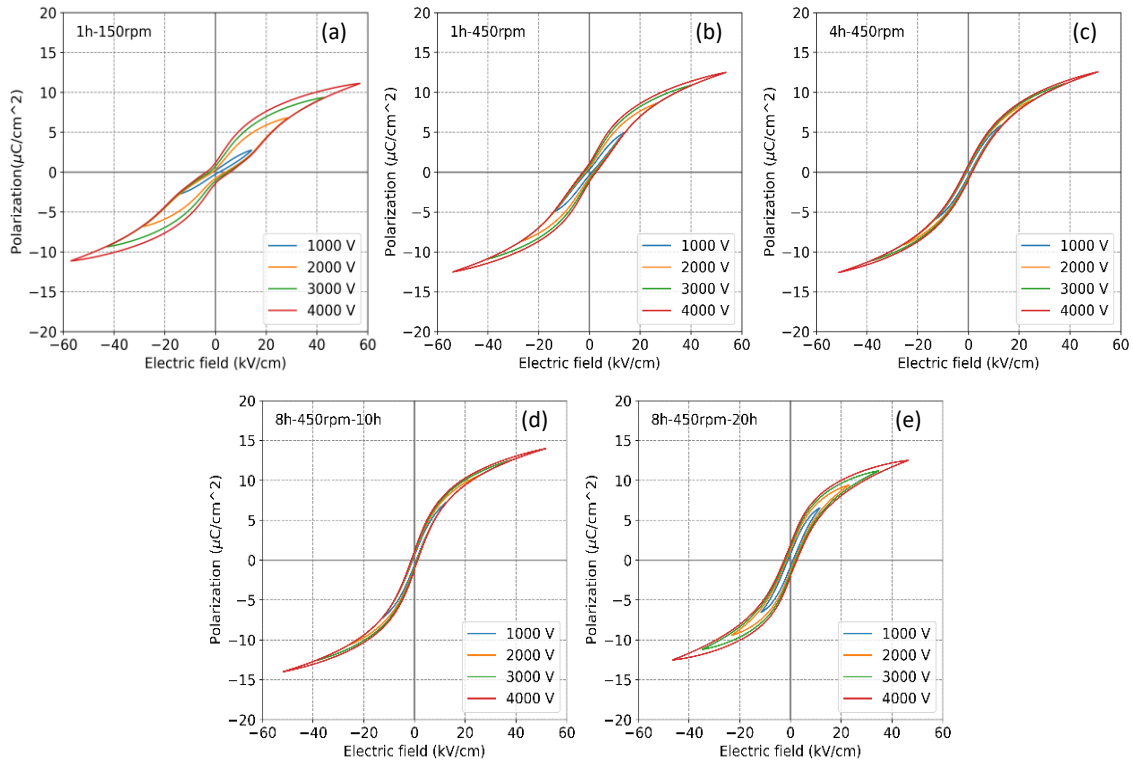


Fig. 3-14 *P-E* loops of the MnNb co-doped samples with different syntheses: (a) 1h-150rpm; (b) 1h-450rpm; (c) 4h-450rpm; (d) 8h-450rpm-10h; (e) 8h-450rpm-20h

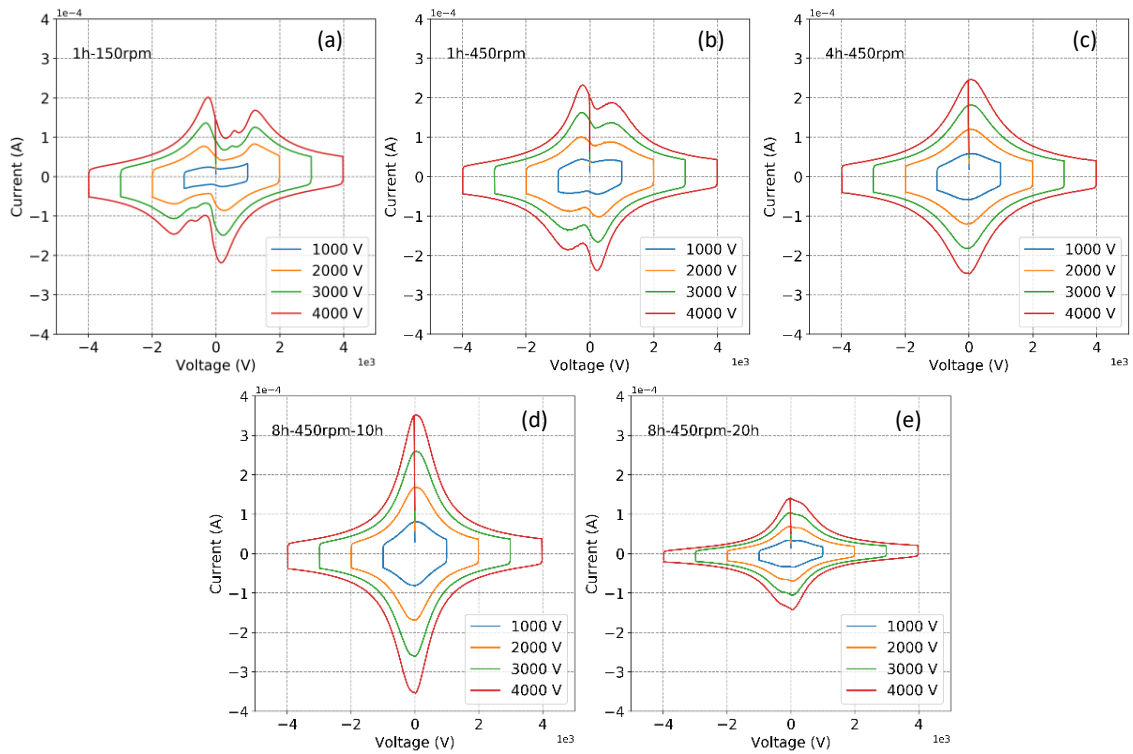


Fig. 3-15 *I-V* curves of the MnNb co-doped samples with different syntheses: (a) 1h-150rpm; (b) 1h-450rpm; (c) 4h-450rpm; (d) 8h-450rpm-10h; (e) 8h-450rpm-20h

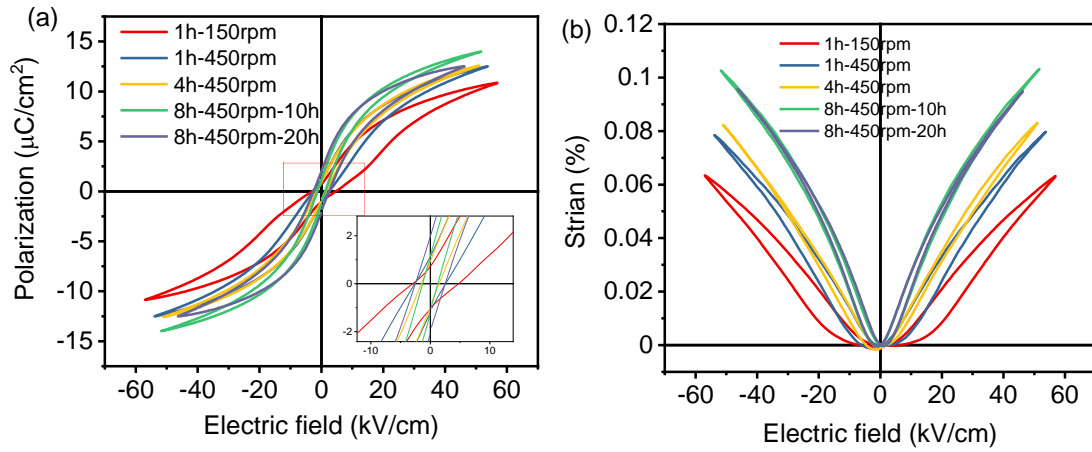


Fig. 3-16  $P$ - $E$  loops and strain-polarization loops of the MnNb co-doped samples with the various syntheses applied the same voltage. Inset is to indicate  $P_r$  and  $E_c$

Table 3-2 The  $P_r$ ,  $E_c$ , and normalized strain  $d_{33}$  at  $E_{max}$  for the samples with different synthesis processes

Sample	1h-150rpm	1h-450rpm	4h-450rpm	8h-450rpm-10h	8h-450rpm-20h
$P_{r+}$ ( $\mu\text{C}/\text{cm}^2$ )	0.720	1.136	0.948	1.164	1.977
$P_{r-}$ ( $\mu\text{C}/\text{cm}^2$ )	-0.969	-1.046	-0.803	-0.951	-1.824
$E_{c+}$ (kV/cm)	4.758	2.566	1.472	1.240	2.499
$E_{c-}$ (kV/cm)	-2.964	-2.599	-1.524	-1.308	-2.522
$S_{max}/E_{max}$ (pm/V)	105	148	163	200	205

### 3.4 Conclusions

The effect of the synthesis process of MnNb co-doped BaTiO<sub>3</sub> samples, especially the ball milling time and speed rate, is investigated on the microstructure, optical and electrical properties. It is found that the ball milling parameters have a significant influence on the microstructure and ferroelectric properties. After increasing the milling time and speed, the co-doped samples show an almost cubic phase at room temperature. The phase transition temperature shifts down to close to ambient temperature. In contrast, the optical absorption is weakly affected, if any, and the onset of absorption energy for all the samples is lower to 1.5 eV. The synthesis procedure has, therefore, a more negligible effect on optical absorption. That means that we can enhance the optical absorption by co-doping and minimizing the effect on ferroelectric properties using optimized synthesis parameters.

## 3.5 Supporting Information

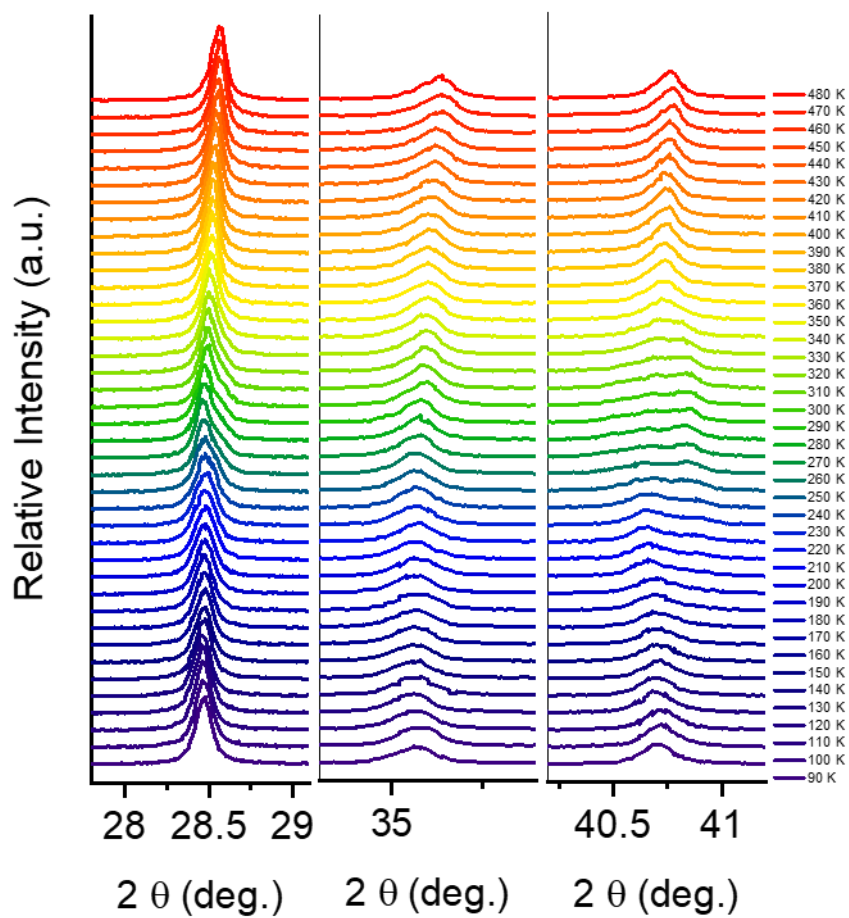


Fig. S 3-1 The XRD patterns versus temperature for sample 0.05MnNb by ball milling 1h-150rpm

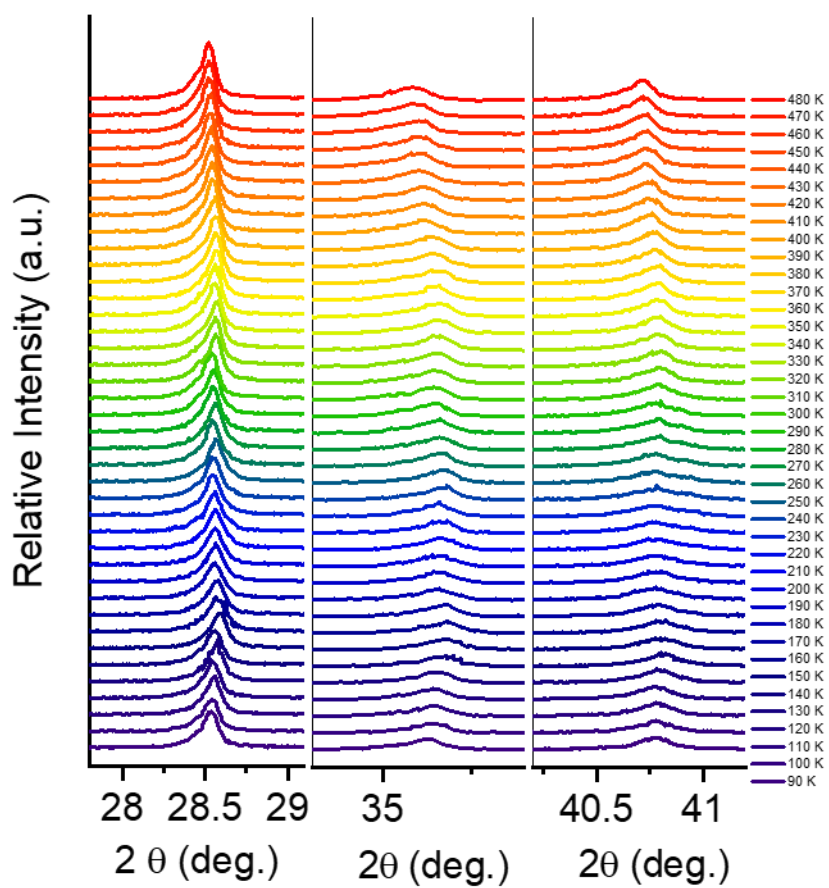


Fig. S 3-2 The XRD patterns versus temperature for sample 0.10MnNb by ball milling 1h-150rpm

### 3.5 Supporting Information

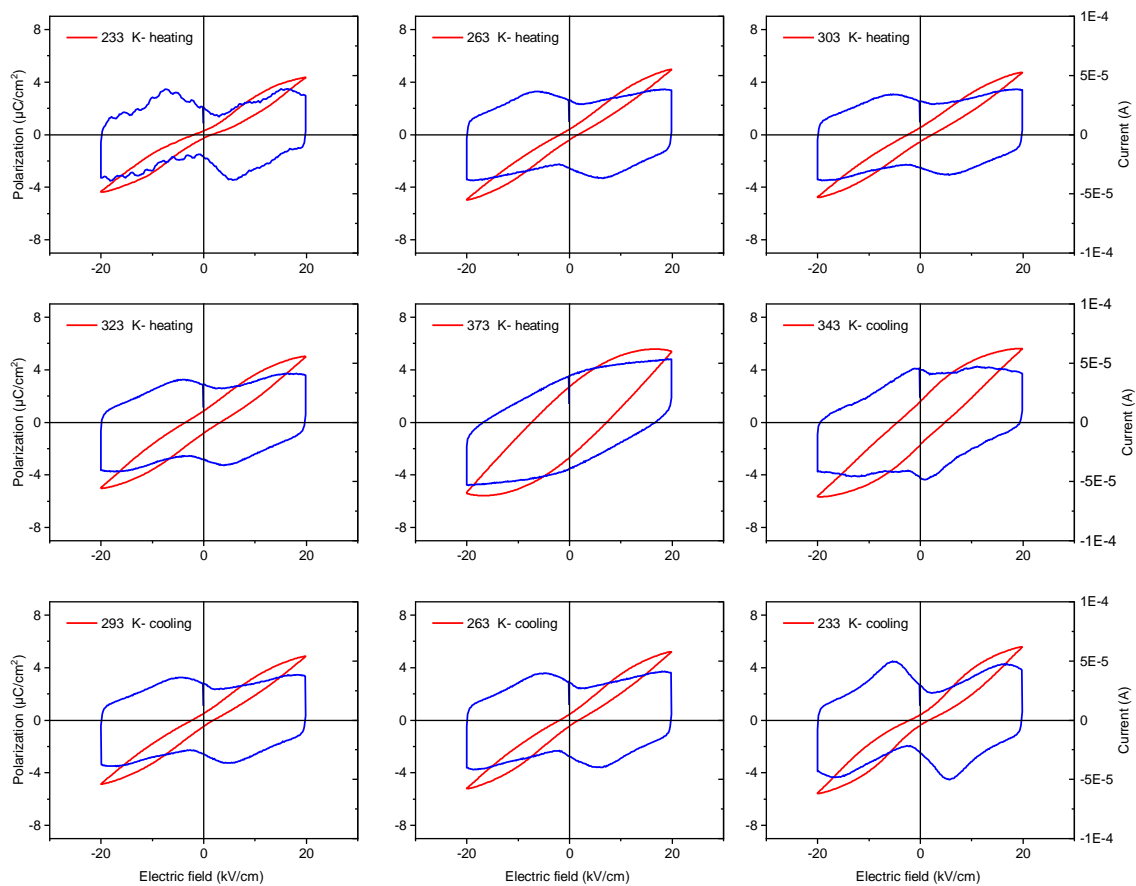


Fig. S 3-3 The  $P-E$  hysteresis loops and  $I-E$  oops as a function of the temperature of sample 1h-150rpm

### 3 The impact of synthesis conditions on the properties of Mn and Nb co-doped BaTiO<sub>3</sub>

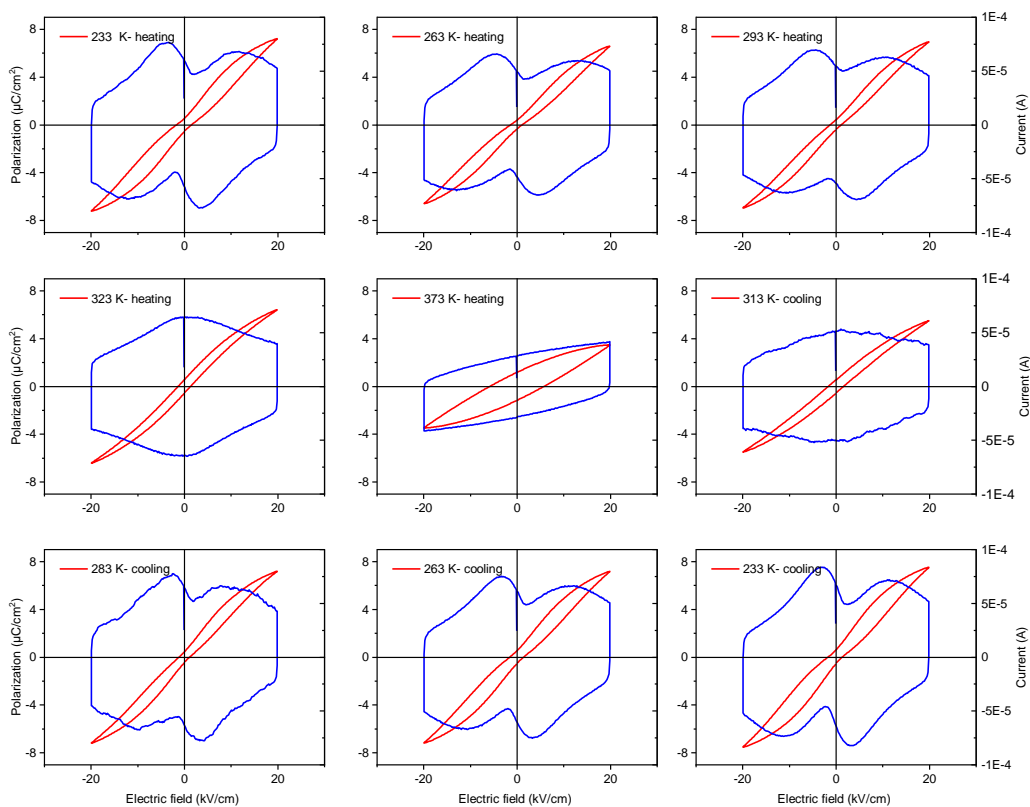


Fig. S 3-4 The  $P$ - $E$  hysteresis loops and  $I$ - $E$  oops as a function of the temperature of sample 1h-450rpm

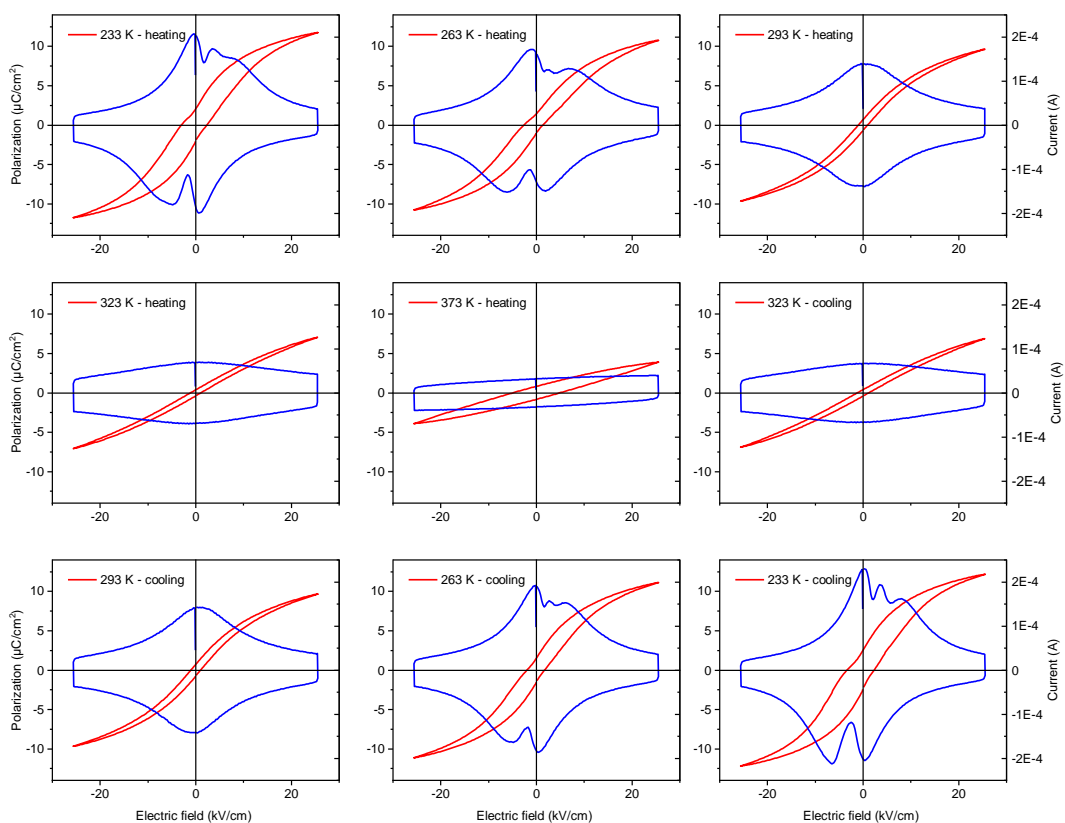


Fig. S 3-5 The  $P$ - $E$  hysteresis loops and  $I$ - $E$  oops as a function of the temperature of sample 4h-450rpm

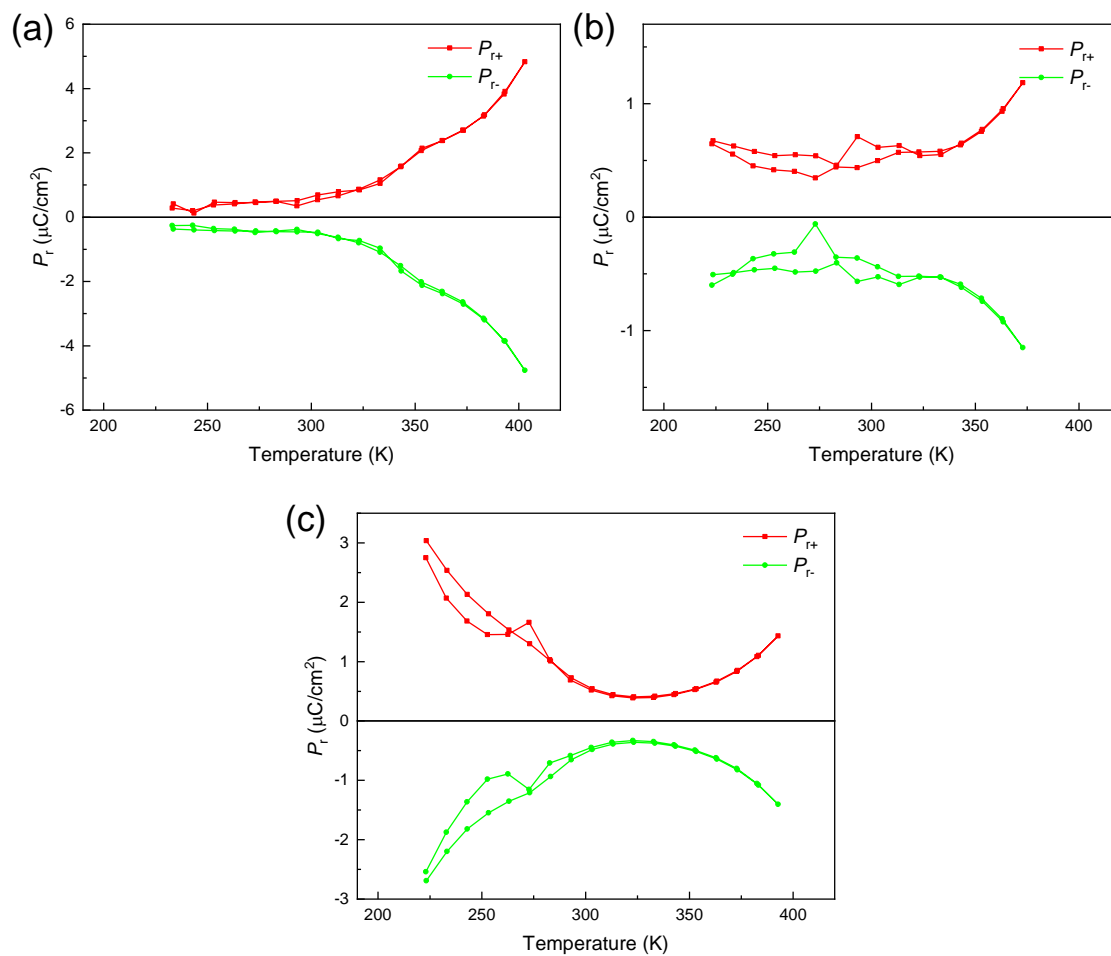


Fig. S 3-6 Variation of remnant polarization versus temperature of sample (a) 1h-150rpm; (b)1h-450rpm and (c) 4h-450rpm

# 4 Optical absorption of ferroelectric $(X^{3+}, Y^{5+})$ co-doped $BaTiO_3$

## Abstract

The combination of significant polarization and large light absorption is a challenge in ferroelectric materials. Here we report the optical absorption of  $BaTiO_3$  co-doped with trivalent and pentavalent transition metal ions replacing the  $Ti^{4+}$  cation, i.e.  $BaTi_{1-x}(X_{1/2}Y_{1/2})_xO_3$  ( $X = Sc, Mn, Fe, Co$ ;  $Y = Nb, Ta$ ; with  $x = 0.075$ ). We investigate the optical absorption behavior as a function of different pairs of co-dopants as well as physical properties such as ferroelectricity and piezoelectricity. X-ray diffraction and Raman spectroscopy measurements show that the tetragonality and polar coherence length decrease after co-doping, which affects the ferroelectric properties. It was found that the onset of absorption can decrease down to 1.5 eV, especially for the  $(Co^{3+}, Nb^{5+})$  co-doped samples, which simultaneously exhibit higher polarization than with the other co-doped ions. The measured photoconductivity confirms that the  $(Co^{3+}, Nb^{5+})$  doping has higher absorption than others. Our Density Functional Theory calculations show that codoping inserts intragap levels which are responsible for lowering the energy of optical absorption, which is in full agreement with our experimental observations. This work opens new perspectives for the use of ferroelectrics in optoelectronic devices.

## 4.1 Introduction

The lack of inversion symmetry inherent to ferroelectric materials, whose electrical polarization can be controlled by external electric fields, has attracted a large and wide interest for their potential optical and photonic applications, e.g., in photovoltaic solar cells, photocatalysts, or innovative elasto-optic devices.<sup>[8-11]</sup> Unlike conventional semiconductor p-n junctions, their so-called bulk photovoltaic (PV) effect can generate

voltages larger than the bandgap.<sup>[12,22,32]</sup> Moreover, new functionalities related to the coupling between their polarization and the PV effect are conceivable. Unfortunately, most ferroelectric materials suffer from a large bandgap, typically larger than 3 eV. This results in poor absorption of the solar spectrum, causing low energy conversion efficiency in most ferroelectric-based solar cells. Lowering the bandgap while maintaining decent ferroelectric properties (large remnant polarization, low losses upon switching) is therefore a crucial step towards applications of ferroelectrics in photovoltaic-based devices and beyond.

Many ferroelectrics crystallize in the perovskite  $ABO_3$  structure. A typical example is the model ferroelectric material  $BaTiO_3$  (BTO), whose bandgap is 3.3 eV. Note that calculations<sup>[122]</sup> have shown that while BTO has an indirect bandgap between  $\Gamma$ -R Brillouin zone points, the direct bandgap ( $\Gamma$ - $\Gamma$ ) is very close in energy (less than 0.05 eV whatever the hybrid functional). As a result in the following, a direct bandgap is assumed. The wide bandgap in  $BaTiO_3$  is electronically characterized by a valence band (VB) derived from O  $2p$  states and a conduction band (CB) originating from the B-site transition metal  $3d$  states ( $3d^0$  for  $Ti^{4+}$ ).<sup>[10]</sup> The strong hybridization between the aforementioned orbitals (especially  $3d^0$  states) causes symmetry breaking and leads to polar displacements at the origin of ferroelectric polarization. Therefore, altering the bandgap may also significantly impact the polarization and the related ferroelectric properties. A compromise between having a narrower bandgap while keeping a significant polarization amplitude is thus necessary.

Bandgap engineering strategies have already been devised in an attempt to increase optical absorption. Most studies have focused on tuning the oxygen vacancy concentration, alloying solutions, or chemical substitutions. Control of the oxygen vacancy concentration has been carried out in works on  $(1-x)BaTiO_3-xBaNi_{1/2}Nb_{1/2}O_{3-\delta}$  and  $(1-x)BaTiO_3-xBaCo_{1/2}Nb_{1/2}O_{3-\delta}$ , which exhibit a reduced bandgap of about 1.3 eV compared to 3.3 eV obtained in BTO.<sup>[85,86]</sup> In Wu et al.'s work<sup>[87]</sup>, by changing the ratio of Ni and Nb to modify the concentration of oxygen vacancies, the optical bandgap of doped  $BaTiO_3$  was significantly reduced down to 1.5 eV. Next, alloying was envisioned as a possible route to bandgap reduction in ferroelectrics, for instance, alloys based on the classical ferroelectric  $KNbO_3$  (KNO). Grinberg *et al.* mixed KNO with  $BaNi_{1/2}Nb_{1/2}O_{3-\delta}$

to introduce Ni<sup>2+</sup> on the B-site and oxygen vacancies, creating an additional electronic band within the bandgap region. The obtained solid solution still exhibited ferroelectricity, while the bandgap was reduced to the range of 1.1-2 eV.<sup>[98]</sup> Similar reports of solid solutions of KNO with BaFe<sub>1/2</sub>Nb<sub>1/2</sub>O<sub>3</sub>, BaCo<sub>1/2</sub>Nb<sub>1/2</sub>O<sub>3-δ</sub>, BiYbO<sub>3</sub>, and LaFeO<sub>3</sub> showed that the bandgap could be shifted down to 1.7 eV, 2.4 eV, 2.2 eV, and 2.6 eV, respectively.<sup>[101,102,104,106]</sup>

At last, several studies have focused on bandgap engineering by chemical substitution. Among those, reports on substitutions on the A-site of the perovskite showed a minor effect on the bandgap value. For instance, Bi/Li co-doped BTO (Ba<sub>1-x</sub>(Bi<sub>0.5</sub>Li<sub>0.5</sub>)<sub>x</sub>TiO<sub>3</sub>) exhibits nearly the same bandgap (3.2 eV<sup>[14]</sup>) like pure BTO. The inefficiency of this approach can be understood in light of the nature of the states forming the VB and CB described earlier. It is worth noting that a large voltage for this polycrystalline system (Ba<sub>1-x</sub>(Bi<sub>0.5</sub>Li<sub>0.5</sub>)<sub>x</sub>TiO<sub>3</sub>) was explained by the covalent bonding and the nature of the Bi-based orbitals, favoring the current shift of the PV effect.<sup>[14]</sup> Similar observations were made with doping on the B-site, e.g., in Ba(Ti<sub>1-x</sub>Sn<sub>x</sub>)O<sub>3</sub> and [Ba(Zr<sub>0.2</sub>Ti<sub>0.8</sub>)O<sub>3</sub>]<sub>0.5</sub>[(Ba<sub>0.7</sub>Ca<sub>0.3</sub>)TiO<sub>3</sub>]<sub>0.5</sub>.<sup>[78,140]</sup> In these compounds the proximity of phase transitions is believed to increase the open-circuit photovoltage. When the substitution on the B-site is made with transition metal acceptors like Fe<sup>3+</sup>, Mn<sup>3+</sup>, Co<sup>3+</sup>, Cr<sup>3+</sup> or Ni<sup>2+</sup>, the bandgap tends to decrease. For example, the substitution of Ti<sup>4+</sup> by Cr<sup>3+</sup> in BTO shows a redshift of the absorption edge due to *d-d* band transitions between the Cr<sup>3+</sup> center and the Ti<sup>4+</sup> sites.<sup>[77]</sup> A similar strategy has been adopted in BiFeO<sub>3</sub> compounds doped with Mn<sup>3+</sup> (3d<sup>4</sup>). It was found that defect states develop within the bandgap that act as a scaffold for photogeneration.<sup>[76]</sup> The photogenerated power can be further enhanced by introducing donor and acceptor levels within the bandgap, as done in Fe-doped BaTiO<sub>3</sub>, through Fe<sup>2+</sup> and Fe<sup>3+</sup>, respectively, allowing to activate a PV effect that is mediated through successive Fe<sup>3+</sup>/Fe<sup>2+</sup> redox cycles.<sup>[74]</sup> However, doping with Cr<sup>3+</sup>, Mn<sup>3+</sup> or Fe<sup>3+</sup> usually deteriorates the ferroelectric properties. This can be understood in the framework of the simple tight-binding model of Khomskii as a consequence of the partially occupied nature of the 3d-orbitals of these ions.<sup>[81]</sup> In addition, the use of Fe<sup>3+</sup> and Fe<sup>2+</sup> as substitutes for Ti<sup>4+</sup> ions leads to a charge imbalance, which results in leakage currents that prevent proper polarization measurements.

To mitigate this latter flaw of charge imbalance, Das *et al.* employed a different approach by reducing the bandgap by co-doping with  $\text{Mn}^{3+}$  and  $\text{Nb}^{5+}$  pairs (replacing two  $\text{Ti}^{4+}$  ions). Eventually, a relatively stable polarization was maintained.<sup>[84]</sup> Compared to doping with a single ion<sup>[77]</sup>, the absorption edge of the co-doped BTO presents a more pronounced redshift. In such co-doping strategy,  $\text{Mn}^{3+}$  induces intra-gap states, a reduction of the bandgap and a partial loss of polarization which is minimized thanks to a strong Jahn–Teller (JT) effect.  $\text{Nb}^{5+}$  ( $d^0$ ), on the other hand, acts as a charge compensator, also capable to stabilize ferroelectric ground states in a similar way to ferroelectric niobates.<sup>[16]</sup> It was also shown by the first-principles theory that  $(1-x)\text{BaTiO}_3-x\text{BaMg}_{1/2}\text{Mo}_{1/2}\text{O}_3$  shows good photovoltaic performance because of the charge balance created by  $\text{Mg}^{2+}$  and  $\text{Mo}^{6+}$  ions, and an increased conduction bandwidth created by the Ti–O–Mo bonds.<sup>[88]</sup>

From reports in literature, it is clear that co-doping could be the best route to (i) decrease the bandgap and (ii) maintain very good ferroelectric properties. There is, however, a need to better understand the effects of different co-dopants on the optical and electrical properties of ferroelectrics. In that endeavour, we employ both experimental and theoretical tools on the model ferroelectric material,  $\text{BaTiO}_3$ . Co-doping with various ion pairs on the B-site is realized to form the  $\text{BaTi}_{1-x}(\text{X}_{1/2}\text{Y}_{1/2})_x\text{O}_3$  system, and the resulting electrical and optical properties of these compounds are systematically reported herein and compared. We considered several couples of ( $\text{X}^{3+}$ ,  $\text{Y}^{5+}$ ) co-dopants that keep the total average charge of +4 on the substituted Ti site, *i.e.* ( $\text{Sc}^{3+}, \text{Nb}^{5+}$ ), ( $\text{Mn}^{3+}, \text{Nb}^{5+}$ ), ( $\text{Fe}^{3+}, \text{Nb}^{5+}$ ), ( $\text{Co}^{3+}, \text{Nb}^{5+}$ ) and ( $\text{Mn}^{3+}, \text{Ta}^{5+}$ ). For each couple we selected either  $\text{Nb}^{5+}$ , which has empty  $d^0$  orbitals thus favors the polarizability of BTO, or  $\text{Ta}^{5+}$  ions, which also have empty  $d^0$  orbitals but is less ferroelectrically-active. Indeed,  $\text{KTaO}_3$  is an incipient ferroelectric that exhibits some polarizability only at low temperature, while a compound like  $\text{KNbO}_3$  is a room-temperature ferroelectric with similar properties to  $\text{BaTiO}_3$ .<sup>[141,142]</sup> With the exception of  $\text{Sc}^{3+}$  which has  $d^0$  states, all  $\text{X}^{3+}$  ions such as  $\text{Mn}^{3+}$ ,  $\text{Fe}^{3+}$ ,  $\text{Co}^{3+}$  have partially filled  $d$ -states, *i.e.*  $3d^4$ ,  $3d^5$ , and  $3d^6$ , respectively. We thus expect that only  $\text{Co}^{3+}$  will significantly impact the electronic band structure.

Herein, we report the effects of co-doping on the structure, ferroelectric and

piezoelectric properties of BTO. The optical absorption behavior is measured and compared to the theoretical one calculated using Density Functional Theory (DFT). We reveal by comparing the results from different pairs of co-dopants that the electronic bandgap is weakly changed, if any, while the unfilled  $d^{n \neq 0}$  states introduce extra bands within this bandgap that help absorb light below the bandgap by pushing down the onset of absorption to 1.5 eV. Finally, the photoresponse as a function of the wavelength for the best samples is measured, further demonstrating that the co-doping can favor the optical absorption and PV performance.

## 4.2 Experimental procedure

### 4.2.1 Material preparation

BaTi<sub>0.925</sub>(X<sub>1/2</sub>Y<sub>1/2</sub>)<sub>0.075</sub>O<sub>3</sub> ceramics (abbreviated as XY, where X stands for Sc<sup>3+</sup>, Mn<sup>3+</sup>, Fe<sup>3+</sup> or Co<sup>3+</sup>, and Y stands for Nb<sup>5+</sup> or Ta<sup>5+</sup>) were fabricated by the conventional solid-state reaction method. The starting raw materials were: BaCO<sub>3</sub> (STREM 99.9%), TiO<sub>2</sub> (PROLABO 99%), Sc<sub>2</sub>O<sub>3</sub> (STREM 99%), Mn<sub>2</sub>O<sub>3</sub> (STREM 99%), Fe<sub>2</sub>O<sub>3</sub> (ALFA PRDUKTE 99.9%), Co<sub>3</sub>O<sub>4</sub> (ALFA AESAR 99.7%), Nb<sub>2</sub>O<sub>5</sub> (ALFA AESAR 99.9%) and Ta<sub>2</sub>O<sub>5</sub> (FLUKA 99.9%). Only BaCO<sub>3</sub> being very hygroscopic compared to TiO<sub>2</sub> was preheated at 500 °C for 5 hours to remove any absorbed moisture. Then, the raw powders were weighed in stoichiometric amounts and mixed by ball-milling in ethanol. After drying, the homogenized powder was pressed into pellets and calcined at 900 °C for 12 hours. After subsequent grinding the calcined powder was again pressed into pellets of about 8 mm diameter and 1 mm thick with polyvinyl alcohol (PVA with 35 wt.%) as a binding agent. The pellets were then sintered at 1250~1280 °C for 10 hours. The amounts of dopants was fixed for all ionic pairs to x=7.5 %, which was found to be the optimal concentration for (Mn<sup>3+</sup>, Nb<sup>5+</sup>) co-doping.<sup>[84]</sup>

### 4.2.2 Characterization

X-ray diffraction (XRD) patterns were obtained on a Bruker D2 phase diffractometer using Cu-K<sub>α</sub> radiation ( $\lambda=1.5406 \text{ \AA}$ ) with  $20^\circ \leq 2\theta \leq 60^\circ$  and steps of  $0.02^\circ$  with 2 s per

step. Raman spectroscopy was recorded at room temperature using a Labram-Horiba spectrometer equipped with a He-Ne, 633 nm laser. The microstructure of the sintered ceramics was analyzed by a field-emission scanning electron microscope (FE-SEM; JSM7600, Jeol Ltd., Tokyo, Japan), operated in backscattered electron mode.

The sintered pellets were ground into powders for diffuse reflectance spectra. Room-temperature diffuse reflectance spectra were collected in the wavelength range of 200-900 nm using Perkin Elmer UV-visible NIR spectroscopy (Lambda 850) equipped with a Harrick Praying Mantis TM diffuse reflectance accessory using non-absorbing BaSO<sub>4</sub> as a reference. The optical band gap was estimated by the Tauc plot of the absorption determined using the Kubelka-Munk formula  $F_{KM} = k/s = (1-R)^2/(2R)$  where  $R$  is the raw reflectance,  $k$  the absorption coefficient, and  $s$  the scattering coefficient.<sup>[121]</sup>

The polished pellets were coated with silver electrodes on both sides to measure the ferroelectric properties. The polarization-electric-field (P-E) hysteresis loops and piezoelectric strain-electric-field (S-E) loops were recorded by applying a triangular waveform with a frequency of 5 Hz in silicone oil using an AixACCT TF-2000 ferroelectric tester system.

For the photovoltaic measurements, gold electrodes were sputtered on both sides. Before testing, all the samples were pre-poled at 30 kV/cm at 150 °C and field-cooled. The photoresponse under dark and different wavelength laser source conditions versus time were measured under a bias of 10 V using a Keithley Model 6430 sub-femtoAmp remote source meter. The laser sources were 325 nm (30 mW, IK Series He-Cd LASER), 405 nm and 532 nm (both with a power 10 mW, Class IIIb Laser), respectively.

### 4.2.3 Computational Methods

We performed density functional theory (DFT) calculations using the Vienna Ab-initio Software Package (VASP)<sup>[143–147]</sup>. Structural relaxation was performed on a 3x3x3 BaTiO<sub>3</sub> supercell (135 atoms) using the PBESol exchange functional. A plane wave cut-off of 550 eV was used, alongside a 1 × 1 × 1  $\Gamma$ -centered k-mesh. Fermi-Dirac occupation with 25 meV smearing was employed. Convergence criteria on the energy and forces were respectively set to 10<sup>-6</sup> eV and 10<sup>-3</sup> eV/Å. The density of states and optical dielectric

constant were subsequently calculated on a  $3 \times 3 \times 3$  k-mesh. The optical dielectric constant was calculated in the Independent Particle Approximation (IPA).<sup>[148]</sup>

## 4.3 Results and Discussion

### 4.3.1 The microstructure of undoped BTO and co-doped BTO

Fig. 4-1a shows that the room temperature X-ray diffraction patterns of all the samples are very close to that of undoped BTO specimen in its room-temperature tetragonal phase (JCPDS card #05-0626). No parasitic phase could be evidenced on the basis of these X-ray diffractograms. A representative microstructure of the ceramics is shown in Fig. 4-1b, showing the example of (Mn<sup>3+</sup>, Nb<sup>5+</sup>), with grain size typically smaller than 10  $\mu\text{m}$ . As shown in Fig. 4-1c, the tetragonality, represented by the  $c/a$  ratio with  $a$  and  $c$  being the tetragonal unit cell parameters determined from the diffraction patterns analysis, drops significantly for each pair of co-dopants as compared to the undoped BTO. This is expected as non-ferroelectrically active ions (such as Sc<sup>3+</sup>, Mn<sup>3+</sup>, Fe<sup>3+</sup>, Co<sup>3+</sup>) are replacing the ferro-active Ti<sup>4+</sup> ions. These results also indicate that a lower ferroelectricity is expected as the  $c/a$  is, in the case of the tetragonal polar symmetry, directly proportional to the square of the polarization.<sup>[149]</sup> Note that in the case of (Mn<sup>3+</sup>, Nb<sup>5+</sup>) co-dopants the decrease of  $c/a$  is significantly lower than for the other dopants and might be related to the strong JT distortions about Mn<sup>3+</sup> that adequately couple the Mn<sup>3+</sup>-O<sub>6</sub> octahedra to the overall ferroelectric BaTiO<sub>3</sub> lattice as recently revealed using X-ray absorption spectroscopy.<sup>[16]</sup> Such an effect, if any, seems to be much weaker in the case of Co<sup>3+</sup> dopant which is also a JT active ion. It is also worth mentioning that when (Mn<sup>3+</sup>, Nb<sup>5+</sup>) is replaced by (Mn<sup>3+</sup>, Ta<sup>5+</sup>), the positive effect of Mn on the polarization is reduced because of the less-polarizable Ta<sup>5+</sup> compared to Nb<sup>5+</sup>. In Table 4-1, we also reported the volume of the unit cell, determined from the XRD patterns, with respect to the average ionic radius for each (X<sup>3+</sup>, Nb<sup>5+</sup>) pair i.e.,  $r_{\text{ave}} = (r_X + r_{\text{Nb}})/2$ . It can be seen that the volume depends on the substitution elements confirming the dopants have been inserted into the BTO unit cell. For instance, because Sc<sup>3+</sup> has a larger radius (74.5 pm) and Co<sup>3+</sup> has a smaller one (55 pm) compared to Ti<sup>4+</sup> (60.5 pm) the

### 4.3 Results and Discussion

volume of ( $\text{Sc}^{3+}$ ,  $\text{Nb}^{5+}$ ) and ( $\text{Co}^{3+}$ ,  $\text{Nb}^{5+}$ ) co-doping increase and decreases respectively compared to that of pure BTO.

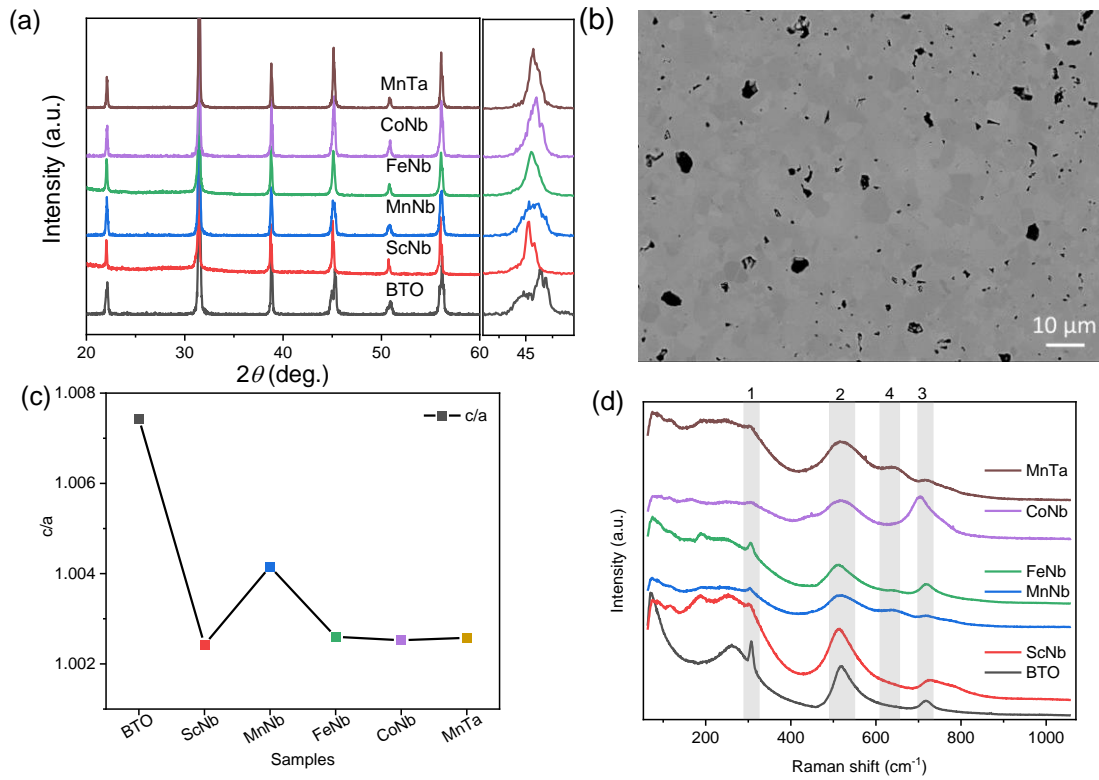


Fig. 4-1 (a) XRD patterns of the pure BTO and co-doped BTO samples measured at room temperature. (b) Typical microstructure of the ceramics (here the case of ( $\text{Mn}^{3+}$ ,  $\text{Nb}^{5+}$ ) co-doping). Black areas are pores and the different shades of grains come from different grain orientations as commonly observed in polycrystalline ceramics. (c) Tetragonality i.e.  $c/a$  ratio depends on the dopants. (d) Raman spectra of undoped BTO and the co-doped samples collected at room temperature

Table 4-1 Volume of the unit cell, remnant polarization  $P_r$ , coercive field  $E_c$  and maximum strain  $S_{\text{max}}$  at 40 kV/cm as a function of the average ionic radius  $r_{\text{ave}}$  for each ( $\text{X}^{3+}$ ,  $\text{Nb}^{5+}$ ) pair (using Shannon ionic radius data)

Composition	Volume ( $\text{\AA}^3$ )	$P_r$ ( $\mu\text{C}/\text{cm}^2$ )	$E_c$ (kV/cm)	$S_{\text{max}}$ (%)	$r_{\text{ave}}$ ( $\text{\AA}$ )
BTO	64.54	6.384	3.632	0.164	0.61
$\text{Sc}^{3+}$ , $\text{Nb}^{5+}$	64.75	1.632	2.255	0.0660	0.695
$\text{Mn}^{3+}$ , $\text{Nb}^{5+}$	64.37	0.663	3.428	0.0404	0.61
$\text{Fe}^{3+}$ , $\text{Nb}^{5+}$	64.55	0.228	3.803	0.00884	0.595
$\text{Co}^{3+}$ , $\text{Nb}^{5+}$	64.44	8.652	5.939	0.0737	0.595
$\text{Mn}^{3+}$ , $\text{Ta}^{5+}$	64.41	1.055	2.292	0.0622	0.61

Fig. 4-1d shows the room temperature Raman spectra for all samples. The typical Raman spectrum of undoped BTO shows three major groups of Raman-active bands (denoted 1 to 3 in Fig. 4-1d), which are the fingerprints of the BTO tetragonal phase.<sup>[116]</sup> In the range between 200-400  $\text{cm}^{-1}$ , which is usually attributed to vibrations associated to polar  $\text{BO}_6$  octahedra in ferroelectric perovskite oxides<sup>[117]</sup>, there is a sharp peak at 305  $\text{cm}^{-1}$ , corresponding to  $\text{B1(TO)}/\text{E(TO+LO)}$  modes (TO and LO refer to transverse and longitudinal optic modes, respectively), representative of the long-range ferroelectric phase related to the cooperative displacement of  $\text{Ti}^{4+}$  in Ti-O chains<sup>[117]</sup>. The two bands at 520  $\text{cm}^{-1}$  and 720  $\text{cm}^{-1}$ , assigned to the  $\text{A1(TO)}/\text{E(TO)}$  and  $\text{A1(LO)}/\text{E(LO)}$  modes, respectively, are dominated by oxygen vibrations (bending and stretching) of the  $\text{TiO}_6$  octahedra. The co-doping of BTO has a clear impact on both the intensity and the width of the sharp mode at 305  $\text{cm}^{-1}$  that is related to the polar order. While the intensity of the mode can be related to the decrease of the tetragonality, i.e., polarization amplitude, its broadening is related to the lifetime of the associated phonon. The clear increase in the half-width of the Raman peaks with co-doping in Fig. 4-1d thus hints that coherence length in the tetragonal phase is shortened when co-dopants are added. In other words, the doping not only reduces the tetragonality and the polarization magnitude, but also induces some clustering through disorder which might originate from chemical defects/dopants or local chemical order, static/dynamic atomic shifts and oxygen octahedral distortion (e.g., because of JT effect) or local symmetry change.<sup>[16,85,118]</sup> Such a disorder results in a relaxation of the Raman selection rules and may explain the broadening as well as the asymmetries of bands located at 520  $\text{cm}^{-1}$  and 720  $\text{cm}^{-1}$  in Fig. 4-1d. These latter are also regarded as an indicator of ferroelectricity as they have mixed A and E characters, which further points to the fact that co-doping indeed partially disrupts the long-range ferroelectric order. Note that the disorder is also observed in the low wavenumber region around 200  $\text{cm}^{-1}$ , as is observed in the cubic phase of pure BTO (expected to show no active Raman mode in case of strict selection rules) because of reminiscent  $\text{Ti}^{4+}$  polar displacements.<sup>[116]</sup> The Raman spectra of samples co-doped with Mn or Fe also exhibit a Raman active mode at 635  $\text{cm}^{-1}$  (denoted 4). As the Mn ion is JT active, it may thus lead to extra modes because of local distortions resulting in selection rule relaxation. However, Fe is not JT active and Co, which is JT active, does not

show the 635  $\text{cm}^{-1}$  mode. Rather, it is believed that such an extra band corresponds to the  $A_{1g}$  mode of the hexagonal phase of BTO.<sup>[114,115,120,150–153]</sup> Indeed, it is known that partial substitution of  $\text{Ti}^{4+}$  for transition metal ions can stabilize the hexagonal polymorph of BTO at room temperature.<sup>[154]</sup> Such phase is believed to be present only in trace amounts as no extra Bragg peaks can be revealed in the diffraction patterns. Note that a few works have also attributed this extra band to the presence of oxygen vacancies.<sup>[118]</sup> As a result, the existence of the hexagonal phase and/or oxygen vacancies may imply the presence of mixed valence transition metal ions (e.g.,  $\text{Mn}^{3+}/\text{Mn}^{4+}$  or  $\text{Co}^{3+}/\text{Co}^{4+}$ ).

### 4.3.2 The ferroelectric properties of undoped BTO and co-doped BTO

In order to characterize the ferroelectric and piezoelectric properties of all our samples, the polarization versus electric field ( $P$ - $E$ ) hysteresis loops and the strain versus electric field ( $S$ - $E$ ) curves measured at room temperature are shown in Fig. 4-2, respectively (see also Table 4-1). In the case of undoped BTO (black in Fig. 4-2), a typical ferroelectric  $P$ - $E$  hysteresis loop and a butterfly-like  $S$ - $E$  curve are obtained, indicative of the ferroelectric and piezoelectric character, respectively. When co-doping with ( $\text{Fe}^{3+}$ ,  $\text{Nb}^{5+}$ ), these aforementioned features are suppressed and the  $P$ - $E$  curve shows a linear dielectric behavior, while the  $S$ - $E$  curve displays a parabolic-like shape, typical of electrostriction (i.e.  $S \propto E^2$  while piezoelectricity shows a linear dependency, i.e.  $S \propto E$ ). Note that electrostriction is a universal feature occurring in all insulators, including the non-ferroelectric ones, while all ferroelectrics are piezoelectrics. Table 4-1 also shows that there is a good correlation between the  $c/a$  ratio and the strain and polar response. The tetragonality decrease observed in Fig. 4-1c upon doping is indeed consistent with the reduction of the polarization amplitude displayed in Fig. 4-2a, which, in the extreme case of ( $\text{Fe}^{3+}$ ,  $\text{Nb}^{5+}$ ) doping, drops to roughly zero. Moreover, our Raman investigation shows that doping increases the chemical/polar disorder, e.g., through the broadening of the 305  $\text{cm}^{-1}$  Raman mode. In the case of ( $\text{Fe}^{3+}$ ,  $\text{Nb}^{5+}$ ), the induced disorder appears strong enough to suppress the long range polar order despite the unit cell remaining on average tetragonal. Some uncorrelated local polar regions most likely remain due to the persistence of the 305  $\text{cm}^{-1}$  mode. Comparing with other ( $X^{3+}$ ,  $\text{Nb}^{5+}$ ) pairs, iron is found

here not only to disrupt the long-range polar correlation as evidenced from Raman data, but also to completely destroy the macroscopic polarization character (see Table 4-1) and to lead to a non-polar tetragonal symmetry.

In the case of ( $Mn^{3+}$ ,  $Nb^{5+}$ ) doping, the  $P$ - $E$  curve shows a “pinched” loop with remnant polarization close to zero (blue in Fig. 4-2) and reduced coercive field  $E_C$  compared to pure BTO (Table 4-1). Such “pinching” was attributed to defect dipoles<sup>[125]</sup> where defects associates with oxygen vacancies form, e.g.,  $2Mn_{Ti}-V_O^{2+}$ . The defect complexes can also impact the photovoltaic response.<sup>[74]</sup> In addition to the pinched nature of its  $P$ - $E$  loop, ( $Mn^{3+}$ ,  $Nb^{5+}$ ) co-doped BTO shows a decreased piezoelectric response (Table 4-1), with a clear electrostrictive nature observable from the  $S$ - $E$  loop, plotted in blue in Fig. 4-2 b. This can be understood as a result of the disruption of the long range polar order and formation of polar clusters. Such clustering is also likely to occur in the case of ( $Mn^{3+}$ ,  $Ta^{5+}$ ) and ( $Sc^{3+}$ ,  $Nb^{5+}$ ), as both also exhibit a slim  $P$ - $E$  loop (without “pinching” like in ( $Mn^{3+}$ ,  $Nb^{5+}$ ) samples). Usually, the slim loops are associated to the so-called ferroelectric relaxors known to be characterized by polar clusters.<sup>[155]</sup> Interestingly, doping pairs that show the most degraded ferroelectric properties correlate with those exhibiting a marked Raman peak around  $635\text{ cm}^{-1}$  associated with the parasitic hexagonal phase and/or oxygen vacancies in Fig. 4-1d. On the contrary, the loop showing strongest ferroelectric and piezoelectric character from the doped samples is observed for ( $Co^{3+}$ ,  $Nb^{5+}$ ) co-doping (see purple in Fig. 4-2a, b and Table 4-1), and accordingly shows little to no peak around  $635\text{ cm}^{-1}$  in Fig. 4-1b. Despite retaining good ferroelectric properties, ( $Co^{3+}$ ,  $Nb^{5+}$ ) co-doped samples exhibit a 56 % lower maximum effective piezoelectric coefficient ( $d_{\text{eff}} = S_{\text{max}}/E_{\text{max}}$ ) and about 33% larger coercive field (i.e. 14 kV/cm). The remnant polarization ( $2P_r = 17\text{ }\mu\text{C}/\text{cm}^2$ ), on the other hand, is larger than in undoped BTO. These values suggest that the JT distortion due to Co ions may adequately couple to the overall polarization of BTO. Nevertheless, given the swollen-shape of the  $P$ - $E$  loop, some leakage currents are not excluded and may parasitically contribute to the total polarization response.

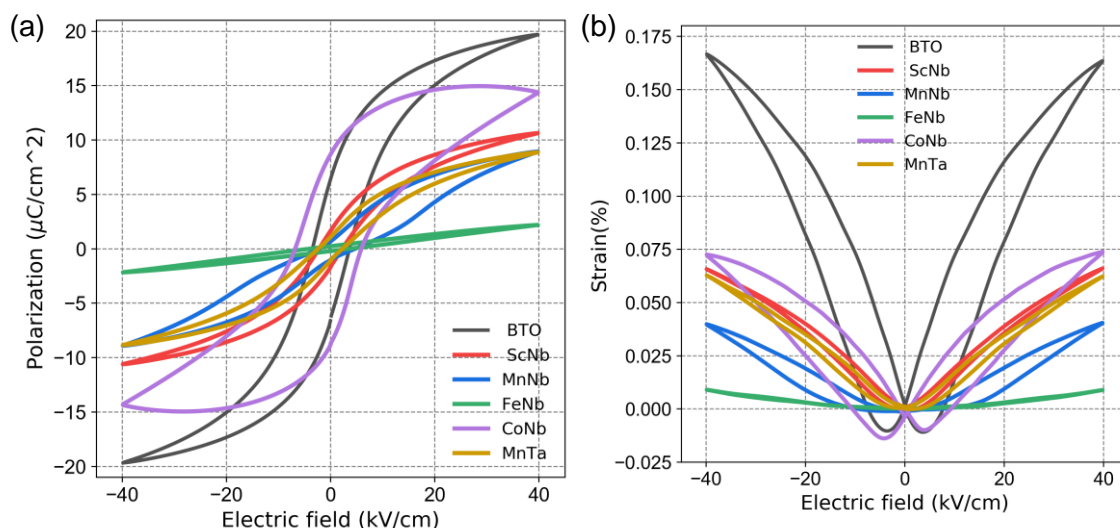


Fig. 4-2 (a) P-E and (b) S-E loops for undoped and co-doped BTO

### 4.3.3 The optical absorption of undoped BTO and co-doped BTO

Let us now have a look at the light absorption properties of the co-doped samples. Fig. 4-3a and the zoom in Fig. 4-3b present Tauc plots involving the Kubelka-Munk function  $F$  (a proxy for the absorption coefficient) versus photon energy as determined from diffuse reflectance spectroscopy experiments. The plots indicate that the optical bandgap of undoped BTO is 3.4 eV (see intersection of the linear fit with the x-axis in Fig. 4-3a), with the onset of absorption at 3.2 eV, as observed in Fig. 4-3b. With doping, the bandgap as determined using Tauc plots decreases to about 3.3 eV for ( $\text{Sc}^{3+}$ ,  $\text{Nb}^{5+}$ ), to 3.2 eV for ( $\text{Fe}^{3+}$ ,  $\text{Nb}^{5+}$ ), and to 3.0 eV for ( $\text{Mn}^{3+}$ ,  $\text{Nb}^{5+}$ ), ( $\text{Mn}^{3+}$ ,  $\text{Ta}^{5+}$ ) and ( $\text{Co}^{3+}$ ,  $\text{Nb}^{5+}$ ). Note that it is difficult to accurately determine the bandgap using Tauc plots with such absorption curves, as there is some degree of arbitrariness to locate the appropriate energy region for the linear fit. Hence, we found it important to additionally extract the onset of absorption which can be seen as the optical bandgap in contrast to the electronic bandgap separating the conduction band from the valence band.

Interestingly, while the bandgap of the doped samples extracted from Tauc plots in Fig. 4-3a only moderately decreases, a much larger variation is observed when considering the absorption onset (Fig. 4-3b). Indeed, from 3.2 eV in undoped BTO, the absorption onset drops to 2.75 eV for ( $\text{Sc}^{3+}$ ,  $\text{Nb}^{5+}$ ) and ( $\text{Fe}^{3+}$ ,  $\text{Nb}^{5+}$ ), then to 1.9 eV for ( $\text{Mn}^{3+}$ ,  $\text{Nb}^{5+}$ ) and ( $\text{Mn}^{3+}$ ,  $\text{Ta}^{5+}$ ), finally reaching 1.5 eV for ( $\text{Co}^{3+}$ ,  $\text{Nb}^{5+}$ ). The value of the absorption

onset thus strongly depends on the  $X^{3+}$  transition metal element. As an illustration, in the case of Mn-samples, both ( $Mn^{3+}$ ,  $Nb^{5+}$ ) and ( $Mn^{3+}$ ,  $Ta^{5+}$ ) have almost identical optical absorption curves. Interestingly, despite similar absorption properties, both samples display different ferroelectric-like features, as described above. Among the  $X^{3+}$  dopant ions, Sc ion shows less effect on the absorption than Fe, while the impact of Mn and Co is significantly stronger. This can be understood by the partially filled  $d^{n \neq 0}$  orbitals of  $Fe^{3+}$ ,  $Mn^{3+}$  and  $Co^{3+}$  as well as the JT effect of both  $Mn^{3+}$  and  $Co^{3+}$  ions in contrast to the  $3d^0$  orbitals of  $Sc^{3+}$ .

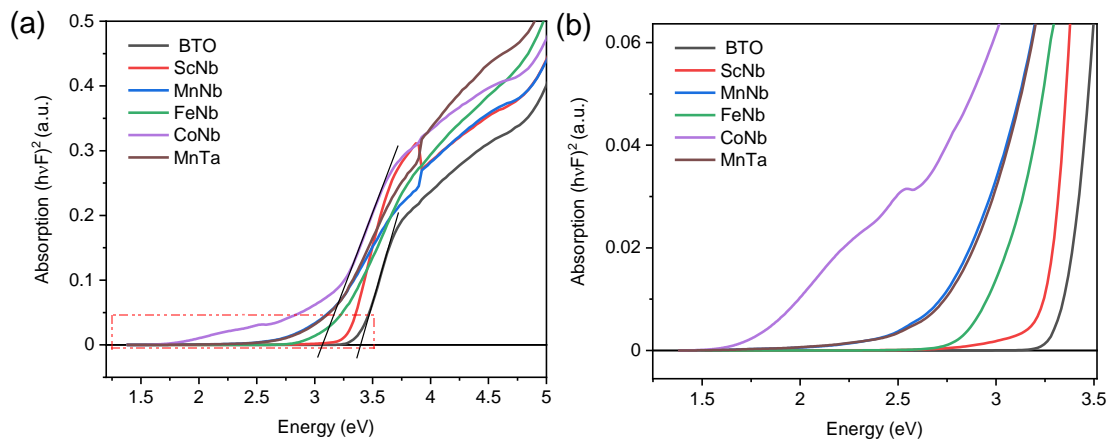


Fig. 4-3 (a) Absorption as a function of incident energy for all the compositions, the intersection of the lines (indicative here for undoped BTO and ( $Co^{3+}$ ,  $Nb^{5+}$ ) doped BTO) with the abscissa axis gives the bandgap value according to Tauc plot (b) zoom in of the absorption curve

In order to get a deeper insight into the band structure and its consequences on the absorption properties, DFT calculations were performed. Fig. 4-4 displays the density of electronic states (DOS) for undoped BTO, ( $Sc^{3+}$ ,  $Nb^{5+}$ ), ( $Mn^{3+}$ ,  $Nb^{5+}$ ) and ( $Co^{3+}$ ,  $Nb^{5+}$ ) co-doped samples. The electronic bandgap using the GGA-PBESol exchange-correlation functional is underestimated as it is found to be 2.5 eV in undoped BTO (Fig. 4-4a). As expected, the conduction band (CB) has a strong Ti  $3d$ -character, while the valence band is mainly due to O  $2p$ -orbitals. It is interesting to note that whatever the doping (Fig. 4-4 b-d), these features are kept and the CB and VB remain dominated by Ti- and O-orbitals. Consequently and while underestimated, the bandgap is found almost unchanged whatever the dopants, which is consistent with our experimental findings (see Fig. 4-3a). Interestingly, the partially filled  $d^{n \neq 0}$  orbitals of  $Mn^{3+}$  and  $Co^{3+}$  (also for  $Fe^{3+}$ , not shown here) bring new intragap electronic bands (Fig. 4-4c-d), as also previously

reported,<sup>[16,76,84]</sup> which is not the case of  $\text{Sc}^{3+}$  with  $3d^0$  orbitals (Fig. 4-4b). These extra bands inevitably impact on the absorption as we found experimentally (see Fig. 4-3b). Note that the band structure is impacted by the  $d^{n \neq 0}$  orbitals of the transition metals and thus  $\text{Sc}^{3+}$ ,  $\text{Nb}^{5+}$  as  $\text{Ta}^{5+}$  have no effects on the band structure; indeed, the density of states of  $(\text{Mn}^{3+}, \text{Nb}^{5+})$  and  $(\text{Mn}^{3+}, \text{Ta}^{5+})$  (not shown here) are similar and the experimental absorption curves are identical, as described previously.

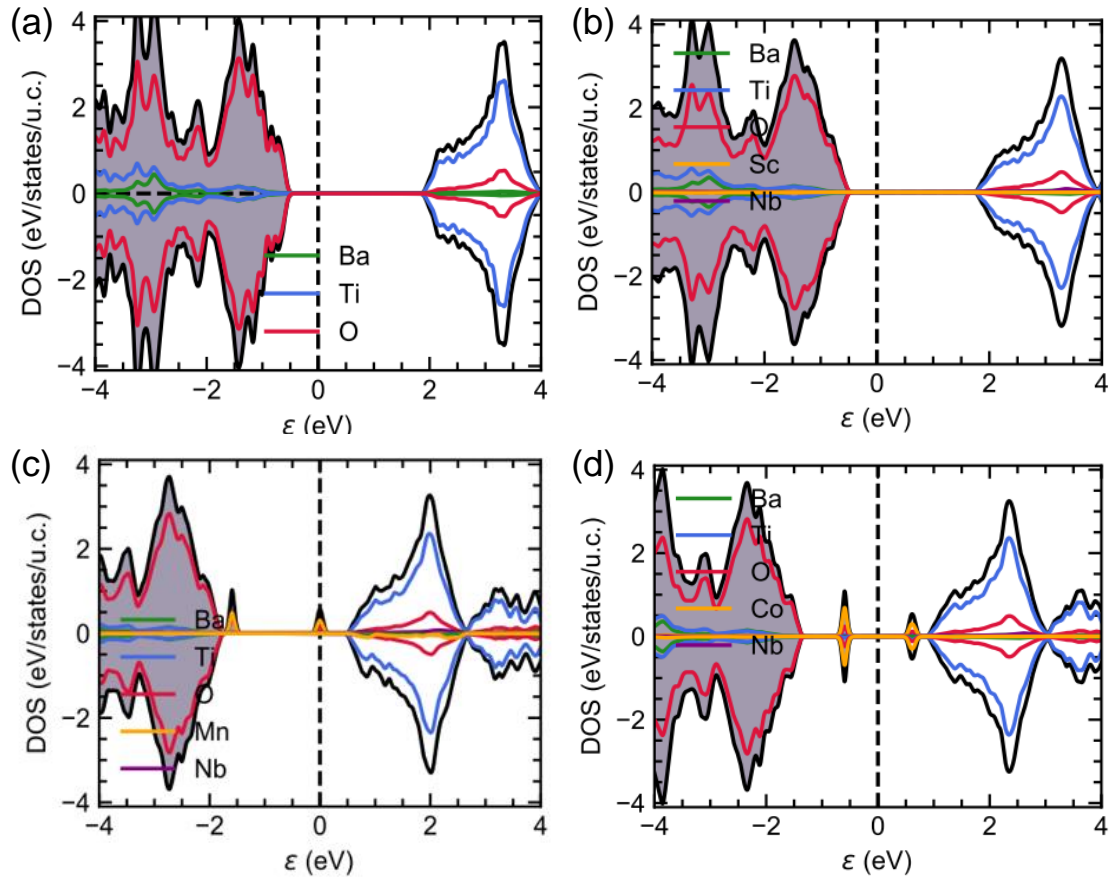


Fig. 4-4 The density of states of (a) undoped BTO, (b)  $(\text{Sc}^{3+}, \text{Nb}^{5+})$ , (c)  $(\text{Mn}^{3+}, \text{Nb}^{5+})$  and (d)  $(\text{Co}^{3+}, \text{Nb}^{5+})$  co-doped samples

Using these calculation results, it is also possible to calculate at 0K the imaginary part of permittivity  $\epsilon''$  which is involved in the absorption. Fig. 4-5a-c displays  $\epsilon''$  (both components, i.e. parallel and perpendicular to the polarization, the latter being along the [111] rhombohedral direction because the calculations are done at 0 K in the rhombohedral phase) for  $(\text{Sc}^{3+}, \text{Nb}^{5+})$ ,  $(\text{Mn}^{3+}, \text{Nb}^{5+})$  and  $(\text{Co}^{3+}, \text{Nb}^{5+})$ , respectively. The absorption of undoped BTO is added for comparison (black lines in Fig. 4-5). It is interesting to see that the calculated absorption curves are in very good qualitative agreement with the experimental data. Indeed, it is remarkable to see that, *e.g.*, in case

of ( $Co^{3+}$ ,  $Nb^{5+}$ ), the experimental absorption curve (Fig. 4-3b) is very similar to the calculated one (Fig. 4-5c). Interestingly, and as suspected from the DOS plotted in Fig. 4-4b, the absorption spectrum of the ( $Sc^{3+}$ ,  $Nb^{5+}$ ) co-doping pair is similar to that of undoped BTO; this is because none of the doping ( $Sc$  or  $Nb$ ) provides partially filled  $d$  states. A similar result was found experimentally in Fig. 4-3. Both undoped BTO and ( $Sc^{3+}$ ,  $Nb^{5+}$ ) co-doped BTO exhibit a steep absorption above the bandgap. In contrast, co-doping strategies involving  $d^{n \neq 0}$  ions such as  $Co^{3+}$  and  $Mn^{3+}$  show a smoothed absorption that starts to rise below the bandgap, due to the intra-gap states seen in Fig. 4-4c-d that provide a springboard for additional absorption e.g. optical transition between either occupied  $X^{3+}$   $d$ -states and the conduction band or between the valence band and the empty  $X^{3+}$   $d$ -state band. It is worth mentioning here that these results also highlight the difficulties one has to face when experimentally determining the bandgap value using the Tauc plot.

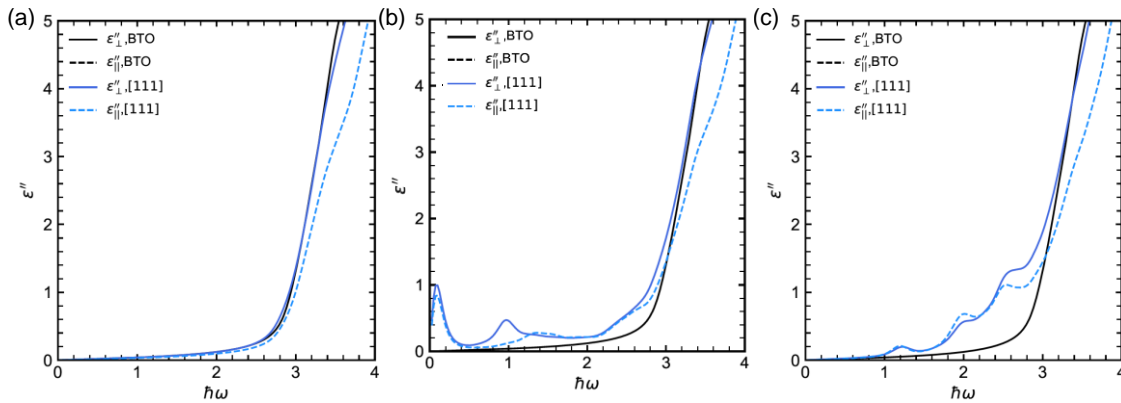


Fig. 4-5 Imaginary part of the permittivity stastic of (a) ( $Sc^{3+}$ ,  $Nb^{5+}$ ), (b) ( $Mn^{3+}$ ,  $Nb^{5+}$ ) and (c) ( $Co^{3+}$ ,  $Nb^{5+}$ ) samples compared to undoped BTO

#### 4.3.4 The photoresponse with light illumination

Another way to attest of the enhanced absorption efficiency when doping with  $Mn$  and  $Co$  is to measure the photoresponse when light is illuminating the sample using a perpendicular electrode configuration (see Fig. 4-6a). Fig. 4-6b-d shows the time dependence of the current under 10 V bias (photoconductivity) with the light switching on/off with laser diodes with wavelength 325 nm, 405 nm and 532 nm, corresponding to an energy of about 3.8 eV, 3.1 eV and 2.3 eV, respectively. Despite some residual leakage current, observed in dark conditions and associated to free carriers or defects,

when the laser is on there is a clear stable photogenerated current. At times  $t$  when the light is on (off) this current rises (or drops) until reaching a plateau that is the steady state. The initial transient current jump is associated to a pyroelectric current due to the sudden heating (cooling) of the sample when the laser diode is on (off). Interestingly, the photoconductivity changes according to the illuminating wavelength value as well as to the type of doping with respect to undoped BTO. For undoped BTO whose experimental electronic bandgap obtained using Tauc plot is 3.4 eV and the optical bandgap, i.e. the real absorption onset is 3.2 eV (see Fig. 4-3), there is no detectable current (except jumps of pyroelectric current) when the incident energy is lower than the absorption onset (i.e. 2.3 eV in Fig. 4-6d or 3.1 eV in Fig. 4-6c). In contrast, it becomes significant when illuminated using above bandgap light of 3.8 eV (325 nm). When co-doping with ( $\text{Mn}^{3+}$ ,  $\text{Nb}^{5+}$ ) and ( $\text{Co}^{3+}$ ,  $\text{Nb}^{5+}$ ), the absorption onset shifts down to 1.9 eV and 1.5 eV, respectively, which explains why we do see photogenerated response even using the lowest energy diode, i.e. 2.3 eV (532 nm). Moreover, as expected from absorption spectra (Fig. 4-3), the photoresponse of ( $\text{Co}^{3+}$ ,  $\text{Nb}^{5+}$ ) is higher than that of ( $\text{Mn}^{3+}$ ,  $\text{Nb}^{5+}$ ) and ( $\text{Sc}^{3+}$ ,  $\text{Nb}^{5+}$ ), which supports all previous experimental and theoretical results. Interestingly, ( $\text{Co}^{3+}$ ,  $\text{Nb}^{5+}$ ) co-doped samples show also the best ferroelectric properties among the investigated co-doped BTO and thus could be considered as a good potential candidate for photovoltaic-based applications.

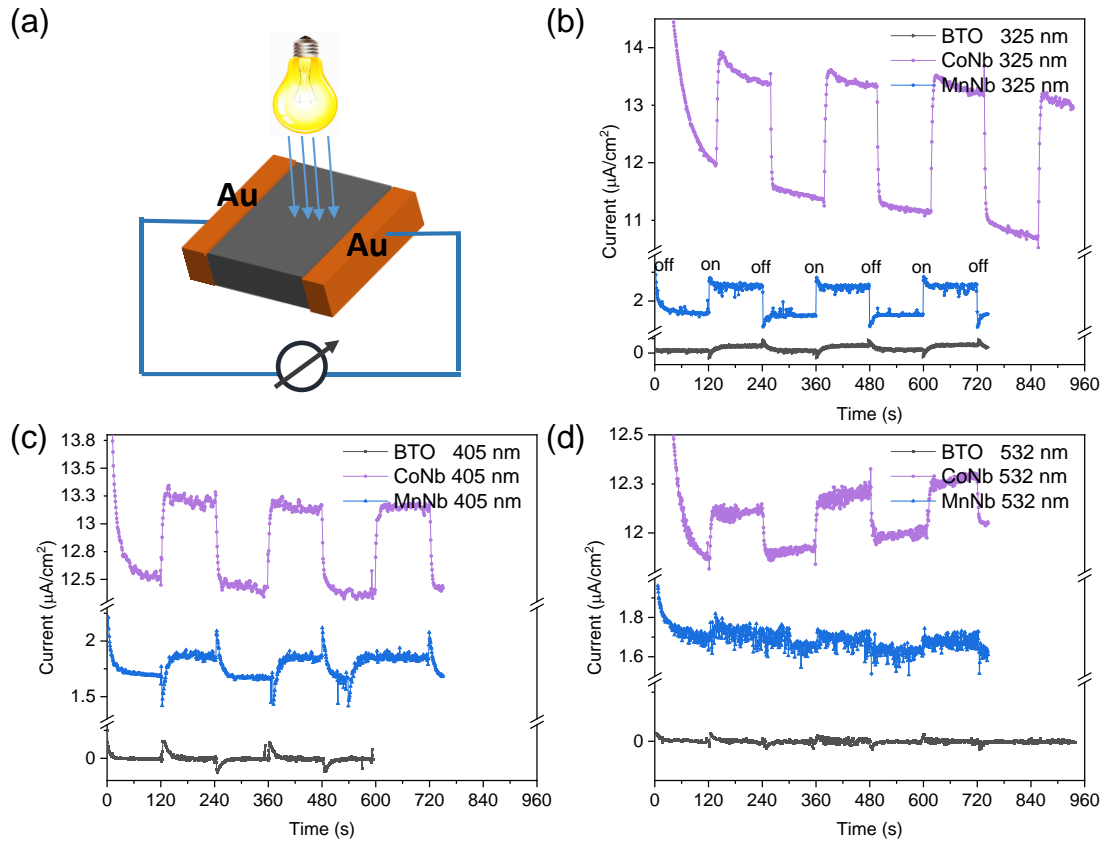


Fig. 4-6 (a) Device configuration for the photoelectric measurement. (b – c) The photoresponse versus time curves with laser (325 nm, 405 nm, 532 nm) of undoped BTO, ( $\text{Co}^{3+}$ ,  $\text{Nb}^{5+}$ ), and ( $\text{Mn}^{3+}$ ,  $\text{Nb}^{5+}$ ) samples.

## 4.4 Conclusions

In this work, two different transition metal ions are introduced into BTO to substitute the  $\text{Ti}^{4+}$  in the B site of the perovskite, while keeping the overall charge balance. The co-doping with  $3d^{n \neq 0}$  ions introduces intra-gap levels within the bandgap of BTO and improves the absorption (by lowering the energy). The onset of absorption can be significantly decreased down to 1.5 eV for co-dopants ( $\text{Co}^{3+}$ ,  $\text{Nb}^{5+}$ ) while retaining very good ferroelectric properties. The experimental optical absorption results are well supported by ab-initio calculations. Such a chemical approach appears as an excellent strategy to decrease the optical bandgap, and increase the optical absorption in BTO and can be largely extended to other ferroelectrics, making it available for the development of the next generation of high-performance ferroelectric-based photovoltaic devices.



# 5 Optical absorption of ferroelectric $(X^{2+}, Y^{6+})$ co-doped $BaTiO_3$

## Abstract

In this section, based on DFT calculation showing a decrease of the bandgap, different  $(X^{2+}, Y^{6+})$  co-substitution on B or both A-B sites of  $BaTiO_3$  ceramics are fabricated by conventional solid-state reaction. The compositions considered are  $BaTi_{1-x}(X_{1/2}Y_{1/2})_xO_3$  ( $X = Mg, Zn, Ni$ , and  $Y = Mo, W$ ), and the A-B site co-doped with  $Ba_{1-x}Ni_xTi_{1-3/2x}Y_xO_3$  ( $Y = Mo, W$ ), respectively. First, after doping, it is difficult to obtain pure samples without impurities except for  $(Mg^{2+}, W^{6+})$  co-doped with low substitution concentration. The optical absorption shows a slight change, especially in the case of co-doping on both A-B sites.  $BaTiO_3$  doped with  $(Zn^{2+}, Mo^{6+})$  on B sites presents better ferroelectric properties than the other systems. Besides,  $(Zn^{2+}, Mo^{6+}/W^{6+})$  co-doped  $BaTiO_3$  show also improved energy storage efficiency properties thanks to its slim ferroelectric loop, which opens another application for the  $(X^{2+}, Y^{6+})$  co-substituted  $BaTiO_3$ .

## 5.1 Introduction

The recently reported works of the bandgap engineering on  $BaTiO_3$  are mainly focused on the substitution on the A-site or B-site with one dopant or co-substituted with alkali metals or transition metals, like  $(Bi^{3+}, Li^+)^{[14]}$ ,  $(La^{3+}, Na^+)^{[71]}$  doping on the A-site and the  $(Mn^{3+}/Co^{3+}, Nb^{5+})$  co-doping on B-site<sup>[84,86]</sup>, etc. All the studies have suggested that the bandgap reduces due to the creation of the intra-energy levels by the oxygen vacancies or the increase of octahedral distortion changing the band structure. In addition to  $(X^{3+}, Y^{5+})$  co-doped BTO to narrow the bandgap thanks to intra-gap states, there are also some works on the chemical substitution in BTO by  $(X^{2+}, Y^{6+})$  ions (like  $Mg^{2+}, Zn^{2+}, Ni^{2+}, Mo^{6+}$ , and  $W^{6+}$ ). Recently, it has been reported that BTO substituted with  $Mo^{6+}$  and  $Mg^{2+}$

on the B-site yields an energy bandgap of 2.6 eV in the rhombohedral phase, using first-principles calculation while maintaining the electric polarization.<sup>[88]</sup> The decrease of the bandgap is due to the higher electronegativity of  $\text{Mo}^{6+}$  (2.16) than  $\text{Ti}^{4+}$  (1.54), which reduces the energy cost of charge transfer from the O 2p states to the conduction band.<sup>[156]</sup> Most of  $(\text{X}^{2+}, \text{Y}^{6+})$  doped BTO are investigated for microwave dielectric resonators, like  $x\text{Ba}(\text{Mg}_{1/2}\text{W}_{1/2})\text{O}_3-(1-x)\text{BaTiO}_3$  ( $x = 0.40-1.0$ ),<sup>[157]</sup>  $(\text{Zn}^{2+}, \text{W}^{6+})$ ,  $(\text{Ni}^{2+}, \text{W}^{6+})$ ,  $(\text{Co}^{2+}, \text{W}^{6+})$ , and  $(\text{Sr}^{2+}, \text{Mg}^{2+}, \text{W}^{6+})$ ,<sup>[158-161]</sup> which always have a high amount of substitution to get a stable hexagonal phase interesting for this application.

According to our density functional theory calculations, the bandgap of BTO can be indeed modified by substitution with transition metals  $(\text{X}^{2+}, \text{Y}^{6+})$  on the A site, B site, or both. As shown in Fig. 5-1, the optical absorption is improved compared to the pure BTO with doping on A-B sites and A sites. In addition, from the plot of the density of states (shown in Fig. 5-2), the substitution with  $(\text{Ni}^{2+}, \text{Mo}^{6+})$  and  $(\text{Ni}^{2+}, \text{W}^{6+})$  on A-B sites or A sites exhibits more intra-gap states between the valence band and conduction band, which can improve the optical absorption of BTO in the visible range.

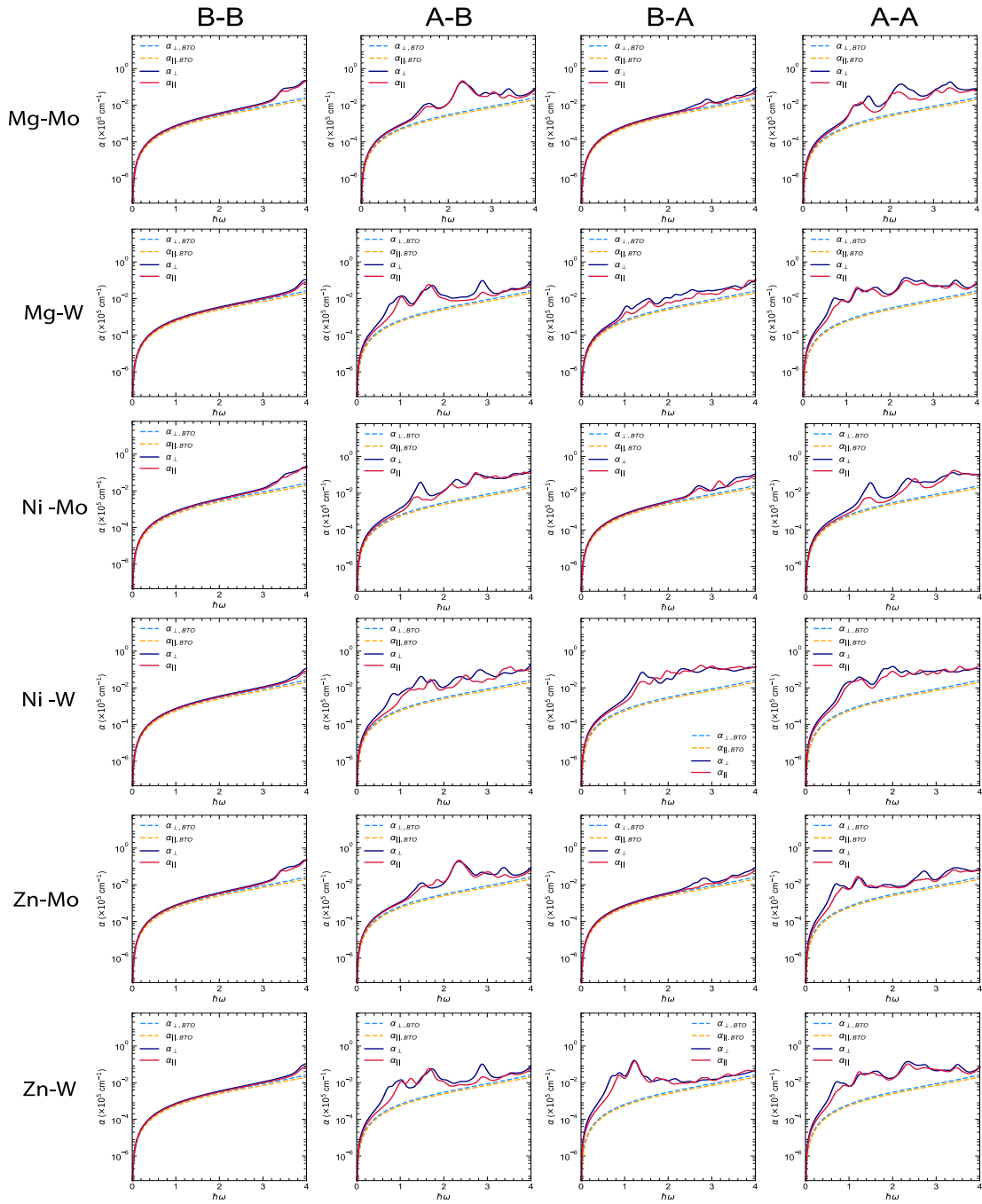


Fig. 5-1 The optical absorption efficiency of different compositions of ( $X^{2+}$ ,  $Y^{6+}$ ) co-doped BTO

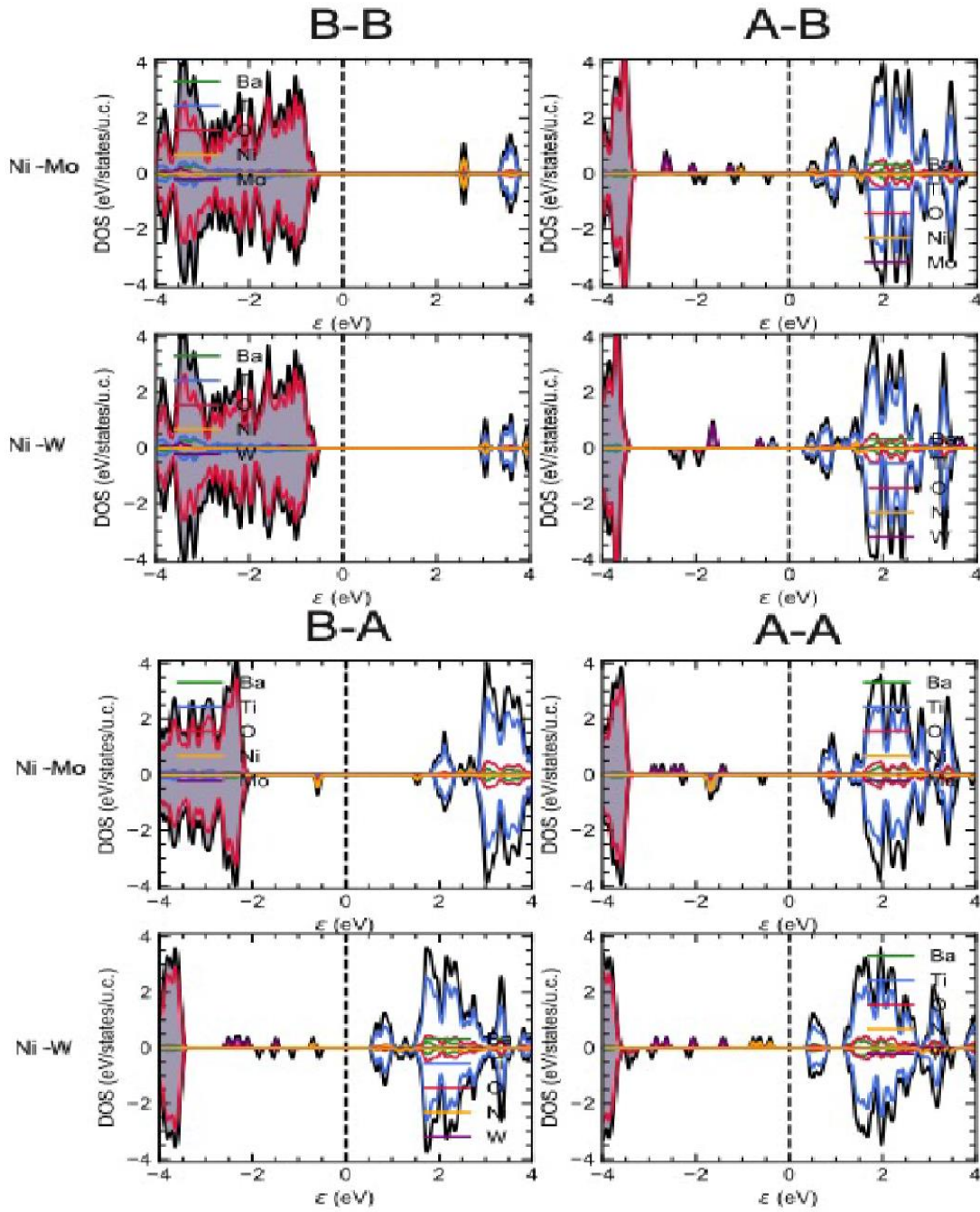


Fig. 5-2 The density of states of different compositions of ( $\text{Ni}^{2+}$ ,  $\text{Mo}^{6+}$ ) and ( $\text{Ni}^{2+}$ ,  $\text{W}^{6+}$ ) co-doped BTO

In this chapter, we have first investigated the influence of co-substitution with ( $\text{Mg}^{2+}$ ,  $\text{W}^{6+}$ ) on B-site on the bandgap of BTO experimentally. Then the composition  $\text{BaTi}_{1-x}(\text{X}_{1/2}\text{Y}_{1/2})_x\text{O}_3$  with  $X = \text{Zn}$ ,  $\text{Ni}$ , and  $Y = \text{Mo}$ ,  $\text{W}$ , with concentration  $x = 0.075$  was designed and fabricated. Besides, we have also studied the co-substitution on the A-B site with  $\text{Ni}^{2+}$  on A site, and  $\text{Mo}^{6+}$ ,  $\text{W}^{6+}$  substituting  $\text{Ti}^{4+}$  on the B site. All the samples are prepared using the conventional solid-state method. The optical absorption results

demonstrate that although the bandgap has only a slight change, the ( $Zn^{2+}$ ,  $Mo^{6+}/W^{6+}$ ) co-doping on the A-B site shows more bandgap decrease than the other compositions. The polarization properties of all the compositions are also investigated. ( $Zn^{2+}$ ,  $Mo^{6+}/W^{6+}$ ) doped BTO shows better ferroelectric properties at room temperature, while the ( $Mg^{2+}/Ni^{2+}$ ,  $W^{6+}$ ) co-doping presents weak ferroelectric properties. It is interesting to note that ( $Zn^{2+}$ ,  $W^{6+}$ ) doped BTO also exhibits an increase of energy storage efficiency, reaching more than 87 % compared to pure BTO.

## 5.2 Experimental procedure

Different ( $X^{2+}$ ,  $Y^{6+}$ ) doped BaTiO<sub>3</sub> ceramic samples were fabricated by traditional solid-state reaction. The starting reagents used were BaCO<sub>3</sub> (Strem 99.9%), TiO<sub>2</sub> (Prolabo 99%), MgO (Aldrich Chemical 98%), ZnO (Aldrich Chemical 99.99%), WO<sub>3</sub> (Alfa Aesar 99.8%), MoO<sub>3</sub> (Sublimed 99.95%). BaCO<sub>3</sub> and MgO were preheated at 500 °C and 800°C for 5 hours respectively to remove any absorbed moisture. Then, the powders were mixed in appropriate mass by wet ball-milling in ethanol. After drying at 100°C, the powders were calcined at 1000°C for 12 hours. Thereafter, the powders were ground with polyvinyl alcohol (PVA) (35 wt. %) added and then were pressed into pellets. The pellets were sintered under 1250 °C-1340°C for 10 hours.

## 5.3 Results and Discussion

### 5.3.1 BaTi<sub>1-x</sub>(Mg<sub>1/2</sub>W<sub>1/2</sub>)<sub>x</sub>O<sub>3</sub> ( $x = 0.025 \sim 0.5$ ) solid solutions

The XRD patterns of ( $Mg^{2+}$ ,  $W^{6+}$ ) doped BTO samples at room temperature are shown in Fig. 5-3. It is found that there is no significant secondary phase detected for the doping amount of  $x = 0.05 - 0.10$ , but with increasing  $x$ , it is difficult to form the pure phase. As shown in  $x = 0.20$  and  $x = 0.25$ , some BaWO<sub>4</sub> phase and some hexagonal phase (marked by diamond and dot symbols, respectively) are formed (indexed to the Powder Diffraction Standards Card (JCPDS card #72-0746 and 34-0129). By increasing the doping

concentration continually, for  $x = 0.5$ , the parasitic phases become dominant. It is challenging to obtain the pure phase, and it is probably because the radius of  $\text{Mg}^{2+}$  is larger than  $\text{Ti}^{4+}$  ( $\text{Mg}^{2+}$ , 0.72 Å;  $\text{W}^{6+}$ , 0.60 Å;  $\text{Ti}^{4+}$ , 0.61 Å), which can also induce the distortion of the Ti-O octahedra. Even by increasing the sintering temperature to a much higher temperature, the pure phase cannot be obtained.

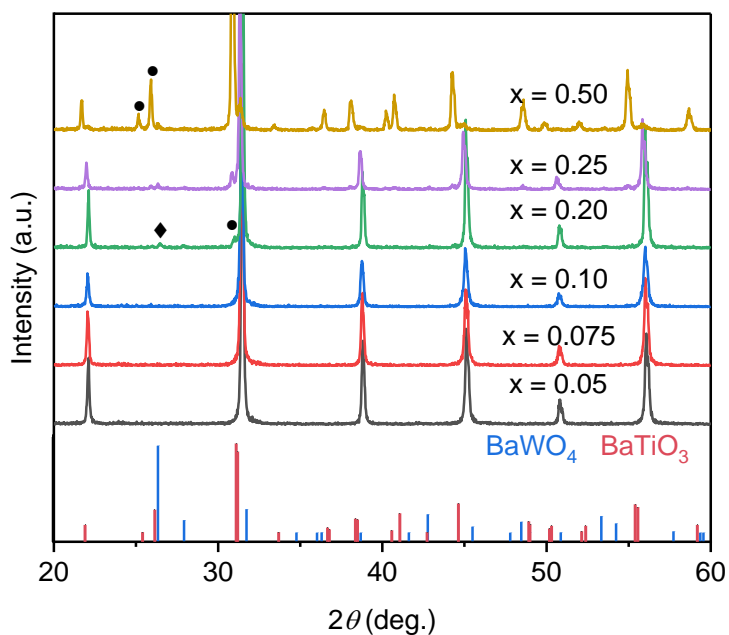


Fig. 5-3 XRD patterns of  $(\text{Mg}^{2+}, \text{W}^{6+})$  co-doped BTO measured at room temperature

The optical absorption of  $(\text{Mg}^{2+}, \text{W}^{6+})$  co-doped BTO powders was collected by measuring the diffuse reflectance. Fig. 5-4 shows the absorption spectra transformed by the Kubelka-Munk function. While our DFT calculations suggest a decrease of the bandgap, unexpectedly, we can see that the bandgap presents a slight increase with increasing the doping concentration compared to the pure BTO, changing from 3.40 eV for BTO to 3.5 eV for  $x = 0.25$ , and 3.7 eV for doping with  $x = 0.5$ , the composition with a strong contribution from a parasitic phase. It is interesting to note that the bandgap can be decreased by sintering at a higher temperature (see in Fig. 5-4b). The bandgap of sample  $x = 0.05$  changes from 3.42 eV at 1220 °C to 3.27 eV at 1270 °C sintering; For the sample doped with  $x = 0.25$ , it decreases from 3.50 eV to 3.43 eV. The higher sintering temperature could increase the grain size, which may have an influence (even slight) on optical absorption in contrast to the  $(\text{X}^{3+}, \text{Y}^{5+})$  dopants.

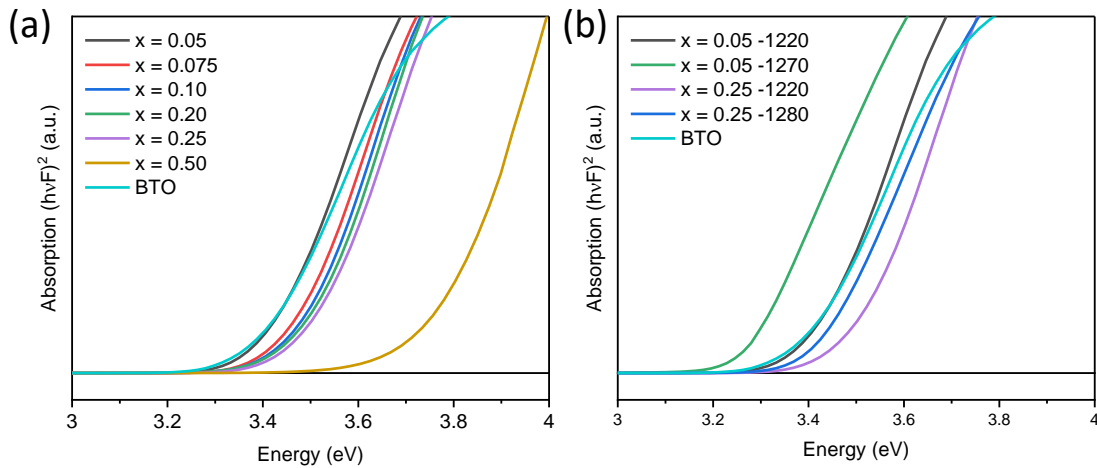


Fig. 5-4 Absorption spectra of the (Mg<sup>2+</sup>, W<sup>6+</sup>) co-doped BTO (a) sintered at the same temperature; (b) sintered at different temperature

### 5.3.2 BaTi<sub>1-x</sub>(X<sub>1/2</sub>Y<sub>1/2</sub>)<sub>x</sub>O<sub>3</sub> (X= Ni or Zn, Y = W or Mo, x = 0.075) solid solutions

In addition to the (Mg<sup>2+</sup>, W<sup>6+</sup>) co-doped BTO, different divalent and hexavalent cations substituting Ti ions, BaTi<sub>0.925</sub>(X<sub>1/2</sub>Y<sub>1/2</sub>)<sub>0.075</sub>O<sub>3</sub> (where X stands for Ni<sup>2+</sup>, Zn<sup>2+</sup>, Fe<sup>3+</sup> or Co<sup>3+</sup>, and Y stands for W<sup>6+</sup> or Mo<sup>6+</sup>) were also investigated. Fig. 5-5 presents the XRD patterns of Ni<sup>2+</sup>/Zn<sup>2+</sup> and W<sup>6+</sup>/Mo<sup>6+</sup> doped BaTiO<sub>3</sub>. It is found that only (Ni<sup>2+</sup>, W<sup>6+</sup>) co-doping can obtain a pure phase, while (Zn<sup>2+</sup>, W<sup>6+</sup>) and (Zn<sup>2+</sup>, Mo<sup>6+</sup>) co-doped BTO show a small amount of secondary phase BaWO<sub>4</sub>. In Fig. 5-5, an additional sintering at a higher temperature (1340 °C) after the first sintering step at 1280 °C increases the amount of secondary phase.

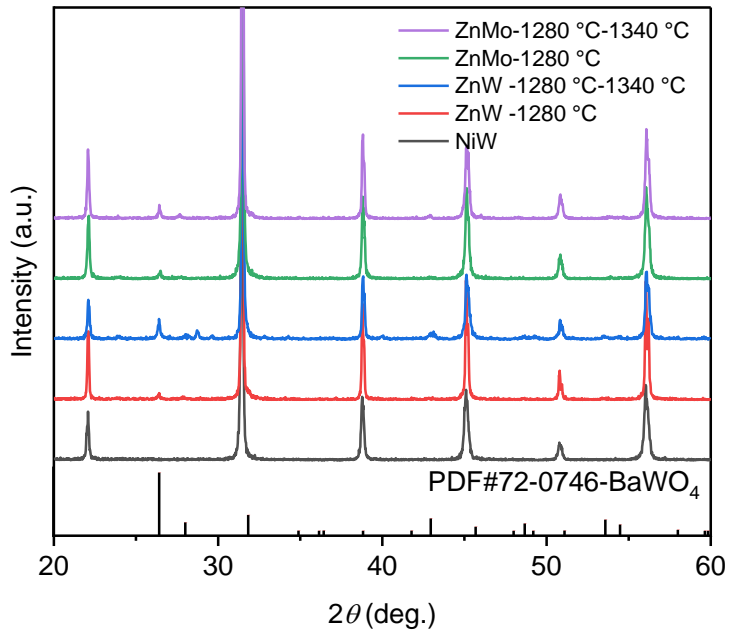


Fig. 5-5 XRD patterns of samples ( $X^{2+}$ ,  $Y^{6+}$ ) co-doped BTO measured at room temperature

The optical absorption of ( $X^{2+}$ ,  $Y^{6+}$ ) co-doped BTO is presented in Fig. 5-6. Compared to pure BTO, the bandgap of ( $Ni^{2+}$ ,  $W^{6+}$ ) remains unchanged with the same value (3.40 eV) as the pure BTO, and the samples doped with ( $Zn^{2+}$ ,  $W^{6+}$ ) and ( $Zn^{2+}$ ,  $Mo^{6+}$ ) show only a slight, if any, decrease,  $\sim 3.4$  eV and 3.3 eV, respectively. It is interesting to note that in contrast to  $Mg^{2+}$  doping, the bandgap of  $Zn^{2+}$  doping does not change, as only a slight decrease is observed.

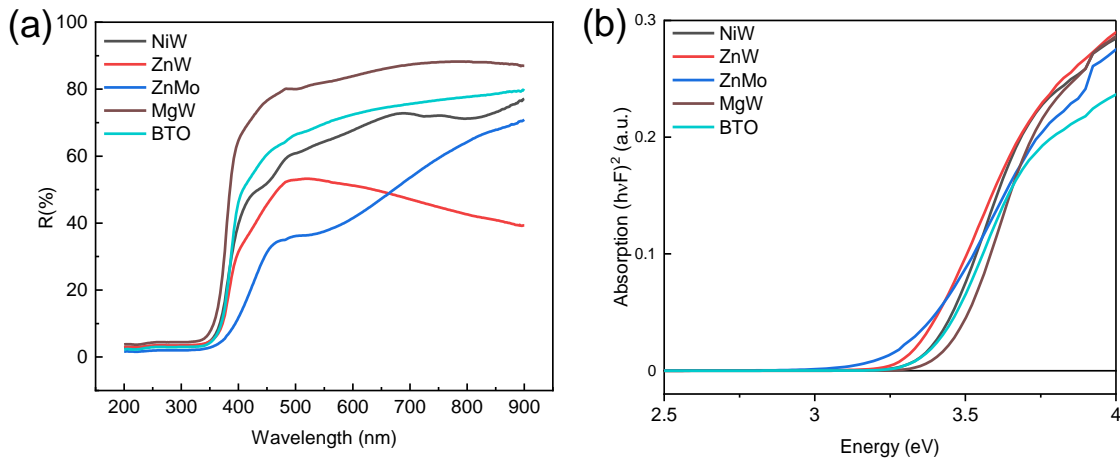


Fig. 5-6 Absorption spectra of ( $X^{2+}$ ,  $Y^{6+}$ ) co-doped BTO (a) UV-Vis diffuse reflectance spectra of; (b) Absorption versus Energy

The real part of the permittivity ( $\epsilon'$ ) variation and the loss factor ( $\tan\delta$ ) at 10 kHz depending on temperature are shown in Fig. 5-7. The ferroelectric to paraelectric phase

transition ( $T_c$  or  $T_{max}$ ) is at 317 K for the (Zn<sup>2+</sup>, Mo<sup>6+</sup>) doping and 252 K for (Zn<sup>2+</sup>, W<sup>6+</sup>) doping. The transition temperature is independent of the frequency, which indicates that the system exhibits a ferroelectric characteristic and rather a weak ferroelectric type than a relaxor behavior.

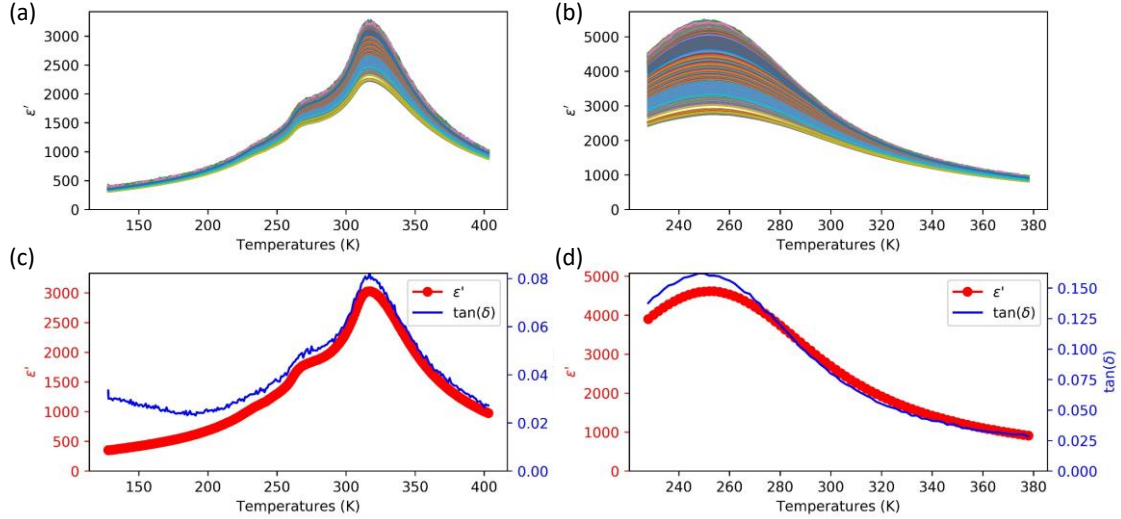


Fig. 5-7 Temperature dependence of permittivity of the sample (a) (Zn<sup>2+</sup>, Mo<sup>6+</sup>) and (b) (Zn<sup>2+</sup>, W<sup>6+</sup>) doping at a different frequency; the permittivity and dielectric loss at around 10 kHz of the sample (c) (Zn<sup>2+</sup>, Mo<sup>6+</sup>) and (d) (Zn<sup>2+</sup>, W<sup>6+</sup>) doping

In contrast, the ferroelectric hysteresis loops show a slim shape, resembling a relaxor ferroelectric (Fig. 5-8). Compared to the pure BTO (shown in Chapter 4,  $P_r = 6.38 \mu\text{C}/\text{cm}^2$ ,  $E_c = 3.63 \text{ kV}/\text{cm}$ ), the polarization and coercive electric field both decrease, and  $P_r = 1.13 \mu\text{C}/\text{cm}^2$ ,  $E_c = 1.38 \text{ kV}/\text{cm}$  for sample of (Zn<sup>2+</sup>, Mo<sup>6+</sup>) doping and  $P_r = 0.40 \mu\text{C}/\text{cm}^2$ ,  $E_c = 1.07 \text{ kV}/\text{cm}$  for (Zn<sup>2+</sup>, W<sup>6+</sup>) doping. Of course, (Zn<sup>2+</sup>, Mo<sup>6+</sup>) and (Zn<sup>2+</sup>, W<sup>6+</sup>) doped BTO present better ferroelectric properties than the (Mg<sup>2+</sup>, W<sup>6+</sup>) co-doping, which has no ferroelectric behavior at room temperature due to its cubic phase structure, shown in Fig. S 5-1. However, we have found that the energy storage density is enhanced obviously with (Zn<sup>2+</sup>, Mo<sup>6+</sup>) and (Zn<sup>2+</sup>, W<sup>6+</sup>) co-doping. The recoverable energy storage density ( $W_{rec}$ ) and the energy storage efficiency ( $\eta$ ) are determined by the polarization ( $P$ ) and the applied electric field ( $E$ ), through the following formulas<sup>[162,163]</sup>:

$$W_{rec} = \int_{P_r}^{P_{max}} E dP \quad (5-1)$$

$$W = \int_0^{P_{max}} E dP \quad (5-2)$$

$$\eta = \frac{W_{rec}}{W} \quad (5-3)$$

where the  $P_{max}$  is the maximum polarization under the maximum electric field,  $P_r$  is the remnant polarization at zero electric fields. In the present work, the remnant polarization is decreased by doping, and the energy storage efficiency improves. It is found that  $(Zn^{2+}, W^{6+})$  co-doped BTO displays a high efficiency  $\eta = 87.3 \%$ , as well as the  $(Zn^{2+}, Mo^{6+})$  doping with an efficiency value  $\eta = 82.8 \%$  at an electric field  $E_c = 40$  kV/cm, much higher than pure BTO ( $\eta = 50.4\%$ ).

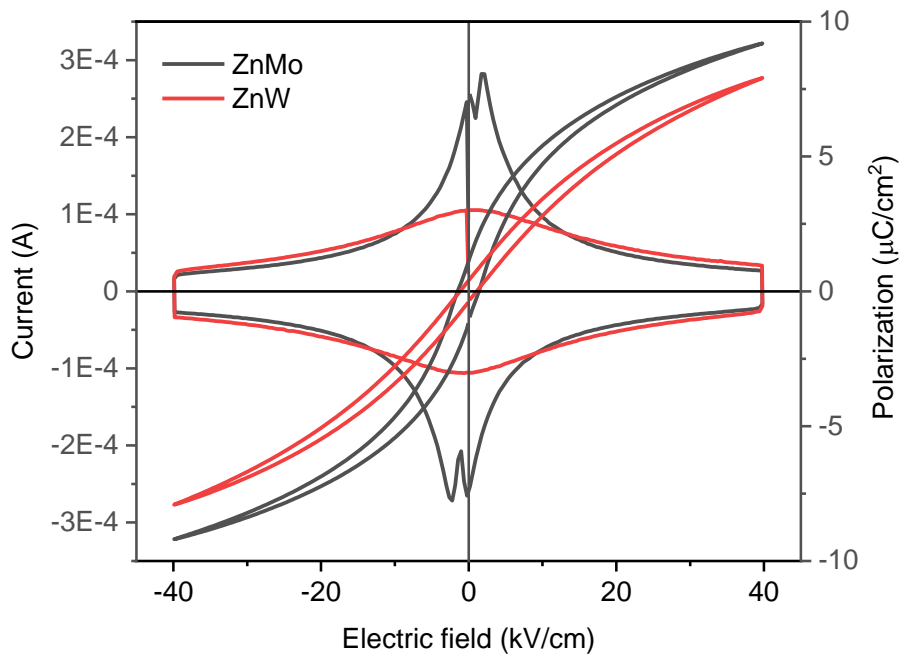


Fig. 5-8 The hysteresis loops ( $P$ - $E$ ) and current versus electric field ( $I$ - $E$ ) loops of the sample  $(Zn^{2+}, Mo^{6+})$  and  $(Zn^{2+}, W^{6+})$  co-doped BTO

By measuring the variation of polarization loops as a function of temperature, as shown in Fig. 5-9, it is found that the loops are turning to slimmer shape with the increase of temperature.  $(Zn^{2+}, Mo^{6+})$  co-doping of BTO shows a ferroelectric phase transition around 310-323 K, above which linear loops typical of dielectric behavior are observed. This is consistent with the dielectric constant showing a  $T_c$  at about 317 K. For the  $(Zn^{2+}, W^{6+})$  co-doped BTO, the polarization loops start to present linear behavior at about room temperature while the dielectric constant shows a dielectric anomaly at a much lower temperature, i.e.,  $T_{max}$  252 K.

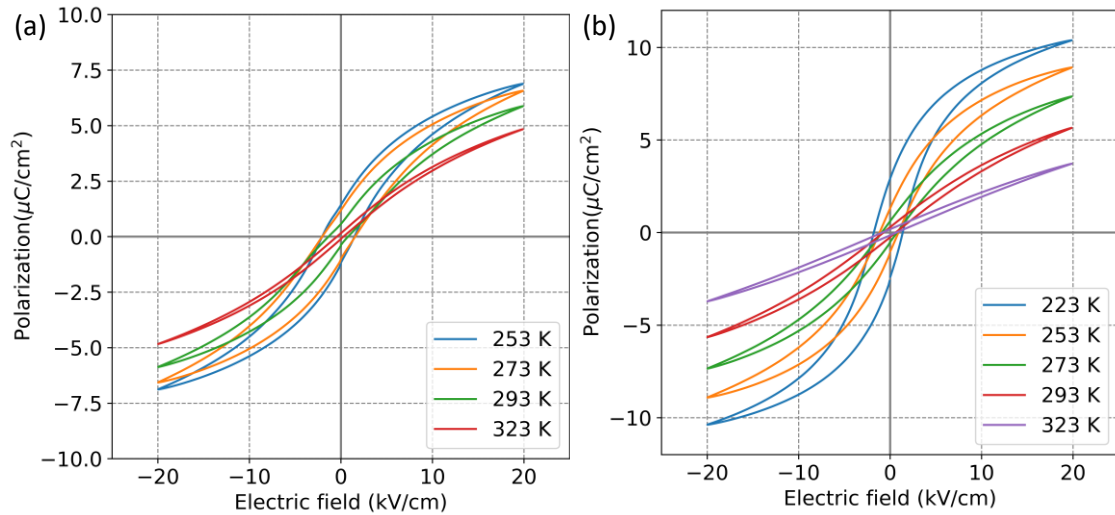


Fig. 5-9 The hysteresis loops ( $P$ - $E$ ) as a function of the temperature of (a) ( $Zn^{2+}$ ,  $Mo^{6+}$ ) and (b) ( $Zn^{2+}$ ,  $W^{6+}$ ) co-doped BTO

### 5.3.3 $Ba_{1-x}X_xTi_{1-3/2x}Y_xO_3$ ( $X = Ni$ , $Y = W$ or $Mo$ , $x = 0.075$ ) solid solutions

Furthermore, we have designed doping on both A and B sites via  $Ni^{2+}$  substituting  $Ba^{2+}$  and using  $W^{6+}$  or  $Mo^{6+}$  to substitute  $Ti^{4+}$ . Here, the one powder is obtained by the second calcination, and the other one is sintered as a pellet before crushing into powder. Then, the two powders can be compared to see the effect of calcination/sintering. All samples are accompanied by an amount of  $BaWO_4$ , seen in Fig. 5-10. It is found that the peak of (200) in the sample of ( $Ni^{2+}$ ,  $Mo^{6+}$ ) co-doping splits into two peaks (002) and (200) (see in Fig. 5-10b); while only one peak is observed in the case of ( $Ni^{2+}$ ,  $W^{6+}$ ) doping, which suggests that ( $Ni^{2+}$ ,  $Mo^{6+}$ ) co-doped BTO is tetragonal at room temperature; while ( $Ni^{2+}$ ,  $W^{6+}$ ) doped sample presents less tetragonality a cubic-like structure. Note also that the amount of  $BaWO_4$  is much more important in the case of ( $Ni^{2+}$ ,  $W^{6+}$ ) doping.

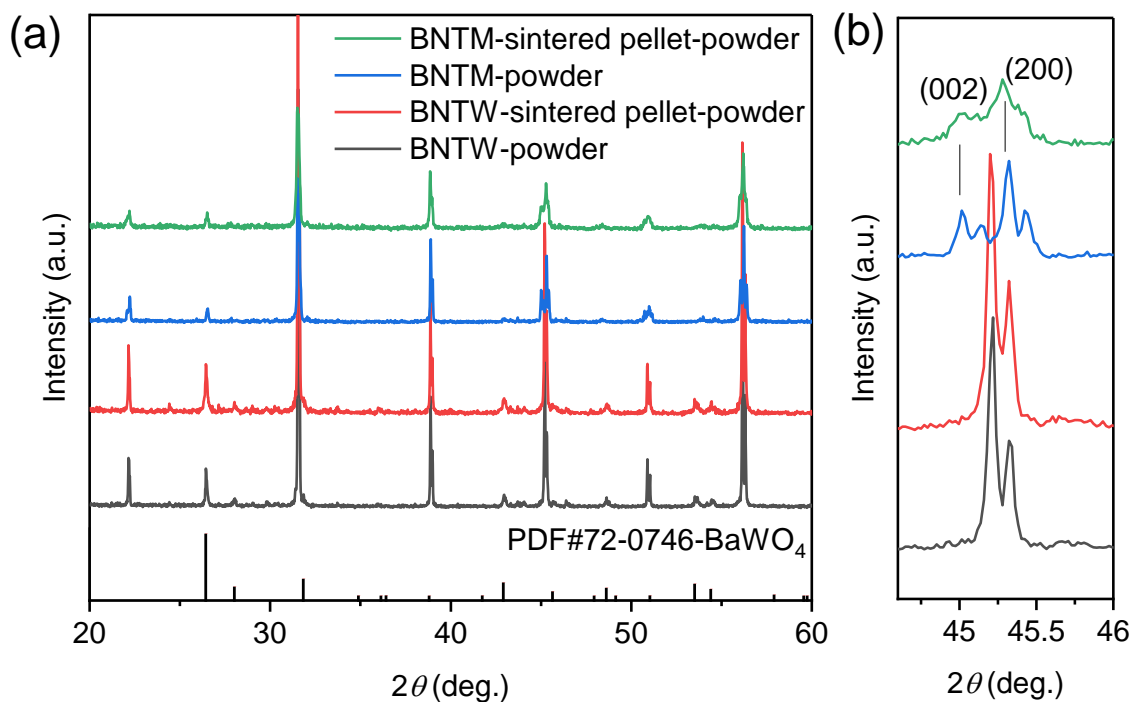


Fig. 5-10 XRD patterns of the samples ( $\text{Ni}^{2+}$ ,  $\text{Mo}^{6+}$ ) and ( $\text{Ni}^{2+}$ ,  $\text{W}^{6+}$ ) co-doped BTO at room temperature

Fig. 5-11 exhibits the optical absorption of ( $\text{Ni}^{2+}$ ,  $\text{Mo}^{6+}$ ) and ( $\text{Ni}^{2+}$ ,  $\text{W}^{6+}$ ) co-doped BTO powder obtained via different synthesis routes. It is observed that the doping on both A-B sites shows a low effect on the bandgap. Note that the powders from the second calcination display better absorption than the ones obtained from the crushed pellet. For instance, the powder of ( $\text{Ni}^{2+}$ ,  $\text{W}^{6+}$ ) doped BTO shows a bandgap value of 3.14 eV instead of 3.25 eV for the sample from the crushed pellet. However, because of the existence of the parasitic phase, it is not easy to understand the optical absorption behavior of the samples, as the parasitic phase can probably have an effect on the total absorption, which still needs to be explored.

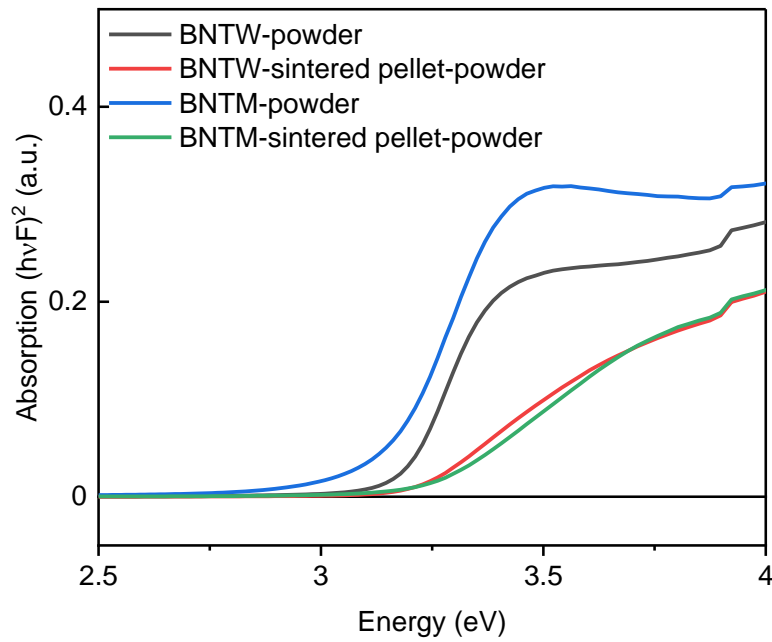


Fig. 5-11 Absorption spectra versus Energy of the samples ( $Ni^{2+}$ ,  $Mo^{6+}$ ) and ( $Ni^{2+}$ ,  $W^{6+}$ ) co-doped BTO at room temperature

The temperature and frequency dependence of the dielectric constant are shown in Fig. 5-12. The sample doping with ( $Ni^{2+}$ ,  $Mo^{6+}$ ) shows a dielectric anomaly peak  $T_m/T_c$  at about 368 K, related to the phase transition from tetragonal to cubic phase, while it is at about 223 K for sample doping with ( $Ni^{2+}$ ,  $W^{6+}$ ). This can be connected to the XRD results and the ferroelectric properties shown in Fig. S 5-2, because indeed ( $Ni^{2+}$ ,  $Mo^{6+}$ ) and ( $Ni^{2+}$ ,  $W^{6+}$ ) co-doped BTO show tetragonal and cubic-like structures at room temperature, respectively. It is also interesting to note that compared to the doping by ( $Zn^{2+}$ ,  $Mo^{6+}$ ), ( $Zn^{2+}$ ,  $W^{6+}$ ), or ( $Mg^{2+}$ ,  $W^{6+}$ ) on the B site, the doping with  $W^{6+}$  leads to a large decrease of  $T_{max}$ , and decreases the ferroelectric properties.

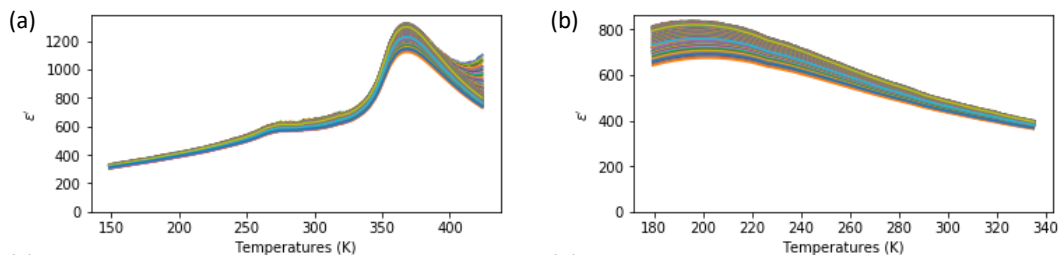


Fig. 5-12 The permittivity of (a) ( $Ni^{2+}$ ,  $Mo^{6+}$ ) and (b) ( $Ni^{2+}$ ,  $W^{6+}$ ) co-doped BTO as a function of temperature and frequency

## 5.4 Conclusions

In this chapter, we have investigated the effect of different ( $X^{2+}$ ,  $Y^{6+}$ ) co-substitutions of BTO on B and both A-B sites. Despite the promises from our DFT calculation suggesting a significant decrease of the bandgap and a higher optical absorption, our experimental results show that the optical absorption has a tiny change compared to the BTO co-doped with ( $X^{3+}$ ,  $Y^{5+}$ ) ions. It is found very challenging to get a pure phase; there is always some parasitic phase, except for ( $Mg^{2+}$ ,  $W^{6+}$ ) co-doped BTO in a low amount of substitution. The decrease of the phase transition temperature or ferroelectric properties are also observed. Note that ( $Zn^{2+}$ ,  $Mo^{6+}/W^{6+}$ ) doping on B sites shows improved energy storage efficiency properties, which opens another application for the ( $X^{2+}$ ,  $Y^{6+}$ ) co-substituted  $BaTiO_3$ . Further studies to better understand the effect of ( $X^{2+}$ ,  $Y^{6+}$ ) doping are still needed from both the theoretical and experimental points of view.

## 5.5 Supporting information

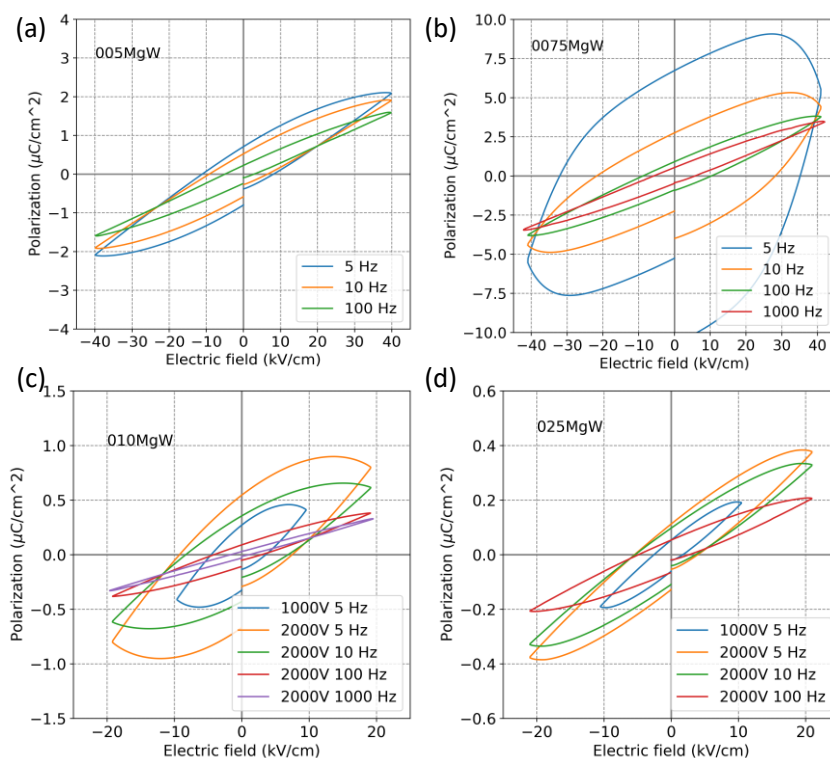


Fig. S 5-1 The hysteresis loops ( $P$ - $E$ ) of selective samples of ( $Mg^{2+}$ ,  $W^{6+}$ ) co-doped BTO

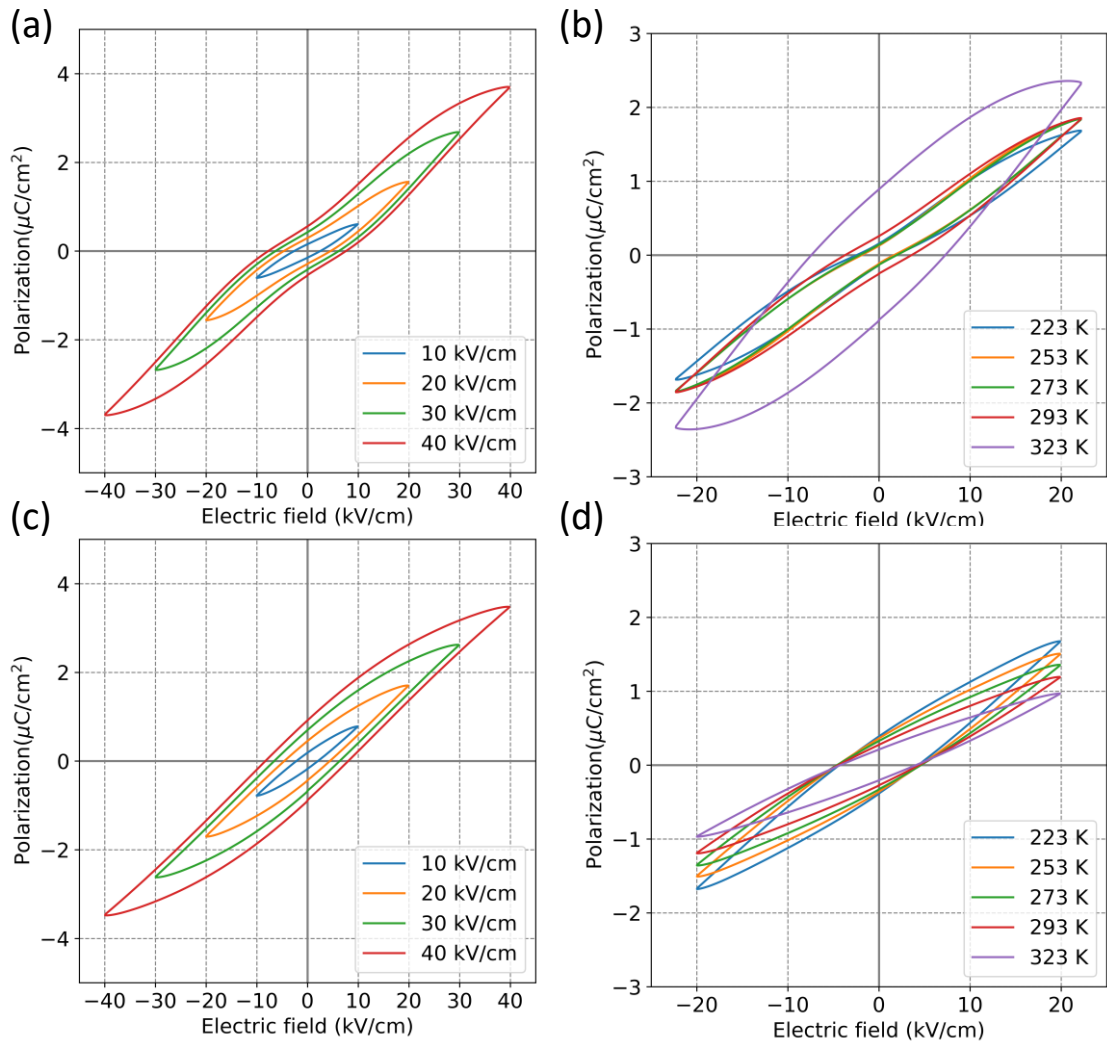


Fig. S 5-2 The hysteresis loops ( $P$ - $E$ ) of the samples ( $\text{Ni}^{2+}$ ,  $\text{Mo}^{6+}$ ) (a, b) and ( $\text{Ni}^{2+}$ ,  $\text{W}^{6+}$ ) (c, d) co-doped BTO at room temperature and versus temperature



# 6 Conclusions and perspectives

## 6.1 Conclusions

The challenge of photovoltaic devices based on ferroelectrics is that most ferroelectrics have a typical bandgap larger than 3 eV, limiting the absorption of the solar spectrum. Generally, the bandgap of perovskite oxides ( $ABO_3$ ) can be tuned by chemical substitution. We have found that the co-doping with ( $X^{3+}$ ,  $Y^{5+}$ ) with  $3d^{\neq 0}$  ions is helpful to reduce the bandgap and keep good remnant polarization, which is suitable for the use of photovoltaic devices.

First,  $BaTiO_3$  co-doped on the  $Ti^{4+}$  sites by ( $Mn^{3+}$ ,  $Nb^{5+}$ ),  $BaTi_{1-x}(Mn_{1/2}Nb_{1/2})_xO_3$ , was investigated. Dielectric measurements show that the ferroelectric phase transition temperature ( $T_c$ ) abruptly shifts towards lower temperatures with the increase of doping concentration. The ferroelectric deterioration increases with the increase of doping levels, and there are weak ferroelectric properties with doping higher than 0.075. The bandgap decreases from 3.4 eV for pure  $BaTiO_3$  to 2.5 eV for sample  $x = 0.15$ , respectively. Besides, the onset of the absorption drops down to 1.5 eV, which is promising for solar energy harvesting. We have also investigated the influence of doping concentration on the phase transition by the different measurements as a function of temperature.

We have also investigated the effects of the synthesis parameters on the microstructure, electrical and optical properties of  $BaTi_{1-x}(Mn_{1/2}Nb_{1/2})_xO_3$  ( $x = 0.075$ ) materials. The bandgap changes from 3.0 eV to 2.7 eV by increasing the milling time and rate, but the onset of absorption shows a tiny change on different synthesis conditions. The Curie temperature  $T_c$  presents a high variation on the synthesis conditions, specifically it depends on the ball-milling rate. The shorter time and lower speed of milling lead to the inhomogeneous distribution of the dopants, causing inhibited grain growth, higher porosity, and even some phase separation. By increasing the milling rate and time, a

homogeneous distribution of dopants is obtained. Despite the gradual degradation of the ferroelectric properties with increasing material homogeneity, further improvement of the optical absorption is achieved. It can be a good strategy to minimize the impact on ferroelectric properties using proper synthesis parameters.

The optical absorption for different trivalent and pentavalent ion ( $X^{3+}$ ,  $Y^{5+}$ ) co-doped  $BaTiO_3$  was also investigated. X-ray diffraction and Raman spectroscopy measurements show that the tetragonality and the polar coherence length decrease after co-doping, impacting the ferroelectric features. It is found that ( $Co^{3+}$ ,  $Nb^{5+}$ ) co-doping shows higher remnant polarization than the others, and the onset of absorption for this doping can decrease down to 1.5 eV. We have also confirmed this by Density Functional Theory calculations, demonstrating that the co-doping with  $3d^{\neq 0}$  ions inserts intra-gap levels responsible for artificially reducing the bandgap, fully in line with our experimental observations. The measured photoconductivity confirms that ( $Co^{3+}$ ,  $Nb^{5+}$ ) doping has superior absorption than the others. This work provides a strategy for the application of ferroelectrics in optoelectronic devices.

Finally, different divalent and hexavalent ions ( $X^{2+}$ ,  $Y^{6+}$ ) are also considered for co-doping  $BaTiO_3$  on the B site or both A-B sites. It is very challenging to obtain the pure perovskite phase and the doping is found to significantly alter the dielectric and ferroelectric properties. While the energy storage efficiency is enhanced by ( $Zn^{2+}$ ,  $Mo^{6+}/W^{6+}$ ) co-doping on the B site, whatever the co-doping, the optical absorption shows a slight change, which is in contrast to our DFT results. Because of the existence of the parasitic phases, these systems still need to be improved in the future.

## 6.2 Perspectives

We have found that the co-doping with ( $X^{3+}$ ,  $Y^{5+}$ ) with  $3d^{\neq 0}$  ions is helpful to reduce the bandgap of BTO and keep good remnant polarization at the same time, especially doping with ( $Co^{3+}$ ,  $Nb^{5+}$ ). So accordingly, we have started to grow thin films of ( $Co^{3+}$ ,  $Nb^{5+}$ ) co-doped BTO with thickness lower than 100 nm. By reducing the diffusion length, an improvement of the photocurrent and power conversion efficiency is strongly expected.

Note that it is also interesting to control the photocurrent by applying various stimuli in addition to light, such as e.g. electric field, temperature or pressure to provide more functionalities. Moreover, as we have already mentioned, it is also meaningful to study other photovoltaic related properties such as the photocatalytic activity as well as the photostriction, widening the applicative possibilities of these as-designed photoferroelectrics.

### 6.2.1 $(\text{Co}^{3+}, \text{Nb}^{5+})$ doped BTO thin film

$(\text{Co}^{3+}, \text{Nb}^{5+})$  doped BTO thin films were grown on  $\text{SrTiO}_3$  (STO) (001) substrates by pulsed laser deposition (PLD) at the Univ. d'Amiens Jules Verne with the help of H. Bouyanfif. We have already tried different growth conditions, i.e. temperature, gas pressure and distance between target and the substrate, to get good quality thin films. Fig. 6-1 and Fig. 6-2 show the X-ray  $2\theta$ - $\omega$  diffraction of the doped films grown under different conditions. The sharp peaks are from the STO substrate. From Fig. 6-1 it is observed that the (002) reflection of doped BTO forms two broad peaks with an increase of temperature, which probably come from a/c direction of domains. These preliminary results are promising but still, there is a need to further optimize the growth conditions of these doped films.

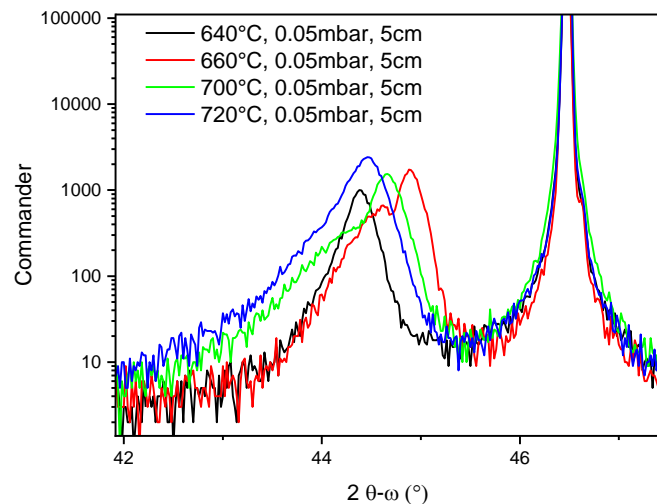


Fig. 6-1 XRD of  $(\text{Co}^{3+}, \text{Nb}^{5+})$  doped BTO thin films grown at different temperatures

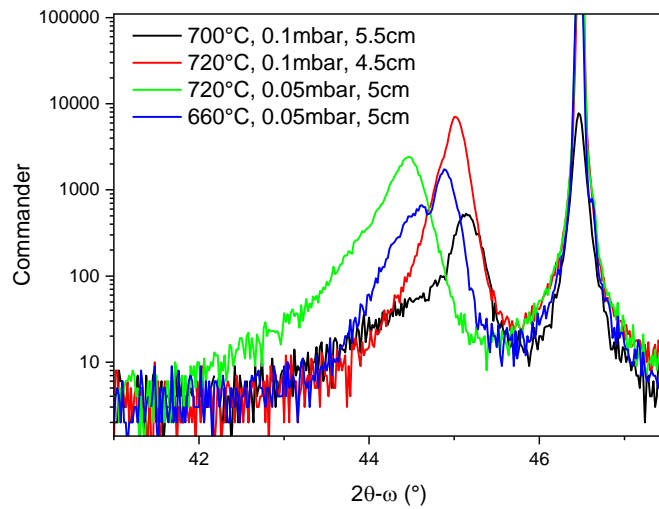


Fig. 6-2 XRD patterns of  $(\text{Co}^{3+}, \text{Nb}^{5+})$  doped BTO thin films grown at different conditions

## 6.2.2 Optical absorption of $(\text{Co}^{3+}, \text{Nb}^{5+})$ co-doped BFO

Because  $\text{BiFeO}_3$  (BFO) is one of the most studied photoferroelectric materials because of its lower bandgap compared to BTO,  $(\text{Co}^{3+}, \text{Nb}^{5+})$  co-doped BFO was also fabricated by the traditional solid-state reaction method, and pure BFO also prepared using the solid-state method. The preliminary results of the absorption are depicted in Fig. 6-3. Further works are still under progress to identify the potential of co-doped BFO materials.

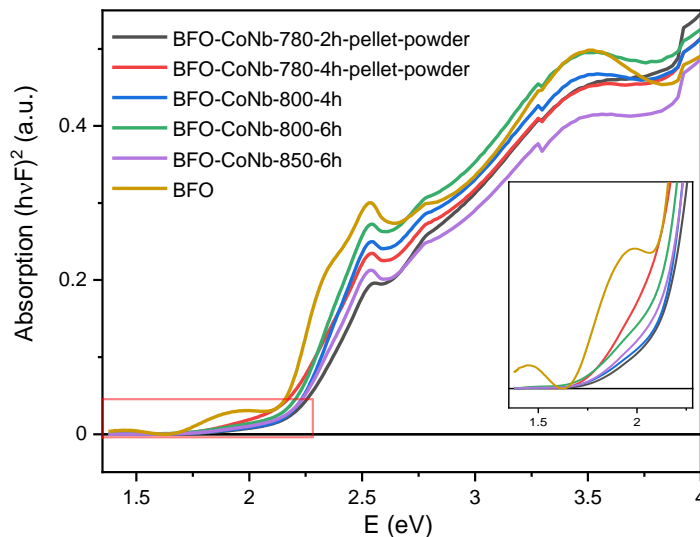


Fig. 6-3 The absorption of pure BFO and  $(\text{Co}^{3+}, \text{Nb}^{5+})$  doped BFO by sintering in different conditions; Inset shows the zoom part of selective in red rectangle

# References

- [1]. Shockley, W., & Queisser, H. J. (1961). Detailed Balance Limit of Efficiency of p-n Junction Solar Cells. *Journal of Applied Physics*, 32(3), 510–519. <https://doi.org/10.1063/1.1736034>
- [2]. Rühle, S. (2016). Tabulated values of the Shockley–Queisser limit for single junction solar cells. *Solar Energy*, 130, 139–147. <https://doi.org/10.1016/j.solener.2016.02.015>
- [3]. Geisz, J. F., France, R. M., Schulte, K. L., Steiner, M. A., Norman, A. G., Guthrey, H. L., Young, M. R., Song, T., & Moriarty, T. (2020). Six-junction III–V solar cells with 47.1% conversion efficiency under 143 Suns concentration. *Nature Energy*, 5(4), 326–335. <https://doi.org/10.1038/s41560-020-0598-5>
- [4]. Rao, A., & Friend, R. H. (2017). Harnessing singlet exciton fission to break the Shockley–Queisser limit. *Nature Reviews Materials*, 2(11), 17063. <https://doi.org/10.1038/natrevmats.2017.63>
- [5]. Lines, M. E., & Glass, A. M. (2001). *Principles and applications of ferroelectrics and related materials*. Oxford university press.
- [6]. Chandra, P., & Littlewood, P. B. (2007). A Landau primer for ferroelectrics. *Physics of Ferroelectrics*, 69–116.
- [7]. Casella, L., & Zaccone, A. (2021). Soft mode theory of ferroelectric phase transitions in the low-temperature phase. *Journal of Physics: Condensed Matter*, 33(16), 165401. <https://doi.org/10.1088/1361-648x/abdb68>
- [8]. Lejman, M., Vaudel, G., Infante, I. C., Chaban, I., Pezeril, T., Edely, M., Nataf, G. F., Guennou, M., Kreisel, J., Gusev, V. E., & others. (2016). Ultrafast acousto-optic mode conversion in optically birefringent ferroelectrics. *Nature Communications*, 7(1), 1–10. <https://doi.org/10.1038/ncomms12345>
- [9]. Lopez-Varo, P., Bertoluzzi, L., Bisquert, J., Alexe, M., Coll, M., Huang, J., Jimenez-Tejada, J. A., Kirchartz, T., Nechache, R., Rosei, F., & Yuan, Y. (2016). Physical aspects of ferroelectric semiconductors for photovoltaic solar energy conversion. *Physics Reports*, 653(August), 1–40. <https://doi.org/10.1016/j.physrep.2016.07.006>
- [10]. Paillard, C., Bai, X., Infante, I. C., Guennou, M., Geneste, G., Alexe, M., Kreisel, J., & Dkhil, B. (2016). Photovoltaics with ferroelectrics: Current status and beyond. *Advanced Materials*, 28(26), 5153–5168. <https://doi.org/10.1002/adma.201505215>
- [11]. Sando, D., Yang, Y., Paillard, C., Dkhil, B., Bellaiche, L., & Nagarajan, V. (2018). Epitaxial

- ferroelectric oxide thin films for optical applications. *Applied Physics Reviews*, 5(4), 41108. <https://doi.org/10.1063/1.5046559>
- [12]. Yang, S. Y., Seidel, J., Byrnes, S. J., Shafer, P., Yang, C.-H., Rossell, M. D., Yu, P., Chu, Y.-H., Scott, J. F., Ager, J. W., & others. (2010). Above-bandgap voltages from ferroelectric photovoltaic devices. *Nature Nanotechnology*, 5(2), 143–147. <https://doi.org/10.1038/nnano.2009.451>
- [13]. Fang, L., You, L., Zhou, Y., Ren, P., Shih Lim, Z., & Wang, J. (2014). Switchable photovoltaic response from polarization modulated interfaces in BiFeO<sub>3</sub> thin films. *Applied Physics Letters*, 104(14), 142903. <https://doi.org/10.1063/1.4870972>
- [14]. Pal, S., Swain, A. B., Biswas, P. P., Murali, D., Pal, A., Nanda, B. R. K., & Murugavel, P. (2018). Giant photovoltaic response in band engineered ferroelectric perovskite. *Scientific Reports*, 8(1), 1–7. <https://doi.org/10.1038/s41598-018-26205-x>
- [15]. Lee, D., Baek, S. H., Kim, T. H., Yoon, J.-G., Folkman, C. M., Eom, C. B., & Noh, T. W. (2011). Polarity control of carrier injection at ferroelectric/metal interfaces for electrically switchable diode and photovoltaic effects. *Physical Review B*, 84(12), 125305. <https://doi.org/10.1103/PhysRevB.84.125305>
- [16]. Mukherjee, S., Phuyal, D., Segre, C. U., Das, S., Karis, O., Edvinsson, T., & Rensmo, H. (2021). Structure and Electronic Effects from Mn and Nb Co-doping for Low Band Gap BaTiO<sub>3</sub> Ferroelectrics. *Journal of Physical Chemistry C*, 125(27), 14910–14923. <https://doi.org/10.1021/acs.jpcc.1c02539>
- [17]. Fan, Z., Sun, K., & Wang, J. (2015). Perovskites for photovoltaics: a combined review of organic–inorganic halide perovskites and ferroelectric oxide perovskites. *Journal of Materials Chemistry A*, 3(37), 18809–18828. <https://doi.org/10.1039/c5ta04235f>
- [18]. Chynoweth, A. G. (1956). Surface Space-Charge Layers in Barium Titanate. *Physical Review*, 102(3), 705–714. <https://doi.org/10.1103/PhysRev.102.705>
- [19]. Glass, A. M., der Linde, D., Auston, D. H., & Negran, T. J. (1975). Excited state polarization, bulk photovoltaic effect and the photorefractive effect in electrically polarized media. *Journal of Electronic Materials*, 4(5), 915–943. <https://doi.org/10.1007/BF02660180>
- [20]. Sturman, B. I., Fridkin, V. M., & Bradley, J. E. S. (2021). *The photovoltaic and photorefractive effects in noncentrosymmetric materials*. Routledge.
- [21]. Zenkevich, A., Matveyev, Y., Maksimova, K., Gaynutdinov, R., Tolstikhina, A., & Fridkin, V. (2014). Giant bulk photovoltaic effect in thin ferroelectric BaTiO<sub>3</sub> films. *Physical Review B*, 90(16), 161409. <https://doi.org/10.1103/PhysRevB.90.161409>
- [22]. Glass, A. M., Von Der Linde, D., & Negran, T. J. (1974). High-voltage bulk photovoltaic effect and the photorefractive process in LiNbO<sub>3</sub>. *Applied Physics Letters*, 25(4), 233–235.

- <https://doi.org/10.1063/1.1655453>
- [23]. Spanier, J. E., Fridkin, V. M., Rappe, A. M., Akbashev, A. R., Polemi, A., Qi, Y., Gu, Z., Young, S. M., Hawley, C. J., Imbrenda, D., Xiao, G., Bennett-Jackson, A. L., & Johnson, C. L. (2016). Power conversion efficiency exceeding the Shockley–Queisser limit in a ferroelectric insulator. *Nature Photonics*, *10*(9), 611–616. <https://doi.org/10.1038/nphoton.2016.143>
- [24]. Ji, W., Yao, K., & Liang, Y. C. (2011). Evidence of bulk photovoltaic effect and large tensor coefficient in ferroelectric BiFeO<sub>3</sub> thin films. *Physical Review B*, *84*(9), 94115. <https://doi.org/10.1103/PhysRevB.84.094115>
- [25]. Fridkin, V. M. (2001). Bulk photovoltaic effect in noncentrosymmetric crystals. *Crystallography Reports*, *46*(4), 654–658. <https://doi.org/10.1134/1.1387133>
- [26]. Moubah, R., Rousseau, O., Colson, D., Artemenko, A., Maglione, M., & Viret, M. (2012). Photoelectric effects in single domain BiFeO<sub>3</sub> crystals. *Advanced Functional Materials*, *22*(22), 4814–4818. <https://doi.org/10.1002/adfm.201201150>
- [27]. Meyer, B., & Vanderbilt, D. (2002). Ab initio study of ferroelectric domain walls in PbTiO<sub>3</sub>. *Physical Review B*, *65*(10), 104111. <https://doi.org/10.1103/PhysRevB.65.104111>
- [28]. Seidel, J., Martin, L. W., He, Q., Zhan, Q., Chu, Y.-H., Rother, A., Hawkridge, M. E., Maksymovych, P., Yu, P., Gajek, M. ea, & others. (2009). Conduction at domain walls in oxide multiferroics. *Nature Materials*, *8*(3), 229–234. <https://doi.org/10.1038/nmat2373>
- [29]. Seidel, J., Fu, D., Yang, S.-Y., Alarcón-Lladó, E., Wu, J., Ramesh, R., & Ager III, J. W. (2011). Efficient photovoltaic current generation at ferroelectric domain walls. *Physical Review Letters*, *107*(12), 126805. <https://doi.org/10.1103/PhysRevLett.107.126805>
- [30]. Alexe, M., & Hesse, D. (2011). Tip-enhanced photovoltaic effects in bismuth ferrite. *Nature Communications*, *2*(1), 1–5. <https://doi.org/10.1038/ncomms1261>
- [31]. Alexe, M. (2012). Local mapping of generation and recombination lifetime in BiFeO<sub>3</sub> single crystals by scanning probe photoinduced transient spectroscopy. *Nano Letters*, *12*(5), 2193–2198. <https://doi.org/10.1021/nl300618e>
- [32]. Bhatnagar, A., Chaudhuri, A. R., Kim, Y. H., Hesse, D., & Alexe, M. (2013). Role of domain walls in the abnormal photovoltaic effect in BiFeO<sub>3</sub>. *Nature Communications*, *4*(1), 1–8. <https://doi.org/10.1038/ncomms3835>
- [33]. Choi, T., Lee, S., Choi, Y. J., Kiryukhin, V., & Cheong, S.-W. (2009). Switchable ferroelectric diode and photovoltaic effect in BiFeO<sub>3</sub>. *Science*, *324*(5923), 63–66. <https://doi.org/10.1126/science.1168636>
- [34]. Qin, M., Yao, K., & Liang, Y. C. (2009). Photovoltaic mechanisms in ferroelectric thin films with the effects of the electrodes and interfaces. *Applied Physics Letters*, *95*(2), 22912. <https://doi.org/10.1063/1.3182824>

- [35]. Qin, M., Yao, K., Liang, Y. C., & Shannigrahi, S. (2007). Thickness effects on photoinduced current in ferroelectric  $(\text{Pb}_{0.97}\text{La}_{0.03})(\text{Zr}_{0.52}\text{Ti}_{0.48})\text{O}_3$  thin films. *Journal of Applied Physics*, *101*(1), 14104. <https://doi.org/10.1063/1.2405732>
- [36]. Yao, K., Gan, B. K., Chen, M., & Shannigrahi, S. (2005). Large photo-induced voltage in a ferroelectric thin film with in-plane polarization. *Applied Physics Letters*, *87*(21), 212906. <https://doi.org/10.1063/1.2136228>
- [37]. Ge, C., Jin, K.-J., Wang, C., Lu, H.-B., Wang, C., & Yang, G.-Z. (2011). Numerical investigation into the switchable diode effect in metal-ferroelectric-metal structures. *Applied Physics Letters*, *99*(6), 63509. <https://doi.org/10.1063/1.3624849>
- [38]. Fan, Z., Ji, W., Li, T., Xiao, J., Yang, P., Ong, K. P., Zeng, K., Yao, K., & Wang, J. (2015). Enhanced photovoltaic effects and switchable conduction behavior in  $\text{BiFe}_{0.6}\text{Sc}_{0.4}\text{O}_3$  thin films. *Acta Materialia*, *88*, 83–90. <https://doi.org/10.1016/j.actamat.2015.01.021>
- [39]. Yi, H. T., Choi, T., Choi, S. G., Oh, Y. S., & Cheong, S.-W. (2011). Mechanism of the switchable photovoltaic effect in ferroelectric  $\text{BiFeO}_3$ . *Advanced Materials*, *23*(30), 3403–3407. <https://doi.org/10.1002/adma.201100805>
- [40]. Yuan, G.-L., & Wang, J. (2009). Evidences for the depletion region induced by the polarization of ferroelectric semiconductors. *Applied Physics Letters*, *95*(25), 252904. <https://doi.org/10.1063/1.3268783>
- [41]. Xing, J., Jin, K.-J., Lu, H., He, M., Liu, G., Qiu, J., & Yang, G. (2008). Photovoltaic effects and its oxygen content dependence in  $\text{BaTiO}_{3-\delta}/\text{Si}$  heterojunctions. *Applied Physics Letters*, *92*(7), 71113. <https://doi.org/10.1063/1.2884320>
- [42]. Yang, C.-H., Seidel, J., Kim, S. Y., Rossen, P. B., Yu, P., Gajek, M., Chu, Y.-H., Martin, L. W., Holcomb, M. B., He, Q., & others. (2009). Electric modulation of conduction in multiferroic Ca-doped  $\text{BiFeO}_3$  films. *Nature Materials*, *8*(6), 485–493. <https://doi.org/10.1038/nmat2432>
- [43]. Qin, M., Yao, K., & Liang, Y. C. (2008). High efficient photovoltaics in nanoscaled ferroelectric thin films. *Applied Physics Letters*, *93*(12), 122904. <https://doi.org/10.1063/1.2990754>
- [44]. Chen, G., Zou, K., Yu, Y., Zhang, Y., Zhang, Q., Lu, Y., & He, Y. (2020). Effects of the film thickness and poling electric field on photovoltaic performances of  $(\text{Pb},\text{La})(\text{Zr},\text{Ti})\text{O}_3$  ferroelectric thin film-based devices. *Ceramics International*, *46*(4), 4148–4153. <https://doi.org/10.1016/j.ceramint.2019.10.131>
- [45]. Cui, X., Li, Y., Li, X., & Hao, X. (2020). Enhanced photovoltaic effect in  $\text{Bi}_2\text{FeMo}_{0.7}\text{Ni}_{0.3}\text{O}_6$  ferroelectric thin films by tuning the thickness. *Journal of Materials Chemistry C*, *8*(4), 1359–1365. <https://doi.org/10.1039/C9TC04973H>

- [46]. Fan, Z., Yao, K., & Wang, J. (2014). Photovoltaic effect in an indium-tin-oxide/ZnO/BiFeO<sub>3</sub>/Pt heterostructure. *Applied Physics Letters*, 105(16), 162903. <https://doi.org/10.1063/1.4899146>
- [47]. Zhang, Y., Yang, L., Zhang, Y., Ding, Z., Wu, M., Zhou, Y., Diao, C., Zheng, H., Wang, X., & Lin Wang, Z. (2020). Enhanced Photovoltaic Performances of La-Doped Bismuth Ferrite/Zinc Oxide Heterojunction by Coupling Piezo-Phototronic Effect and Ferroelectricity. *ACS Nano*, 14(8), 10723–10732. <https://doi.org/10.1021/acsnano.0c05398>
- [48]. Zhang, J., Su, X., Shen, M., Dai, Z., Zhang, L., He, X., Cheng, W., Cao, M., & Zou, G. (2013). Enlarging photovoltaic effect: combination of classic photoelectric and ferroelectric photovoltaic effects. *Scientific Reports*, 3(1), 2109. <https://doi.org/10.1038/srep02109>
- [49]. Zheng, F., Zhang, P., Wang, X., Huang, W., Zhang, J., Shen, M., Dong, W., Fang, L., Bai, Y., Shen, X., Sun, H., & Hao, J. (2014). Photovoltaic enhancement due to surface-plasmon assisted visible-light absorption at the artificial surface of lead zirconate–titanate film. *Nanoscale*, 6(5), 2915–2921. <https://doi.org/10.1039/C3NR05757G>
- [50]. Zheng, F., Xin, Y., Huang, W., Zhang, J., Wang, X., Shen, M., Dong, W., Fang, L., Bai, Y., Shen, X., & Hao, J. (2014). Above 1% efficiency of a ferroelectric solar cell based on the Pb(Zr,Ti)O<sub>3</sub> film. *Journal of Materials Chemistry A*, 2(5), 1363–1368. <https://doi.org/10.1039/C3TA13724D>
- [51]. Yan, J.-M., Wang, K., Xu, Z.-X., Ying, J.-S., Chen, T.-W., Yuan, G.-L., Zhang, T., Zheng, H.-W., Chai, Y., & Zheng, R.-K. (2021). Large ferroelectric-polarization-modulated photovoltaic effects in bismuth layered multiferroic/semiconductor heterostructure devices. *Journal of Materials Chemistry C*, 9(9), 3287–3294. <https://doi.org/10.1039/D0TC05638C>
- [52]. Afzal, A. M., Javed, Y., Hussain, S., Ali, A., Yaqoob, M. Z., & Mumtaz, S. (2020). Enhancement in photovoltaic properties of bismuth ferrite/zinc oxide heterostructure solar cell device with graphene/indium tin oxide hybrid electrodes. *Ceramics International*, 46(7), 9161–9169. <https://doi.org/10.1016/j.ceramint.2019.12.166>
- [53]. Zhang, Y., Su, H., Li, H., Xie, Z., Zhang, Y., Zhou, Y., Yang, L., Lu, H., Yuan, G., & Zheng, H. (2021). Enhanced photovoltaic-pyroelectric coupled effect of BiFeO<sub>3</sub>/Au/ZnO heterostructures. *Nano Energy*, 85, 105968. <https://doi.org/10.1016/j.nanoen.2021.105968>
- [54]. Renuka, H., Joshna, P., Wani, W. A., Venkataraman, B. H., Ramaswamy, K., & Kundu, S. (2020). Plasmonic gold nanorods mediated p-BFCrO/n-rGO heterojunction in realizing efficient ferroelectric photovoltaic devices. *Materials Science in Semiconductor Processing*, 109, 104937. <https://doi.org/10.1016/j.mssp.2020.104937>
- [55]. Lu, Y., Fan, Z., Liang, F., Yang, Z., Z., T. L., Zeyu, Z., Guohong, M., Daniel, S., Andrivo, R., Le,

- W., Lei, C., M., R. A., & Junling, W. (2021). Enhancing ferroelectric photovoltaic effect by polar order engineering. *Science Advances*, 4(7), eaat3438. <https://doi.org/10.1126/sciadv.aat3438>
- [56]. Yang, H., Fred, F., Zhizhong, C., Adam, P. W., A., S. M., Zhe, Z., Yuwei, G., Ryan, H., Jie, J., Jing, F., Lifu, Z., Baiwei, W., Yiping, W., Daniel, G., F., P. E., Zonghuan, L., Xin, S., Toh-Ming, L., Hua, Z., ... Jian, S. (2021). A chiral switchable photovoltaic ferroelectric 1D perovskite. *Science Advances*, 6(9), eaay4213. <https://doi.org/10.1126/sciadv.aay4213>
- [57]. Luo, Z., Yang, M., Liu, Y., & Alexe, M. (2021). Emerging Opportunities for 2D Semiconductor/Ferroelectric Transistor-Structure Devices. *Advanced Materials*, 33(12), 2005620. <https://doi.org/10.1002/adma.202005620>
- [58]. Li, H., Li, F., Shen, Z., Han, S.-T., Chen, J., Dong, C., Chen, C., Zhou, Y., & Wang, M. (2021). Photoferroelectric perovskite solar cells: Principles, advances and insights. *Nano Today*, 37, 101062. <https://doi.org/10.1016/j.nantod.2020.101062>
- [59]. Kim, D. J., Lu, H., Ryu, S., Bark, C. W., Eom, C. B., Tsymbal, E. Y., & Gruverman, A. (2012). Ferroelectric tunnel memristor. In *Nano Letters* (Vol. 12, Issue 11, pp. 5697–5702). <https://doi.org/10.1021/nl302912t>
- [60]. Guo, R., You, L., Zhou, Y., Shih Lim, Z., Zou, X., Chen, L., Ramesh, R., & Wang, J. (2013). Non-volatile memory based on the ferroelectric photovoltaic effect. *Nature Communications*, 4(1), 1990. <https://doi.org/10.1038/ncomms2990>
- [61]. Kundys, D., Cascales, A., Makhort, A. S., Majjad, H., Chevrier, F., Doudin, B., Fedrizzi, A., & Kundys, B. (2020). Optically Rewritable Memory in a Graphene--Ferroelectric-Photovoltaic Heterostructure. *Physical Review Applied*, 13(6), 64034. <https://doi.org/10.1103/PhysRevApplied.13.064034>
- [62]. Cheng, S., Fan, Z., Rao, J., Hong, L., Huang, Q., Tao, R., Hou, Z., Qin, M., Zeng, M., Lu, X., Zhou, G., Yuan, G., Gao, X., & Liu, J.-M. (2020). Highly Controllable and Silicon-Compatible Ferroelectric Photovoltaic Synapses for Neuromorphic Computing. *IScience*, 23(12), 101874. <https://doi.org/10.1016/j.isci.2020.101874>
- [63]. Kundys, B., Viret, M., Colson, D., & Kundys, D. O. (2010). Light-induced size changes in BiFeO<sub>3</sub> crystals. *Nature Materials*, 9(10), 803–805. <https://doi.org/10.1038/nmat2807>
- [64]. Kundys, B. (2015). Photostrictive materials. *Applied Physics Reviews*, 2(1), 11301. <https://doi.org/10.1063/1.4905505>
- [65]. Cui, Y., Briscoe, J., & Dunn, S. (2013). Effect of Ferroelectricity on Solar-Light-Driven Photocatalytic Activity of BaTiO<sub>3</sub>-Influence on the Carrier Separation and Stern Layer Formation. *Chemistry of Materials*, 25(21), 4215–4223. <https://doi.org/10.1021/cm402092f>

- [66]. Guo, L., Zhong, C., Cao, J., Hao, Y., Lei, M., Bi, K., Sun, Q., & Wang, Z. L. (2019). Enhanced photocatalytic H<sub>2</sub> evolution by plasmonic and piezotronic effects based on periodic Al/BaTiO<sub>3</sub> heterostructures. *Nano Energy*, 62, 513–520. <https://doi.org/10.1016/j.nanoen.2019.05.067>
- [67]. Sun, B., Guo, T., Zhou, G., Ranjan, S., Jiao, Y., Wei, L., Zhou, Y. N., & Wu, Y. A. (2021). Synaptic devices based neuromorphic computing applications in artificial intelligence. *Materials Today Physics*, 18, 100393. <https://doi.org/10.1016/j.mtphys.2021.100393>
- [68]. Wu, L., Podpirka, A., Spanier, J. E., & Davies, P. K. (2019). Ferroelectric, Optical, and Photovoltaic Properties of Morphotropic Phase Boundary Compositions in the PbTiO<sub>3</sub>–BiFeO<sub>3</sub>–Bi(Ni<sub>1/2</sub>Ti<sub>1/2</sub>)O<sub>3</sub> System. *Chemistry of Materials*, 31(11), 4184–4194. <https://doi.org/10.1021/acs.chemmater.9b00996>
- [69]. Pal, S., Swain, A. B., Biswas, P. P., & Murugavel, P. (2020). Linear bulk photovoltaic effect and phenomenological study in multi-phase co-existing ferroelectric system. *Journal of Physics: Condensed Matter*, 32(48), 485701. <https://doi.org/10.1088/1361-648x/abac23>
- [70]. Pal, S., Muthukrishnan, S., Sadhukhan, B., N. V., S., Murali, D., & Murugavel, P. (2021). Bulk photovoltaic effect in BaTiO<sub>3</sub>-based ferroelectric oxides: An experimental and theoretical study. *Journal of Applied Physics*, 129(8), 084106. <https://doi.org/10.1063/5.0036488>
- [71]. Alkathy, M. S., Eiras, J. A., & Raju, K. C. J. (2021). Energy storage enhancement and bandgap narrowing of lanthanum and sodium co-substituted BaTiO<sub>3</sub> ceramics. *Ferroelectrics*, 570(1), 153–161. <https://doi.org/10.1080/00150193.2020.1839266>
- [72]. Alkathy, M. S., Eiras, J. A., Zabotto, F. L., & Raju, K. C. J. (2021). Structural, optical, dielectric, and multiferroic properties of sodium and nickel co-substituted barium titanate ceramics. *Journal of Materials Science: Materials in Electronics*, 32(10), 12828–12840. <https://doi.org/10.1007/s10854-020-03900-y>
- [73]. Yang, F., Lin, S., Yang, L., Liao, J., Chen, Y., & Wang, C.-Z. (2017). First-principles investigation of metal-doped cubic BaTiO<sub>3</sub>. *Materials Research Bulletin*, 96, 372–378. <https://doi.org/10.1016/j.materresbull.2017.03.023>
- [74]. Noguchi, Y., Taniguchi, Y., Inoue, R., & Miyayama, M. (2020). Successive redox-mediated visible-light ferrophotovoltaics. *Nature Communications*, 11(1), 966. <https://doi.org/10.1038/s41467-020-14763-6>
- [75]. Wang, J., Huang, Y., Guo, W., Xing, Z., Wang, H., Lu, Z., & Zhang, Z. (2021). First-principles calculations of electronic and optical properties of A and B site substituted BaTiO<sub>3</sub>. *Vacuum*, 110530. <https://doi.org/10.1016/j.vacuum.2021.110530>
- [76]. Matsuo, H., Noguchi, Y., & Miyayama, M. (2017). Gap-state engineering of visible-light-active ferroelectrics for photovoltaic applications. *Nature Communications*, 8(1), 1–8.

- <https://doi.org/10.1038/s41467-017-00245-9>
- [77]. Amaechi, I. C., Kolhatkar, G., Youssef, A. H., Rawach, D., Sun, S., & Ruediger, A. (2019). B-site modified photoferroic Cr<sup>3+</sup>-doped barium titanate nanoparticles: microwave-assisted hydrothermal synthesis, photocatalytic and electrochemical properties. *RSC Advances*, *9*(36), 20806–20817. <https://doi.org/10.1039/c9ra03439>
- [78]. Kola, L., Murali, D., Pal, S., Nanda, B. R. K., & Murugavel, P. (2019). Enhanced bulk photovoltaic response in Sn doped BaTiO<sub>3</sub> through composition dependent structural transformation. *Applied Physics Letters*, *114*(18), 183901. <https://doi.org/10.1063/1.5088635>
- [79]. Gupta, R., Bokolia, R., Verma, V., & others. (2021). Improvement in photovoltaic response of bismuth ferrite by tuning its ferroelectric and bandgap properties. *Journal of Materials Science: Materials in Electronics*, *32*(2), 1570–1581. <https://doi.org/10.1007/s10854-020-04925-z>
- [80]. Yan, T.-L., Chen, B., Liu, G., Niu, R.-P., Shang, J., Gao, S., Xue, W.-H., Jin, J., Yang, J.-R., & Li, R.-W. (2017). Improved photovoltaic effects in Mn-doped BiFeO<sub>3</sub> ferroelectric thin films through band gap engineering. *Chinese Physics B*, *26*(6), 67702. <https://doi.org/10.1088/1674-1056/26/6/067702>
- [81]. Khomskii, D. I. (2006). Multiferroics: Different ways to combine magnetism and ferroelectricity. *Journal of Magnetism and Magnetic Materials*, *306*(1), 1–8. <https://doi.org/10.1016/j.jmmm.2006.01.238>
- [82]. Cao, J., Ji, Y., Tian, C., & Yi, Z. (2014). Synthesis and enhancement of visible light activities of nitrogen-doped BaTiO<sub>3</sub>. *Journal of Alloys and Compounds*, *615*, 243–248. <https://doi.org/10.1016/j.jallcom.2014.07.008>
- [83]. Long, P., Chen, C., Pang, D., Liu, X., & Yi, Z. (2019). Optical, electrical, and photoelectric properties of nitrogen-doped perovskite ferroelectric BaTiO<sub>3</sub> ceramics. *Journal of the American Ceramic Society*, *102*(4), 1741–1747. <https://doi.org/10.1111/jace.16026>
- [84]. Das, S., Ghara, S., Mahadevan, P., Sundaresan, A., Gopalakrishnan, J., & Sarma, D. D. (2018). Designing a lower band gap bulk ferroelectric material with a sizable polarization at room temperature. *ACS Energy Letters*, *3*(5), 1176–1182. <https://doi.org/10.1021/acsenergylett.8b00492>
- [85]. Lou, Q., Zeng, J., Man, Z., Zheng, L., Park, C., Kassiba, A., Liu, Y., Chen, X., & Li, G. (2019). The effect of grain boundary on the visible light absorption of BaTi<sub>1-x</sub>[Ni<sub>1/2</sub>Nb<sub>1/2</sub>]<sub>x</sub>O<sub>3-δ</sub> ferroelectric ceramics. *Journal of the American Ceramic Society*, *102*(12), 7405–7413. <https://doi.org/10.1111/jace.16643>
- [86]. Zheng, D., Deng, H., Si, S., Pan, Y., Zhang, Q., Guo, Y., Yang, P., & Chu, J. (2020). Modified

- structural, optical, magnetic and ferroelectric properties in  $(1-x)\text{BaTiO}_3-x\text{BaCo}_{0.5}\text{Nb}_{0.5}\text{O}_{3-6}$  ceramics. *Ceramics International*, *46(5)*, 6073–6078. <https://doi.org/10.1016/j.ceramint.2019.11.068>
- [87]. Wu, L., Akbashev, A. R., Podpirka, A. A., Spanier, J. E., & Davies, P. K. (2019). Infrared-to-ultraviolet light-absorbing  $\text{BaTiO}_3$ -based ferroelectric photovoltaic materials. *Journal of the American Ceramic Society*, *102(7)*, 4188–4199. <https://doi.org/10.1111/jace.16307>
- [88]. Shafir, O., Yang, J., Rappe, A. M., & Grinberg, I. (2019). Ferroelectric barium titanate derivatives containing Mo and Mg for transparent photovoltaic applications. *Journal of Applied Physics*, *126(17)*, 174101. <https://doi.org/10.1063/1.5123675>
- [89]. Nechache, R., Harnagea, C., Li, S., Cardenas, L., Huang, W., Chakrabartty, J., & Rosei, F. (2015). Bandgap tuning of multiferroic oxide solar cells. *Nature Photonics*, *9(1)*, 61–67. <https://doi.org/10.1038/nphoton.2014.255>
- [90]. Li, Y., Cui, X., Sun, N., Du, J., Li, X., Jia, G., & Hao, X. (2019). Region-Dependent and Stable Ferroelectric Photovoltaic Effect Driven by Novel In-Plane Self-Polarization in Narrow-Bandgap  $\text{Bi}_2\text{FeMo}_{0.7}\text{Ni}_{0.3}\text{O}_6$  Thin Film. *Advanced Optical Materials*, *7(3)*, 1801105. <https://doi.org/10.1002/adom.201801105>
- [91]. Weng, B., Xiao, Z., Meng, W., Grice, C. R., Poudel, T., Deng, X., & Yan, Y. (2017). Bandgap Engineering of Barium Bismuth Niobate Double Perovskite for Photoelectrochemical Water Oxidation. *Advanced Energy Materials*, *7(9)*. <https://doi.org/10.1002/aenm.201602260>
- [92]. Gupta, S., Tomar, M., & Gupta, V. (2014). Ferroelectric photovoltaic properties of Ce and Mn codoped  $\text{BiFeO}_3$  thin film. *Journal of Applied Physics*, *115(1)*, 14102. <https://doi.org/10.1063/1.4859575>
- [93]. Pal, P., Rudrapal, K., Maji, P., Roy Chaudhuri, A., & Choudhury, D. (2021). Toward an Enhanced Room-Temperature Photovoltaic Effect in Ferroelectric Bismuth and Iron Codoped  $\text{BaTiO}_3$ . *The Journal of Physical Chemistry C*, *125(9)*, 5315–5326. <https://doi.org/10.1021/acs.jpcc.0c10655>
- [94]. Alkathy, M. S., Lente, M. H., & Eiras, J. A. (2021). Bandgap narrowing of  $\text{Ba}_{0.92}\text{Na}_{0.04}\text{Bi}_{0.04}\text{TiO}_3$  ferroelectric ceramics by transition metals doping for photovoltaic applications. *Materials Chemistry and Physics*, *257(September 2020)*, 123791. <https://doi.org/10.1016/j.matchemphys.2020.123791>
- [95]. Wang, D., Wang, G., Lu, Z., Al-Jlaihawi, Z., & Feteira, A. (2020). Crystal structure, phase transitions and photoferroelectric properties of  $\text{KNbO}_3$ -based lead-free ferroelectric ceramics: A brief review. *Frontiers in Materials*, *7*, 91. <https://doi.org/10.3389/fmats.2020.00091>

- [96]. Pascual-González, C. (2017). *Processing-composition-structure effects on the optical band gap of KNbO<sub>3</sub>-based ceramics*. Sheffield Hallam University (United Kingdom).
- [97]. Bai, Y., Siponkoski, T., Peräntie, J., Jantunen, H., & Juuti, J. (2017). Ferroelectric, pyroelectric, and piezoelectric properties of a photovoltaic perovskite oxide. *Applied Physics Letters*, 110(6), 63903. <https://doi.org/10.1063/1.4974735>
- [98]. Grinberg, I., West, D. V., Torres, M., Gou, G., Stein, D. M., Wu, L., Chen, G., Gallo, E. M., Akbashev, A. R., Davies, P. K., & others. (2013). Perovskite oxides for visible-light-absorbing ferroelectric and photovoltaic materials. *Nature*, 503(7477), 509–512. <https://doi.org/10.1038/nature12622>
- [99]. Zhou, W., Deng, H., Yang, P., & Chu, J. (2014). Structural phase transition, narrow band gap, and room-temperature ferromagnetism in [KNbO<sub>3</sub>]<sub>1-x</sub>[BaNi<sub>1/2</sub>Nb<sub>1/2</sub>O<sub>3-δ</sub>]<sub>x</sub> ferroelectrics. *Applied Physics Letters*, 105(11), 111904. <https://doi.org/10.1063/1.4896317>
- [100]. Guerra, J. D. S., Silva, M. C. O., Silva, A. C., Oliveira, M. A., Mendez-Gonzalez, Y., Monte, A. F. G., M'Peko, J.-C., & Hernandez, A. C. (2020). Structural, electrical and optical properties of (K,Ba)(Nb,Ni)O<sub>3-δ</sub> electroceramics: Oxygen vacancy and grain size effects. *Ceramics International*, 46(12), 20201–20206. <https://doi.org/10.1016/j.ceramint.2020.05.100>
- [101]. Yu, L., Deng, H., Zhou, W., Yang, P., & Chu, J. (2017). Band gap engineering and magnetic switching in a novel perovskite (1-x)KNbO<sub>3</sub>-xBaNb<sub>1/2</sub>Fe<sub>1/2</sub>O<sub>3</sub>. *Materials Letters*, 202, 39–43. <https://doi.org/10.1016/j.matlet.2017.05.077>
- [102]. Yu, L., Jia, J., Yi, G., Shan, Y., & Han, M. (2016). Bandgap tuning of [KNbO<sub>3</sub>]<sub>1-x</sub>[BaCo<sub>1/2</sub>Nb<sub>1/2</sub>O<sub>3-δ</sub>]<sub>x</sub> ferroelectrics. *Materials Letters*, 184, 166–168. <https://doi.org/10.1016/j.matlet.2016.08.044>
- [103]. Liang, Y., & Shao, G. (2019). First principles study for band engineering of KNbO<sub>3</sub> with 3d transition metal substitution. *RSC Advances*, 9(13), 7551–7559. 10.1039/C9RA00289H
- [104]. Pascual-Gonzalez, C., Schileo, G., & Feteira, A. (2016). Band gap narrowing in ferroelectric KNbO<sub>3</sub>-Bi(Yb,Me)O<sub>3</sub> (Me= Fe or Mn) ceramics. *Applied Physics Letters*, 109(13), 132902. <https://doi.org/10.1063/1.4963699>
- [105]. Li, C., Jiang, K., Jiang, J., Hu, Z., Liu, A., Hu, G., Shi, W., & Chu, J. (2020). Enhanced photovoltaic response of lead-free ferroelectric solar cells based on (K,Bi)(Nb,Yb)O<sub>3</sub> films. *Physical Chemistry Chemical Physics*, 22(6), 3691–3701. <https://doi.org/10.1039/C9CP06291B>
- [106]. Elicker, C., Pascual-González, C., Gularte, L. T., Moreira, M. L., Cava, S. S., & Feteira, A. (2018). Photoresponse of KNbO<sub>3</sub>-AFeO<sub>3</sub> (A= Bi<sup>3+</sup> or La<sup>3+</sup>) ceramics and its relationship with bandgap narrowing. *Materials Letters*, 221, 326–329. <https://doi.org/10.1016/j.matlet.2018.03.089>

- [107]. Pascual-Gonzalez, C., Schileo, G., Murakami, S., Khesro, A., Wang, D., Reaney, I. M., & Feteira, A. (2017). Continuously controllable optical band gap in orthorhombic ferroelectric  $\text{KNbO}_3\text{-BiFeO}_3$  ceramics. *Applied Physics Letters*, *110*(17), 172902. <https://doi.org/10.1063/1.4982600>
- [108]. Shafir, O., Bai, Y., Juuti, J., & Grinberg, I. (2020). Visible-Light-Absorbing Potassium Niobate-Titanate-Molybdate Ferroelectrics. *Physical Review Applied*, *14*, 004052. <https://doi.org/10.1103/PhysRevApplied.14.044052>
- [109]. Jiang, Y., Ning, H., & Yu, J. (2018). Optical bandgap tuning of ferroelectric semiconducting  $\text{BiFeO}_3$ -based oxide perovskites via chemical substitution for photovoltaics. *AIP Advances*, *8*(12), 125334. <https://doi.org/10.1063/1.5053634>
- [110]. Liu, H., Chen, J., Jiang, X., Pan, Z., Zhang, L., Rong, Y., Lin, Z., & Xing, X. (2017). Controllable negative thermal expansion, ferroelectric and semiconducting properties in  $\text{PbTiO}_3\text{-Bi}(\text{Co}_{2/3}\text{Nb}_{1/3})\text{O}_3$  solid solutions. *Journal of Materials Chemistry C*, *5*(4), 931–936. <https://doi.org/10.1039/C6TC03939A>
- [111]. Jona, F., & Shirane, G. (1962). *Ferroelectric crystals, international series of monographs on solid state physics*. Pergamon press Oxford, UK:
- [112]. Li, Y., Liu, Q., Yao, T., Pan, Z., Sun, Z., Jiang, Y., Zhang, H., Pan, Z., Yan, W., & Wei, S. (2010). Hexagonal  $\text{BaTi}_{1-x}\text{Co}_x\text{O}_3$  phase stabilized by Co dopants. *Applied Physics Letters*, *96*(9), 91905. <https://doi.org/10.1063/1.3337110>
- [113]. Nayak, S. K., Langhammer, H. T., Adeagbo, W. A., Hergert, W., Mueller, T., & Boettcher, R. (2015). Chromium point defects in hexagonal  $\text{BaTiO}_3$ : A comparative study of first-principles calculations and experiments. *Physical Review B*, *91*(15), 155105. <https://doi.org/10.1103/PhysRevB.91.155105>
- [114]. Dang, N. V., Phan, T.-L., Thanh, T. D., Lam, V. D., & Hong, L. V. (2012). Structural phase separation and optical and magnetic properties of  $\text{BaTi}_{1-x}\text{Mn}_x\text{O}_3$  multiferroics. *Journal of Applied Physics*, *111*(11), 113913. <https://doi.org/10.1063/1.4725195>
- [115]. Nguyen, H. M., Dang, N. V., Chuang, P.-Y., Thanh, T. D., Hu, C.-W., Chen, T.-Y., Lam, V. D., Lee, C.-H., & Hong, L. V. (2011). Tetragonal and hexagonal polymorphs of  $\text{BaTi}_{1-x}\text{Fe}_x\text{O}_{3-\delta}$  multiferroics using x-ray and Raman analyses. *Applied Physics Letters*, *99*(20), 202501. <https://doi.org/10.1063/1.3662389>
- [116]. Venkateswaran, U. D., Naik, V. M., & Naik, R. (1998). High-pressure Raman studies of polycrystalline  $\text{BaTiO}_3$ . *Physical Review B*, *58*(21), 14256–14260. <https://doi.org/10.1103/PhysRevB.58.14256>
- [117]. Pokorný, J., Pasha, U. M., Ben, L., Thakur, O. P., Sinclair, D. C., & Reaney, I. M. (2011). Use of Raman spectroscopy to determine the site occupancy of dopants in  $\text{BaTiO}_3$ . *Journal of*

- Applied Physics*, 109(11), 114110. <https://doi.org/10.1063/1.3592192>
- [118]. Veerapandiyan, V. K., Khosravi, S., Canu, G., Feteira, A., Buscaglia, V., Reichmann, K., & Deluca, M. (2020). B-site vacancy induced Raman scattering in BaTiO<sub>3</sub>-based ferroelectric ceramics. *Journal of the European Ceramic Society*, 40(13), 4684–4688. <https://doi.org/10.1016/j.jeurceramsoc.2020.05.051>
- [119]. Sati, A., Pokhriyal, P., Kumar, A., Anwar, S., Sagdeo, A., Lalla, N. P., & Sagdeo, P. R. (2021). Origin of ferroelectricity in cubic phase of Hf substituted BaTiO<sub>3</sub>. *Journal of Physics: Condensed Matter*, 33(16), 165403. <https://doi.org/10.1088/1361-648x/abf0bf>
- [120]. Maldonado-Orozco, M. C., Ochoa-Lara, M. T., Sosa-Márquez, J. E., Talamantes-Soto, R. P., Hurtado-Macías, A., López Antón, R., González, J. A., Holguín-Momaca, J. T., Olive-Méndez, S. F., & Espinosa-Magaña, F. (2019). Absence of ferromagnetism in ferroelectric Mn-doped BaTiO<sub>3</sub> nanofibers. *Journal of the American Ceramic Society*, 102(5), 2800–2809. <https://doi.org/10.1111/jace.16179>
- [121]. Philips-Invernizzi, B., Dupont, D., & Caze, C. (2001). Bibliographical review for reflectance of diffusing media. *Optical Engineering*, 40(6), 1082–1092. <https://doi.org/10.1117/1.1370387>
- [122]. Wemple, S. H. (1970). Polarization Fluctuations and the Optical-Absorption Edge in BaTiO<sub>3</sub>. *Physical Review B*, 2(7), 2679. <https://link.aps.org/doi/10.1103/PhysRevB.2.2679>
- [123]. Tauc, J., Grigorovici, R., & Vancu, A. (1966). Optical Properties and Electronic Structure of Amorphous Germanium. *Physica Status Solidi (B)*, 15(2), 627–637. <https://doi.org/10.1002/pssb.19660150224>
- [124]. Ismail, M. M. (2019). Ferroelectric characteristics of Fe/Nb co-doped BaTiO<sub>3</sub>. *Modern Physics Letters B*, 33(22), 1950261. <https://doi.org/10.1142/S0217984919502610>
- [125]. Li, J., Lv, J., Zhang, D., Zhang, L., Hao, X., Wu, M., Xu, B.-X., Otonicar, M., Lookman, T., & Dkhil, B. (2021). Doping-induced Polar Defects Improve the Electrocaloric Performance of Ba<sub>0.9</sub>Sr<sub>0.1</sub>Hf<sub>0.1</sub>Ti<sub>0.9</sub>O<sub>3</sub>. *Physical Review Applied*, 16(1), 14033. <https://doi.org/10.1103/PhysRevApplied.16.014033>
- [126]. Varshni, Y. P. (1967). Temperature dependence of the energy gap in semiconductors. *Physica*, 34(1), 149–154. [https://doi.org/10.1016/0031-8914\(67\)90062-6](https://doi.org/10.1016/0031-8914(67)90062-6)
- [127]. Rödel, J., Webber, K. G., Dittmer, R., Jo, W., Kimura, M., & Damjanovic, D. (2015). Transferring lead-free piezoelectric ceramics into application. *Journal of the European Ceramic Society*, 35(6), 1659–1681. <https://doi.org/10.1016/j.jeurceramsoc.2014.12.013>
- [128]. Acosta, M., Novak, N., Rojas, V., Patel, S., Vaish, R., Koruza, J., Rossetti Jr, G. A., & Rödel, J. (2017). BaTiO<sub>3</sub>-based piezoelectrics: Fundamentals, current status, and perspectives. *Applied Physics Reviews*, 4(4), 41305. <https://doi.org/10.1063/1.4990046>

- [129]. Verma, K. C., & Kotnala, R. K. (2016). Multiferroic approach for Cr, Mn, Fe, Co, Ni, Cu substituted BaTiO<sub>3</sub> nanoparticles. *Materials Research Express*, 3(5), 55006. <https://doi.org/10.1088/2053-1591/3/5/055006>
- [130]. Liu, W., & Ren, X. (2009). Large piezoelectric effect in Pb-free ceramics. *Physical Review Letters*, 103(25), 257602. <https://doi.org/10.1103/PhysRevLett.103.257602>
- [131]. Ismail, F. A., Osman, R. A. M., & Idris, M. S. (2016). Review on dielectric properties of rare earth doped barium titanate. *AIP Conference Proceedings*, 1756(1), 90005. <https://doi.org/10.1063/1.4958786%0A>
- [132]. Boujelben, F., Khemakhem, H., & Simon, A. (2012). Effect of Mn and Nb Doped BaTiO<sub>3</sub> in the Dielectric Properties in the Ba(Mn<sub>1/2</sub>Nb<sub>1/2</sub>)<sub>x</sub>Ti<sub>1-x</sub>O<sub>3</sub>. *Journal of Electronic Materials*, 41(8), 2250–2255. <https://doi.org/10.1007/s11664-012-2027-4>
- [133]. Chang, C.-Y., Huang, C.-Y., Wu, Y.-C., Su, C.-Y., & Huang, C.-L. (2010). Synthesis of submicron BaTiO<sub>3</sub> particles by modified solid-state reaction method. *Journal of Alloys and Compounds*, 495(1), 108–112. <https://doi.org/10.1016/j.jallcom.2010.01.096>
- [134]. Chen, G., Peng, X., Fu, C., Cai, W., Gao, R., Fan, P., Yi, X., Yang, H., Ji, C., & Yong, H. (2018). Effects of sintering method and BiFeO<sub>3</sub> dopant on the dielectric and ferroelectric properties of BaTiO<sub>3</sub>–BiYbO<sub>3</sub> based solid solution ceramics. *Ceramics International*, 44(14), 16880–16889. <https://doi.org/10.1016/j.ceramint.2018.06.126>
- [135]. Ghayour, H., & Abdellahi, M. (2016). A brief review of the effect of grain size variation on the electrical properties of BaTiO<sub>3</sub>-based ceramics. *Powder Technology*, 292, 84–93. <https://doi.org/10.1016/j.powtec.2016.01.030>
- [136]. Chen, G., Chen, J., Pei, W., Lu, Y., Zhang, Q., Zhang, Q., & He, Y. (2019). Bismuth ferrite materials for solar cells: Current status and prospects. *Materials Research Bulletin*, 110, 39–49. <https://doi.org/10.1016/j.materresbull.2018.10.011>
- [137]. Yang, M.-M., Luo, Z.-D., Kim, D. J., & Alexe, M. (2017). Bulk photovoltaic effect in monodomain BiFeO<sub>3</sub> thin films. *Applied Physics Letters*, 110(18), 183902. <https://doi.org/10.1063/1.4983032>
- [138]. Semenov, A., Dedyk, A., Mylnikov, I., Pakhomov, O., Es'kov, A., Anokhin, A., Krylov, V., Burovikhin, A., Pavlova, Y., & Tselev, A. (2019). Mn-Doped BaTiO<sub>3</sub> Ceramics: Thermal and Electrical Properties for Multicaloric Applications. *Materials*, 12(21), 3592. <https://doi.org/10.3390/ma12213592>
- [139]. Ren, X. (2004). Large electric-field-induced strain in ferroelectric crystals by point-defect-mediated reversible domain switching. *Nature Materials*, 3(2), 91–94. <https://doi.org/10.1038/nmat1051>
- [140]. Swain, A. B., Murali, D., Nanda, B. R. K., & Murugavel, P. (2019). Large Bulk Photovoltaic

- Response by Symmetry-Breaking Structural Transformation in Ferroelectric  $[\text{Ba}(\text{Zr}_{0.2}\text{Ti}_{0.8})\text{O}_3]_{0.5}[(\text{Ba}_{0.7}\text{Ca}_{0.3})\text{TiO}_3]_{0.5}$ . *Physical Review Applied*, 11(4), 44007. <https://doi.org/10.1103/PhysRevApplied.11.044007>
- [141]. Liang, L., Li, Y. L., Chen, L.-Q., Hu, S. Y., & Lu, G.-H. (2009). Thermodynamics and ferroelectric properties of  $\text{KNbO}_3$ . *Journal of Applied Physics*, 106(10), 104118. <https://doi.org/10.1063/1.3260242>
- [142]. Ang, C., Bhalla, A. S., & Cross, L. E. (2001). Dielectric behavior of paraelectric  $\text{KTaO}_3$ ,  $\text{CaTiO}_3$ , and  $(\text{Ln}_{1/2}\text{Na}_{1/2})\text{TiO}_3$  under a dc electric field. *Physical Review B*, 64(18), 184104. <https://doi.org/10.1103/PhysRevB.64.184104>
- [143]. Kresse, G., & Hafner, J. (1993). Ab initio molecular dynamics for liquid metals. In *Physical Review B* (Vol. 47, Issue 1, pp. 558–561). <https://doi.org/10.1103/PhysRevB.47.558>
- [144]. Kresse, G., & Hafner, J. (1994). Ab initio molecular-dynamics simulation of the liquid-metalamorphous- semiconductor transition in germanium. In *Physical Review B* (Vol. 49, Issue 20, pp. 14251–14269). <https://doi.org/10.1103/PhysRevB.49.14251>
- [145]. G. Kresse and J. Furthmüller. (1996). Efficient iterative schemes for ab initio total-energy calculations using a plane-wave basis set. *Physical Review B*, 54, 11169. <https://doi.org/10.1021/acs.jpca.0c01375>
- [146]. Kresse, G., & Furthmüller, J. (1996). Efficiency of ab-initio total energy calculations for metals and semiconductors using a plane-wave basis set. In *Computational Materials Science* (Vol. 6, Issue 1, pp. 15–50). [https://doi.org/10.1016/0927-0256\(96\)00008-0](https://doi.org/10.1016/0927-0256(96)00008-0)
- [147]. Joubert, D. (1999). From ultrasoft pseudopotentials to the projector augmented-wave method. In *Physical Review B - Condensed Matter and Materials Physics* (Vol. 59, Issue 3, pp. 1758–1775). <https://doi.org/10.1103/PhysRevB.59.1758>
- [148]. Gajdoš, M., Hummer, K., Kresse, G., Furthmüller, J., & Bechstedt, F. (2006). Linear optical properties in the projector-augmented wave methodology. *Physical Review B*, 73(4), 45112. <https://doi.org/10.1103/PhysRevB.73.045112>
- [149]. Qi, T., Grinberg, I., & Rappe, A. M. (2010). Correlations between tetragonality, polarization, and ionic displacement in  $\text{PbTiO}_3$ -derived ferroelectric perovskite solid solutions. *Physical Review B*, 82(13), 134113. <https://doi.org/10.1103/PhysRevB.82.134113>
- [150]. Yamaguchi, H., Uwe, H., Sakudo, T., & Sawaguchi, E. (1987). Raman-Scattering Study of the Soft Phonon Modes in Hexagonal Barium Titanate. *Journal of the Physical Society of Japan*, 56(2), 589–595. <https://doi.org/10.1143/JPSJ.56.589>
- [151]. Rani, A., Kolte, J., & Gopalan, P. (2015). Phase formation, microstructure, electrical and magnetic properties of Mn substituted barium titanate. *Ceramics International*, 41(10, Part B), 14057–14063. <https://doi.org/10.1016/j.ceramint.2015.07.023>

- [152]. Phan, T.-L., Zhang, P., Grinting, D., Yu, S. C., Nghia, N. X., Dang, N. V., & Lam, V. D. (2012). Influences of annealing temperature on structural characterization and magnetic properties of Mn-doped BaTiO<sub>3</sub> ceramics. *Journal of Applied Physics*, *112*(1), 13909. <https://doi.org/10.1063/1.4733691>
- [153]. Kirianov, A., Ozaki, N., Ohsato, H., Kohzu, N., & Kishi, H. (2001). Studies on the Solid Solution of Mn in BaTiO<sub>3</sub>. *Japanese Journal of Applied Physics*, *40*(Part 1, No. 9B), 5619–5623. <https://doi.org/10.1143/jjap.40.5619>
- [154]. Wang, J., Zhang, H., Li, Y., & Li, Z. (2010). Phase component and conductivities of Co-doped BaTiO<sub>3</sub> thermistors. *Journal of Materials Science: Materials in Electronics*, *21*(8), 811–816. <https://doi.org/10.1007/s10854-009-9997-x>
- [155]. Zhao, C., Huang, Y., & Wu, J. (2020). Multifunctional barium titanate ceramics via chemical modification tuning phase structure. *InfoMat*, *2*(6), 1163–1190. <https://doi.org/10.1002/inf2.12147>
- [156]. Eng, H. W., Barnes, P. W., Auer, B. M., & Woodward, P. M. (2003). Investigations of the electronic structure of d<sup>0</sup> transition metal oxides belonging to the perovskite family. *Journal of Solid State Chemistry*, *175*(1), 94–109. [https://doi.org/10.1016/S0022-4596\(03\)00289-5](https://doi.org/10.1016/S0022-4596(03)00289-5)
- [157]. Takahashi, H., Ayusawa, K., & Sakamoto, N. (1997). Microwave Dielectric Properties of Ba(Mg<sub>1/2</sub>W<sub>1/2</sub>)O<sub>3</sub>–BaTiO<sub>3</sub> Ceramics. *Japanese Journal of Applied Physics*, *36*(Part 1, No. 9A), 5597–5599. <https://doi.org/10.1143/jjap.36.5597>
- [158]. Tian, C., Yue, Z., Zhou, Y., & Li, L. (2013). Crystal structures and microwave dielectric properties of Zn,W co-substituted BaTiO<sub>3</sub> perovskite ceramics. *Journal of Solid State Chemistry*, *197*, 242–247. <https://doi.org/10.1016/j.jssc.2012.08.054>
- [159]. Zhao, F., Yue, Z., Pei, J., Zhuang, H., Gui, Z., & Li, L. (2007). Structure and Microwave Dielectric Properties of Hexagonal Ba[Ti<sub>1-x</sub>(Ni<sub>1/2</sub>W<sub>1/2</sub>)<sub>x</sub>]O<sub>3</sub> Ceramics. *Journal of the American Ceramic Society*, *90*(8), 2461–2466. <https://doi.org/10.1111/j.1551-2916.2007.01801.x>
- [160]. Tian, C., Yue, Z., Meng, S., & Zhou, Y. (2012). Structures and Microwave Dielectric Properties of Ba[Ti<sub>1-x</sub>(Co<sub>0.5</sub>W<sub>0.5</sub>)<sub>x</sub>]O<sub>3</sub> (x = 0.40-0.90) Perovskite Ceramics. *Journal of the American Ceramic Society*, *95*(5), 1645–1650. <https://doi.org/10.1111/j.1551-2916.2011.05045.x>
- [161]. Lin, Y.-J., Wang, S.-F., Chen, S.-H., Liao, Y.-L., & Tsai, C.-L. (2015). Microwave dielectric properties of (Ba<sub>1-x</sub>Sr<sub>x</sub>)(Mg<sub>0.5</sub>W<sub>0.5</sub>)O<sub>3</sub> ceramics. *Ceramics International*, *41*(7), 8931–8935. <https://doi.org/10.1016/j.ceramint.2015.03.166>
- [162]. Hu, Q., Tian, Y., Zhu, Q., Bian, J., Jin, L., Du, H., Alikin, D. O., Shur, V. Y., Feng, Y., & Xu, Z. (2020). Achieve ultrahigh energy storage performance in BaTiO<sub>3</sub>–Bi(Mg<sub>1/2</sub>Ti<sub>1/2</sub>)O<sub>3</sub> relaxor

ferroelectric ceramics via nano-scale polarization mismatch and reconstruction. *Nano Energy*, 67, 104264. <https://doi.org/10.1016/j.nanoen.2019.104264>

- [163]. Li, Y., Liu, Y., Tang, M., Lv, J., Chen, F., Li, Q., Yan, Y., Wu, F., Jin, L., & Liu, G. (2021). Energy storage performance of BaTiO<sub>3</sub>-based relaxor ferroelectric ceramics prepared through a two-step process. *Chemical Engineering Journal*, 419, 129673. <https://doi.org/10.1016/j.cej.2021.129673>

# Résumé français de la thèse

Les matériaux ferroélectriques sont caractérisés par une polarisation spontanée, et cette brisure de symétrie peut être mise à profit pour séparer des porteurs de charges photogénérés. Le défi est que la plupart des ferroélectriques ont une bande interdite supérieure à 3 eV, limitant leur absorption du spectre solaire. Généralement, la bande interdite des oxydes de structure pérovskite  $ABO_3$  peut être manipulée par substitution chimique. Dans ce travail, nous montrons que le co-dopage ( $X^{3+}$ ,  $Y^{5+}$ ) avec des ions  $3d^{z0}$  permet d'améliorer l'absorption optique tout en conservant une bonne polarisation rémanente, ce qui permet leur utilisation potentielle dans des dispositifs photovoltaïques.

Tout d'abord, un co-dopage ( $Mn^{3+}$ ,  $Nb^{5+}$ ) de  $BaTiO_3$  sur le site de  $Ti^{4+}$  ( $BaTi_{1-x}(Mn_{1/2}Nb_{1/2})_xO_3$ ) a été étudiée. Les mesures diélectriques montrent que la température de transition de phase ferroélectrique ( $T_c$ ) se déplace significativement vers des températures plus basses avec l'augmentation de la concentration de dopage. En conséquence, les propriétés ferroélectriques à température ambiante se détériorent avec l'augmentation du taux de dopage en particulier au-delà de 0,075 de dopage. La bande interdite passe de 3,4 eV pour le  $BaTiO_3$  pur à 2,5 eV pour l'échantillon  $x = 0,15$ . Par ailleurs, le début d'absorption se fait dès 1.5 eV, ce qui est prometteur pour la récupération d'énergie solaire. L'influence du taux de dopage sur la structure et la transition de phase a également été étudiée par différentes mesures en fonction de la température.

Nous avons également étudié les effets des paramètres de synthèse sur la microstructure, les propriétés électriques et optiques du système d'absorption optimale  $BaTi_{1-x}(Mn_{1/2}Nb_{1/2})_xO_3$  ( $x = 0,075$ ). La bande interdite passe de 3,0 eV à 2,7 eV en augmentant le temps et la vitesse de broyage lors du mécanobroyage du mélange des poudres de départ, alors que le début de l'absorption ne montre qu'un léger changement quelles que soient les conditions de synthèse. La température de Curie  $T_c$  présente une forte variation avec les conditions de synthèse, notamment en fonction de la vitesse de broyage. Le temps le plus court et la vitesse de broyage la plus faible

conduisent à une distribution inhomogène des dopants, provoquant une croissance des grains inhibée, une porosité plus élevée et même une certaine séparation de phases. En augmentant la vitesse et le temps de broyage, une répartition homogène des dopants est alors obtenue. Malgré la dégradation progressive des propriétés ferroélectriques avec l'homogénéité croissante des matériaux, une amélioration de l'absorption optique est obtenue. Cela peut être une bonne stratégie d'utiliser des paramètres de synthèse appropriés pour minimiser l'impact négatif sur les propriétés ferroélectriques tout en conservant de bonnes propriétés d'absorption.

L'absorption optique de différents ions trivalents et pentavalents ( $X^{3+}$ ,  $Y^{5+}$ ) co-dopant  $BaTiO_3$  est également étudiée. Les mesures de diffraction des rayons X et de spectroscopie Raman montrent que la tétragonalité et la longueur de cohérence polaire diminuent avec le codopage, impactant les caractéristiques ferroélectriques. On constate que le co-dopage ( $Co^{3+}$ ,  $Nb^{5+}$ ) montre une polarisation résiduelle plus élevée que pour les autres dopants, et le début d'absorption de ce dopage peut diminuer jusqu'à 1,5 eV. Nous avons consolidé ce résultat par des calculs de la Théorie de la Fonctionnelle Densité (DFT), qui montrent que le co-dopage avec des ions  $3d^{z0}$  permet d'insérer des niveaux intra-gap qui vont être responsables de la réduction 'artificielle' de la bande interdite. Ceci est tout à fait en accord avec nos observations expérimentales. La photoconductivité mesurée confirme aussi que le dopage ( $Co^{3+}$ ,  $Nb^{5+}$ ) a une absorption supérieure aux autres couples de dopants. Ce travail propose une stratégie d'amélioration de l'absorption optique qui peut être mise à profit pour l'application des ferroélectriques dans des dispositifs optoélectroniques.

Enfin, différents ions divalents et hexavalents ( $X^{2+}$ ,  $Y^{6+}$ ) sont également considérés pour le co-dopage du  $BaTiO_3$  sur le site du  $Ti^{4+}$  ou sur les sites  $Ba^{2+}$  et  $Ti^{4+}$  à la fois. Il est très difficile d'obtenir la phase pure de la structure pérovskite  $ABO_3$  exempte de phases parasites et le dopage altère considérablement les propriétés diélectriques et ferroélectriques. Bien que dans certains systèmes des propriétés peuvent être améliorées comme l'efficacité du stockage d'énergie renforcée par le co-dopage ( $Zn^{2+}$ ,  $Mo^{6+}/W^{6+}$ ) sur le site B, quel que soit le co-dopage, l'absorption optique ne montre qu'un léger changement, ce qui contraste avec nos résultats de DFT. Du fait de l'existence des phases parasites, ces systèmes nécessitent encore d'être améliorés à l'avenir car d'après

nos résultats de DFT, ils pourraient être très prometteurs pour absorber largement l'énergie du spectre solaire.